

# **Hydrate formation in near surface ocean sediments**

Thesis submitted for the degree of Doctor of Philosophy at  
the University of Leicester

by

**Ameena Penelope Camps BSc MSc**

**Department of Geology**

**University of Leicester**

**September 2008**

UMI Number: U237970

All rights reserved

INFORMATION TO ALL USERS

The quality of this reproduction is dependent upon the quality of the copy submitted.

In the unlikely event that the author did not send a complete manuscript and there are missing pages, these will be noted. Also, if material had to be removed, a note will indicate the deletion.



UMI U237970

Published by ProQuest LLC 2013. Copyright in the Dissertation held by the Author.  
Microform Edition © ProQuest LLC.

All rights reserved. This work is protected against  
unauthorized copying under Title 17, United States Code.



ProQuest LLC  
789 East Eisenhower Parkway  
P.O. Box 1346  
Ann Arbor, MI 48106-1346

*For my Grandmother, Gladys.*

*Whose warm smile continues to light the darkest of days.*

*Forever in my heart.*

A. P. C.

# **Hydrate formation in near surface ocean sediments**

by

**Ameena Penelope Camps BSc MSc**

**Department of Geology, University of Leicester**

Rising carbon dioxide (CO<sub>2</sub>) atmospheric emissions are currently contributing to climate change. Underground storage of CO<sub>2</sub> is one proven method which may help to reduce atmospheric emissions. Conventional warm, deep underground storage practices involve the storage of supercritical CO<sub>2</sub>. An additional storage method, receiving little attention is the storage of CO<sub>2</sub> as a liquid and hydrate, which may offer benefits over conventional methods. Hydrates are crystalline ice-like solids composed of a cage of 'host' water molecules and one or more 'guest' molecules. The majority of natural hydrates are composed of methane, existing worldwide along continental margins and in permafrost settings, receiving wide, varied interest. The aims of this research project were to assist in understanding hydrate formation, stability, and scientific aspects of CO<sub>2</sub> storage as a liquid and CO<sub>2</sub> hydrate. These have been addressed by two investigatory pathways: hydrate stability modelling, and hydrate formation within sediments (in synthetic CO<sub>2</sub> hydrates and natural methane hydrates). Developed computer models predict large regions offshore Western Europe with the potential to store considerable volumes of CO<sub>2</sub> as a hydrate. Laboratory experiments have also shown CO<sub>2</sub> hydrate to form rapidly and relatively easily in sandy sediments, cementing the sediment grains. In water-rich environments hydrate appears to create pore-filling cement impeding further CO<sub>2</sub> flow to underlying sediments, which may aid trapping of an underlying liquid store. Fortunate acquisition of natural hydrate cores from Cascadia Margin also allowed investigation of natural methane hydrate formation; revealing a number of well-preserved methane hydrate morphologies, and complex brine filled pore networks within the hydrate, resulting from different rates of growth. Results highlight a number of research areas, which need addressing through further investigations. However, these preliminary investigations support CO<sub>2</sub> storage as a hydrate as a potential feasible storage method, and this method should be pursued further as an emissions reducing mitigation strategy.

## Acknowledgements

The research for this thesis has been undertaken at the British Geological Survey, Keyworth, and the University of Leicester's Department of Geology between September 2003 and September 2007. All experimental investigations have taken place in the British Geological Survey laboratories, and computer modelling has been split between institutes including BGS, Edinburgh, Leicester University, but primarily at BGS, Keyworth.

I owe a debt of gratitude to my supervisors Prof. Mike Lovell from the University of Leicester, and Dr Christopher Rochelle from the BGS. This research would not have been possible without their supervision, guidance, patience, understanding and most importantly, friendship throughout the past four years. You truly are the best supervisors a student could ask for. Thank you.

I would like to thank Dr David Long, from the BGS, Edinburgh, for providing me with his hydrate stability computer program `hydcalc.exe`, for temperature, pressure and geothermal gradient data from the Rockall Trough and the Faeroe-Shetland Channel, and for his assistance in the construction of `hydcalcCO2.exe`. I would like to thank Mr Tony Milodowski, at the BGS, Keyworth, for his SEM and mineralogical expertise, for operating the SEM during hydrate investigations, and for his help and assistance throughout this study. I would also like to thank Mr Keith Bateman, Dr Peter Jackson, Dr David Gunn, and Dr John Rees from the BGS, Keyworth, and Dr Mike Norry, Prof. Andy Saunders, and Mrs Janette Thompson from the University of Leicester's Department of Geology, for their help and advice during this research project.

Special thanks go to Dr Tim Brewer from the University of Leicester's Department of Geology for his advice, assistance, and nagging during this research project, and for his moans, quick wit and laughter. Sleep well.

I would also like to stress my deepest gratitude to the University of Leicester and BGS hydrate team. What a team! Working with you all has been an honour and a privilege, and I will always remember our discussions shared over a cup of tea, or a hearty pint.

Thanks also go to Mr John Frank Williams for his kind words of advice, his warm friendship, and for keeping me sane in the strange world of academia.

My final and greatest thanks go to my dear LLM, king of kings. Your light, love, compassion, empathy, and deepest friendship, have given me the hope I have longed for in the unfathomable, and often painful world in which we live. Thank you for finding me. I wish for the day when the time stealers can no longer play their wicked games.

I would like to acknowledge BODC for supplying bathymetry and CTD data, and ICES and Ifremer for CTD cast data. Erik Lindberg is thanked for the use of the Sintef CO<sub>2</sub> density model.

I also acknowledge the Natural Environment Research Council for funding under grant NER/S/A/2003/11923, the Society of Petrophysicists and Well-Log Analysts (SPWLA), and the BGS - University Collaboration Advisory Committee for financial support.

# CONTENTS

Figure Index	1-7
--------------	-----

## CHAPTER 1 Introduction

1. Introduction	8-13
-----------------	------

## CHAPTER 2 The Role of Anthropogenic and Natural Carbon Stores in Climate Change

2. The Role of Anthropogenic and Natural Carbon Stores in Climate Change	14-48
2.1 Climate Change and the Greenhouse Effect	16-23
2.2 Carbon Capture and Storage	23-34
2.2.1 Carbon Capture	23-27
2.2.1.1 <i>Flue gas separation</i>	24-26
2.2.1.2 <i>Oxy-fuel combustion</i>	26-27
2.2.1.3 <i>Pre-combustion capture</i>	27
2.2.2 Carbon Storage	27-34
2.2.2.1 <i>Ocean disposal</i>	28-30
2.2.2.2 <i>Underground Storage</i>	30-34
2.3 Natural Gas Hydrates	34-46
2.3.1 A brief history of hydrates	35
2.3.2 What are hydrates?	35-37
2.3.3 Where are hydrates found?	37-39
2.3.4 Hydrate formation and its investigation	39-43
2.3.5 Interest in hydrates	43-46
2.4 Conclusions	46-48

## CHAPTER 3 Mapping Hydrate Stability Zones

3. Mapping Hydrate Stability Zones	49-105
3.1 Methodology	52-60
3.1.1 Hydrate stability program construction	52-53
3.1.2 Data acquisition and interpretation	54-60
3.1.2.1 <i>Data for the north and north-west of Scotland</i>	54-55
3.1.2.2 <i>Data for offshore Western Europe</i>	55-60
3.2 Mapping Hydrate Stability Zones Offshore Scotland	61-72
3.2.1 Oceanographic Setting	61-62
3.2.2 Predicted Hydrate Stability Zones	62-67
3.2.3 Discussion	67-71
3.2.3.1 <i>Evidence for natural methane hydrate</i>	69-70
3.2.3.2 <i>Carbon dioxide storage potential</i>	70-71
3.2.4 Conclusions	71-72

3.3	Mapping Hydrate Stability Zones offshore western Europe	73-105
3.3.1	Oceanographic Setting	73-74
3.3.2	Carbon dioxide hydrate stability	75-76
3.3.3	Methane hydrate stability	76-77
3.3.4	CO <sub>2</sub> density and solubility	77-86
	3.3.4.1 <i>CO<sub>2</sub> and seawater density at the base of the hydrate stability zone</i>	78-86
3.3.5	Discussion	86-95
	3.3.5.1 <i>Data collection and interpretation</i>	86-88
	3.3.5.2 <i>Difference in CO<sub>2</sub> and CH<sub>4</sub> hydrate stability zone thickness</i>	88-90
	3.3.5.3 <i>Significance of results</i>	90-94
3.3.6	Conclusions	94-95
3.4	Modelling and contouring errors	96-103
3.4.1	Use of CSMHYD for pressure predictions	96-97
3.4.2	Constants derived from CSMHYD	97-99
3.4.3	Sensitivity to pressure, temperature and geothermal gradient	99
3.4.4	1.1°C offset	100-101
3.4.5	Density and solubility	101
3.4.6	Contouring grid errors	102-103
3.5	Conclusions	103-105

## CHAPTER 4 Experimental Procedures

4.	Experimental procedures	106-115
4.1	Hydrate sample formation and preservation	107-108
4.2	Visual observations	109-111
4.3	Sample handling and SEM imaging	111-115

## CHAPTER 5 Laboratory Investigation of Carbon Dioxide Hydrate

5.	Laboratory Investigation of Carbon Dioxide Hydrate	116-159
5.1	Different Ice morphologies	117-122
5.2	CO <sub>2</sub> hydrate morphologies and salt inclusion during formation	122-146
	5.2.1 Investigated CO <sub>2</sub> hydrate samples	124-138
	5.2.2 Different CO <sub>2</sub> hydrate morphologies	139-141
	5.2.3 Hydrate formation effects on surrounding sediment	141-146
5.3	Discussion	147-159
	5.3.1 CO <sub>2</sub> hydrate morphologies and salt fabrics	147-150
	5.3.2 Salt inclusion during other mineralization processes	150-151
	5.3.2.1 <i>High-temperature salt inclusion</i>	150-151
	5.3.2.2 <i>Formation of sea ice</i>	151

5.3.3	Hydrate formation within sediments	151-153
5.3.4	Significance of experimental results	153-157
5.3.4.1	<i>Storage of CO<sub>2</sub></i>	153-155
5.3.4.2	<i>Desalination</i>	155
5.3.4.3	<i>Natural hydrate</i>	155-157
5.4	Conclusions	157-159

## CHAPTER 6 Investigation of Natural Methane Hydrate

6.	Investigation of Natural Methane Hydrate	160-186
6.1	Introduction	161-162
6.2	Cascadia Margin	162-166
6.2.1	Oceanographic Setting	162-163
6.2.2	Geological Setting	163
6.2.3	Specific site location details	164-166
6.2.3.1	<i>Site U1327</i>	164-165
6.2.3.2	<i>Site U1328</i>	165-166
6.3	Initial observations of hydrate cores	166-169
6.4	BSEM imaging	170-177
6.4.1	Natural methane hydrate morphologies and related salt fabrics	170-173
6.4.2	Natural methane hydrate salt fabrics	174-177
6.5	Discussion	178-185
6.6	Conclusions	185-186

## CHAPTER 7 Discussion

7.	Discussion	187-204
7.1	Are there suitable sites offshore Western Europe for carbon storage as a liquid and hydrate, and if so where are they?	188-193
7.2	What short-term effects will hydrate formation have on the hosting sediment? and how do sediment-hosted hydrates form?	194-196
7.3	Is carbon storage as CO <sub>2</sub> hydrate within sub-seabed sediments a feasible storage method?	196-199
7.4	What potential problems could be encountered?	199-202
7.5	What gaps remain in our knowledge?	203-204
7.6	Are there any further implications to this research?	204

**CHAPTER 8 Conclusions**

8. Conclusions	205-211
<b>References</b>	212-236
<b>Units</b>	237
<b>Publications</b>	238-239
<b>Presentations</b>	239-240
<b>Press Releases</b>	240

**APPENDIX A****APPENDIX B**

# FIGURE INDEX

## CHAPTER 1 Introduction

## CHAPTER 2 The Role of Anthropogenic and Natural Carbon Stores in Climate Change

**Figure 2.1.** Global temperature changes over the past 140 years, and the past 1000 years in the Northern Hemisphere (taken from IPCC, 2001). 17

**Figure 2.2.** Global carbon dioxide, nitrous oxide, and methane concentrations since 1000AD. Sulphate aerosol concentrations are also included since 1400 (taken from IPCC, 2001). 18

**Figure 2.3.** Schematic diagram of proposed storage of CO<sub>2</sub> as a liquid and hydrate in sub-seabed cool aquifers (courtesy of Dr D Long, and the British Geological Survey). 34

**Figure 2.4.** Worldwide map showing approximate locations of known and inferred gas hydrates. Adapted from Knelvolden (1998) and Kvenvolden & Lorenson (2001). 39

## CHAPTER 3 Mapping Hydrate Stability Zones

**Figure 3.1.1.** Model flow diagram for hydcalcCO2.exe expressing processes involved in the calculation of the depth to the base of the CO<sub>2</sub> hydrate stability zone. 53

**Table 3.1.** Intermediate temperature gradient equations applied to bathymetry data between latitude bands of 56°N and 60°N to smooth the bottom water temperature grid. 58-59

**Figure 3.1.2(a)** Bottom water temperature (°C) grid for hydrate and density predictions offshore Western Europe. **(b)** Ocean temperature (°C) profiles from collected CTD data for regions highlighted in (a). 60

**Figure 3.2.1(a)** Bathymetry of the British and Icelandic Continental Shelves, showing the line of cross section, and regional water masses with current pathways (adapted from Howe et al, 2005). **(b)** Cross section of Bottom Water Temperatures across the offshore study region, created from CTD data used in program predictions. 63

**Figure 3.2.2 (a)** Bathymetric map offshore UK showing the position of the study area north of Scotland. **(b)** Faeroe-Shetland Channel CTD temperature profile with annotated regional water masses, **(c)** Faeroe-Shetland Channel contoured bathymetry and **(d)** Contoured bottom water temperatures taken from used dataset. 64

<b>Figure 3.2.3 (a)</b> Bathymetric map offshore UK showing the position of the study area west of Scotland. <b>(b)</b> Northern Rockall Trough CTD temperature profile with annotated regional water masses, <b>(c)</b> Northern Rockall Trough contoured bathymetry and <b>(d)</b> Contoured bottom water temperatures taken from Rockall Trough dataset.	65
<b>Figure 3.2.4.</b> Depth to the base of the methane hydrate stability zone below the seabed (m) in the Faeroe-Shetland Channel <b>(a)</b> and the Rockall Trough <b>(b)</b> .	66
<b>Figure 3.2.5.</b> Depth to the base of the carbon dioxide stability zone below the seabed in the Faeroe-Shetland Channel <b>(a)</b> and the Rockall Trough <b>(b)</b> .	67
<b>Figure 3.2.6.</b> Histogram of calculated geothermal gradients offshore north and west of Scotland with an added normal curve.	69
<b>Figure 3.3.1.</b> Water depth below sea-level (m) off the western European Continental Shelf.	74
<b>Figure 3.3.2.</b> Predicted depth to the base of the CO <sub>2</sub> hydrate stability zone offshore western Europe (m).	75
<b>Figure 3.3.3.</b> Predicted depth (m) to the base of the methane hydrate stability zone offshore Western Europe.	77
<b>Figure 3.3.4.</b> Carbon dioxide density (kg/m <sup>3</sup> ) at the base of the CO <sub>2</sub> hydrate stability zone off the western European Continental Shelf.	80
<b>Figure 3.3.5.</b> Contour plot of the variation of CO <sub>2</sub> density (kg/m <sup>3</sup> ) with pressure (depth in metres) and temperature (°C).	81
<b>Figure 3.3.6.</b> Seawater (35ppm) density (kg/m <sup>3</sup> ) at the base of the carbon dioxide hydrate stability zone off the western European continental shelf.	82
<b>Figure 3.3.7.</b> Contour plot of seawater density (kg/m <sup>3</sup> ) with pressure (depth in metres) and temperature (°C).	83
<b>Figure 3.3.8.</b> Density difference between liquid CO <sub>2</sub> and seawater (kg/m <sup>3</sup> ) off the western European Continental Shelf.	85
<b>Figure 3.3.9.</b> Temperature (°C) profiles for <b>(a)</b> Norwegian Sea and Baltic Sea <b>(b)</b> Iberian Basin, Bay of Biscay and offshore the Moroccan coast <b>(c)</b> Offshore the west of the British Isles (50°N – 56°N).	87
<b>Figure 3.3.10.</b> Depth-Temperature stability diagram for CO <sub>2</sub> hydrate and CH <sub>4</sub> hydrate in pure water and seawater (pressure represented as depth (m)) (Sloan,1998).	89
<b>Figure 3.3.11.</b> Predicted depth to the base of the methane hydrate stability zone (m) offshore western Europe with identified sites of natural methane hydrate occurrence (inferred and sampled).	92

<b>Figure 3.4.1.</b> Graphical comparison of carbon dioxide P-T predicted using CSMHYD (●), experimental results (+) from various sources provided in Sloan (1998) and pressure predictions using HWHydrateGUI (◇).	97
<b>Figure 3.4.2 (a)</b> Pressure predictions for carbon dioxide hydrate results from Sloan's model (●) and their <b>(b)</b> comparison with constants derived from regression of such data (constants 1 ( ), constants 2 (□), constants 3 (*)).	98
<b>Figure 3.4.3.</b> Depth-Temperature stability diagram for CO <sub>2</sub> hydrate and CH <sub>4</sub> hydrate in pure water and seawater (pressure represented as depth (m)). Repeat of Figure 3.3.10.	101

## CHAPTER 4 Experimental Procedures

<b>Figure 4.1(a).</b> Schematic diagram of a simple batch experiment; with water and sand in a PTFE liner inside a stainless steel pressure vessel, which when sealed is pressurised with CO <sub>2</sub> . <b>(b)</b> Image of batch experiments inside the cooled incubator.	108
<b>Table 4.1.</b> Step-by-step experimental procedures for CO <sub>2</sub> hydrate sample formation and preservation.	110
<b>Figure 4.2(a)</b> Image of pressure vessel containing 4 plastic tubes initially totally filled with seawater ice ball/sediment mixes before pressurisation and experimental run time. <b>(b)</b> Sediment/CO <sub>2</sub> hydrate sample with a domed base. <b>(c)</b> Pressure vessel containing sample with a very disturbed surface texture after depressurisation. <b>(d)</b> Sample from (c) with a surface water ice layer and some hoar frost.	111
<b>Figure 4.3.</b> Image of the Leo 435VP SEM with a fitted cryogenic sample handling cold stage facility and the designed sample handling transfer box.	112
<b>Figure 4.4.</b> Diagram showing the interior construction of the BSEM and the sample/electron beam interaction, expressing the differing sample penetration depths of electrons used to construct images.	113

## CHAPTER 5 Laboratory Investigation of Carbon Dioxide Hydrate

<b>Figure 5.1(a)</b> Quartz dominated sand matrix filled with water ice. <b>(b)</b> Spherical ice balls with radiating fibrous hoar frost ice crystals. <b>(c)</b> Hexagonal ice plates formed between sediment grains. <b>(d)</b> Spherical ice crystals formed on the surface of a sand grain. <b>(e)</b> Spherical ice crystals, hydro-halite and CO <sub>2</sub> hydrate formed around a sediment grain. <b>(f)</b> Hydro-halite within a CO <sub>2</sub> hydrate/sediment matrix.	119
--	-----

- Figure 5.2(a)** Hydro-halite within a CO<sub>2</sub> hydrate/ sediment matrix. **(b)** ‘Flower bouquet’ of ice crystals on the surface of CO<sub>2</sub> hydrate with surrounding ice balls and small salt globules. **(c)** Stacked hydro-halite crystals with ice balls, flowers and plates. **(d)** Branches of stacked hydro-halite crystals (c) forming a skeletal leaf pattern within a sediment pore. **(e)** Higher magnification image of (d) showing branch-like nature of the hydro-halite crystals and surrounding ice balls. **(f)** Hexagonal ice plate lying on the surface of CO<sub>2</sub> hydrate with salt globules and ice balls. 120
- Figure 5.3(a).** EDXA analysis of salt precipitated between hydrate and hydro-halite crystals. **(b)** EDXA analysis of hydro-halite crystals. **(c)** EDXA analysis of CO<sub>2</sub> hydrate crystals. 121
- Figure 5.4.** Chart to show the investigatory pathways followed for each experimental run. 124
- Figure 5.5(a)** BSEM image of carbon dioxide hydrate needles forming downwards into quartz rich sand with salt ‘veins’ separating and included within the formed hydrate. **(b)** BSEM image of a part of (a) at higher magnification of identifying dendritic radiating salt needles forming a delicate ‘net-like’ salt fabric. **(c)** BSEM image of CO<sub>2</sub> hydrate needles with salt precipitated along grain boundaries and included within. **(d)** BSEM image of the same area as (a) after ablating some of the hydrate sample. 126
- Figure 5.6(a)** BSEM image of CO<sub>2</sub> hydrate formed within coarse quartz rich sand using seawater spherical ice balls. **(b)** Higher magnification BSEM image of CO<sub>2</sub> hydrate crystals formed within a void of a CO<sub>2</sub> hydrate spherical shell which was previously filled by seawater ice. **(c)** Lower magnification BSEM image of (b) after 30 minutes of ablation. **(d)** BSEM image of granoblastic ‘melt structure’ CO<sub>2</sub> hydrate. 128
- Figure 5.7(a)** BSEM image of ‘holey’ hydrate within a CO<sub>2</sub> hydrate ‘curl’. **(b)** BSEM image of ‘Pea-pod’ hydrate. **(c)** BSEM image of (b) after etching at -140°C. **(d)** CL image of (b) showing the different phases which seem to be present. 129
- Figure 5.8(a)** BSEM image of crystalline CO<sub>2</sub> hydrate formed within medium quartz rich unconsolidated sand dampened with artificial seawater solution. **(b)** BSEM image of CO<sub>2</sub> hydrate crystals forming around quartz sand grains, with a larger crystal growing outwards into a gas filled pore space. 131
- Figure 5.9(a)** BSEM image of a CO<sub>2</sub> hydrate lens formed within medium grained quartz rich sand near the interface with Wyoming bentonite clay. **(b)** BSEM image of pore-filling CO<sub>2</sub> hydrate cementing sand grains. **(c)** BSEM image of pore-filling ice pseudomorphs of CO<sub>2</sub> hydrate enveloping a sand grain with pronounced intergranular honeycomb salt and clay fabrics between hydrate crystals after ablating to -100°C. **(d)** BSEM image of granoblastic CO<sub>2</sub> hydrate along the clay-sand interface. **(e)** BSEM image of acicular CO<sub>2</sub> hydrate. **(f)** BSEM image of the sand-clay interface after full ablation to 0°C showing the nature of clay and salt fabrics within the sample. 133

**Figure 5.10(a)** BSEM image of CO<sub>2</sub> hydrate formed as a lens within medium grained quartz rich sand (355-600 µm) fully saturated with deionised water. **(b)** ‘Melt-structure’ polyhedral CO<sub>2</sub> hydrate crystals formed alongside a sediment grain. **(c)** ‘Vesicular’ CO<sub>2</sub> hydrate which has grown into a large void within the sample. **(d)** Lower magnification image of (c). 135

**Figure 5.11(a)** BSEM image of crystalline deionised water CO<sub>2</sub> hydrate cementing dampened quartz rich sand. **(b)** Lower magnification image of (a) showing sand grains completely encrusted with euhedral CO<sub>2</sub> hydrate crystals. 136

**Figure 5.12(a)** BSEM image of euhedral CO<sub>2</sub> hydrate crystals formed within artificial seawater. **(b)** Higher magnification BSEM image of part of (a) identifying densely packed hydrate crystalline grains with small salt inclusions within the hydrate crystals. **(c)** Lower magnification BSEM image (a). **(d)** BSEM image of remaining salt fabric present within the sample after ablation for 60 minutes. 138

**Figure 5.13(a)** BSEM image of CO<sub>2</sub> hydrate needles forming hydrate sheets on contact with underlying quartz rich sand. **(b)** BSEM image of CO<sub>2</sub> hydrate growing up to a sand grain separated by a layer of ice. **(c)** BSEM image of a transition between hydrate and ice (formerly seawater) in the lower sediment layer marked by a growth front representing the self-limiting nature of hydrate formation. **(d)** BSEM image revealing sand and salt fabrics after full ablation of hydrate and ice. 143

**Figure 5.14(a)** BSEM image of euhedral crystalline pore-filling CO<sub>2</sub> hydrate cementing quartz rich sand grains formed within a CO<sub>2</sub> rich system. **(b)** Lower magnification BSEM image of (a). **(c)** BSEM image after partial ablation showing pore-filling ice pseudomorphs with pronounced intergranular honeycomb salt and clay fabrics, formed in a water rich system. **(d)** BSEM image of euhedral, crystalline deionised water, CO<sub>2</sub> hydrate cementing quartz rich sand grains formed in a CO<sub>2</sub> rich system. **(e)** BSEM image of hydrate formed as pore-filling cement within the sand horizon, as acicular crystals growing from the sand into the clay horizon, and as discrete crystals formed from individual nucleation point within the clay. **(f)** BSEM image of the sand-clay interface after full ablation showing the nature of clay and salt fabrics within the sample. 146

**Table 5.1.** The range of carbon dioxide hydrate and salt fabrics seen during BSEM and EDXA analysis of laboratory formed samples. Explanations for these resulting fabrics are proposed to be different formation rates as a result of formation conditions. 148

**Figure 5.15.** Diagram to show simplified version of the proposed hydrate growth model for the formation of imaged salt fabrics. 149

**Figure 5.16.** Proposed sediment-hosted hydrate pore growth models for CO<sub>2</sub> hydrate formed during this studies experimental investigations. 152

**Figure 5.17.** Pressure (depth) - Temperature pure methane hydrate stability plot derived from CSMHYD.exe (Sloan, 1998) for varying halite concentrations. 157

## CHAPTER 6 Laboratory Investigation of Natural Methane Hydrate

**Figure 6.1.** Map showing the locations of Expedition 311 Cascadia Margin hydrate investigation sites offshore Oregon. Taken from IODP, 2006. 164

**Figure 6.2(a)** Digital image of split 1328B core. BGS copyright. **(b)** Annotated digital image of the split 1328B core, showing the 2 halves used for sub-sampling. 168

**Figure 6.3(a)** Digital image of split 1327C core. BGS copyright. **(b)** Annotated digital image of the split 1327C core, showing the 2 halves used for sub-sampling. 169

**Figure 6.4(a)** BSEM image showing a contact zone between ‘dense’ methane hydrate and gas-rich ‘micro-porous’ methane hydrate, with increasing trapped gas bubble size away from the contact zone. **(b)** BSEM image of ‘crystalline’ methane hydrate showing interstitial precipitated salt along grain boundaries. **(c)** BSEM image of ‘acicular’ methane hydrate formed within fine-grained sediment. **(d)** BSEM image showing methane hydrate ‘laminae’ within fine-grained sediment. 171

**Figure 6.5(a)** BSEM image of gas-rich ‘micro-porous’ methane hydrate formed around a gas bubble. **(b)** BSEM image of methane hydrate ‘pods’ formed within fine-grained sediment. **(c)** BSEM image of ‘vesicular’ hydrate growing within fine-grained sediment and into an open gas-filled pore space. **(d)** BSEM image of ‘crystalline’ hydrate with inter-granular pore spaces filled with precipitated salt and clay. 172

**Figure 6.6(a)** BSEM image of ‘bubbly’ ice from 1327C. Small proto-pyrite-framboids can be seen within the sample. **(b)** BSEM image of ‘bubbly’ ice, from 1327C, surrounding and filling a foraminifera. 173

**Figure 6.7.** BSEM of methane hydrate sub-sample from 1328B, showing the distribution of different hydrate morphologies present within the sample, formed around micro-channels. 175

**Figure 6.8(a)** BSEM of sample area shown in Figure 6.7 after partial sample ablation revealing inter-granular salt (brine) filled pore networks, and different salt concentrations and distributions present within the sample. **(b)** BSEM higher magnification image of the inter-granular pore networks. **(c)** BSEM image showing revealed salt between ‘dense’ hydrate after partial sample ablation. 176

**Figure 6.9** (a) 3D BSEM of dendritic salt crystals which have formed ‘honeycomb’ salt fabrics representing brine filled inter-granular pore-networks between euhedral and subhedral methane hydrate crystals. (b) Lower magnification 3D BSEM image showing ‘honeycomb’ salt fabrics and their relation to the underlying fine-grained sediment. (c) Lower magnification 3D BSEM image showing different salt fabrics revealed after sample ablation. 177

**Figure 6.10** (a) Combined panoramic BSEM image showing a full c.12mm methane hydrate sample (part of which has been seen previously in Figure 6.7). (b) Annotated full scale sketch of (a) showing the distribution of different methane hydrate morphologies, different salt fabrics and the fine-grained sediment. 179

**Figure 6.11(a)** BSEM image of pore-filling ice pseudomorphs of CO<sub>2</sub> hydrate enveloping a sand grain with pronounced intergranular honeycomb salt and clay fabrics between hydrate crystals after partial ablation. (b) BSEM image of acicular carbon dioxide hydrate formed within a water-rich environment after partial ablation. 181

**Figure 6.12.** BSEM image of a sub-sample from U1327C, showing a sandy matrix filled with gas-rich ‘bubbly’ ice thought to represent disseminated methane hydrate prior to sample handling during recovery. 182

## CHAPTER 7 Discussion

**Figure 7.1.** The predicted base to the hydrate stability zone (m) with posted major CO<sub>2</sub> sources along the Western European coastline within close proximity to the CO<sub>2</sub> hydrate stability zone. CO<sub>2</sub> source emissions are in Tonnes per year and sourced data was collected between 1996 and 2002 (Holloway, 1996; 2002). 193

**Figure 7.2.** Schematic diagram of the sub-sea hydrate stability zone (HSZ). If there was considerable warming of sub-seabed sediments within this zone, the base of the HSZ would rise into shallower sediments, reducing the volume of the HSZ. 202

## CHAPTER 8 Conclusions

# **CHAPTER 1**

## **Introduction**

## 1. Introduction

The sequestration of carbon dioxide (CO<sub>2</sub>) is actively being considered as a method of reducing atmospheric emissions from power plants. Such emissions are considered as one of the factors contributing to current global warming trends. Carbon dioxide atmospheric concentrations have increased by a third since the industrial revolution, leading to an increased temperature of 0.6 °C in the last century. Should no action be taken to prevent emissions increase, temperatures could rise by as much as 5.8 °C this century (DTI, 2003; IPCC, 2005). The sequestration process involves capture of CO<sub>2</sub> from industrial gases and storage of such. Various storage methods have been proposed, including storage on the bed of oceans as a liquid or hydrate (Marchetti, 1977; Murray et al., 1996), direct injection into the oceans (Haugan & Drange, 1992), injection into deep aquifers, exhausted oil/gas reservoirs and, into shallower sediments (e.g. Baklid et al., 1996; IEA GHG, 1998; IPCC, 2005). CO<sub>2</sub> migration into shallower sediments may still occur during deep storage; therefore investigation of CO<sub>2</sub> interactions with shallower sediments is crucial for both deep and shallow storage validation. Effective long-term storage will depend on stable trapping of the injected CO<sub>2</sub>. This could be by physical trapping beneath an impermeable caprock, by solubility trapping in formation pore waters, or by mineralogical trapping in secondary precipitates (e.g. Bachu et al., 1994; Rochelle et al., 2006). Under certain pressure/temperature conditions CO<sub>2</sub> hydrate forms. Sequestered CO<sub>2</sub>, either migrating into, or injected into shallower sediments, may rapidly form CO<sub>2</sub> hydrate providing a self-sealing storage mechanism. The immobile hydrate would be trapped underground, preventing further migration to surface sediments (Kiode et al., 1997; House et al., 2006; Camps et al., 2006).

Hydrates (also known as clathrates) are ice-like, crystalline structures composed of water and one or more host gas molecules. Natural hydrates on Earth are dominated by methane hydrate; however, natural CO<sub>2</sub> hydrate has been discovered in the Okinawa Trough, offshore Japan (Sakai et al, 1990). Since their reported discovery in 1810 by Sir Humphrey Davy (see review Sloan, 1998), hydrates have been researched in the laboratory. Interest in hydrate research has rapidly gained pace in more recent years, and is moving into the foreground of global climate debates. Current worldwide interest includes their role in past and present climate change, in the carbon cycle, as a

future energy resource (for natural gas extraction), as a desalination agent, as a trigger of submarine landslides, and as a carbon dioxide store. Although current research in hydrates is extensive and varied, there remains a general lack of understanding of the processes and effects of hydrate formation within sediments. A thorough understanding of hydrate formation within sediments, including the effects of pressure, temperature, sediment characteristics, and salinity on hydrate formation, is critical for many research disciplines such as for the earth system science, CO<sub>2</sub> storage, natural hazards, and energy community.

The rationale behind this PhD study is to understand key scientific aspects underpinning the feasibility of carbon storage as CO<sub>2</sub> hydrate within sub-seabed sediments. To help to scope the potential of this storage approach this PhD study investigates the effects of temperature; pressure, sediment characteristics, and salinity on hydrate formation with an aim to answer the following questions:

- Are there suitable sites offshore Western Europe for carbon storage as liquid CO<sub>2</sub> and CO<sub>2</sub> hydrate?
- What short-term effects will hydrate formation have on the hosting sediment?
- How do sediment-hosted hydrates form?
- Is carbon storage as CO<sub>2</sub> hydrate a feasible storage method?

Research will use experimental and modelling techniques to investigate hydrate formation and stability within sediments. The findings from this investigation are presented in the following thesis chapters, providing a background to the study, a description of the methods used, the results produced, the limitations and implications of such, and the importance of further research to expand knowledge in this field.

This thesis has been written as a series of chapters, divided into research themes, with each chapter containing a detailed discussion of each theme. These chapters have then been divided into sub-chapters. An overview of each chapter is provided below.

## **Chapter 2: The Role of Anthropogenic and Natural Carbon Stores in Climate Change.**

This chapter provides a detailed overall background to the whole study and highlights the importance of the research in a global context. This introduces climate change science, the current political agenda of global warming, the likely costs involved and environmental consequences if global temperatures continue to rise at the present rate. The chapter then discusses possible solutions to the global warming problem, including carbon dioxide capture and storage. This leads to a sub-chapter on carbon capture and storage (CCS), presenting different CO<sub>2</sub> capture and storage methods, and introducing the more novel method of storage as liquid CO<sub>2</sub> and CO<sub>2</sub> hydrate. The following sub-chapter then discusses background knowledge on both methane and carbon dioxide hydrate, discussing natural occurrence, formation conditions, and a general overview of previous research. The chapter draws to a close with bulleted conclusions drawn from the preceding sub-chapters.

## **Chapter 3: Mapping Hydrate Stability Zones.**

This chapter relates to computer modelling investigations and introduces the specific background of the research. This leads to a sub-chapter presenting the methodology, describing the development of each model and how data have been acquired and interpreted for hydrate stability zone calculations. The following sub-chapters presents the findings for the two modelling investigations undertaken: the initial investigation mapping the Faeroe-Shetland Channel and the northern Rockall Trough, and the expansion of this research to offshore the western European continental margin. Each of these sub-chapters provides the oceanographic setting of the region, the modelling results, a discussion of the findings, and bulleted conclusions. The final sub-chapters discuss possible errors associated with the models and subsequent contouring of calculated results, and the overall conclusions of the results.

#### **Chapter 4: Experimental Procedures.**

This chapter provides an overall introduction to the following experimental chapters (Chapters 5 and 6), detailing laboratory experimental procedures and materials used during the production of hydrate samples, sample handling practices and the development of such with increasing experience, and cryogenic-BSEM techniques used during investigations, including the advantages of the used techniques.

#### **Chapter 5: Laboratory Investigation of Carbon Dioxide Hydrate.**

Carbon dioxide hydrate experimental investigation. This chapter begins with a brief introduction followed by a sub-chapter on the ice morphologies identified during the BSEM investigations whose identification was necessary to help distinguish between ices and hydrate. Carbon dioxide hydrate experimental results are presented with a sub-chapter on various CO<sub>2</sub> hydrate morphologies and salt fabrics discovered; these are presented through detailed sample descriptions, and a discussion of the sediment/hydrate interactions within these samples. This is followed by a detailed discussion of the findings and the significance these results may have on the wider research community, together with bulleted conclusions.

#### **Chapter 6: Laboratory Investigation of Natural Methane Hydrate.**

Investigation of natural methane hydrate recovered from sub-seabed sediments in the Cascadia Margin, during IODP expedition 311. This chapter begins by introducing Cascadia Margin, offshore Oregon, providing its oceanographic and geological setting, and details on the hydrate cores' specific site locations. The following sub-chapters present initial visual observations of the cores, and consequent BSEM investigation. The findings of natural methane hydrate investigations are sub-divided into various methane hydrate morphologies and salt fabrics observed, and the sediment/hydrate interactions within the hydrate samples. This is followed by a detailed discussion of the findings, and bulleted conclusions.

## **Chapter 7: Discussion.**

This chapter provides a general discussion of all the research undertaken during this study, and the relevance of the results. This discussion begins by presenting the initial aims of the project, and is divided into sub-chapters, each of which discusses whether these aims have been answered. The limitations and significance of this study are considered in a global context in context, and the chapter draws to a close by discussing knowledge gaps which remain and could be answered in further research projects.

## **Chapter 8: Conclusions.**

Finally, this chapter provides concise conclusions of all of the research presented and discussed, drawn from previous chapters and highlights the main research findings, their importance, and areas which require further research.

References used during the production of this thesis are provided in the subsequent references section. SI units used within the thesis are then presented, and abstracts, articles and presentations produced during the course of research project are listed in the final pages. An appendix of results and images excluded from thesis chapters has been produced at the end of the thesis. This appendix provides data produced including computer models, temperature and depth data, experimental laboratory records, specific details of each experimental run, and images not presented in earlier chapters.

## **CHAPTER 2**

### **The Role of Anthropogenic and Natural Carbon Stores in Climate Change**

## **2. The Role of Anthropogenic and Natural Carbon Stores in Climate Change**

Fossil fuel combustion has caused a dramatic increase in atmospheric carbon dioxide concentrations, which is believed to be having a substantial effect on global climate (IPCC, 2005). Since the industrial revolution atmospheric levels of carbon dioxide have increased by one third leading to a global temperature increase of 0.6 °C in the 20th century due to an enhanced greenhouse effect. If emissions continue at the current rate global temperature may increase by as much as 5.8 °C by the end of the 21<sup>st</sup> Century (DTI, 2003; IPCC, 2005) with significant consequences.

It has been proposed carbon dioxide could be captured from industrial gases and stored. Such a procedure would aid the overall reduction of atmospheric greenhouse gas emissions currently contributing to global warming. There are various storage methods being investigated including direct disposal into the oceans, iron fertilisation of the oceans and underground storage by injection into warm, deep aquifers or exhausted oil/gas reservoirs (Haugan & Drange, 1992; Baklid et al., 1996; IEA GHG, 1998; IPCC, 2005). Underground storage schemes are already in place storing carbon dioxide in its supercritical phase under warm, deep conditions. Although current carbon capture and storage investigations have focussed on storing supercritical carbon dioxide there is another more novel approach, which may provide additional sites to those suitable for supercritical storage: namely storage as a liquid and hydrate within deep water cool sub-seabed sediments (Kjode et al., 1997; House et al., 2006; Camps et al., 2006).

This chapter provides a review of the current view on climate change and global warming, discusses possible methods for the reduction of atmospheric carbon dioxide concentrations, including proposed storage as a liquid and hydrate, and highlights current knowledge and interest on clathrate hydrates, providing background information on the topical research presented within this thesis.

## 2.1 Climate Change and the Greenhouse Effect

Present day climate change is now accepted by a majority of scientists, though there remains some debate by a small proportion of the scientific community (Jaworowski, 2007). Although natural fluctuations in temperature have occurred throughout Earth history there has been a particularly rapid increase since the industrial revolution (Figure 2.1). From the mid to late 19<sup>th</sup> century through to the 21<sup>st</sup> century the Earth has warmed by a total of 0.76 °C, with eleven of the last 12 years (1995-2006) ranking among the 12 warmest years in the instrumental record of global surface temperatures (IPCC, 2007). In parallel to global temperature rise is an increase in atmospheric carbon dioxide (CO<sub>2</sub>) concentrations (Figure 2.2). It is these increasing levels of CO<sub>2</sub> which are thought to be one of the main causes of climate change, increasing by more than a third since the industrial revolution and currently rising more rapidly than ever before, with a continued upward trend in the early years of the 21<sup>st</sup> century (IPCC, 2005). This is believed to be as a result of human industry combined with other activities such as deforestation. Each year approximately seven thousand million tonnes of carbon are added to the atmosphere, with a residence time of more than a hundred years (Houghton, 1999; IPCC, 2005).

Global warming due to increased atmospheric CO<sub>2</sub> concentrations can be explained by the natural greenhouse effect. The Earth emits thermal radiation, as do all objects. Gases, which constitute the majority of the Earth's atmosphere neither absorb nor emit thermal radiation, however a proportion of atmospheric gases, particularly CO<sub>2</sub> and water vapour absorb some of the thermal radiation leaving the Earth's surface. This creates a partial 'blanket', warming the Earth, and is known as the natural greenhouse effect (see Houghton, 1999 for a full review).

The natural greenhouse effect is largely due to water vapour and CO<sub>2</sub>. The quantity of water vapour in the atmosphere is mostly due to surface ocean temperature, which is not directly related to human activities. However, the carbon dioxide atmospheric concentration levels have increased dramatically due to human activity, enhancing the greenhouse effect. Increased concentrations of carbon dioxide have contributed to approximately 70% of the enhanced greenhouse effect to date; about 24% due to increased methane concentrations and 6% due to nitrous oxide (Houghton, 1999)

(Figure 2.2). Fossil fuel burning accounts for approximately 75% of current CO<sub>2</sub> emissions and is the dominant form (86%) of energy utilised in the world (IPCC, 2001; IPCC, 2005). Global primary energy consumption is growing with demand, at an average rate of 1.6% annually between 1995 and 2001, with CO<sub>2</sub> emissions increasing by 1.4% annually during the same period of time (slightly below that of the energy consumption) (IPCC, 2005).

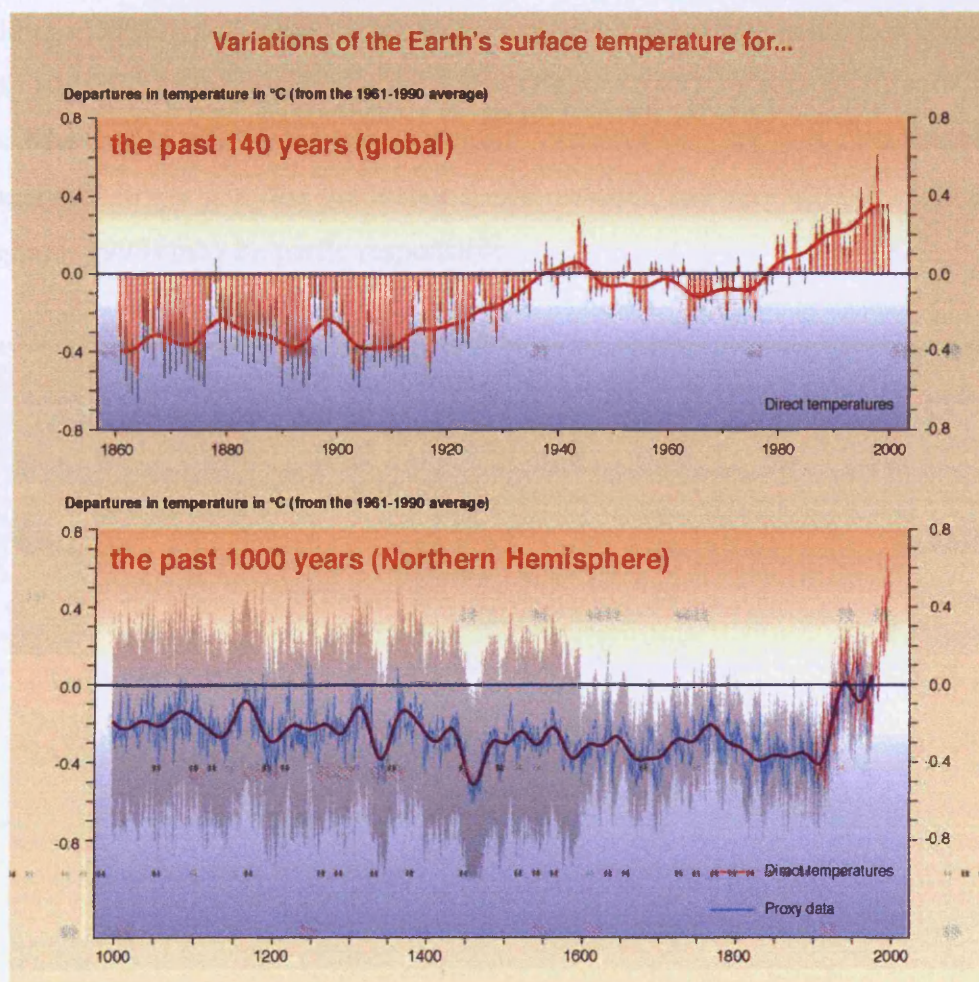


**Figure 2.1.** Global temperature changes over the past 140 years, and the past 1000 years in the Northern Hemisphere (taken from IPCC, 2001).

The increase in fossil fuel burning since the industrial revolution has resulted in atmospheric concentrations of CO<sub>2</sub> increasing from 280ppmv in c.1700 to 379ppmv in 2005, far exceeding the natural concentration range in the last 650,000 years (IPCC, 2007). The annual concentration growth rate was larger in the last 10 years than it has been since the beginning of continuous direct measurements, with an average 1.9ppmv

per year increase between 1995 and 2005 (IPCC, 2007). In addition to CO<sub>2</sub>, methane concentrations have increased from 0.7ppmv in c.1800 to 1.8ppmv in 2005, and N<sub>2</sub>O concentrations are about 15% greater than during pre-industrial times (Figure 2.2; IPCC, 2007). The increased methane concentrations may be explained by changing farming practices, such as using wet-tropical land for rice paddies (particularly in Southeast Asia) producing methane through plant decay, and increased numbers of cattle and other livestock producing large quantities of methane through digestion (Ruddiman, 2001). Although atmospheric methane concentrations are low compared to CO<sub>2</sub> it has 16 times the potential greenhouse effect of a CO<sub>2</sub> molecule (Houghton, 1999). The causes of increased nitrous oxide concentrations are less clear however; the chemical industry (e.g. nylon production), deforestation and agricultural practices (Houghton, 1999) may be partly responsible.

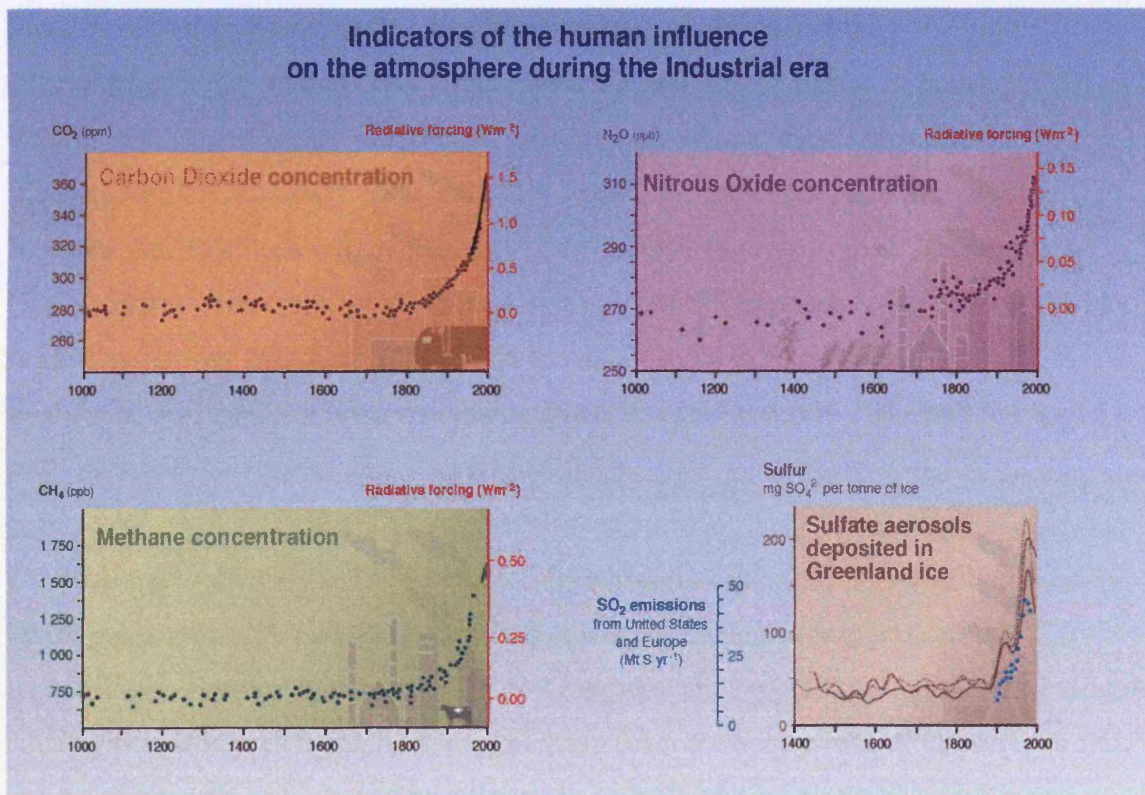


**Figure 2.2.** Global carbon dioxide, nitrous oxide, and methane concentrations since 1000AD. Sulphate aerosol concentrations are also included since 1400 (taken from IPCC, 2001).

Other atmospheric gases also influence climate change, although to a lesser extent. These include chloro- and hydrochlorofluorocarbons (CFCs and HCFCs) which are being phased out under the terms of the Montreal Protocol, hydrofluorocarbons (HFCs),

perfluorocarbons (PFCs), sulphurhexafluoride (SF<sub>6</sub>), carbon monoxide (CO), nitrogen monoxide (NO) and nitrogen dioxide (NO<sub>2</sub>). CFCs and HCFCs have long residence times and have a seriously damaging climatic effect including the destruction of ozone (O<sub>3</sub>). Although strong greenhouse gases the depletion of ozone slightly impedes the global warming effect of the CFC gases.

The Earth's global temperature is predicted to rise by a further 1.1 to 6.4 °C during the 21<sup>st</sup> century (based on likely temperature ranges in emission projection scenarios) with a predicted temperature rise of 0.4 °C in the next two decades (IPCC, 2007). Even if all the greenhouse gas and aerosol concentrations were kept constant at year 2000 levels we would still expect to see a 0.1 °C increase per decade (IPCC, 2007). To place such a temperature rise into perspective there is a global average temperature difference of about 5 or 6°C between the coldest part of an ice age and the warm period between ice ages, therefore such an increase would represent a significant change in climate (Houghton, 1999). We are also likely to see a global sea-level rise of between 0.18 and 0.59 m and a global ocean surface pH decrease of between 0.14 and 0.35 units this Century (see IPCC, 2007). Increases in precipitation are very likely in the high-latitudes, and decreases as much as 20% are likely in the sub-tropical land regions (IPCC, 2007). The IPCC predicts an additional 80million people could be exposed to flood risks by the 2080s, of which 60% are likely to be in the poorest regions of South East Asia. A 45 cm sea level rise in Bangladesh would result in 10% land loss and 5.5 million people being placed at risk (DTI, 2003).

Other climatic effects would include acceleration in irreversible losses of biodiversity, including coral reef bleaching, loss of mangrove swamps and impacts on fish populations. Temperature impacts in polar regions are expected to be the most evident causing permafrost thawing, ice sheet melting (in some projections Arctic late-summer sea ice disappears entirely by the latter end of the 21<sup>st</sup> Century (IPCC, 2007)), and species re-distribution.

One possible greenhouse effect under considerable debate is related to the North Atlantic Ocean. Heat is transported from the equator polewards mostly by the atmosphere but also by ocean currents, with warm water near the surface and cold water at deeper levels. The best known part of this circulation is the Gulf Stream, which

transports warm water from the Caribbean northwards. A branch of the Gulf Stream, the North Atlantic Drift, is part of the thermohaline circulation (THC), transporting warmth to the North Atlantic, where its effect in warming the atmosphere contributes to warming Europe. The evaporation of ocean water in the North Atlantic increases the salinity of the water and decreases its temperature, increasing the density of water at the surface. Sea ice formation further increases the salinity. This dense water then sinks and the circulation stream continues in a southerly direction (Open University, 1995). Global warming could lead to an increase in freshwater in the northern oceans, by melting glaciers and increasing precipitation, lowering its salinity and possibly slowing or stopping deep water formation driving the THC, which could lead to a drop in temperature in the North Atlantic surface waters by as much as 5 °C (Ruddiman, 2001). In addition, the North Atlantic is currently a major sink for CO<sub>2</sub>, and so slowing or stopping deep water formation may cause atmospheric CO<sub>2</sub> levels to rise, further increasing temperatures (Ruddiman, 2001). Based on current model simulations it is very likely the THC of the Atlantic Ocean will slow down in the 21<sup>st</sup> Century, with an average reduction of 25% by 2100, however temperatures are predicted to continue to increase and it is believed very unlikely that the THC will undergo an abrupt transition during this Century (IPCC, 2007).

There are indications the impacts of climate change have been noted in the past century. The global mean sea level rose by an average of 1-2 mm per year during the 20<sup>th</sup> century, with a total estimated rise of 0.17 m during this period (IPCC, 2007). Both summer and autumn arctic sea ice has thinned by as much as 40% and global snow cover has decreased by 10% since the 1960s. Ice cap retreat has been seen from many mountain peaks such as Mt. Kilimanjaro and over the past 5 years the usage of the Thames barrier has increased to an average of six times a year in comparison with once every two years in the 1980's (DTI, 2003). The El Nino event frequency and intensity have also increased since the 1970s. Therefore, the effects of global warming are already having a worldwide impact.

If no action is taken to re-stabilise global climate the world as a whole could suffer from effects of temperature change including droughts, floods and extreme weather.

Although, as yet, there is no international consensus on the suitable stabilisation levels of CO<sub>2</sub>, in 1997 EU member states agreed to aim for a global temperature increase of no

more than 2 °C above the pre-industrial level; hence a CO<sub>2</sub> concentration below 550ppmv (DTI, 2003; Stern, 2007). To achieve stabilisation of CO<sub>2</sub> at a level of 550ppmv global emissions would need to be reduced by between 7 and 70% by 2100 (depending on the stabilisation model), and if the target concentration were lowered to 450ppmv even greater reductions (50-90%) would be necessary (IPCC, 2001; IPCC, 2005). The UK has a Kyoto Protocol commitment to reduce greenhouse gas emissions by 12.5% below 1990 levels by 2008-12 and a national goal for 20% reduction in CO<sub>2</sub> emissions by 2010. The UNFCCC has an ambition of reducing greenhouse gas emissions in developed countries by 60% by 2050, however, major contributors to global emissions (US, Australia, China and India) have not, to date, agreed to the Kyoto Protocol (DTI, 2003; Stern, 2007). Developing countries such as China and India must also assist in emission reductions as they currently account for 40% of global CO<sub>2</sub> emissions and could possibly exceed emissions of developed countries by 2020.

The level of CO<sub>2</sub> emissions can be seen to depend on the size of the human population, the level of global wealth, the energy intensity of the global economy, and the emissions arising from the production and use of energy (IPCC, 2005). This can be visualised using the equation (Kaya., 1995; IPCC., 2005):

$$\text{CO}_2 \text{ emissions per country} = \text{Population} \times (\text{GDP/Population}) \times (\text{Total energy/GDP}) \times (\text{Total emissions/Total energy})$$

Population and average energy use are rising, whilst the amount of energy required per unit GDP is slowly falling (IPCC, 2001), therefore to reduce CO<sub>2</sub> emissions it is necessary to significantly reduce emissions from energy technology.

There are many methods of reducing atmospheric carbon dioxide levels including the European carbon emissions trading scheme. To achieve a 60% reduction by 2050 renewable energy usage is important, possibly requiring at least 30% of global electricity generation from renewable sources such as wind, tidal and solar energy (DTI, 2003). Between 1992 and 2002, installed wind power generation capacity grew by 30% per year (Gipe, 2004; IPCC, 2005) and solar electricity generation also increased by about 30% per year (World Energy Assessment, 2004; IPCC, 2004). Increased usage of nuclear energy would aid targets due to lower production of CO<sub>2</sub> emissions, though its

role is likely to be determined by politics and public opinion (IPCC, 2005).

Improvements in efficiency of energy conversion and switching from high-carbon to low-carbon fuels would also reduce emissions, with a typical reduction of 420 kg CO<sub>2</sub> MWh<sup>-1</sup> for a change from coal to gas in electricity generation (IPCC, 2005). Reduction in energy usage in homes and business would also be required to meet targets; therefore focus on building regulations is essential.

If annual greenhouse-gas emissions to the atmosphere remain at the current equivalent level of approximately 42 Gt (Gigatonnes) of CO<sub>2</sub> each year, concentrations of CO<sub>2</sub> in the atmosphere could reach over 650ppmv by the end of the 21<sup>st</sup> Century, increasing the global mean temperature by at least 3 °C (since pre-industrial times) (Stern, 2007).

However, annual emissions are still rising and are likely to continue do so as developing countries increase their energy demand as they strive for economic growth. With continued increases in global emissions the global mean temperature could rise by 5-6 °C since pre-industrial times by the end of the century, and with such a temperature rise models predict abrupt and large-scale climate change could cost an estimated 5-10% loss in global GDP, with poor countries suffering much greater losses (Stern, 2007). Costs of extreme weather alone could reach 0.5-1% of the world GDP by the middle of the century, and will rise as global temperatures increase (Stern, 2007). If mitigation strategies are rapidly put into place the costs of capping global emissions and therefore limiting the effects of climate change could be kept to a minimum of approximately 1% of the global GDP (Stern, 2007), significantly less than the costs of climate change itself. However, mitigation costs increase dramatically with increased time delay, and hence it is extremely important to act immediately.

Although alternative energies are available, many countries appear to be committed to fossil fuel usage to meet energy demand, and developing countries striving for economic growth are becoming increasingly dependant upon fossil fuel power generation. Recent reports suggests the UK is not succeeding in effectively reducing our CO<sub>2</sub> emissions to meet Kyoto protocol deadlines (Randerson, 2007) therefore an active method of reducing our emissions must be put into practice. No single technology or process will deliver the emission reductions required, but a proven method of effectively reducing our emissions, Carbon Capture and Storage (CCS), has the potential, capturing CO<sub>2</sub> from point sources before its release into the atmosphere

and storing it within another domain of our planet such as the geosphere, terrestrial biosphere or oceans. CCS technologies have the advantage that their large scale deployment could allow the continued use of fossil fuels over the medium to long term with substantial cuts in emissions (Stern, 2007) whilst alternative large-scale energy supplies are developed. It has been forecast that even with the encouragement of low-carbon technologies fossil fuels may still represent half the world's energy supply by 2050, and therefore without CCS stabilising emissions would require a dramatic growth in low-carbon technologies (Stern, 2007), which is most probably unrealistic. Although CCS does not solve the problem of increased emissions from the transport sector, CCS from power generation point sources could be used to reduce the release of CO<sub>2</sub> from one of the largest global contributors to the emissions problem.

## **2.2 Carbon Capture and Storage**

### **2.2.1 Carbon Capture**

The most accessible potential sources for CCS are fossil fuelled power plants, which emit more than a third of global CO<sub>2</sub> emissions. These plants include conventional pulverised-coal steam power plants, natural gas fired combined cycle plants and advanced power generation systems, including coal or natural gas combustion plants using; integrated coal gasification, combined cycles, hydrogen turbines, fuel cells, enriched air or oxygen to aid combustion and CO<sub>2</sub> cycling (IPCC, 2005). In addition, several industries produce concentrated streams of CO<sub>2</sub> as a by-product, such as from the iron and steel production, cement manufacture, oil refining and in the petrochemical industry (IEA, 2001). CO<sub>2</sub> capture may also be practical from producing hydrogen fuels from carbon-rich feed stocks, i.e. natural gas, coal and biomass (Herzog & Golomb, 2004).

Many capturing methods and facilities are available. Unfortunately, the collection and capture process from flue gas streams results in the reduction of plant efficiency, with capture alone reducing the thermal efficiency of a coal plant by as much as 35% (GESAMP, 1997), accounting for 30% of the total energy content from the coal. An additional 10% of the fuel would be required to liquefy and compress the CO<sub>2</sub> for

sequestration (Golomb, 1993). These percentages could be reduced with future improvements.

Current capture technologies increase the unit cost of the electricity production, with an increase of 35-70% for natural gas combined cycle plant, 40-85% for a new pulverised coal plant and 20-55% for an integrated gasification combined cycle plant. Overall the cost of electricity for fossil fuel plants with capture ranges from 43-86 US\$ MWh<sup>-1</sup> compared to 31-61 US\$ MWh<sup>-1</sup> for similar plants without (IPCC, 2005). This does not include costs for transport and storage. The lowest capture costs are associated with industrial processes such as coal-based hydrogen production plants, as low as 2 US\$/tCO<sub>2</sub> (IPCC, 2005), and these processes may offer the initial opportunities for CCS to be put into practice.

Carbon capture processes differ considerably, but generally may be separated into three categories; flue gas separation, oxy-fuel combustion and pre-combustion separation. The process used for capture is largely dependant on the quantity of CO<sub>2</sub> present in the flue gas (as well as the nature and age of the plant) and contaminants present in the feed gas. The CO<sub>2</sub> content in flue gases varies from about 3% in gas turbine plants (Langeland & Wilhelmsen, 1993), which is similar to a natural gas combined plant, to concentrations of 14% from a coal-fired power plant. In some specialised petrochemical processes concentrations may be as high as 80% and coal based plants with oxygen fuel and CO<sub>2</sub> recycling can produce CO<sub>2</sub> flue gas concentrations as high as 92% (Greenpeace International, 2003; IPCC, 2007).

### ***2.2.1.1 Flue gas separation***

At present, several carbon dioxide separation and capture plants use one or more methods to produce CO<sub>2</sub>, which will be explained in further detail. Produced CO<sub>2</sub> can then be used for industrial and commercial markets, for example to produce carbonated beverages, dry ice and urea. An alternative is to store the separated CO<sub>2</sub> rather than releasing into the atmosphere. Although separation processes are relatively expensive, profits may outweigh the costs, directly or indirectly.

- *Chemical and Physical Absorption*

Carbon dioxide can be removed from gas streams by physical or chemical absorption. Physical absorption in a solvent is dependant on temperature and pressure with absorption at high pressures and low temperatures, and absorbed CO<sub>2</sub> can then be regenerated using heat or pressure reduction. Such processes may be used when the partial pressure of CO<sub>2</sub> is high (>525Pa). Typical physical absorbents include glycol-based compounds e.g. Selexol (dimethylether of polyethylene glycol) and Rectisol (cold methanol) (IEA, 2004).

Chemical absorption is preferred for low to moderate CO<sub>2</sub> partial pressures, manipulating acid base neutralization reactions due to the acidity of CO<sub>2</sub>. The most commonly used basic solvents are alkanolamines such as monoethanolamine (MEA), diethanoamine (DEA), and methyldiethanolamine (MDEA). When used for CO<sub>2</sub> capture in a power plant the flue gas is bubbled through the solvent in a packed absorber column, during which the solvent removes the CO<sub>2</sub>. After capture the solvent passes through a regenerator unit, stripping CO<sub>2</sub> by counter flowing steam at 100-120 °C. The water vapour is condensed leaving a concentrated CO<sub>2</sub> stream (over 99%), which can be used or stored and, the amine can then be re-used for further capture (Herzog & Golomb, 2004).

- *Physical and Chemical adsorption*

Solid adsorbents, such as zeolites and activated carbon may be used to separate CO<sub>2</sub> from gas mixtures (IEA, 2004). Such solids have a high-surface area, which can be reproduced artificially by the creation of very fine surface porosity through surface activation methods using steam, oxygen or CO<sub>2</sub>. These methods are practiced commercially but are unattractive for CO<sub>2</sub> capture from flue gases due to the limited availability of suitable adsorbents, as well as due to processing expense (IEA, 2001).

- *Low-temperature Distillation*

Liquefaction and purification of CO<sub>2</sub> from gas streams, of a high purity (>90%), by low-temperature distillation, is used commercially. The process purifies a low-boiling-temperature liquid by evaporation and condensation. The method of low-temperature distillation is most effective when feed gases contain components with significantly different boiling points, and with high pressures. The production of the liquid CO<sub>2</sub> is beneficial to sequestration however, combustion by-products in flue gases would require removal before operating this procedure and, if other components present in the feed gas have freezing points above operating temperatures, removal would be necessary to eliminate the risk of freezing and blocking of equipment.

- *Gas-Separation membranes*

To reduce separation costs gas membrane systems are being developed, with many suitable membranes having the potential to capture CO<sub>2</sub> effectively. Gas separation membranes rely on physical or chemical interaction difference between components present in the feed gas and the membrane in use (IEA, 2004). This results in one component preferentially permeating through the membrane. Many different membranes exist however, only a few are suitable for CO<sub>2</sub> removal from flue gas streams. There are many advantages to membrane separation systems (see Herzog & Golomb, 2004), however, multiple separations or recycling is required for many feed streams, resulting in increased complexity, energy used and expense (IEA, 2001).

### ***2.2.1.2 Oxy-fuel combustion***

Oxy-fuel combustion eases the separation of CO<sub>2</sub> after combustion in air. By burning the fossil fuels in pure or enriched oxygen the flue gas produced would contain mainly CO<sub>2</sub> and H<sub>2</sub>O. Some of the flue gas would need to be retained for flame temperature control and, water vapour in the non-recycled flue gas can then be condensed, leaving CO<sub>2</sub>.

As simple as this may sound, separation would be necessary to separate oxygen from nitrogen in the air. On a large scale the air separation unit (ASU) could possibly use as much as 15% of a power plants output, requiring greater fossil fuel usage (Herzog & Golomb, 2004). This cost may be outweighed by the sale of other gases produced during air separation, e.g. argon and nitrogen.

### ***2.2.1.3 Pre-combustion capture***

Pre-combustion capture offers advantages such as an undiluted CO<sub>2</sub> stream, with the containing stream generally at elevated pressure and so, more efficient separation systems can be applied (Herzog & Golomb, 2004). This method is used in integrated gasification combined cycle (IGCC) plants. In these plants the coal is gasified prior to electricity generation (DTI, 2003). The synthesis gas is composed of CO and H<sub>2</sub>; the CO is reacted with water producing CO<sub>2</sub>, which is consequently captured. The H<sub>2</sub> can be sent to a turbine to produce electricity and, the hydrogen gas also has the potential to be used as transportation fuel in fuel cells (Herzog & Golomb, 2004).

The main problem with this capturing mechanism is currently pulverised coal (PC) power plants produce electricity at a lower cost when compared with IGCC plants (IEA, 2004). Gasification facilities exist worldwide, which do not generate electricity. These facilities synthesise gas and other by-products. The Great Plains Synfuel Plant, near Beulah, North Dakota, gasifies 16,326 metric tons per day of lignite coal, producing approximately 7million cubic meters of CO<sub>2</sub> per day. This gas is compressed and piped to the Weyburn oil field where it is used for enhanced oil recovery (Herzog & Golomb, 2004).

## **2.2.2 Carbon Storage**

Various methods for CO<sub>2</sub> sequestration have been proposed including ocean iron fertilisation and ocean fertilisation with macronutrients, direct disposal of liquid CO<sub>2</sub> into the oceans via land based pipelines into deep water, storage as a hydrate on the bed of oceans, formation of a liquid lake in the deep ocean, mineral carbonation, industrial use of captured CO<sub>2</sub> and underground storage as a supercritical phase within deep

aquifers or exhausted oil/gas fields (Greenpeace, 2003; IEA, 2001; IPCC, 2005). Storage methods most relevant to this thesis will be discussed in further detail.

### ***2.2.2.1 Ocean disposal***

Direct disposal of CO<sub>2</sub> into the oceans is currently prohibited due to international law. In the 1996 Protocol to the London Convention it was agreed that:

“ ‘Dumping’ means: any deliberate disposal into the sea of wastes or other matter from vessels, aircraft. Platforms or other man-made structures at sea; [...as well as] any storage of wastes or other matter in the seabed and the subsoil thereof from vessels aircraft platforms or other man-made structures at sea.” (Article I, 4.1.1 and I, 4,1,1.2 of the 1996 Protocol to the London Convention).

Although the disposal of waste CO<sub>2</sub> into the oceans is currently illegal under international law, research into possible methods of such continues:

- ***Direct disposal of liquid CO<sub>2</sub> into the oceans***

At depths of less than 500m introduction of liquid CO<sub>2</sub> by pipelines into the ocean would create bubble plumes of CO<sub>2</sub> gas, which would dissolve in the seawater. The dissolvable quantity possible at 200-400 m below sea level would be approximately 100 mol/m<sup>3</sup>, resulting in an increase in seawater density of 8 kg/m<sup>3</sup>. Increased density means if CO<sub>2</sub> was injected near-shore gravity currents could transport the CO<sub>2</sub> rich waters to greater depths (Haugan & Drange, 1992). However, the retention time of such would be relatively short, approximately 50 years, as there is no guarantee of increased density due to many surface processes (Golomb et al, 1992).

- ***Formation of a liquid lake of CO<sub>2</sub> in the deep oceans***

At approximately 3000 m water depth CO<sub>2</sub> becomes denser than seawater. Therefore, if CO<sub>2</sub> was to be injected into the deep sea at depths greater than approximately 3000 m the CO<sub>2</sub> would sink to the bottom forming a liquid CO<sub>2</sub> lake (Marchetti, 1977). Such a lake may form a hydrate layer at its surface inhibiting

dissolution and could remain there for centuries. Calculations have suggested a CO<sub>2</sub> lake formed from ten years of operation from 1 GW of a coal power plant would cover 654,500 m<sup>2</sup> of the sea floor to a depth of 80.9 m, containing 58 million tonnes of liquefied CO<sub>2</sub> (Wong & Hirai, 1997). This would be equivalent to a disk with a 900 m diameter containing approximately 265 times the volume of the Hindenburg air ship. In practice dispersal due to bottom currents would result in a thinner, widely spread lake which could have impacts on the marine environment.

- ***Disposal of CO<sub>2</sub> hydrate on the bed of oceans***

The placement of solid CO<sub>2</sub> hydrate blocks on to the seabed at great depth may also produce a pool of liquid CO<sub>2</sub>, or simply lie on the seabed surface; however, the industrial production of CO<sub>2</sub> hydrate is much more expensive than production of liquid CO<sub>2</sub>. One proposed method by Murray et al (1996) includes shaping the hydrate as a torpedo and leaving it to fall through the water column to the seafloor where it could penetrate into soft underlying sediments, allowing permanent storage after natural chemical sequestration.

Ocean storage would reduce the chance of human population damage should gas be released due to remoteness of storage sites, but there are many possible impacts. Deep disposal in seawater may produce solid CO<sub>2</sub> hydrate and liquid brine; the produced acidified, dense brine would displace seawater and react with underlying sediment. This brine could cause plant and animal mortality through oxygen depletion (Harrison et al, 1995). Models suggest highly significant pH reductions as a result of CO<sub>2</sub> injection; waters with a pH below 7.5 are likely to cover a volume of 1500 km<sup>3</sup> of seawater from the source if CO<sub>2</sub> was introduced as a droplet plume from ten power plants. A larger area of lower pH would be formed in shallower water (Johnston & Santillo, 2004). Reductions in pH would have a large effect on marine and benthic ecosystems. Other gases present in the captured gas for sequestration such as sulphur dioxides, nitrogen oxides and trace metals could also present environmental problems.

Possible environmental problems, but most importantly the fact ocean storage is prohibited by international law means development of other sequestration methods is

extremely important for carbon storage, such as injection into sub-seabed geological formations.

#### **2.2.2.2 Underground storage**

Underground storage is a practical feasible method of effectively sequestering large quantities of CO<sub>2</sub> from point sources (e.g. Haugen & Eide, 1996; Holloway et al., 1996; Baines & Worden 2004a; IPCC, 2005; Rochelle et al., 2006). In fact injection of CO<sub>2</sub> for disposal is already a proven technology and has been practised since 1996 by the Norwegian state oil company Statoil in the North Sea Sleipner field. Approximately 1 million tonnes per year of CO<sub>2</sub> produced from the gas field are injected into a porous sandstone aquifer beneath impermeable shale (Baklid et al., 1996; IEA GHG, 1998; Greenpeace International, 2003). A similar quantity is injected annually at the Weyburn oil field, southern Saskatchewan, Canada where it is used for enhanced oil recovery (EOR) (Malik & Islam, 2000; Wilson & Monea, 2004; IPCC, 2005; Rochelle et al., 2006). Smaller scale projects are also taking place around the world, as interest increases in CCS as a viable climate change mitigation method.

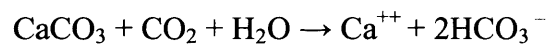
The extraction of natural gas and petroleum from underground reservoirs has created depleted reservoirs with porous rocks and trap structures able to contain gas and liquids. Impermeable cap rocks prevent gas leakage and therefore, underground natural gas and petroleum reservoirs appear suitable for long-term CO<sub>2</sub> storage. A depleted gas reservoir will contain CO<sub>2</sub> to the same pressure as the primary formation pressure of the natural gas before extraction and the cap rock generally maintains the primary pressure (Kiode et al., 1997). Cooler reservoirs with a lower geothermal gradient have the potential to store greater volumes of CO<sub>2</sub> (see *Cool underground storage of CO<sub>2</sub>*). However, known oil and gas reservoirs have a relatively low volume when compared to aquifers and therefore, the greatest potential for CO<sub>2</sub> storage lies within aquifers.

In Europe there is the potential to store 806.1 Gt of CO<sub>2</sub> mostly in the North Sea in the Norwegian sector and the UK (Holloway et al., 1996). About 95% of this storage would be in deep saline aquifers and only about 5% in depleted oil and gas fields (DTI, 2003). However, storage in oil and gas fields can only be possible if fully depleted and

currently, as a result, many reservoirs are unavailable. Offshore aquifers offer vast potential alone, with the possibility of storing approximately 700 years of European emissions from thermal power generation (Holloway et al., 1996).

The injection of CO<sub>2</sub> into oil and gas reservoirs may also have a financial benefit and this has been utilised in North America and Canada. Enhanced oil recovery (EOR) in a number of projects in North America consists of injection of CO<sub>2</sub> into oilfields. During this process the majority of CO<sub>2</sub> used can remain in the oilfield effectively sequestering the greenhouse gas (DTI, 2003). Enhanced oil recovery could potentially allow additional oil recovery of 200 million tonnes over 20 years, in comparison with the current annual oil production of 130 million tonnes globally (DTI, 2003).

The disposal of CO<sub>2</sub> into sub-seabed formations appears more acceptable than on land as they are more remote and ocean dilution prevents air emission. In addition, calcareous sediment on the sea floor could interact with CO<sub>2</sub> forming bicarbonate ions, which are more soluble than CO<sub>2</sub> itself (Kjode et al., 1997):



There are two principal methods of underground storage being investigated: conventional deep, warm storage of CO<sub>2</sub> in its supercritical phase, and the lesser known, more novel deep, cool storage of CO<sub>2</sub> as a liquid and hydrate. The concepts of these are discussed in further detail.

### ***Deep, warm underground storage of CO<sub>2</sub>***

The processes involved in underground storage in its conventional form are as follows. The captured CO<sub>2</sub> gas is compressed and transported via pipeline to the injection site. Following transportation the CO<sub>2</sub> can be injected via wells into deep reservoir rocks capped by low permeability seals, such as clays and shales. If the CO<sub>2</sub> is injected at a depth of approximately 800 metres or more, pressure and temperature conditions will increase past the point at which CO<sub>2</sub> becomes supercritical (c. 31 °C, 74 bar). In its supercritical phase CO<sub>2</sub> is likely to have a density of about 0.7 g/cm<sup>3</sup>, far denser than

gaseous CO<sub>2</sub>, and consequentially will occupy less volume, increasing storage potential (Rochelle et al., 2006).

Once injected, the CO<sub>2</sub> is stored in a free state as a buoyant phase below an impermeable caprock; however, over time it will dissolve into the reservoir formation water. Once dissolved, it will no longer be subjected to buoyancy driven upward migration, and over longer timescales the dissolved CO<sub>2</sub> will react with minerals to precipitate calcite or other carbonate minerals, immobilising the CO<sub>2</sub> as a solid phase and storing it for geological timescales (Bachu et al., 1994; Rochelle et al., 2004; Camps et al., 2006; Rochelle et al., 2006). The extent of such mineral trapping will be dependant on a number of factors including the composition of the porewater, and the in-situ pressure and temperature. Natural CO<sub>2</sub> fields demonstrate the potential for effective long-term trapping (Zheng et al., 2001; Rochelle et al., 2006).

### ***Cool underground storage of CO<sub>2</sub>***

Carbonate minerals are not the only solid phases capable of trapping CO<sub>2</sub>. Under high pressure, low temperature conditions a solid CO<sub>2</sub> phase can precipitate: CO<sub>2</sub> hydrate. Natural hydrates exist worldwide in sub-seabed sediments along continental margins and within permafrost regions (see section 2.3), and it is their formation which leads to the investigation of a more novel underground storage method: storage as a liquid and hydrate.

This cool storage approach has received relatively little attention, even though it may offer many advantages for long-term containment (see chapter 3 and chapter 7 for further details). The use of CO<sub>2</sub> hydrate as a primary trapping mechanism has been considered in several studies (Kiode et al., 1997; Camps et al., 2006; House et al., 2006; Rochelle et al., 2006). This would involve injecting liquid CO<sub>2</sub> into deep-water or sub-permafrost sediments, just below the CO<sub>2</sub> hydrate stability zone (where temperatures are a little too warm for hydrate to be stable). The slightly buoyant CO<sub>2</sub> would rise into cooler rocks lying at an approximate depth of 200-400 m below the seafloor (dependent upon pressure and temperature conditions) within the hydrate stability zone, and under these conditions hydrate would become stable (assuming water availability). CO<sub>2</sub> storage could therefore be stable at depths of 300 m below the seafloor in many easily

accessible areas (Kiode et al., 1997). Precipitation of CO<sub>2</sub> hydrate within pore spaces could form an impermeable ‘cap’ preventing any further migration (Figure 2.3). Should any upward migration of stored liquid CO<sub>2</sub> through this cap occur the CO<sub>2</sub> would simply rise further into the hydrate stability zone and again form hydrate, possibly creating a self-sustaining re-sealing trapping mechanism (Sakai et al., 1990; Brewer et al., 1999). This approach may offer storage sites around in addition to those suitable for warm, deep, supercritical CO<sub>2</sub> storage.

Additionally, CO<sub>2</sub> hydrate formation could be used as a secondary trapping mechanism for deeper, warmer supercritical stores of CO<sub>2</sub>. The injection of carbon dioxide into deep reservoirs in its liquid or supercritical phase may result in CO<sub>2</sub> migrating upwards to cooler parts of aquifers, saturating groundwater and as a result could form solid hydrate, creating an impermeable ‘back-up’ cap preventing CO<sub>2</sub> leakage from deeper injection sites should any migration occur.

To offset the costs involved in underground storage CO<sub>2</sub> hydrates are also being researched for the possible recovery of methane. Several studies have investigated the injection of CO<sub>2</sub> to liberate methane gas from natural sediment-hosted gas hydrates, replacing the methane hydrate with CO<sub>2</sub> hydrate (Nakano, 1998; IEA, 2001; Kvamme, 2007). However, the practicalities of this may prove difficult, especially due to the sporadic distribution of natural gas hydrates within ocean floor sediments and the likelihood of contaminants being present in the recovered gas stream.

Injection into sub-seabed formations is already in practice but relatively little research has been conducted on the effect on the surrounding sediment and the marine environment. Although the formation of CO<sub>2</sub> hydrate at depth impedes migration the possibility of CO<sub>2</sub> leakage must still be considered. Research into the interaction of CO<sub>2</sub> with near ocean sediment is necessary, into the effect of hydrate formation on marine biological communities, as well as the nature of hydrates within sediment to ensure the stability and suitability of such storage methods, and it is this knowledge gap which will be addressed within this study (see following chapters 3, 5, 6, and 7).

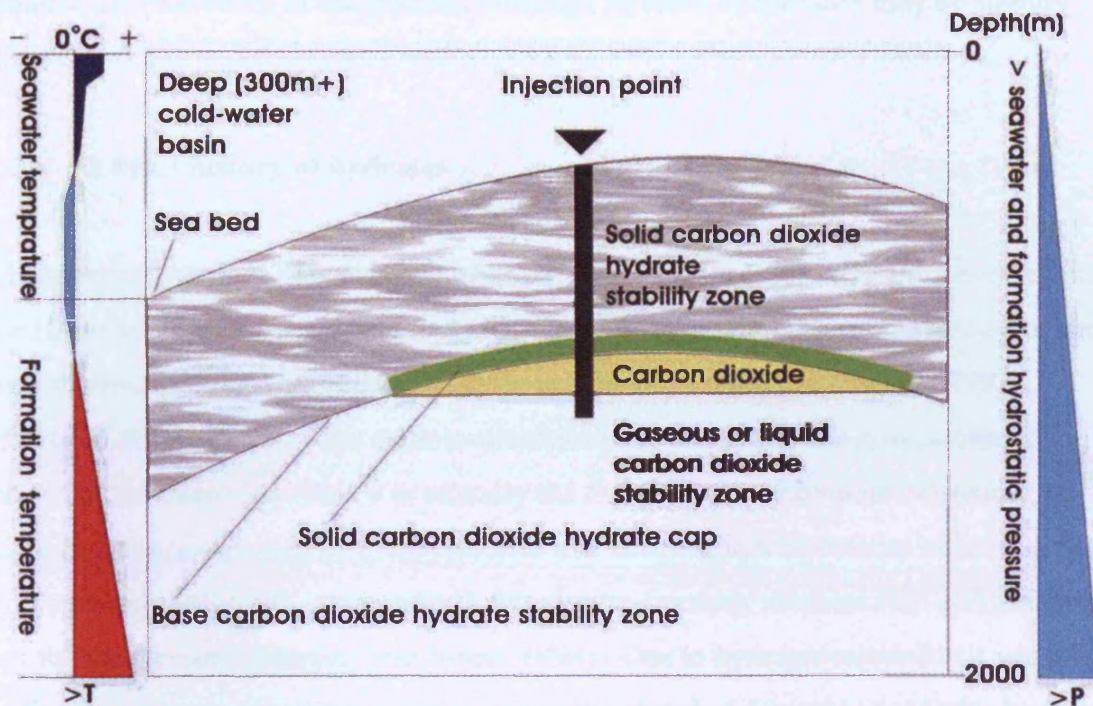


**Figure 2.3.** Schematic diagram of proposed storage of CO<sub>2</sub> as a liquid and hydrate in sub-seabed cool aquifers (courtesy of Dr D Long, and the British Geological Survey).

The mitigation costs involved in CCS ranges from between 1 and 270 US\$/tCO<sub>2</sub> (IPCC, 2005) dependent on the type of technology used, with transport costs ranging from 0-5 US\$/tCO<sub>2</sub>, and geological storage and monitoring ranging from 0.6-8.3 US\$/tCO<sub>2</sub> (IPCC, 2005). Therefore, the biggest variability lies within the capture of CO<sub>2</sub> from point sources. Costs involved in the proposed storage as a liquid and hydrate remains unknown, although this method would use similar infrastructure as used in conventional storage practices, and therefore costs are assumed to lie within the same range.

### 2.3 Natural Gas Hydrates

To scope the suitability and stability of CO<sub>2</sub> storage as a liquid and hydrate it is important to fully understand forced CO<sub>2</sub> hydrate formation within sediments, for which natural in-situ formation can provide valuable information. Unfortunately there are very few natural CO<sub>2</sub> hydrates on Earth; therefore natural methane hydrates provide a

suitable alternative for investigations, although formation processes may be slightly different.

### **2.3.1 A brief history of hydrates**

Chemists have known about the existence of hydrates since the early 19<sup>th</sup> century when Sir Humphrey Davy gained acknowledgement for witnessing the crystallisation of the first chlorine hydrate (see Berecz & Balla-achs, 1983; Henriot & Mienert, 1998). However, although Davy has been credited for their discovery it is now commonly believed Sir Joseph Priestley was actually the first to discover hydrate existence. In 1778 Priestley conducted cold experiments in a Birmingham laboratory observing SO<sub>2</sub> impregnating water and, consequently freezing/re-freezing, whereas HCl and SiF<sub>4</sub> did not follow the same pathway (see Sloan, 1998). Due to hydrates instability it wasn't until thirteen years after Davy's experiments the chemical formula of chlorine hydrate was determined by Faraday – Cl<sub>2</sub>.10H<sub>2</sub>O, showing the chlorine and water remained separate (see Long et al., 2005). After discovery, hydrates were regarded as a mere curiosity until interest grew in the 1930s petroleum industry when gas hydrate formation was discovered as a cause of pipeline blockage in Kazakstan (see Collett et al., 2000). In the 1960s a Russian drilling crew discovered natural methane hydrates in a Siberian gas field (see Makagon, 1981; Sloan, 1998), and in the 70s they were discovered in deep water sediments at outer and polar continental margins. Interest has continued to grow and in more recent years gas hydrates are moving into the foreground of global climate debates.

### **2.3.2 What are hydrates?**

Gas hydrates are crystalline ice-like solids built up of a cage of water 'host' molecules and one or more hydrate forming 'guest' molecules. Although commonly known as hydrates (which will be used through out the remainder of this report) they belong to a sub-group of clathrates, given to the class by Powell (1948) from the Latin 'clathratus' meaning to encage. It is therefore important to note a distinction must be made between these non-stoichiometric clathrate hydrates and stoichiometric hydrate compounds formed when water combines with various salts without forming cages (Sloan, 1998).

The hydrate forming molecules are held by Van der Waals forces within a metastable crystal lattice made of water molecules (Austvik & Loken, 1992). Water molecules crystallise in the isometric crystallographic system (Kvenvolden, 1998), and due to hydrogen bonding form an unstable 3D shell. Within the lattice voids, in cages, non-polar atoms or molecules with low molecular weight and small rotation diameter may enter and form thermodynamically stable hydrates, at high pressures and/or at low temperatures (Austvik & Loken, 1992). The structure of the hydrate means it has an interesting property of being approximately 85% (mol) of water and 15% gas/liquid when all the cages of all three structures are filled (Sloan, 1998), with the majority of hydrates formed with about 90% of the cages filled (Kvenvolden, 1998; Sloan, 1998).

The size of the guest molecule largely determines the hydrate structure. Very small molecules, such as helium, are too small to form a hydrate. The majority of hydrates researched are those composed of molecules of methane, ethane, isobutane, propane, normal butane, nitrogen, carbon dioxide and hydrogen sulphide (Sloan, 1998), but this simply represents a bias due to their main interest in the oil and gas industry. Many other molecules may also form hydrates; including argon, krypton, and solvents such as THF (TetraHydroFuran) (Suga et al, 1992; Koh et al, 1998; Wilson et al, 2005) (which have been widely studied due to their ease of formation), but natural hydrates on Earth are mainly composed of methane. The hydrate skeletal lattice structure depends on the size and shape of the forming molecules in contact with the water (Kvenvolden, 1998; Sloan, 1998). One of three structures is usually formed:

- **Structure I (sI)** is the most common due to guest molecules forming hydrates in which cages are arranged in a body centred cubic structure forming with small gas molecules, such as CH<sub>4</sub>, found in-situ in deep oceans. Structure I cages are large enough to contain methane, ethane and other molecules of a similar diameter, such as carbon dioxide and hydrogen sulphide.
- **Structure II (sII)** hydrates have a diamond lattice structure within a cubic framework forming cages large enough to contain molecules larger than ethane but smaller than pentane.
- **Structure H** is rare and has only been discovered in more recent years. This is hexagonal and requires a smaller molecule for 5<sup>12</sup> and 4<sup>3</sup>5<sup>6</sup>6<sup>3</sup> cages

such as, methane, nitrogen or carbon dioxide. Molecules for the other cage can be very much larger, larger than 0.7 nm but smaller than 0.9 nm, therefore cavities are large enough to contain molecules such as methylcyclohexane and those present in naphtha and gasoline.

The largest molecules of a gas mixture will generally determine the structure of the forming hydrate. A guest molecule/cavity ratio of approximately 0.9 is required for the stability of a basic hydrate, where the stabilising guest molecules range in size between 0.35 and 0.75 nm for structures I and II (Sloan, 1998). Below 0.35 nm an atom or molecule will not stabilise sI and above 0.75 nm molecules are too large for sII.

### **2.3.3 Where are hydrates found?**

Natural hydrates on Earth are mainly restricted to polar and deep oceanic regions (Kvenvolden, 1998). In polar regions they are usually associated with permafrost onshore in continental sediments, and offshore on continental shelves (Kvenvolden, 1998). In deep oceanic regions they have been found in outer continental margins, in sediments where cold bottom waters are present. Hydrate formation does depend on deeper, colder water, however it is important to remember the majority of natural hydrates are methane; hence there is an optimum region around coastlines where most are found due to the supply of rotting methane producing detritus. This source of methane can be either biogenic, formed by microbial methanogenesis at shallow depths, or thermogenic, from geological heating of sediments over a long period of time, but isotopic signatures suggest the majority of naturally occurring hydrates are formed from biogenic methane.

Hydrates exist worldwide, and have been discovered at the seafloor and up to 500 m beneath it. Few sources have been identified by direct sampling with the majority inferred from seismic reflections, well logs, drilling data and pore water-salinity measurements (Collett et al., 2000). However, some of the best described hydrate occurrences are in the Gulf of Mexico (Corthay II, 1998; Milkov, 2000), Blake Ridge (Paull et al, 1996; Kvenvolden, 1998), Cascadia Margin (Riedel et al, 2002; Haeckel et al, 2004; Torres et al, 2004; Peterson et al, 2007), Nankai Trough, Japan (Taira et al., 1991; Ashi et al., 2002; Colwell et al., 2004), Niger Delta (Heggland and Nygaard,

1998; Milkov, 2000), The Black Sea and Caspian Sea (Makagon, 1981; Ginsburg et al, 1990; Milkov, 2000; Kessler et al, 2006), offshore Norway (Ginsburg & Soloviev, 1997; Andreasson et al, 2000; Buenz et al, 2003; Hovland & Svenson, 2006) and India (USGS, 2007), The Gulf of Cadiz (Mazurenko et al., 2003; Ivanov et al., 2007), and various other regions (Kvenvolden, 1998; Collett et al., 2000) (Figure 2.4) including Lake Baikal (Kuzmin et al, 1998; Vanneste et al, 2001). The Lake Baikal hydrate occurrence is slightly more unusual as they are the only known hydrates to exist beneath a freshwater lake. Although the majority of natural samples consist of methane and other hydrocarbons in less significant quantities, natural CO<sub>2</sub> hydrates have also been discovered in the Okinawa Trough, offshore Japan (Sakai et al., 1990). Naturally formed air hydrates have also been reported from about 1000 m depths in the Antarctic polar ice (Craig et al., 1993; Smelik & King, 1997).

Estimation of the global distribution and volume of natural gas hydrates has largely depended on the use of the BSR (Bottom Simulating Reflector). BSRs are a large negative change in acoustic impedance running sub-parallel to the seafloor, and are assumed to represent the base of the hydrate stability zone with free gas (methane) lying beneath (Long et al., 2005). The presence or absence of a BSR has been used to determine the presence or absence of hydrate, however more recently researchers are realising that this assumption is often incorrect (see Long et al., 2005; Holditch et al., 2006 for further details). The negative reflection coefficient used to identify a BSR indicates a reflection interface between higher velocity strata and lower velocity strata (Kvenvolden, 1998), which could also be formed by other geological conditions. Therefore, there is the possibility of overestimating hydrate volumes by assuming the presence of hydrate by the identification of BSRs. Unfortunately, direct sampling and recovery is expensive, and it is still necessary to use indirect techniques such as seismic profiling to determine areas for further exploration, even if they cannot be relied upon completely. Current estimates of global hydrate volumes suggest approximately  $2 \times 10^{14} \text{ m}^3$  of methane could exist within natural hydrate reserves (Soloviev, 2002; Long et al., 2005).

Not only do gas hydrates exist in large volumes on Earth, they may also exist elsewhere in the solar system on icy planetary bodies, such as on Mars, Europa, and Titan (Max & Clifford, 2000; Prieto-Ballesteros et al., 2006; Atreya, 2007; Camps et al., 2007), where

they could represent a large quantity of water locked within the hydrate (with water being a vital component for the presence of life, past or present).

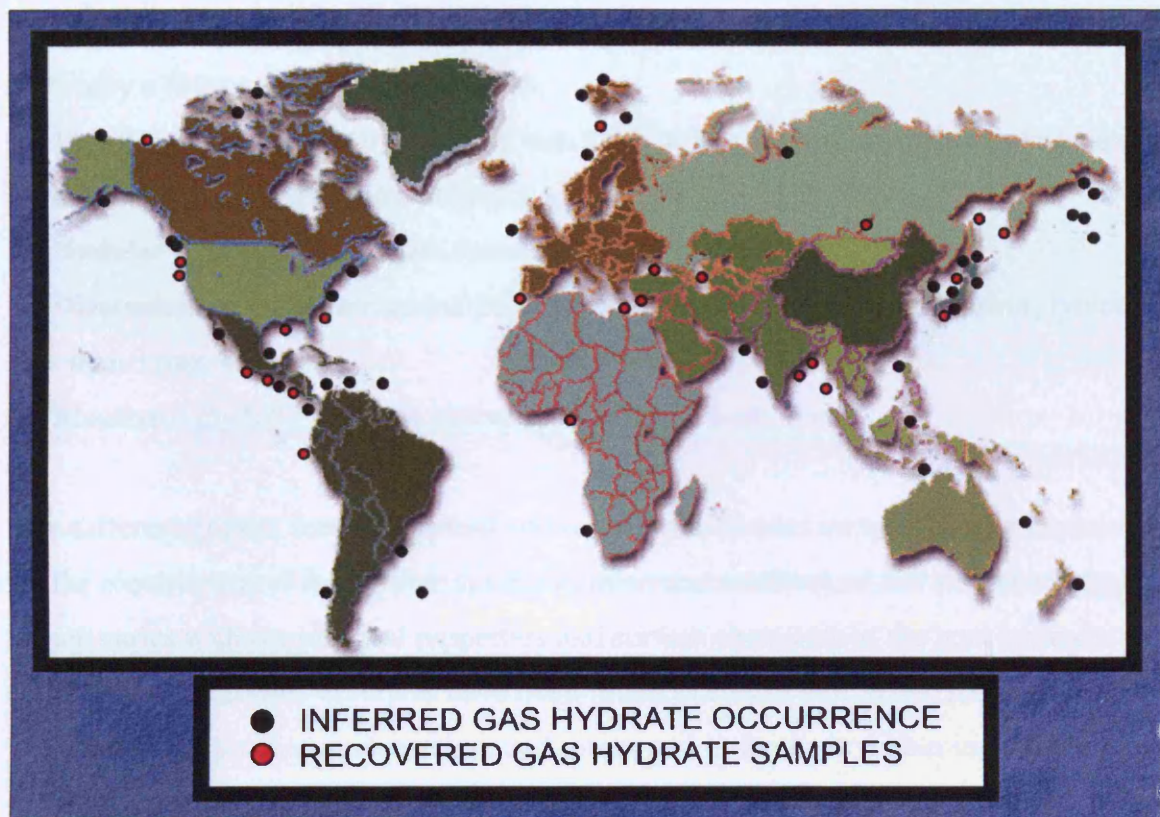


**Figure 2.4.** Worldwide map showing approximate locations of known and inferred gas hydrates. Adapted from Knøvolden (1998) and Knøvolden & Lorenson (2001).

### 2.3.4 Hydrate formation and its investigation

Hydrate accumulations can be classified as structural or stratigraphic. Structural hydrates form from gases rapidly migrating from deeper sources into the hydrate stability zone, and typically result in high gas hydrate concentrations (Holditch et al., 2006). Stratigraphic deposits are described as those forming in permeable sediment layers from slowly migrating localised gases (Holditch et al., 2006). Within these accumulations various different forms of sediment-hosted natural gas hydrate have been found on coring and recovery, and these can be divided into the following (Holditch et al., 2006):

1. **Layer** – A tabular form of hydrate transecting the recovered core and conformable to the bedding. Typically a few centimetres thick.
2. **Lens** – A hydrate layer with a tapering margin.
3. **Vein** – A tabular form of hydrate transecting the core and cutting across the bedding. Typically a few centimetres in thickness.
4. **Veinlet** – Thin, tabular hydrate c. 1 mm thick or less, commonly adjacent to veins or layers, and cutting across the bedding.
5. **Nodular** – Spherical to oblate features, 1-5 cm in diameter.
6. **Disseminated** – Hydrate grains distributed throughout the sediment matrix, typically less than 3 mm wide.
7. **Massive** – Hydrate characterised as greater than 10 cm thick.

The different growth forms commonly observed in recovered samples can be explained by the requirement of the hydrate system to minimize mechanical and surface energy, which varies with the physical properties and surface chemistry of the host sediment (Clennell et al., 2000). Hydrates have been found in coarse sediments, such as sand, fine-grained sediments, such as clays and muds, and in fractures within indurated sediments (Makagon, 1981; Kvenvolden et al., 1993). They appear to form preferentially in sediments with higher porosity, larger pore sizes, and high permeability, and formation is seemingly less favoured within fine-grained sediments (Clennell et al., 2000). This inhibition within fine-grained sediments has been thought to explain shifts in the base of the hydrate stability zone from depths predicted from equilibrium calculations. However, current models suggest even sediments with small pores are likely to contain pores large enough to contain hydrate at equilibrium conditions (Turner et al., 2005). Research suggests hydrate tends to form as discrete layers or lenses within fine-grained muddy marine sediments (Kvenvolden et al., 1993; Booth et al., 1998), as the sediment grains are forced apart as the hydrate forms, whereas in sands and gravels hydrate has been observed as pore filling cement and massive layers (Kvenvolden et al., 1993; Booth et al., 1998; Clennell et al., 2000). However, the processes involved in formation of hydrates within sediment are still poorly understood.

The availability and supply of hydrate forming components influences the rate of hydrate growth, and consequently the form of the hydrate. Although natural methane

hydrate is believed to grow relatively slowly, evidence exists to support natural rapid hydrate formation in marine sediments. At Hydrate Ridge, on the Cascadia Margin, offshore Oregon, methane gas is rapidly transported from depth to the seafloor. During exploration of this region massive methane hydrate, free gas, and pore waters of enhanced salinity were found to co-exist (Hesse, 2003; Torres et al., 2004). The presence of more saline pore waters in gas hydrate samples is a rare and unusual phenomenon, and requires rapid gas hydrate formation when natural diffusion processes have not been able to remove excess salinity. This suggests Cascadia Margin represents an area of rapid hydrate formation with relatively young gas hydrate deposits present in seafloor sediments, as a consequence of the rapid supply dissolved methane (Haekel et al., 2004; Torres et al., 2004). The trapped brines present within these recovered hydrate samples were detected by an enhanced chlorine concentration in the pore waters, however, such elevated concentrations may easily go unnoticed due to pore water freshening during hydrate core retrieval through dissociation, and hence it is possible there are similar rapid growth sites along other hydrate bearing regions (though as yet remain unidentified).

Although the majority of hydrate is preserved as sediment-hosted gas hydrate, hydrate deposits also form directly on the ocean floor, as is the case with the only known example of natural CO<sub>2</sub> hydrate from the Okinawa Trough (Sakai et al., 1990). However, hydrates deposited on the seafloor, or just below the seafloor, are fairly unstable and do not survive for very long.

Unfortunately, few natural hydrate samples have survived for a long enough period of time to allow detailed study, mainly as a result of depressurization and temperature change as they are raised to surface waters, but also as a consequence of the length of time between collection and storage. Sampling techniques are improving and consequently the quantity of samples available for investigation is on the increase. However, artificially produced hydrates are still essential to fully understand their formation and composition.

It is difficult to reproduce an exact representation of the natural environment in the laboratory, but any attempt at doing so complicates the interpretation of experimental results, therefore simplicity in experimental design is necessary. Increasing our

knowledge in basic systems can help to progress research to fully understand the complex network of components influencing formation. Experimental investigations range from pore-scale growth models (Tohidi et al., 2001; Anderson et al., 2007; (with a rigid pore system)), to micro-scale in-situ and post formation observations (Genov et al., 2004; Stern, 2004; Camps et al., 2006; Rochelle et al., 2006), to macro-scale physical property measurements and kinetic models (Moudrakovski et al., 1999; Mork et al., 2000; Stern et al., 2000; Uchida et al., 2000). Basic experimental procedures for the formation of hydrate have not altered significantly in recent years, but there has been a significant increase in physical property characterisation of in-situ sediment-hosted hydrates, both in the laboratory and the field.

Pressurised optical cells have been successfully used to observe hydrate growth within sediment, forming as different morphologies according to the growth conditions (Makagon, 1997; Smelik & King, 1997). Other non-invasive imaging techniques include Nuclear Magnetic Resonance, NMR (Moudrakovski et al., 1999; Mork et al., 2000; Subramanian et al., 2000), X-ray tomography (Mikami et al., 2000; Uchida et al., 2000; Tomutsa et al., 2002), magnetic resonance microimaging, MRM (Moudrakovski et al., 1999; Hirai et al., 2000), scanning electron microscopy, SEM (Genov et al., 2004; Kuhs, 2004; Milodowski et al., 2004; Rochelle et al., 2004; Stern, 2004); X-ray diffraction, XRD (Henning et al., 2000; Takeya et al., 2000; Genov et al., 2004; Huo et al., 2005), and Raman spectroscopy (Sloan, 1998; Henning et al., 2000; Subramanian et al., 2000).

Additionally, in-situ physical property measurements have been made during hydrate formation, including electrical resistivity (Collett et al., 1999; Reidel, 2006) S-wave (shear) and P-wave velocities (Stern et al., 2000), density, thermal conductivity (Stoll & Bryan, 1979; Stern et al., 2000) and rheology (Stern et al., 2000; Durham et al., 2003) have also been investigated as hydrate forms. Thermal conductivity decreases with the formation of hydrate, and is lower than that of ice (Stoll & Bryan, 1979; Knenvolden, 1998). P-wave velocities are not the most effective method of determining the presence of hydrate, and appear to be relatively insensitive to hydrate distributed within the pore space (Sakai et al., 1999), however, S-waves are important in determining whether or not the hydrate is acting as sediment cement increasing its rigidity and strength (Stoll & Bryan, 1979; Sakai et al., 1999). S-wave, P-wave, and electrical resistivity increase

with hydrate formation, with electrical resistivity proven to be the most effective tool for determining the presence of hydrate in the field during wire-line logging (Kvenvolden, 1998). These measurements have been used to estimate the concentration of hydrate within a natural reservoir, however these are bulk average measurements, and can be influenced by localised anomalies, therefore care should be taken on interpretation (see Chapter 6).

With the development of pressurised corers very recent advances now allow 3D measurements of natural hydrate physical properties, actually in-situ and during recovery of samples (HYACINTH project: Trehu et al., 2004; Schultheiss et al., 2006). Pressurised recovery of well-preserved natural hydrate has increased the availability of samples for investigation, and techniques developed through laboratory experiments, such as SEM, NMR, X-ray tomography, can now be used on natural hydrate samples, allowing a more thorough in depth study (see Chapter 6).

### **2.3.5 Interest in hydrates**

Interest in gas hydrates grew when they were discovered as a cause of pipeline blockage in the oil and gas industry. Hydrate research then became necessary for hazard prevention. When crude oil or gas is piped through pressurised pipelines in cold climates enough water and gas may be present to form a solid hydrate plug. Repercussions of hydrate formation are plugging of choke lines, kill lines and blow out preventers (BOP), difficulties in monitoring well pressure, restriction of drill string movement and deterioration in mud properties due to dehydration (Collett et al., 2000). The plug can also act as a projectile destroying the pipe when the pressure difference between the upstream and downstream section increases (Chatti et al., 2004). With this research growth natural hydrates were discovered, revealing far more interesting details about these little crystals, and the role they play in Earth's dynamic environmental system and carbon cycle.

Under present climatic and oceanographic conditions natural gas hydrates represent one of the largest masses of stored organic carbon on this planet (Henriet & Mienert, 1998). In the case of methane hydrate, 1 m<sup>3</sup> of hydrate can contain up to 164 m<sup>3</sup> of gas at standard temperature and pressure, and it is this property, which leads to current

research. Global hydrate reserves are estimated to contain approximately  $2 \times 10^{14} \text{ m}^3$  of methane (Soloviev, 2002), which is about 30 times the quantity available in the atmosphere at present (Long et al., 2005). Methane is a greenhouse gas and has a much greater radiative forcing effect than  $\text{CO}_2$  (16 times). Research indicates these natural reserves have released considerable quantities of methane gas into the atmosphere in the geological past, and therefore represent a possible future environmental hazard, particularly as global temperatures continue to rise (MacDonald, 1990; Kvenvolden, 1998; Kennett et al., 2000; Buffet & Archer, 2004; Kemp et al., 2005). Carbon isotope data with unusually large enrichments of carbon-12 have supplied evidence for 3 methane gas pulses within 2000 years around 183 million years ago (Kemp et al., 2005). This gas release is believed to be a consequence of methane hydrate dissociation as a consequence of global warming driven by volcanic activity and Earth's Milankovitch cycles. The release of this methane and its gradual conversion into  $\text{CO}_2$  caused enhanced global warming, and probably resulted in a mass extinction of more than 50% of marine animals during the same time period (Kemp et al., 2005).

There is also evidence to suggest hydrate dissociation is responsible for rapid increases in methane concentrations during the Pleistocene, observed in the ice-core record. Enhanced continental slope failure during glacial-interglacial transitions is believed to have occurred at the same time as the release of large quantities of methane from gas hydrates (Maslin et al., 2004). Deglaciation events caused sea-level rise and ice-sheet retreat. For deep-water hydrates the increased sea level outweighed the increase in seawater temperature; however this is not the case for hydrate deposits under polar continental shelves. Flooding of the shelf by relatively warm water with the transgression of the polar ocean could cause the destabilisation of methane hydrates, adding to the global warming trend (Kvenvolden, 1998). During glaciation the opposite occurs. Ice caps grow and sea level falls, exposing gas hydrates on the outer continental margin, destabilising the hydrate, but as temperatures decrease hydrates are re-stabilised (Kvenvolden, 1998). Paull et al (1991) suggest the destabilisation of gas hydrate during sea regression releases methane, enhancing global warming, limiting the full effect of glaciation.

An example of the problems that arise when hydrates dissociate can be found off the US Atlantic margin. There, the seafloor slope is about  $5^\circ$  and as such should be stable

(Collett et al, 2000). However, many submarine landslide scars have been observed. The depth of the scars is near to the shallow limit of the hydrate-stability zone. The BSRs are weaker in areas that have experienced landslides, possibly indicating hydrates are no longer present and may have dissociated. Scientists theorize if pressure on the hydrates decreased, as would happen with a fall in sea level during a glacial period, hydrates could dissociate at depth and cause the gas-saturated sediments to slide. Such zones have been detected near the coast of South Carolina, USA, in the region of a huge submarine landslide 66 km wide, where a seismic section indicates massive hydrate formation on either side of the landslide, but no hydrates directly below the slide (Collett et al, 2000).

The large quantity of methane gas trapped within Earth's reservoirs has also lead researchers to envisage natural methane hydrate as a potential future energy resource. Although fossil fuel reserves are currently sufficient to meet worldwide energy needs future short falls could potentially be met by exploitation of gas hydrate deposits. Various projects are presently underway to develop viable extraction schemes, such as the Mallik Gas Hydrate Research Well Program investigation on permafrost deposits in the Canadian Arctic (Dallimore et al., 2002; Chatti et al., 2004), and the western Siberian Messoyhaka gas field (Max et al., 1997; Lee & Holder, 2001). Gas recovery is mainly dependent on hydrate dissociation by either warming or depressurisation, with depressurisation as the favourable method as heat is lost to the reservoir rock and water on warming, reducing the energy efficiency (Lee & Holder, 2001). However, extraction of the gas could be hazardous due to re-formation of hydrates within the pipelines (Chatti et al., 2004), and the unpredictable distribution of gas hydrate deposits could cause difficulties in exploitation. One advantage of the use of the methane from gas hydrates is methane is a less carbon-intensive fuel than oil or coal. Methane produces only half as much CO<sub>2</sub> as coal per unit of combustion products (Lee & Holder, 2001), therefore if methane extraction from hydrates was proved to be viable and energy efficient, reserves near or within developing countries could be exploited in preference to the intensive construction of coal burning power stations which is currently taking place.

There is an additional proposed method for the extraction of methane gas from natural hydrates – methane hydrate replacement with CO<sub>2</sub> hydrate. This process could provide

a zero carbon energy supply by sequestering the CO<sub>2</sub> produced during the combustion of extracted methane (as mentioned in 2.2.2.2). However, research indicates injection of CO<sub>2</sub> would not displace all the methane, and best estimates predict at least 29% of the methane would remain in the hydrate phase (IEA, 2000). The produced gas could therefore be contaminated with significant quantities of CO<sub>2</sub>, which would add to the cost of extraction, as a separation plant would be required (IEA, 2000). In spite of concerns significant interest remains in this method of carbon storage and energy extraction (Kvamme et al., 2007).

Other research areas receiving considerable interest include hydrate as a desalination agent due to the exclusion of ions during formation (McCormack & Anderson, 1995; Javanmardi & Moshfeghian, 2003), hydrate 'slurries' as a secondary refrigerant in refrigeration systems with a low environmental impact (Inaba, 2000; Tanasawa & Takao, 2002) and, as fore mentioned, its potential role as a primary or secondary store of environmentally damaging CO<sub>2</sub> (Kiode et al., 1997; Camps et al., 2006; House et al., 2006; Rochelle et al., 2006). It is this last area which is the focus of the research within this thesis.

## **2.4 Conclusions**

- Since the industrial revolution atmospheric concentrations of carbon dioxide have increased by one third leading to a global temperature increase of 0.6 °C in the 20th century due to an enhanced greenhouse effect. If emissions continue at the current rate global temperature may increase by as much as 5.8 °C by the end of the 21<sup>st</sup> Century with significant consequences.
- If no action is taken to re-stabilise global climate the world as a whole could suffer from effects of temperature change including droughts, floods and extreme weather. To achieve stabilisation of CO<sub>2</sub> at a level of 550ppmv to ensure a global temperature increase of no more than 2 °C global emissions would need to be reduced by between 7 and 70% by 2100.

- If mitigation strategies are rapidly put into place the costs of capping global emissions and therefore limiting the effects of climate change could be kept to a minimum of approximately 1% of the global GDP, significantly less than the costs of climate change itself. However, mitigation costs increase dramatically with increased time delay, and hence it is extremely important to act immediately.
- No single technology or process will deliver the emission reductions required, but a proven method of effectively reducing our emissions, Carbon Capture and Storage (CCS), has the potential, capturing CO<sub>2</sub> from point sources before its release into the atmosphere and storing it within another domain of our planet.
- Underground storage is a practical feasible method of effectively sequestering large quantities of CO<sub>2</sub> from point sources. Injection of CO<sub>2</sub> for disposal is already a proven technology and has been practised since 1996 by the Norwegian state oil company Statoil in the North Sea Sleipner field.
- Conventional storage practices inject CO<sub>2</sub> into deep, warm reservoir or aquifer rocks, and under such conditions it is stored in its supercritical free phase. An additional storage method, which has received relatively little attention, involves injection of CO<sub>2</sub> into deep, cool sub-seabed sediments, below the CO<sub>2</sub> hydrate stability zone. Under these conditions CO<sub>2</sub> would be in its slightly buoyant liquid phase, and as the CO<sub>2</sub> rises into cooler sediments within the hydrate stability zone it could form a solid hydrate phase, creating an impermeable (and possibly self-sealing) 'cap' aiding the trapping of underlying liquid CO<sub>2</sub>.
- Gas hydrates are crystalline ice-like solids built up of a cage of water 'host' molecules and one or more hydrate forming 'guest' molecules. 1 m<sup>3</sup> of hydrate can contain up to 164 m<sup>3</sup> of gas at standard temperature and pressure.
- Natural hydrates exist worldwide and are mainly restricted to polar and deep oceanic regions, with the some of the best described hydrate occurrences in the Gulf of Mexico, Blake Ridge, Cascadia Margin, the Nankai Trough, offshore

Japan, the Gulf of Cadiz, Black and Caspian Seas, Lake Baikal, the Niger Delta, and offshore Norway.

- Interest in hydrates is wide and varied from their role in the carbon cycle; as a natural hazard, as a desalination agent or secondary refrigerant to their potential role as a future energy resource. However, their formation processes remain poorly understood.
- To scope the potential of CO<sub>2</sub> storage as a hydrate it is important to determine suitable offshore areas with suitable conditions (see Chapter 3). Additionally, a full understanding of CO<sub>2</sub> hydrate formation within sediments is necessary to determine the suitability and stability of CO<sub>2</sub> storage as a liquid and hydrate. Laboratory investigations of CO<sub>2</sub> hydrate formation can provide valuable information on such (see Chapter 5), however it is difficult to reproduce the natural environment in the laboratory. Unfortunately there are very few natural CO<sub>2</sub> hydrates on Earth; therefore natural methane hydrates provide a suitable alternative for investigations (see Chapter 6).

## **CHAPTER 3**

### **Mapping Hydrate Stability Zones**

### 3. Mapping Hydrate Stability Zones

#### *Introduction*

Prediction of hydrate stability has been used as a useful tool in borehole drilling to determine the depths at which hydrate formation may become a drilling problem. In more recent years, hydrate stability mapping has been used to identify regions for exploration and sampling. Miles (1995) provided the first map of the depth to the base of the methane hydrate stability zone off the European continental shelf, using a quadratic equation fitted to Pressure-Temperature (P-T) stability curves and a thinned crust model to estimate geothermal gradients. The majority of natural hydrates are dominated by methane, though natural carbon dioxide (CO<sub>2</sub>) hydrates have been discovered in the Okinawa Trough, offshore Japan (Sakai et al, 1990), and they may exist elsewhere in the solar system, such as on Mars or Jupiter's moon Europa (Miller, 1970; Duxbury et al, 2001; Duxbury et al, 2004; Prieto-Ballesteros et al, 2006). In addition, CO<sub>2</sub> hydrates are being researched for their potential use as a greenhouse gas mitigation strategy (Kiode et al., 1997; Rochelle & Camps, 2006; House, 2006; Rochelle et al., 2006). While previous research has focussed on models for methane hydrates no such model exists to estimate CO<sub>2</sub> hydrate stability zones.

Under present climatic and oceanographic conditions natural hydrates represent one of the largest stores of organic carbon on this planet (Henriet & Mienert, 1998), with their distribution mainly restricted to polar and deep oceanic regions (Kvenvolden, 1998). It is the immense quantity of methane locked within these hydrates, and their unique properties, which leads to their wide and varied current interest including their role in submarine landslides (Collett et al., 2000), in global warming events in the geological past (Kvenvolden, 1998; Maslin et al., 2004; Kemp et al., 2005), and their potential as a future energy resource (Lee & Holder, 2001; Ruppel, 2007).

The unique property of gas hydrates to contain as much as 164 m<sup>3</sup> of gas within 1 m<sup>3</sup> of solid hydrate has led to interesting research into its potential use in carbon capture and storage. Greenhouse gas emissions continue to rise at an alarming rate, and at the current rate, global temperatures are predicted to rise by a total of 5.8 °C this century (DTI, 2003, Stern, 2007). Other than a global change in attitude and lifestyle, methods

must be put into place to reduce atmospheric emissions. Although renewable energy sources are available, worldwide dependence on energy from fossil fuels does not appear to be in decline. A practical proven method of reducing environmentally damaging CO<sub>2</sub> emissions to the atmosphere is to store CO<sub>2</sub> in geological reservoirs (Holloway et al, 1996; Baklid et al, 1996; IEA GHG, 1998; Malik & Islam, 2000; Wilson & Monea, 2004; IPCC, 2005; Rochelle et al., 2006). In addition to current warm, deep, supercritical storage technologies, there is a potential storage method which could offer additional storage sites: storage as a liquid and hydrate in cold sub-seabed sediments, beneath deep oceanic waters (Kiode et al., 1997; Rochelle et al., 2006). In deep water offshore regions cold bottom water temperatures and reasonably high pressures could be favourable for storage of liquid CO<sub>2</sub> and solid CO<sub>2</sub> hydrate. Injection of slightly buoyant liquid CO<sub>2</sub> below its hydrate stability zone could lead to the formation of a hydrate 'cap' above a store of liquid CO<sub>2</sub>, which could enhance the sealing capacity of the storage system.

In terms of applying this approach as a means of reducing CO<sub>2</sub> emissions to the atmosphere, pressures and temperatures are suitable for CO<sub>2</sub> hydrate formation offshore north and west Scotland, therefore these offshore regions may also have suitable conditions for carbon storage as a liquid and hydrate. In addition to favourable conditions for CO<sub>2</sub> hydrate formation, the P-T conditions are such that natural methane hydrate may be present. To determine the full potential of carbon stores, both natural and artificial, data have been collected for the northern Rockall Trough and the Faeroe-Shetland Channel and input into computer models, developed to calculate the depth to the base of the methane and CO<sub>2</sub> hydrate stability zones. The predicted thicknesses of the hydrate stability zones are presented and discussed, and the same method has been applied to expand the study to predict CO<sub>2</sub> and methane hydrate stability zone thicknesses off the western European continental shelf, with a view to scoping the potential of this proposed method of CO<sub>2</sub> storage.

### 3.1. Methodology

#### 3.1.1 Hydrate stability program construction

A simple empirical relationship exists for pure methane, pure water hydrate (JOIDES Pollution Prevention and Safety Panel Report, 1992), where equilibrium is governed by the equation:

$$\ln P = A - B/T$$

P is the pressure in kilopascals (kPa), T the temperature in Kelvin (K), and A and B are constants derived from experimental hydrate stability data. The JOIDES report provided A and B values of 38.53 and 8386.8, respectively for a pressure range of 2505 kPa-11556 kPa, and values of 46.74 and 10748.1, respectively for a pressure range of 11556 kPa-80000 kPa. Using this relationship a Visual Basic computer program, `hydcalc.exe`, was developed to enable calculation of the depth to the base of the hydrate stability zone (Long, 1998, 2000). This program uses water depth (m), bottom water temperature (°C) and geothermal gradient (°C/km), with an assumed hydrostatic pressure of 10.17 kg/m<sup>2</sup>. A bottom water temperature offset of 1.1 °C was also included in the model to account for the reduction in hydrate stability when formed in water of seawater salinities (Dickens & Quinby-Hunt, 1994). This program developed for methane hydrate has been modified to calculate CO<sub>2</sub> hydrate stability (as described below).

To modify `hydcalc.exe`, CO<sub>2</sub> hydrate stability P-T diagrams were produced using the `CSMHYD.EXE` of Sloan, 1998 in order to determine the constants required for calculations. The natural log of pressure and the reciprocal of temperature were plotted against one another from data produced by Sloan's hydrate stability relationships, and the data was divided into pressure ranges for linear constants to be determined.

Constants derived for CO<sub>2</sub> hydrate stability program are as follows:

1. Between 1317.17 kPa and 3627.23 kPa A = 40.495, B = 9114.3
2. Between 3627.23 kPa and 41203.53 kPa A = 129.31, B = 34161
3. Between 41203.53 kPa and 114431.6 kPa A = 60.566, B = 14372

Using these constants, the previous assumed hydrostatic pressure of  $10.17 \text{ kg/m}^2$  and assumed  $1.1 \text{ }^\circ\text{C}$  temperature offset (see section 3.4.4 for further discussion), a program to calculate the predicted depth to the base of the  $\text{CO}_2$  hydrate stability zone has been developed, 'hycalcCO2.exe' (Figure 1 and see appendix A for script).

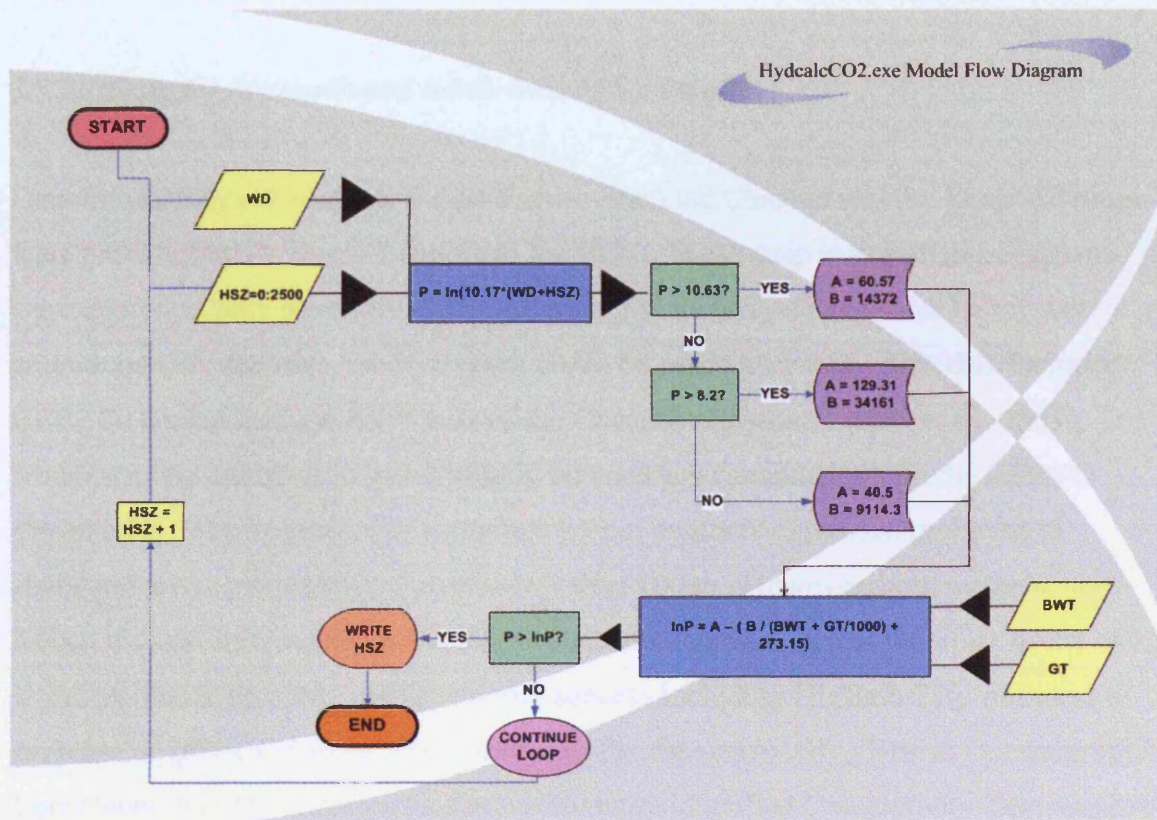


**Figure 3.1.1.** Model flow diagram for hycalcCO2.exe expressing processes involved in the calculation of the depth to the base of the  $\text{CO}_2$  hydrate stability zone. WD = water depth (m), BWT = bottom water temperature ( $^\circ\text{C}$ ), GT = geothermal gradient ( $^\circ\text{C}/\text{km}$ ), HSZ = hydrate stability zone thickness (m), P = pressure (kPa), A and B are derived constants (see text for details).

### **3.1.2 Data acquisition and interpretation**

It was necessary to compile a data set containing latitude, longitude, water depth (m), bottom water temperature (°C) and geothermal gradient (°C/km), for input into the previously constructed `hydcalc.exe` and `hydcalcCO2.exe` computer programs.

#### ***3.1.2.1 Data for the north and north-west of Scotland***

Data for stability calculations for the Faeroe-Shetland Channel and the Rockall Trough were provided by Dr David Long from the BGS. These deep water offshore regions were chosen as they provide the greatest potential for hydrate existence below waters around the UK, and data for these areas could be easily accessed. This data included GEBCO (Global Bathymetric Chart of the Oceans) bathymetry (IOC et al., 2003), which is a one minute grid based largely on contours contained within the GEBCO digital atlas. The derivation of bathymetry from contours expressed problems in shallower areas, particularly at depths less than 100 m. However, both methane and carbon dioxide hydrates are not stable in such shallow waters, and therefore limits any errors present in this data. BGS regional surveys including DigBath 250, was used to supplement GEBCO bathymetry, improving the data set locally. British Oceanographic Data Centre (BODC) with various other literature identified Conductivity-Temperature-Depth (CTD) casts within the study area and have been used to derive bottom water temperatures. This provided a dataset with fairly consistent temperatures, expressing a standard deviation of less than 0.5 °C (Long, 2000).

Geothermal gradient has been assumed from downhole temperature measurements from released well data on the West Shetland Shelf and Slope. The calculated gradients in this region show some variation and appear to have a fairly random distribution, however not enough data were available to construct a grid of geothermal gradients for the study region. Using the available data a 30 °C/km geothermal gradient seemed to approximate observations, and has been used in early estimates of hydrate for the Faeroe-Shetland Channel (Holmes et al., 1995). Although it is acknowledged this provides limitations in the model, this estimated geothermal gradient has been used

throughout the calculated stability predictions (see section 3.2.3 for further discussion on the data available and the limitations of the model).

### ***3.1.2.2 Data for offshore Western Europe***

Expansion of the study area to offshore the western European Continental Margin required an enormous quantity of data, which was obtained from various sources. The British Oceanographic Data Centre holds the General Bathymetric Chart of the Oceans (GEBCO), which contains global bathymetry on a one-minute grid. Bathymetric data in ASCII format, from longitude 20°W to 20°E, and latitude 30°N to 70°N, were downloaded from the BODC website, and compiled to form the basis for further data additions. Unfortunately, no global model exists for bottom water temperature, however; there are sources to obtain CTD cast data. CTD cast temperature data within the chosen bathymetric data area have been downloaded as ASCII data sets from the International Council for the Exploration of the Sea website ([www.ices.dk](http://www.ices.dk)). In addition, data were obtained from the BODC, the Coriolis Data Service organised by Ifremer, and IOS (Institute of Oceanographic Sciences) reports for the North Atlantic.

A geothermal gradient column has been added to the bathymetry data set, using an assumed geothermal gradient of 30 °C/km. This represents a global average geothermal gradient (Lapidus, 1990; Press & Siever, 1998), and is often applied to sites of continental crust (Long, 1998; 2000). This figure has been used in calculations due to a general lack of geothermal gradient data in the study regions offshore the western European continental shelf.

### ***Temperature gradient development***

Available CTD data for casts reaching great depths seems to be scarce, and therefore it was not possible to use actual bottom water temperatures to create temperature models of the NE Atlantic. Therefore, few casts were used to represent the water column's temperature profile, and it is assumed that the water column temperature can be used to estimate bottom water temperature.

The NE Atlantic was divided into areas of specific latitude and longitude, and a representative CTD cast temperature profile, with a high sampling rate, was chosen for each subset. By dividing each cast temperature profile into depth ranges and applying equations to each depth range, five temperature gradient models were developed (Figure 3.1.2). These equations were applied to the bathymetry data set through construction of a Matlab script file for creation of a temperature data column (see Appendix A). The calculated temperature gradients do not account for any stratification temperature effect. The first temperature gradient created applies to offshore the Iberian coast, the Bay of Biscay, and offshore the Moroccan coast (longitude 0° - 20°W, latitude 31°N - 50°N). Equations used to calculate temperature is as follows (T is temperature (°C), D is water depth (m)):

- |     |             |   |
|-----|-------------|---|
| 1.  | 0-62 m      | $T = (-0.0533 * D) + 20.765$                    |
| 2.  | 62-92 m     | $T = (-0.0603 * D) + 20.714$                    |
| 3.  | 92-1615 m   | $T = (0.0000009 * D)^2 - (0.0071 * D) + 16.205$ |
| 4.  | 1615-1979 m | $T = (-0.0062 * D) + 16.626$                    |
| 5.  | 1979-2730 m | $T = (-0.0018 * D) + 7.9157$                    |
| 6.  | 2730-2836 m | $T = (-0.0009 * D) + 5.4982$                    |
| 7.  | 2836-3672 m | $T = (-0.0005 * D) + 4.3412$                    |
| 8.  | 3672-4440 m | $T = (-0.00007 * D) + 2.7625$                   |
| 9.  | 4440-5070 m | $T = (0.0001 * D) + 2.0$                        |
| 10. | >5070 m     | $T = 2.507$                                     |

The temperature gradient for the Norwegian Sea, and the Baltic Sea covers an area of longitude 0° - 20°E, latitude 57°N - 70°N. Equations are as follows:

- |    |             |                            |
|----|-------------|----------------------------|
| 1. | 0-190 m     | $T = -0.0071 * D + 7.3515$ |
| 2. | 190-470 m   | $T = -0.0202 * D + 9.9008$ |
| 3. | 470-630 m   | $T = -0.0048 * D + 3.0371$ |
| 4. | 630-890 m   | $T = -0.0022 * D + 1.4271$ |
| 5. | 890-1010 m  | $T = -0.0011 * D + 0.4977$ |
| 6. | 1010-1550 m | $T = -0.0005 * D - 0.1489$ |
| 7. | 1550-2210 m | $T = -0.0001 * D - 0.6399$ |
| 8. | >2210 m     | $T = -0.93$                |

The southern North Sea temperature gradient data uses different equations to account for warmer temperatures:

- |    |          |                            |
|----|----------|----------------------------|
| 1. | 0-40 m   | $T = 13.055$               |
| 2. | 40-80 m  | $T = -0.0889 * D + 16.451$ |
| 3. | 80-200 m | $T = -0.0156 * D + 10.602$ |
| 4. | >200 m   | $T = -0.007 * D + 9.0$     |

The offshore area to the north and west of the British Isles (longitude 20°W - 0°, latitude 50°N - 70°N) was sub-divided into two areas. Temperatures in the area to the north of latitude 59°N were calculated using the same equations used in the calculation of Norwegian Sea temperatures. However, the temperatures below this latitude (50°N - 59°N) were calculated using equations developed from Rockall Trough CTD data:

- |    |             |                             |
|----|-------------|-----------------------------|
| 1. | 0-770 m     | $T = -0.0008 * D + 10.26$   |
| 2. | 773-1043 m  | $T = -0.007 * D + 14.981$   |
| 3. | 1043-1197 m | $T = -0.0112 * D + 19.463$  |
| 4. | 1197-1499 m | $T = -0.0049 * D + 11.863$  |
| 5. | 1499-1726 m | $T = -0.0027 * D + 8.6371$  |
| 6. | 1726-3047 m | $T = -0.001 * D + 5.7682$   |
| 7. | >3047 m     | $T = -0.00008 * D + 2.8945$ |

The large bottom water temperature decrease northwards of this latitude is a consequence of Norwegian Sea Deep Water (NSDW), which is colder and less saline than Atlantic waters. The exact latitude and longitude at which the bottom water temperatures change is unknown. Therefore, the latitude at which the different temperature gradients apply has been approximated through examination of available CTD cast data. Due to this change in temperature gradient a strong edge effect is created. To minimise this edge effect the difference between the two temperature gradients was calculated and divided into 10 creating 9 sets of intermediate gradients, forming the 5<sup>th</sup> temperature gradient model. These sub-gradients were applied to bathymetry data between latitude bands of 56°N and 60°N (Table 3.1).

Temperature gradient	Depth interval (m)	Temperature equation (4d.p)
1	0-180	$T=-0.0068*D+7.8255$
	180-480	$T=-0.0166*D+9.6518$
	480-620	$T=-0.0048*D+4.0658$
	620-1020	$T=-0.0021*D+2.3868$
	1020-1200	$T=-0.0015*D+1.7464$
	1200-1560	$T=-0.0009*D+1.0281$
	1560-1740	$T=-0.0004*D+0.2678$
	1740-2240	$T=-0.0002*D-0.0225$
	>2240	$T=-0.0001*D-0.2592$
2	0-180	$T=-0.0062*D+8.0960$
	180-480	$T=-0.0149*D+9.7193$
	480-620	$T=-0.0044*D+4.7540$
	620-760	$T=-0.0020*D+3.3031$
	760-1060	$T=-0.0024*D+3.5792$
	1060-1200	$T=-0.0026*D+3.7806$
	1200-1540	$T=-0.0013*D+2.2189$
	1540-1740	$T=-0.0006*D+1.1714$
	1740-2240	$T=-0.0003*D+0.6209$
>2240	$T=-0.0002*D+0.4115$	
3	0-180	$T=-0.0055*D+8.3665$
	180-480	$T=-0.0131*D+9.7870$
	480-620	$T=-0.0039*D+5.4423$
	620-760	$T=-0.0019*D+4.1727$
	760-1040	$T=-0.0031*D+5.0392$
	1040-1200	$T=-0.0036*D+5.6307$
	1200-1540	$T=-0.0017*D+3.3563$
	1540-1740	$T=-0.0009*D+2.0613$
	1740-2240	$T=-0.0004*D+1.2643$
>2240	$T=-0.0003*D+1.0823$	
4	0-180	$T=-0.0048*D+8.6370$
	180-480	$T=-0.0113*D+9.8545$
	480-620	$T=-0.0035*D+6.1305$
	620-760	$T=-0.0017*D+5.0423$
	760-1040	$T=-0.0036*D+6.4574$
	1040-1200	$T=-0.0046*D+7.5518$
	1200-1560	$T=-0.0021*D+4.5204$
	1560-1740	$T=-0.0011*D+2.9691$
	1740-2240	$T=-0.0005*D+1.9077$
>2240	$T=-0.0004*D+1.7530$	
5	0-180	$T=-0.0041*D+8.9075$
	180-480	$T=-0.0096*D+9.9221$
	480-620	$T=-0.0030*D+6.8188$
	620-760	$T=-0.0016*D+5.9120$
	760-1040	$T=-0.0042*D+7.8756$
	1040-1200	$T=-0.0057*D+9.4728$
	1200-1560	$T=-0.0025*D+5.6846$
	1560-1740	$T=-0.0013*D+3.8769$
	1740-2240	$T=-0.0006*D+2.5512$
>2240	$T=-0.0005*D+2.4238$	
6	0-180	$T=-0.0035*D+9.1780$
	180-480	$T=-0.0078*D+9.9897$
	480-620	$T=-0.0026*D+7.5070$
	620-760	$T=-0.0014*D+6.7816$
	760-1040	$T=-0.0047*D+9.2938$
	1040-1200	$T=-0.0067*D+11.3938$
1200-1560	$T=-0.0029*D+6.8487$	

	1560-1740	$T=-0.0016*D+4.7847$
	1740-2240	$T=-0.0007*D+3.1946$
	>2240	$T=-0.0006*D+3.0945$
<b>7</b>	0-180	$T=-0.0028*D+9.4485$
	180-480	$T=-0.0061*D+10.0573$
	480-620	$T=-0.0021*D+8.1953$
	620-760	$T=-0.0013*D+7.6512$
	760-1040	$T=-0.0053*D+10.7121$
	1040-1200	$T=-0.0077*D+13.3149$
	1200-1560	$T=-0.0033*D+8.0128$
	1560-1740	$T=-0.0018*D+5.6925$
	1740-2240	$T=-0.0007*D+3.8380$
	>2240	$T=-0.0007*D+3.7653$
<b>8</b>	0-180	$T=-0.0021*D+9.7190$
	180-480	$T=-0.0043*D+10.1248$
	480-620	$T=-0.0017*D+8.8835$
	620-760	$T=-0.0011*D+8.5208$
	760-1040	$T=-0.0058*D+12.1303$
	1040-1200	$T=-0.0088*D+15.2359$
	1200-1560	$T=-0.0038*D+9.1769$
	1560-1740	$T=-0.0021*D+6.6003$
	1740-2240	$T=-0.0008*D+4.4814$
	>2240	$T=-0.0008*D+4.4360$
<b>9</b>	0-180	$T=-0.0015*D+9.9895$
	180-480	$T=-0.0025*D+10.1924$
	480-620	$T=-0.0012*D+9.5718$
	620-760	$T=-0.0009*D+9.3904$
	760-1040	$T=-0.0064*D+13.5485$
	1040-1200	$T=-0.0098*D+17.1570$
	1200-1560	$T=-0.0042*D+10.3410$
	1560-1740	$T=-0.0023*D+7.5081$
	1740-2240	$T=-0.0009*D+5.1248$
	>2240	$T=-0.0009*D+5.1068$

**Table 3.1.** Intermediate temperature gradient equations applied to bathymetry data between latitude bands of 56°N and 60°N to smooth the bottom water temperature grid (T is temperature (°C) and D is depth (m)).

A Matlab script was compiled to apply the intermediate gradients to the necessary data file, smoothing the bottom water temperatures, allowing an improved grid to be developed for hydrate stability calculations.

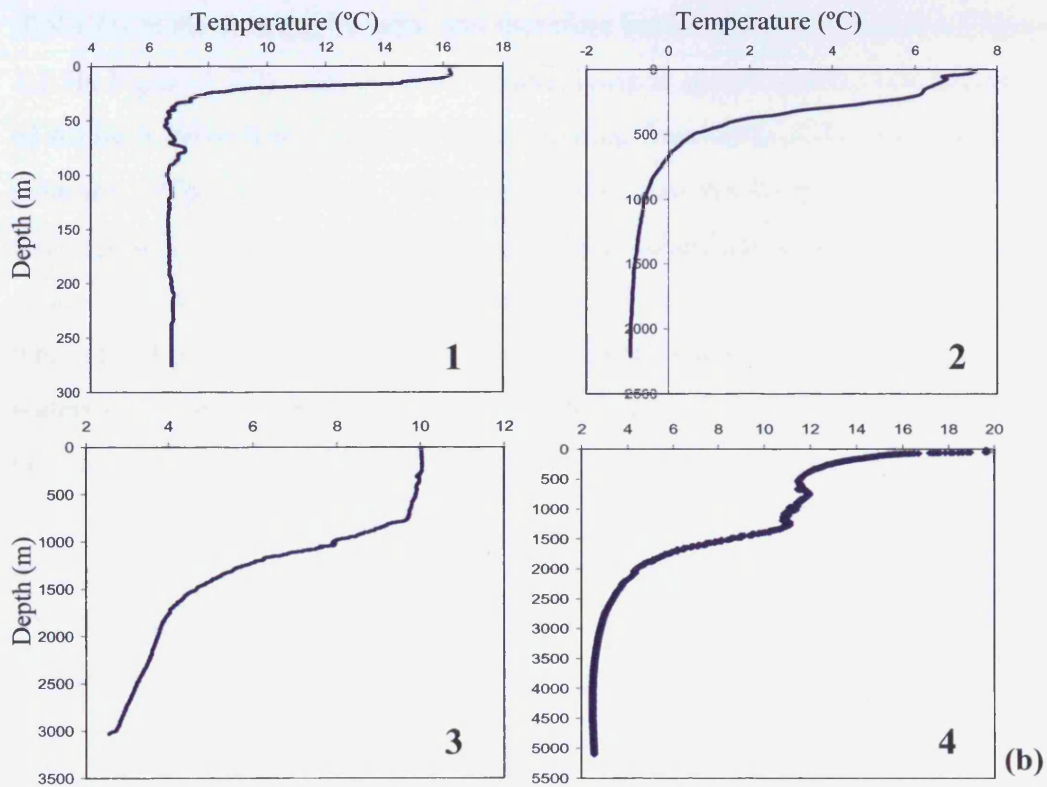
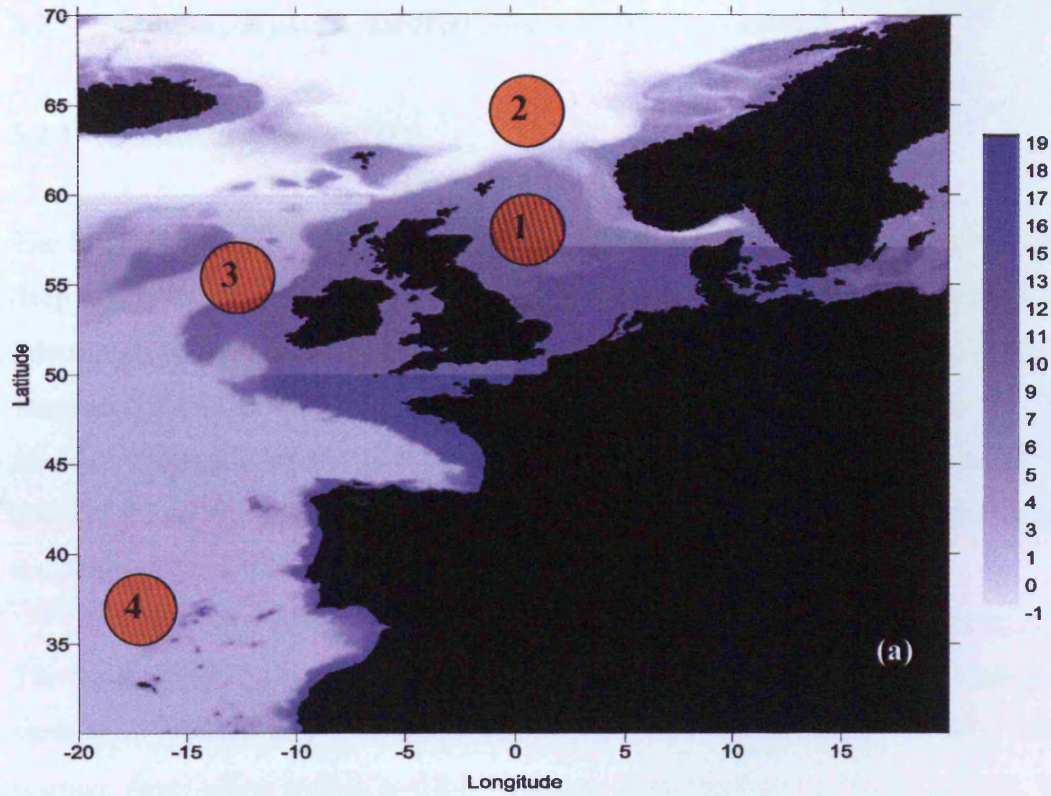


**Figure 3.1.2(a)** Bottom water temperature ( $^{\circ}\text{C}$ ) grid for hydrate and density predictions offshore Western Europe. Note horizontal lines represent unsmoothed change in temperature gradients used to formulate the grid in shallower regions. **(b)** Ocean temperature ( $^{\circ}\text{C}$ ) profiles from collected CTD data for regions highlighted in (a).

## **3.2 Mapping Hydrate Stability Zones Offshore Scotland**

### **3.2.1 Oceanographic setting**

The Rockall Trough lies to the west of the UK (British Isles) and is an intra-continental deep water basin with depths increasing southwards to over 3500 m. The bathymetry is interrupted by igneous seamounts, such as Rosemary Bank and the Anton Dohrn seamount (Howe et al., 2006). To the northeast of the Rockall Trough lies the Faeroe-Shetland Channel, separating the Faeroese plateau from the UK Continental Shelf. This channel reaches depths of 1500-2000 m in its northern entrance and is separated from the Rockall Trough by the Wyville-Thomson Ridge.

The oceanography of the study region is complex. The Faeroe-Shetland Channel surface waters consist of North Atlantic Water (NAW) (Turrell et al., 1999). These warmer, more saline waters possibly originate from the Eastern North Atlantic Waters (ENAW) of the Rockall Trough, and therefore have similar temperatures (Figure 3.2.1b; Figure 3.2.2). Intermediate waters, lying at approximately 400-800 m, consist of Arctic Intermediate Water (AIW) originating from north of the Iceland/Faeroe Ridge (Meinke, 1978; Turrell et al., 1999), and Norwegian Sea Intermediate Water (NSIW), with a possible origin in the Arctic zone of the Iceland and Greenland Seas. The channel's bottom waters consist of Faeroe Shetland Channel Bottom Water (FSCBW), which itself is formed from Norwegian Sea Deep Water (NSDW), originating from waters lying below 800 m in the Norwegian Sea, and overlying intermediate waters (Turrell et al., 1999). These waters are less saline and much colder, causing bottom water temperatures to fall below 0 °C (Figure 3.2.1; Figure 3.2.2). Minimal overflow of these colder waters may occur over the Wyville-Thompson Ridge entraining warmer Atlantic waters, but the overwhelming volume leaves via the Faeroe Bank Channel (Figure 3.2.1b).

The Rockall Trough surface waters consist of Eastern North Atlantic Water (ENAW), extending to a depth of approximately 1200 m. Below this lies North Atlantic Deep Water (NADW), which itself consists of Labrador Sea Water (LSW), Antarctic Bottom Water (AABW), and Norwegian Sea Deep Water (NSDW) (Figure 3.2.1; Figure 3.2.3). NADW forms by overflowing NSDW across the Wyville-Thompson Ridge, which

entrains westward flowing ENAW and northward flowing LSW and AABW (Howe et al., 2006). These Atlantic water temperatures and salinities are considerably higher than those in the Faeroe-Shetland Channel, with bottom waters reaching a minimum of approximately 2.6 °C (Figure 3.2.3).

### **3.2.2 Predicted hydrate stability zones**

The Faeroe-Shetland Channel region studied covers an approximate offshore area of 59.5°N to 62.5°N and 0°W to 7°W (Figure 3.2.2). The Rockall Trough study area is larger between 56°N to 61°N and 6°W to 14°W (Figure 3.2.3).

Data used to calculate hydrate stability zones in the Faeroe-Shetland Channel has a minimum bottom water temperature of -0.85 °C, and a maximum water depth of 1763 m. This compares with a minimum bottom water temperature of 2.62 °C in the Rockall Trough, and a maximum water depth of 3397 m. Bottom water temperatures and water depths have been plotted as filled contour plots to enable comparison with predicted hydrate thickness (Figure 3.2.2 and Figure 3.2.3).

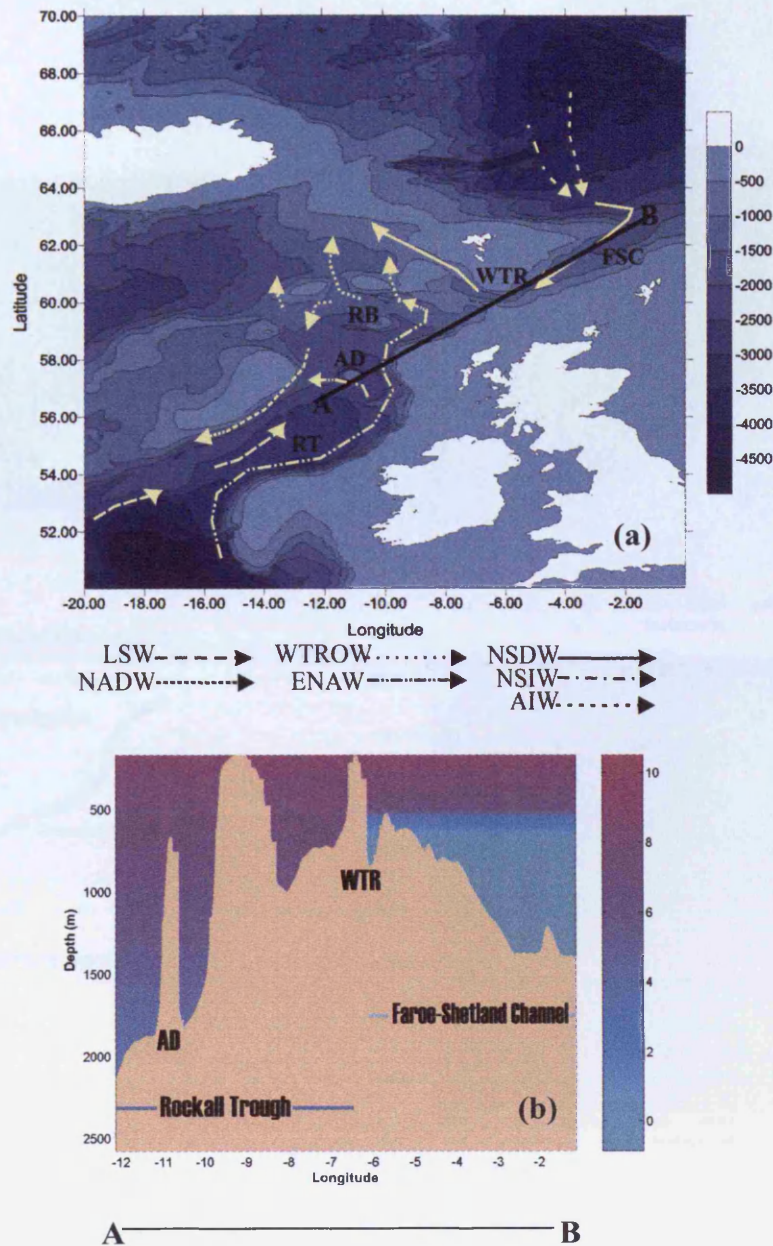


**Figure 3.2.1(a)** Bathymetry of the British and Icelandic Continental Shelves, showing the line of cross section, and regional water masses with current pathways (adapted from Howe et al, 2005). RB – Rosemary Bank seamount, AD – Anton Dohrn seamount, WTR – Wyville Thomson Ridge, FSC – Faroe-Shetland Channel, RT – Rockall Trough, LSW – Labrador Sea Water, NADW – North Atlantic Deep Water, WTROW – Wyville-Thomson Ridge Overflow Water, ENAW – East North Atlantic Water, NSDW – Norwegian Sea Deep Water, NSIW – Norwegian Sea Intermediate Water, AIW – Arctic Intermediate Water. **(b)** Cross section of Bottom Water Temperatures across the offshore study region, created from CTD data used in program predictions.

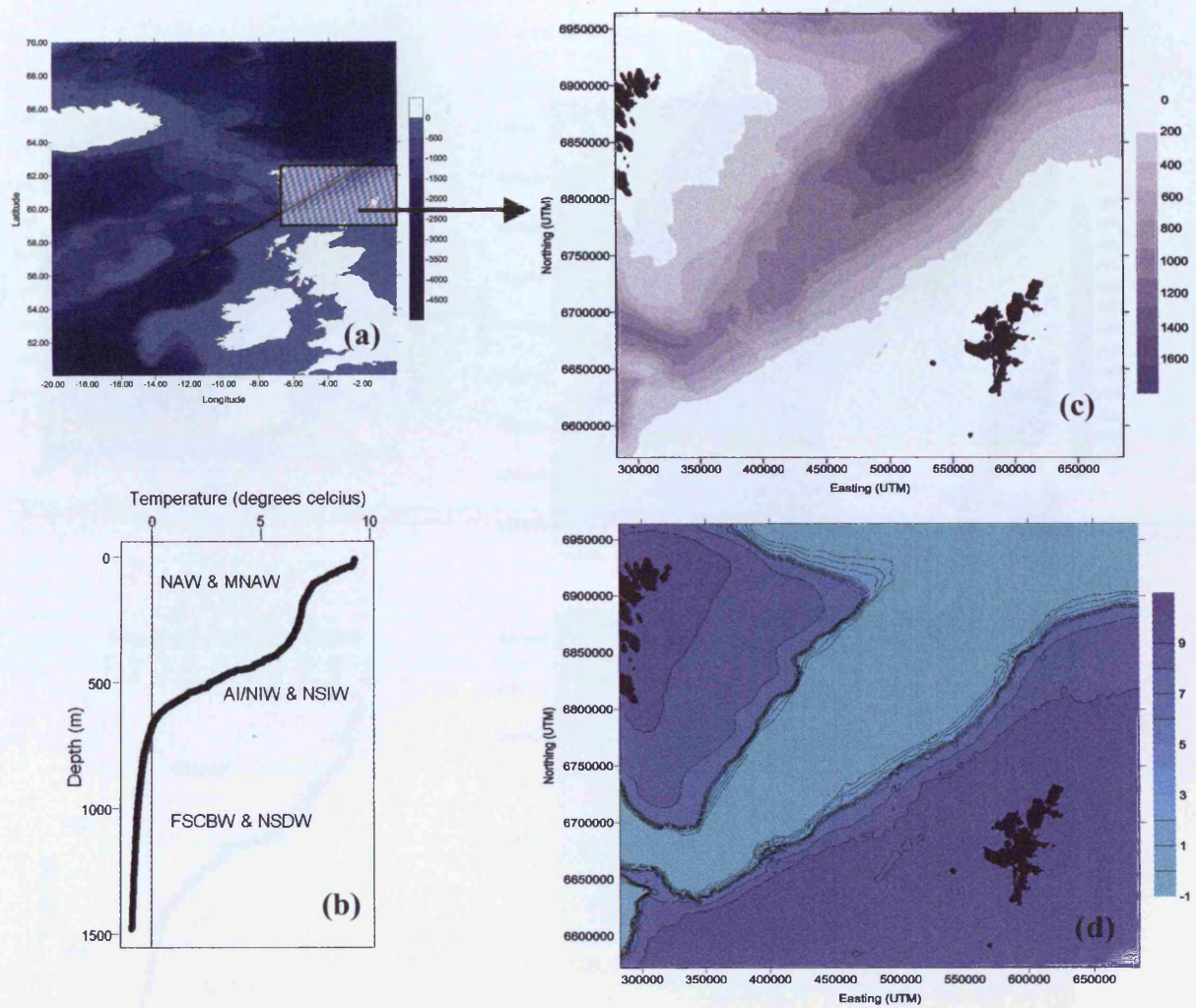


**Figure 3.2.2(a)** Bathymetric map offshore UK showing the position of the study area north of Scotland. **(b)** Faeroe-Shetland Channel CTD temperature profile with annotated regional water masses, **(c)** Faeroe-Shetland Channel contoured bathymetry and **(d)** Contoured bottom water temperatures taken from used dataset.

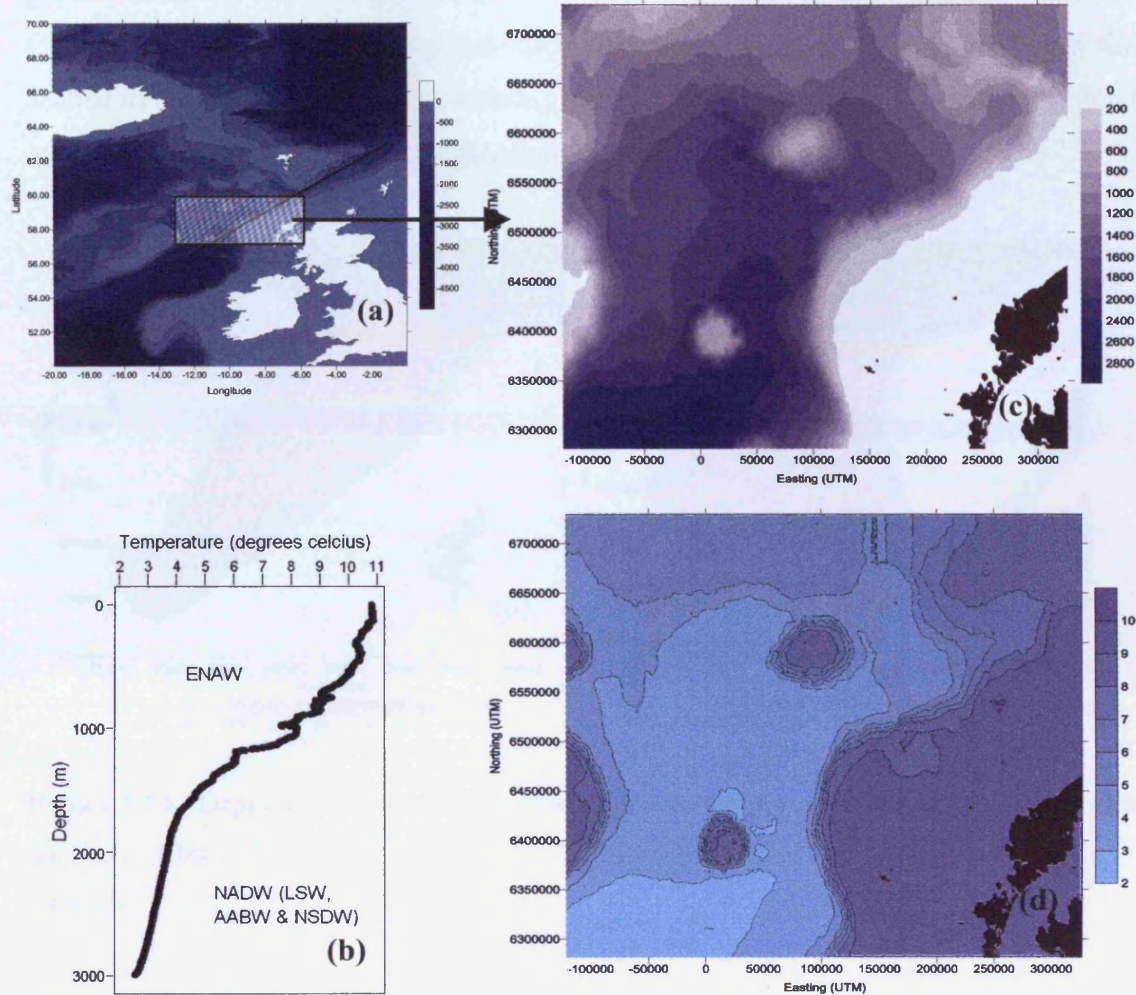


**Figure 3.2.3**(a) Bathymetric map offshore UK showing the position of the study area west of Scotland. (b) Northern Rockall Trough CTD temperature profile with annotated regional water masses, (c) Northern Rockall Trough contoured bathymetry and (d) Contoured bottom water temperatures taken from Rockall Trough dataset.

### *Methane hydrate stability*

The predicted methane hydrate stability zones for these two offshore regions have been plotted using the contouring package SURFER (Figure 3.2.4). In the Faeroe-Shetland Channel the methane stability model calculated a maximum depth of 682 m below the seabed to the base of the hydrate stability zone. This compares with a maximum depth of 668 m below the seabed in the Rockall Trough study region.

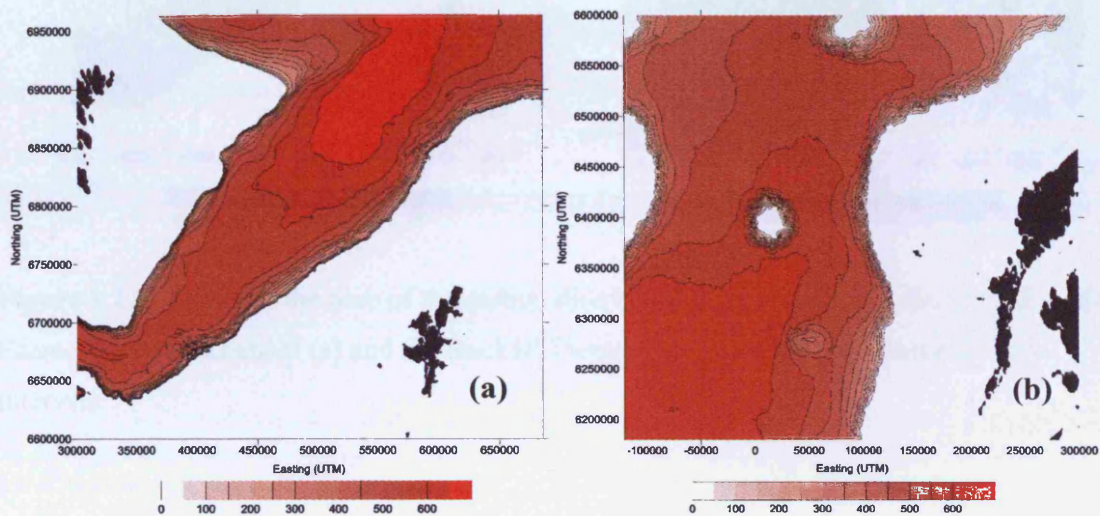


**Figure 3.2.4.** Depth to the base of the methane hydrate stability zone below the seabed (m) in the Faeroe-Shetland Channel (a) and the Rockall Trough (b). Contours are spaced at 50 m intervals.

### *Carbon dioxide hydrate stability*

The predicted carbon dioxide hydrate stability zones for the two offshore regions show a maximum depth of 346 m below the seabed to the base of the hydrate stability zone, in the Faeroe-Shetland Channel. This compares with a maximum depth of 281 m below the seabed in the Rockall Trough.

Carbon dioxide and methane hydrate stability zones extend to greatest depth at the northern end of the Faeroe-Shetland Channel and the southern end of the Rockall Trough. Here water depths increase and bottom water temperatures decrease. Although water depths are greater in the Rockall Trough, the stability zones extend to

greater depths in the Faeroe-Shetland Channel due to much colder bottom waters north of the Wyville-Thomson Ridge.

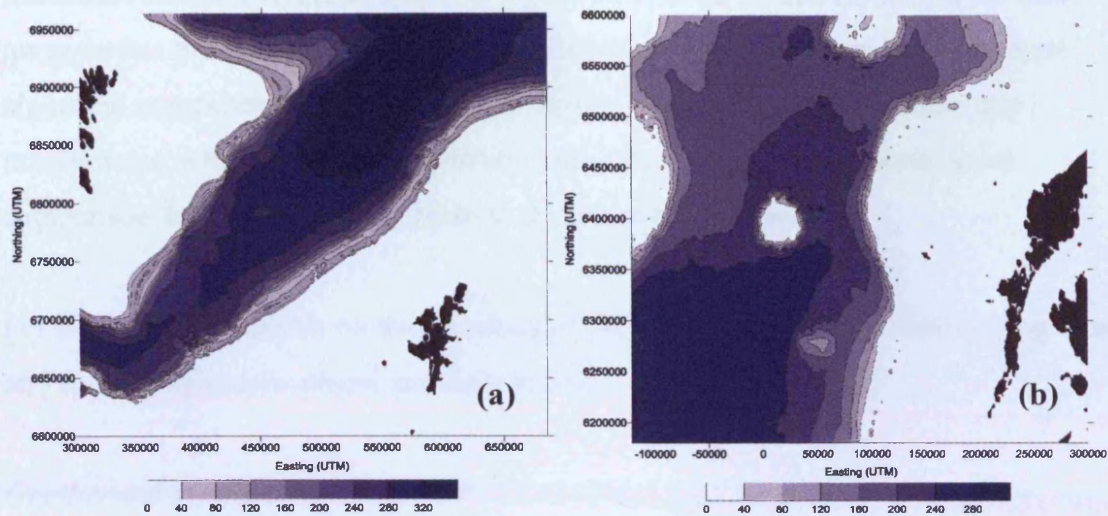


**Figure 3.2.5.** Depth to the base of the carbon dioxide stability zone below the seabed in the Faeroe-Shetland Channel (a) and the Rockall Trough (b). Contours are spaced at 40 m intervals.

Although carbon dioxide hydrate is often considered to be more stable than methane hydrate in the laboratory environment, and is easier to produce than methane hydrate, it has a thinner predicted hydrate stability zone. Carbon dioxide hydrate is more stable at low pressures and temperatures, but with the increase pressure and especially temperature with depth below the seabed, methane hydrate becomes relatively more stable (Figure 3.3.10), explaining the difference in predicted hydrate thicknesses displayed (Figure 3.2.4 and Figure 3.2.5).

### 3.2.3 Discussion

Program predictions for the depth to the base of the methane hydrate stability zone show direct comparison with previous calculations. Miles (1995) predicted the base of the methane hydrate stability zone to lie between 200 and 250 m, using a thinned crust model to estimate continental geothermal gradient (approximately 80 °C/km offshore north and west of Scotland) (also see Rao et al., 2001 for geothermal gradient

estimations). In this study a geothermal gradient of 30 °C has been estimated. If the developed computer program 'hydcalc.exe' uses a geothermal gradient of 80 °C/km, the maximum methane hydrate thickness is predicted to be 236 m, within the same range as that predicted by Miles (1995). However, although the methane hydrate algorithm compares well with estimates above, it is important to consider any inaccuracies, which may affect stability zone calculations. There is no direct comparison for carbon dioxide hydrate thickness predictions.

For a detailed discussion on the accuracy of the hydrate stability computer programs and contouring results please see section 3.4.

### ***Geothermal gradient***

Geothermal gradients collected from downhole temperature measurements (measured at less than 1 km from the seafloor) show wide variation with a fairly random distribution, ranging from 28 °C/km to 67 °C/km (Figure 3.2.6). Re-examination of the available geothermal gradients after calculations with the addition of further downhole measurements determined an average gradient of 45 °C/km, with a standard deviation of 11 °C/km. Although the 30 °C/km gradient used in these calculations lies within 2 standard deviations of the mean, it does lie at the lower end of the main range of measured geothermal gradients (Figure 3.2.6) and the consequence of using this single value would mean calculations tend to over estimate the thickness of the hydrate stability zones, and recent research (Long et al, 2005) suggests a geothermal gradient of 45 °C/km may be more appropriate. Re-calculation of hydrate thickness using the average regional geothermal gradient would decrease the predicted hydrate stability zones. The depth to the base of the methane hydrate stability zone would reduce from 682 m to 436 m in the Faeroe-Shetland channel, and from 668 m to 435 m in the Rockall Trough at its most southerly point. This would compare with depths to the base of the carbon dioxide hydrate stability zone reducing from 346 m to 225 m and from 281 m to 184 m, respectively.

As the program is extremely sensitive to geothermal gradient variations the accuracy of these values continues to represent the greatest level of uncertainty in the model, and may be particularly significant at a localised scale. A map of accurate geothermal

gradient in the study area, at the appropriate depth below seafloor, would be necessary for improved hydrate thickness predictions, though this is beyond the scope of this project. Such a map would be extremely difficult to derive due to the lack of detailed geothermal gradient data, and therefore the hydrate model used within this study is still a useful predictive tool.

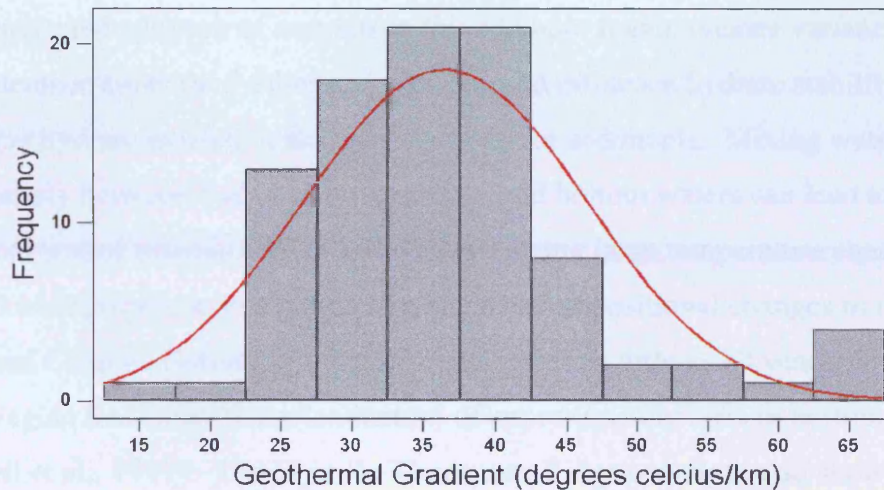


**Figure 3.2.6.** Histogram of calculated geothermal gradients offshore north and west of Scotland with an added normal curve.

### ***3.2.3.1 Evidence for natural methane hydrate***

There appears to be no direct evidence for natural methane hydrate in the study area, but this may be a consequence of a lack of pressurised core samples (Long, 2000).

Mud diapirs have been discovered in the northern end of the Faeroe-Shetland Channel (Long, 2000; Holmes et al, 2003), and similar structures have been associated with gas hydrates in other explored regions. No classic Bottom Simulating Reflectors have been discovered in the Faeroe-Shetland Channel, or the Rockall Trough; however, an anomalous reflector has been mapped in the northern section of the Faeroe-Shetland Channel. This has been found to cross-cut other reflectors and appears at approximately 300-400 m below the seabed (Long and Holmes, 1998). Doubts as to whether this reflector could be attributed to gas trapped below methane hydrate have

proven to be correct with Davies and Cartwright (2002) demonstrating the cross-cutting seismic reflector is an example of a diagenic fossilized Opal A to Opal C/T (Cristobalite/Tridymite) transition. There have been instances of hydrate formation on the seabed resulting from artificial releases of deep methane gas (Long et al, 2005). This confirms conditions are suitable for hydrate formation, as they are in most deep water areas, though natural samples remain undiscovered.

A complicated network of currents in this offshore region creates variations in bottom water temperatures (and salinities) which could influence hydrate stability if natural methane hydrate existed in near surface seafloor sediments. Mixing water masses, particularly between Faeroese intermediate and bottom waters can lead to the development of internal eddies and waves causing large temperature changes. Long-term oceanographic monitoring also indicates compositional changes in the Faeroe-Shetland Channel Bottom Water over time scales as little as 10 years, with a NSDW (Norwegian Sea Deep Water) reduction of approximately 20% in bottom waters (Turrell et al., 1999). The Wyville-Thompson Ridge overflow also shows variation. The volume of water overflowing the ridge, from the Faeroe-Shetland channel into the Rockall Trough, alters considerably, and mixing in descending overflow plumes can cause a bottom water temperature increase of c.3 °C (Sherwin and Turrell, 2005). Such fluctuations would influence the stability of hydrate at the seabed, and therefore it is unlikely natural hydrate would be found in areas with a shallow (thin) hydrate stability zone.

Although pressures and temperatures are suitable for hydrate formation and calculations predict a thick methane gas hydrate stability zone, greater exploration in the Faeroe-Shetland Channel and the Rockall Trough would be necessary to fully determine whether natural gas hydrate is present. Possible methane sources in the two regions have not been investigated within this study, and may help to pin-point suitable areas for further exploration.

### ***3.2.3.2 Carbon dioxide storage potential***

Maximum predicted carbon dioxide hydrate thickness in the Rockall Trough and the Faeroe-Shetland Channel are 280 m and 345 m, respectively for a 30 °C/km geothermal

gradient. Therefore, pressure and temperatures do appear to be in the range required for carbon dioxide storage as a liquid and hydrate, and a significant layer of carbon dioxide hydrate could be formed if all conditions are favourable. Borehole records show sediments within and near the studied areas may have suitable porosity for CO<sub>2</sub> injection and hydrate formation (BGS, 2004). Research shows a reduced porosity limits hydrate formation (Booth et al, 1998; Clennell et al, 2000), and a sandy reservoir would be advantageous for storage. Sandy horizons do appear on borehole logs within the predicted hydrate stability zone, though a more thorough investigation would be necessary to fully quantify the storage potential.

The studied regions are a significant distance offshore, and pipeline costs from the coast would be expensive. However, should offshore platforms be constructed, these potential storage sites would increase their appeal. Alternative regions with storage potential may also occur offshore Western Europe, with thick hydrate stability zones relatively close to shore (see section 3.3.2), and therefore more easily accessible.

#### **3.2.4 Conclusions**

- A computer program has been developed to calculate the predicted depth to the base of the carbon dioxide hydrate and methane hydrate stability zone.
- Data for input into the developed program have been collected within two regions offshore the north and west of Scotland: the Faeroe-Shetland Channel and the Rockall Trough.
- Initial calculations (using a geothermal gradient of 30 °C/km) predict the methane hydrate stability zone to reach a maximum of 682 m below the seabed in the Faeroe-Shetland Channel, and 668 m in the northern Rockall Trough. However, more recent evidence discovered after model calculations suggests a geothermal gradient of 45 °C/km may be more accurate, reducing the predicted stability zones to 436 m and 435 m, respectively.

- No physical evidence has been determined to support the existence of natural methane hydrate in these regions, though the presence of mud diapirs in the Faeroe-Shetland channel may be an indicator of its presence.
- Initial calculations predict the carbon dioxide hydrate stability zone to extend to a depth of 346 m beneath the seafloor in the Faeroe-Shetland Channel, and to a depth of 281 m in the northern Rockall Trough. Using a geothermal gradient of 45 °C/km predicted hydrate stability zones would reduce to 225 m and 184 m, respectively. Therefore, conditions may be suitable for carbon dioxide storage as a liquid and hydrate.
- These calculations could be greatly improved with a detailed map of geothermal gradient data.

### **3.3. Mapping hydrate stability offshore western Europe**

The models developed and discussed in section 3.1 have been applied to a detailed hydrate stability zone thickness localised study for the Rockall Trough and the Faeroe-Shetland channel (see section 3.2). This has been extended to a regional study offshore the western European continental shelf to examine Europe-wide potential for carbon dioxide and methane hydrate stability. A slightly more simplified dataset has been developed to calculate hydrate stability zone thickness over this offshore large region to enable results to be produced during the short timeframe of this project.

#### **3.3.1. Oceanographic Setting**

The study area off the western European continental shelf lies between the geographic positions 20°W, 30°N to 20°E, 30°N and 20°W, 70°N to 20°E. The ocean circulation in this region is complex with numerous water masses forming the North East Atlantic Ocean and associated water bodies. Water depths reach a maximum of 5743 m in the Iberian basin, and temperatures vary according to the associated water mass present, reaching sub-zero bottom water temperatures at higher latitudes. Large topographical features such as the Iceland-Faeroe Rise dominate sections of the seabed in this part of the Atlantic, as well as relatively flat areas, such as the Iberian Abyssal Plain, and deep channels such as the Norwegian Deep and the Rockall Trough. The continental shelf is narrow in most places, with exceptions around the British Isles and northwest France, where it forms the shallow seabed of the North Sea, Irish Sea, Celtic Shelf and the Northern Bay of Biscay (Figure 3.3.1). Many seamounts are present, which influence localised current pathways. These include the Anton Dohrn, the Biscay, and the Vigo seamounts.

The surface waters of the North East Atlantic Ocean are considerably warmer than other ocean areas at similar latitudes. This is due to the large northward transport of heat from low latitudes by the North Atlantic Current. These warmer waters cross the Greenland-Iceland/Iceland-Faeroe Ridge and enter the Nordic Seas and the Arctic, where they are converted to colder water masses, which return southwards over the ridge. Surface waters largely consist of warm northward flowing Eastern North

Atlantic Water (ENAW). Intermediate waters in the region vary considerably, and include water masses such as southward flowing Arctic Intermediate Water (AIW) and Norwegian Sea Intermediate Water (NSIW), northward/eastward flowing Labrador Sea Water (LSW), and Mediterranean Water. Mediterranean Water flows westward from the Mediterranean Sea into the Gulf of Cadiz, descends as a spreading plume, and mixes with overlying Eastern North Atlantic Water. This mixed Mediterranean water creates a higher salinity gradient decreasing westward and northward with a peak salinity of approximately 36.2‰. Bottom waters consist of Norwegian Sea Deep Water (NSDW), Labrador Sea Water (LSW), Arctic Deep Water (ADW) and northward flowing Antarctic Bottom Water (AABW).

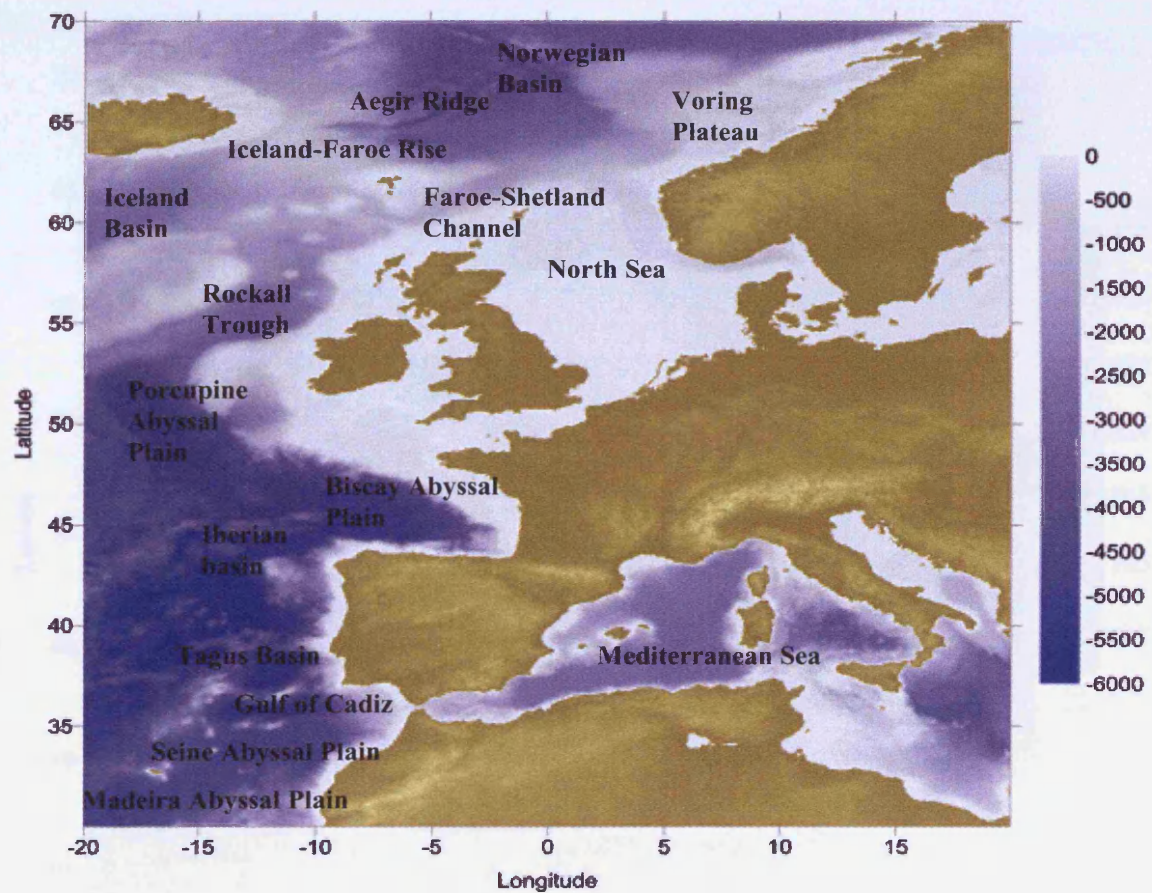


**Figure 3.3.1.** Water depth below sea-level (m) off the western European Continental Shelf.

Temperature profiles and bottom water temperatures for the different regions of the North East Atlantic have been discussed previously (please see section 3.1 and 3.2).

### 3.3.2 Carbon dioxide hydrate stability

A compiled data file of longitude, latitude, water depth (m), bottom water temperature (°C) and geothermal gradient (°C/km) was input into the previously developed `hydcalcCO2.exe` program, to calculate the depth to the base of the carbon dioxide hydrate stability zone.

A grid of the predicted thickness of the CO<sub>2</sub> hydrate stability zone, with 0.1 grid spacing, was created in SURFER, and the results were contoured (Figure 3.3.2). The Mediterranean Sea has been omitted from calculations.

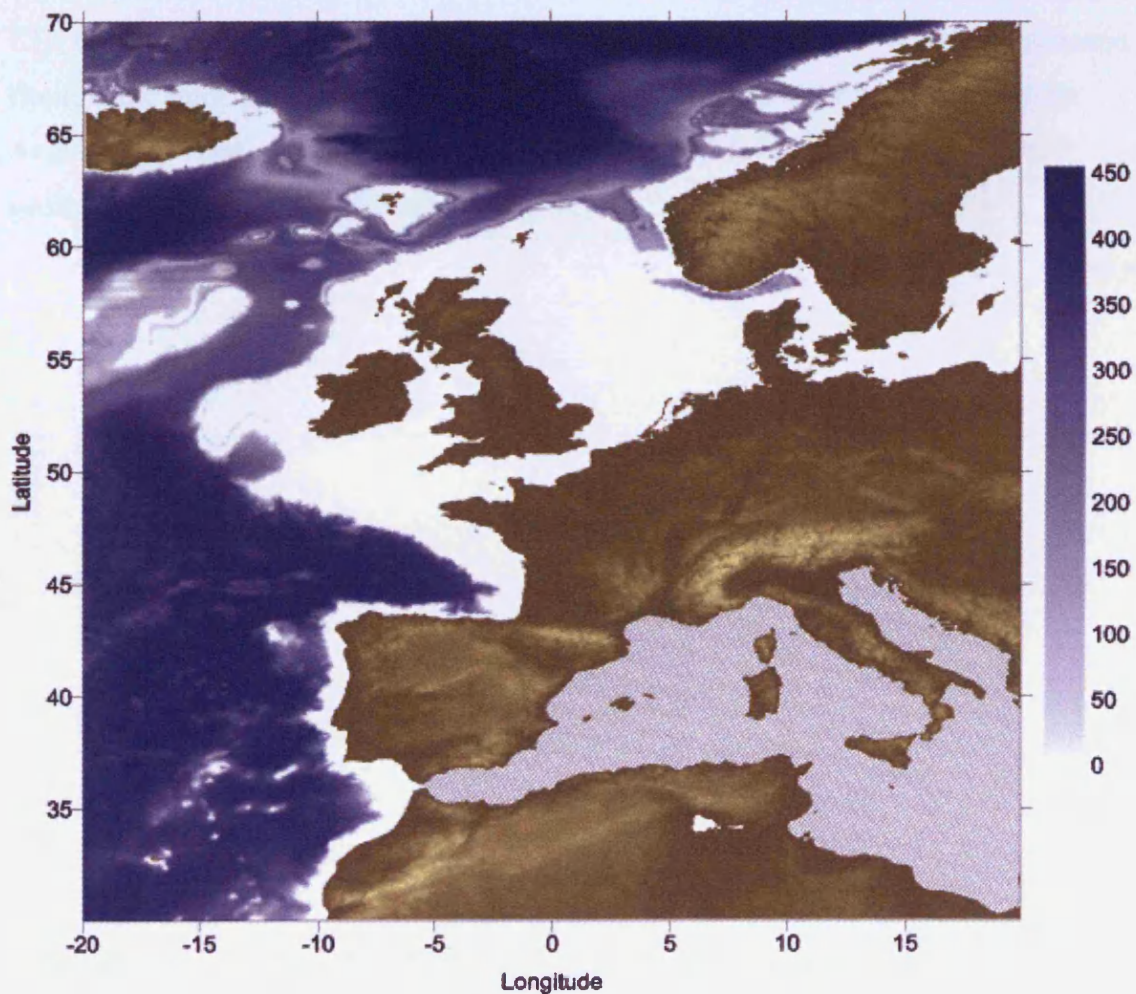


**Figure 3.3.2.** Predicted depth to the base of the CO<sub>2</sub> hydrate stability zone below the seafloor offshore western Europe (m). The Mediterranean has been omitted from this study.

Results predict CO<sub>2</sub> hydrate will be stable over large areas, with the base of the CO<sub>2</sub> hydrate stability zone reaching a maximum depth of 460 m below the ocean floor where water depths exceed 3800 m in the Aegir ridge, Norwegian basin, and bottom water temperatures are at a minimum of approximately -0.9 °C. These calculations use an assumed geothermal gradient of 30 °C/km, as there are no widespread databases of geothermal gradient, and global averages lie between 20 °C/km and 40 °C/km (Lapidus, 1990; Press & Siever, 1998).

### **3.3.3 Methane hydrate stability**

Results predict CH<sub>4</sub> hydrate will also be stable over large areas, with the base of the CH<sub>4</sub> hydrate stability zone reaching a maximum depth of up to 867 m below the ocean floor, at the same geographical position as the CO<sub>2</sub> hydrate stability maxima in the Aegir Ridge, Norwegian Basin (Figure 3.3.3). These calculations use an assumed geothermal gradient of 30 °C/km.

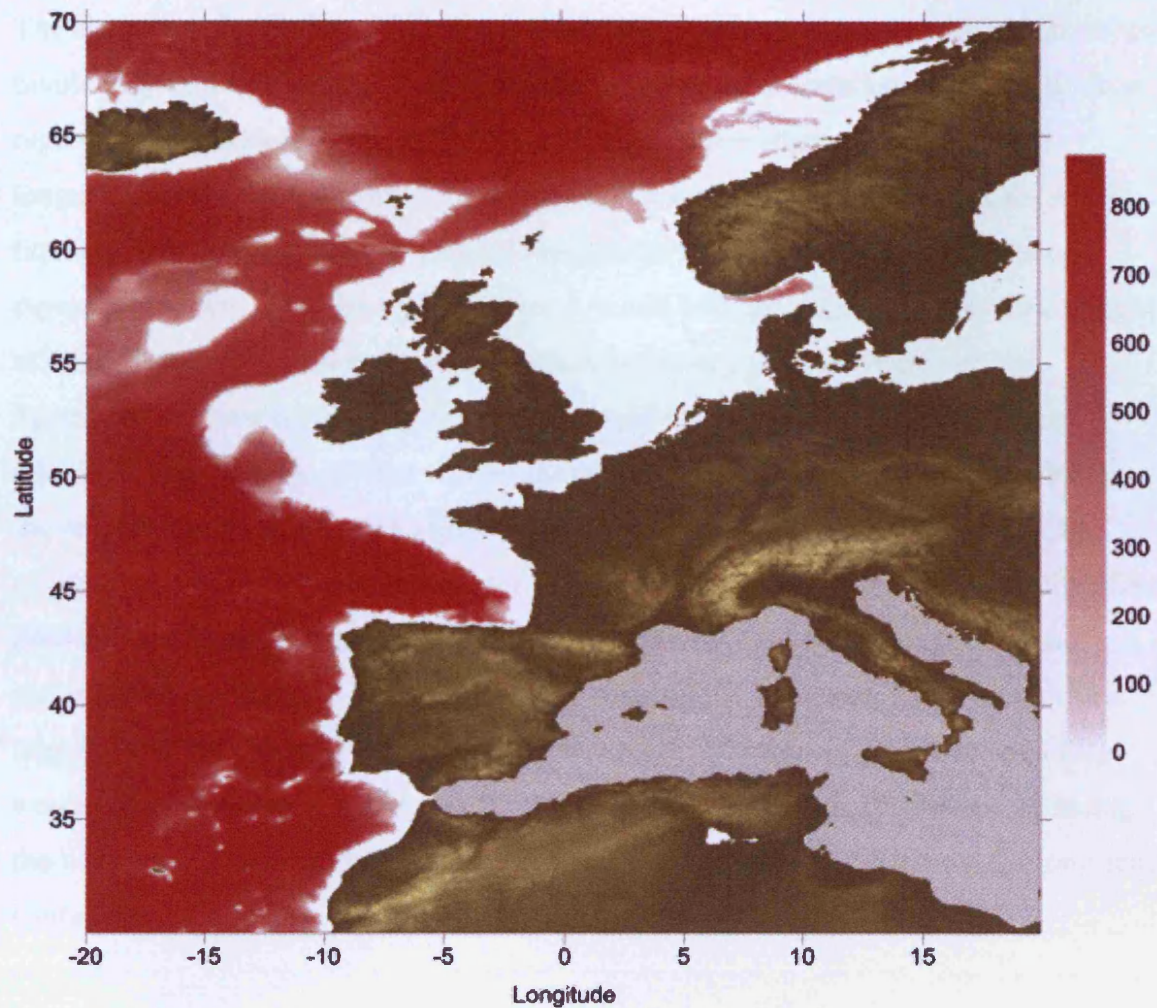


**Figure 3.3.3.** Predicted depth (m) to the base of the methane hydrate stability zone below the seafloor offshore western Europe. The Mediterranean has been omitted from this study.

### 3.3.4 CO<sub>2</sub> density and solubility

Most methods actively being considered for underground CO<sub>2</sub> storage involve *in-situ* conditions above the critical point of CO<sub>2</sub> (i.e. >31.1 °C, >73.8 bar), where a supercritical phase is stable. The density of this supercritical phase will vary with temperature and pressure but may be in the order of 0.7 g/cm<sup>3</sup> (700 kg/m<sup>3</sup>) (Rochelle & Camps, 2006; Rochelle et al., 2006). Storage of supercritical CO<sub>2</sub> would therefore require a low permeability cap-rock to prevent the buoyant CO<sub>2</sub> migrating towards the surface.

The storage method being discussed in this study, storage as a liquid and hydrate, would involve injection of liquid CO<sub>2</sub> into sediments below deep waters or below permafrost regions, where pressures are as high as in a deep aquifer storage system, but temperatures are much lower. Under these conditions the stable phase of CO<sub>2</sub> will be liquid, which is likely to have a higher density (in the order of 0.9 cm<sup>3</sup>) to that of supercritical CO<sub>2</sub>. This means less volume would be required to store the same weight of CO<sub>2</sub>. The increased density would reduce buoyancy forces driving vertical migration, and so a thinner cap-rock may be sufficient to contain the stored CO<sub>2</sub> (Rochelle et al., 2006). Cooler temperatures would also increase its viscosity; hence any migration would be much slower than for supercritical CO<sub>2</sub>. In addition, CO<sub>2</sub> solubility increases with decreasing temperature up to the point of hydrate precipitation. Studies have shown a significant amount of stored CO<sub>2</sub> will be trapped as a dissolved phase and once dissolved, CO<sub>2</sub> is no longer susceptible to the same buoyancy driven migration as free phase CO<sub>2</sub> (Rochelle et al., 2006). Therefore, increased solubility would mean increased concentrations of CO<sub>2</sub> in its trapped dissolved phase, reducing the likelihood of upward migration. All these factors would be beneficial for long-term containment.

To fully comprehend the variability of the density of liquid CO<sub>2</sub> in this storage scenario, and consequently the potential for buoyancy driven upward migration, carbon dioxide and seawater densities have been calculated at the base of the carbon dioxide hydrate stability zone (the liquid CO<sub>2</sub> density below the previously predicted CO<sub>2</sub> hydrate 'cap'). Densities have been calculated for offshore western Europe and results have been contoured.

#### ***3.3.4.1 CO<sub>2</sub> and seawater density at the base of the hydrate stability zone***

A Microsoft Excel function was provided by Eric Lindeberg at SINTEF Petroleum Research for the calculation of carbon dioxide density in kg/m<sup>3</sup> using pressure (bar) and temperature (°C), with an assumed seawater salinity of 35‰. Initial data processing for density calculations involved the creation of two new data columns within the Western European dataset containing total depth at the base of the carbon dioxide hydrate stability zone (water depth (m) + hydrate stability zone thickness (m)), and the

temperature at the base of the hydrate stability zone (hydrate stability zone thickness (m)\*0.03 °C/m + bottom water temperature (°C)). Due to the huge quantity of data used to calculate hydrate stability off the western continental shelf, it was necessary to divide data into sizable pieces to allow input into Excel, using a simple file splitter, 'Splitter Light 4.0' widely available for download from <http://www.martinstoeckli.ch/splitter/>. The newly created columns could then be input into the density function 'CO2\_SW'. The same files were used to calculate seawater density at the base of the hydrate stability zone. Seawater densities have been calculated in Matlab using the widely available function 'sw\_dens', which can be downloaded from the Mathworks website. This uses inputs of salinity (‰), temperature (°C), and pressure (db). After calculation of seawater density and carbon dioxide density it was possible to deduct seawater density from CO<sub>2</sub> density to obtain a density difference (i.e. essentially how buoyant the stored CO<sub>2</sub> would be).

After all calculations had been performed it was necessary to filter the data to ensure only density values are presented for areas where CO<sub>2</sub> hydrate is stable. The filtered data sets were then merged and contoured using the contouring package SURFER. Results are presented as a series of maps with a grid spacing of 0.1 (Figure 3.3.4, 3.3.5).

### *CO<sub>2</sub> density*

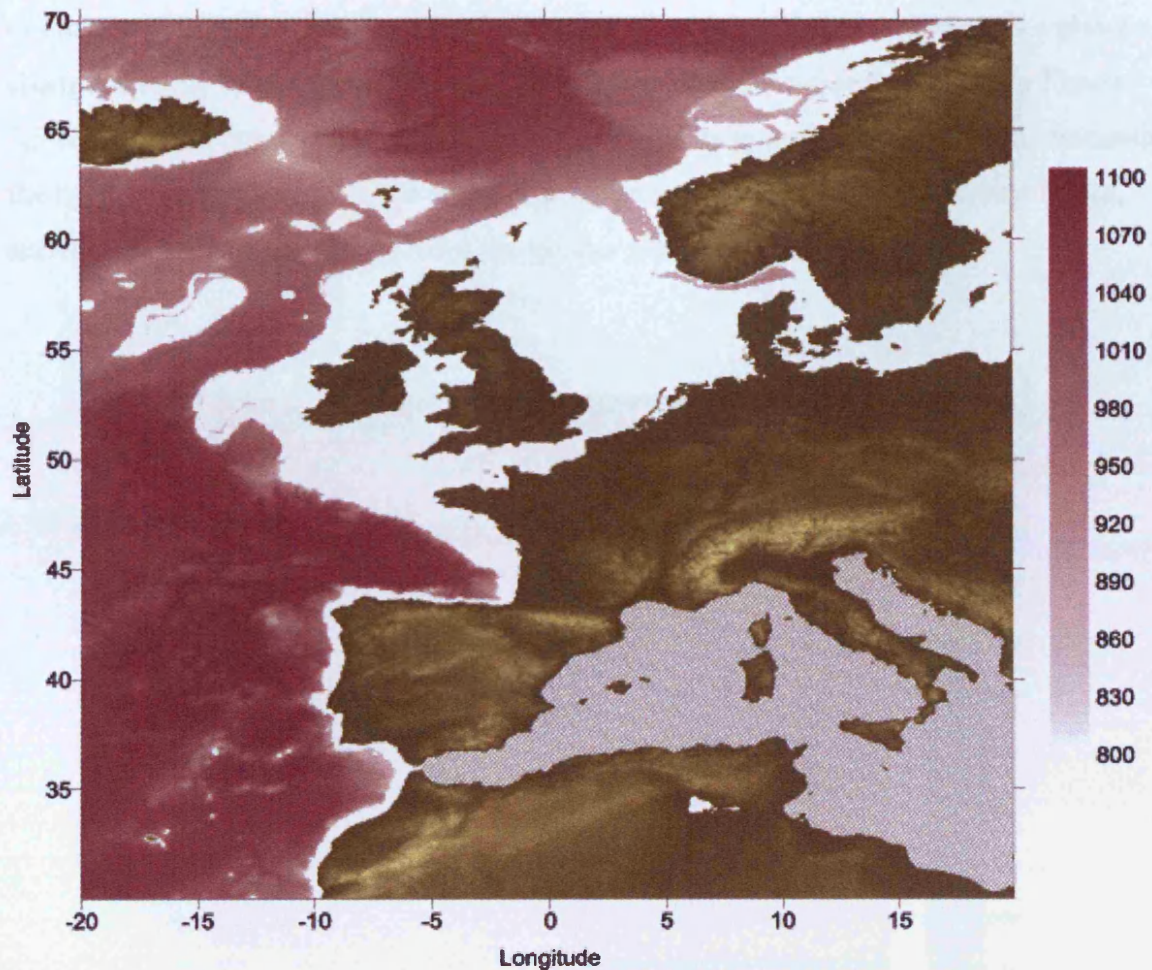


**Figure 3.3.4.** Carbon dioxide density ( $\text{kg/m}^3$ ) at the base of the  $\text{CO}_2$  hydrate stability zone off the western European continental shelf. Contours levels are spaced at  $5 \text{ kg/m}^3$  intervals. The Mediterranean has been omitted from this study.

The minimum carbon dioxide liquid density at the base of the hydrate stability zone off the Western European continental shelf is predicted to be  $822 \text{ kg/m}^3$  ( $0.822 \text{ g/cm}^3$ ) in the Gulf of Cadiz, with a maximum density of  $1092 \text{ kg/m}^3$  ( $1.092 \text{ g/cm}^3$ ) to the west of the Madeira-Tore Rise in the Iberian Basin, where water depths reach their maximum of 5743 m. Greatest  $\text{CO}_2$  densities lie below deep-water sediments offshore the Iberian coast in the Iberian Basin. Densities generally decrease northwards, with lower liquid  $\text{CO}_2$  densities appearing in shallower regions such as the Iceland-Faeroe Rise.

The density of carbon dioxide varies with temperature and pressure, decreasing with increasing temperature and increasing with increasing pressure (Figure 3.3.5). The rate of change with both variables is fairly linear until carbon dioxide experiences a phase change; change from a liquid to a gas. This phase change is clearly visible on Figure 3.3.5. The blue contoured region represents CO<sub>2</sub> density in its gaseous phase. Beneath the hydrate stability zone in the study region the stable phase of CO<sub>2</sub> will be a liquid, and hence densities on Figure 3.3.4 are greater than 800 kg/m<sup>3</sup>.

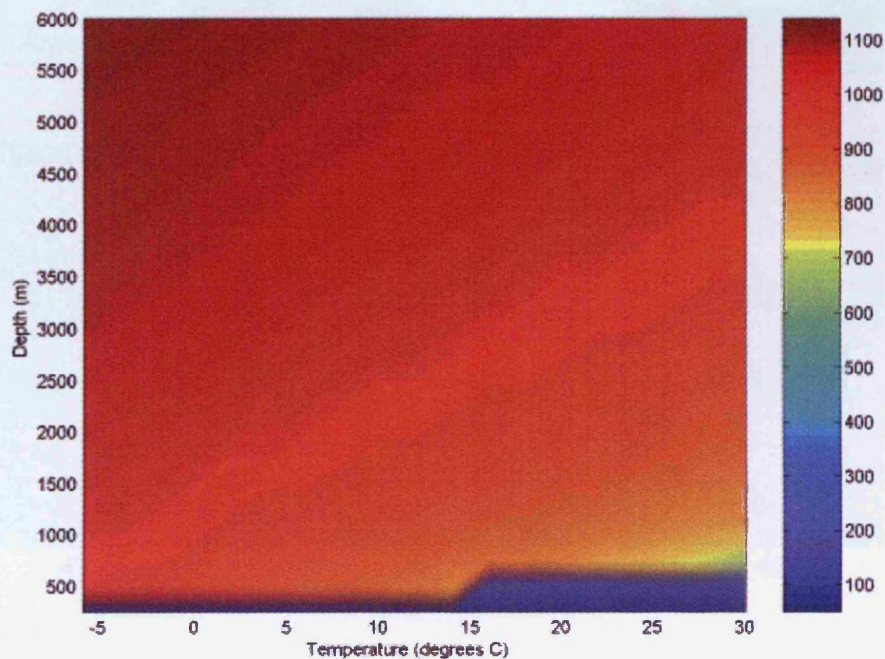


**Figure 3.3.5.** Contour plot of the variation of CO<sub>2</sub> density (kg/m<sup>3</sup>) with pressure (depth in metres) and temperature (°C). The step in density at approximately 15 °C represents a phase change; change from a liquid to a gas.

### Seawater density

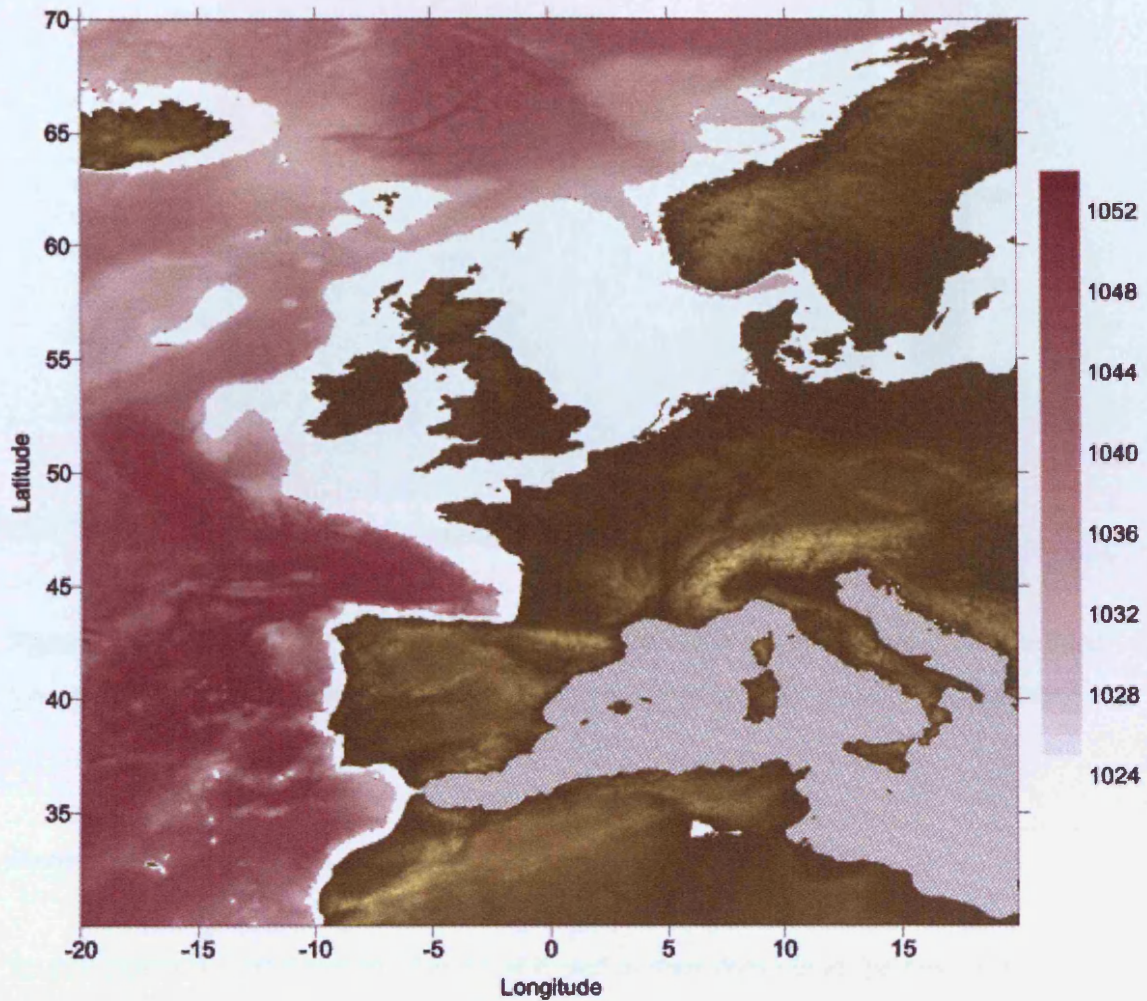


**Figure 3.3.6.** Seawater (35ppm) density ( $\text{kg/m}^3$ ) at the base of the carbon dioxide hydrate stability zone off the western European continental shelf. Contours levels are spaced at  $1 \text{ kg/m}^3$  intervals. The Mediterranean has been omitted from this study.

The maximum seawater density occurs at the same point as that of liquid  $\text{CO}_2$  density reaching  $1052 \text{ kg/m}^3$  to the left of the Madeira-Tore Rise in the Iberian Basin, where water depths reach their maximum of 5743 m. Similarly densities generally decrease northwards, with lower seawater densities appearing in shallower regions.

Seawater density varies with temperature and pressure, decreasing with increasing temperature and increasing with increasing pressure (Figure 3.3.7).

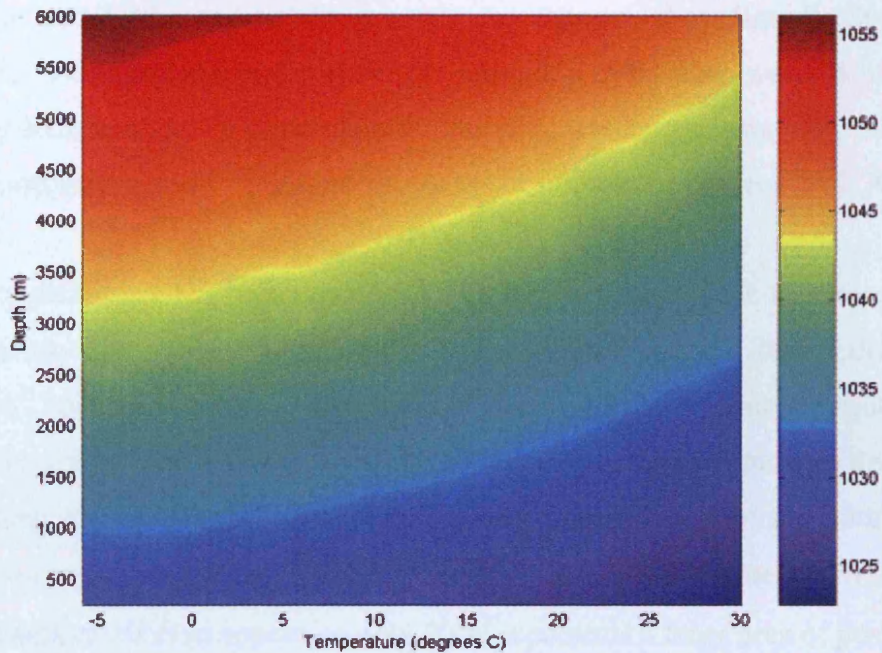


**Figure 3.3.7.** Contour plot of seawater density ( $\text{kg/m}^3$ ) with pressure (depth in metres) and temperature ( $^{\circ}\text{C}$ ). A seawater salinity of 35 ppm has been used for calculation of density.

### *Density difference*

To determine the effective buoyancy of liquid carbon dioxide at the base of the hydrate stability zone, which represents the minimum depth for  $\text{CO}_2$  injection, the difference between  $\text{CO}_2$  and seawater density was calculated. A negative density difference identifies regions where seawater is denser than liquid  $\text{CO}_2$ , and positive values identify areas where liquid  $\text{CO}_2$  is denser than seawater. Depths at which  $\text{CO}_2$  becomes denser than seawater are important for storage scenarios, as a liquid which is denser than seawater will not be subjected to buoyancy driven upward migration (therefore it will sink deeper into the sediments), and thus aid long-term containment. However, the storage of liquid  $\text{CO}_2$  under conditions where  $\text{CO}_2$  becomes denser than seawater would limit the formation of a hydrate ‘cap’, as such is dependent upon slow buoyancy driven upward migration to allow the  $\text{CO}_2$  to enter the hydrate stability zone. The formation of hydrate under these circumstances would rely on  $\text{CO}_2$  being dissolved into the pore waters and diffusing upwards into the hydrate stability zone. Regions with a zero density difference will be neutrally buoyant, and at this point liquid  $\text{CO}_2$  can be

described as an NNAPL (a neutrally-buoyant non-aqueous phase liquid). Stored CO<sub>2</sub> as an NNAPL, or as a dense liquid without the formation of hydrate, would remain within the hosting sediment slowly dissolving into the pore waters, and gradually react to possibly form carbonates (via similar processes described for supercritical CO<sub>2</sub> storage).

The density difference has been contoured, highlighting the regions with zero and positive density difference (Figure 3.3.8). The maximum positive density difference, of 37.98 kg/m<sup>3</sup>, appears in the offshore region of the Iberian/Moroccan peninsula where water depths are at their greatest. Liquid CO<sub>2</sub> density increases rapidly in this region due to a steep continental shelf gradient. Therefore, the majority of the North East Atlantic region covering a longitudinal area of 20°W to approximately 5°W, and a latitudinal area of 30°N to approximately 50°N represents a large area of positive density difference. Hence, any CO<sub>2</sub> injected below the hydrate stability zone in this region wouldn't be subjected to subsequent vertical migration. A similar region appears between Iceland and Norway, from approximately 7°W to 2°E, and 65°N to 70°N. This area has a more apparent zone of 0 density difference, where CO<sub>2</sub> becomes an NNAPL.

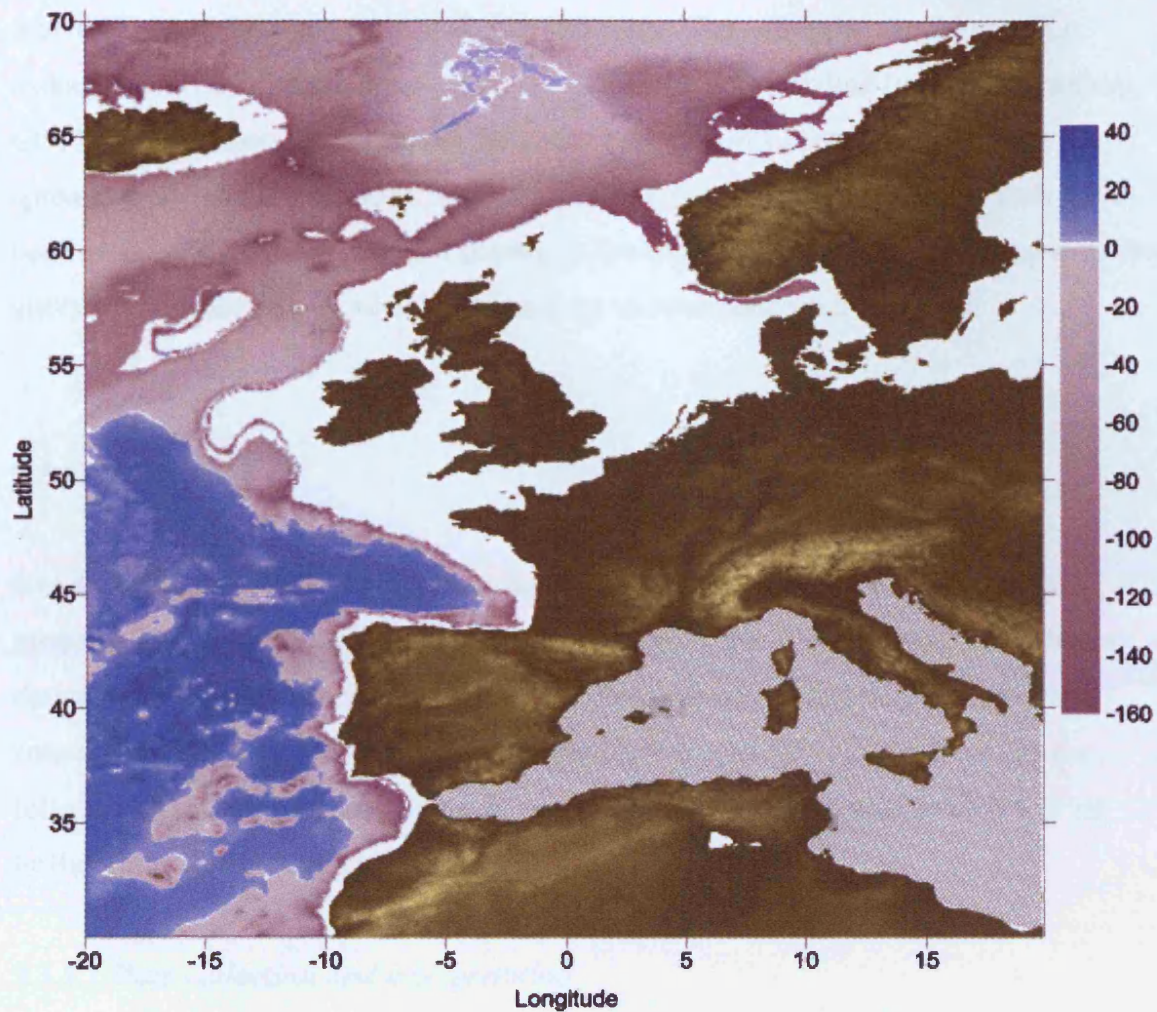


**Figure 3.3.8.** Density difference between liquid CO<sub>2</sub> and seawater (kg/m<sup>3</sup>) off the western European continental shelf. Contours levels are spaced at 2 kg/m<sup>3</sup> density difference intervals. Purple contours indicate areas of negative density difference, and blue contours indicate areas of positive density difference. The white contour, between purple and blue contours represents the area at which CO<sub>2</sub> becomes an NNAPL. The Mediterranean has not been included in this study.

### *CO<sub>2</sub> density at the ocean floor*

There has been considerable interest in the CO<sub>2</sub> density on the ocean floor (see Chapter 2). Various studies have been pursued on possible CO<sub>2</sub> storage methods involving injection of liquid CO<sub>2</sub> directly onto the seabed (Marchetti, 1977; Wong & Hirai, 1997). Although no longer favoured due to international dumping laws (OSPAR and the London Dumping Convention), there are other reasons to determine sea floor regions

where CO<sub>2</sub> density becomes denser than seawater. For example, should any CO<sub>2</sub> leakage occur, from natural or artificial sources below the seabed (without secondary CO<sub>2</sub> hydrate formation) the liquid CO<sub>2</sub> density would be necessary to calculate spreading rates on the seafloor. Calculations of CO<sub>2</sub> density on the ocean floor have been omitted from this study as it is outside the scope of this project, however very little alteration of calculations would be necessary to determine such densities.

### **3.3.5 Discussion**

It is important to consider any inaccuracies which may be present in the predictive model results. Possible errors specifically relating to the western European offshore data are discussed in the following section. Possible model and contouring errors concerning both section 3.2 and 3.3 are discussed in section 3.4. Additionally the following discussion addresses the significance of the model results, which will be further discussed in Chapter 7.

#### ***3.3.5.1 Data collection and interpretation***

Bathymetry data were provided by GEBCO global bathymetry data, which is a one minute grid based largely on contours contained within the GEBCO digital atlas. The derivation of bathymetry from contours expressed problems in shallower areas, particularly at depths less than 100 m. However, CH<sub>4</sub> and CO<sub>2</sub> hydrates do not form in such shallow regions, and therefore limits the errors resulting from GEBCO data.

Bottom water temperature data were derived from regional CTD casts from the BODC, ICES, Ifremer and from published data in various IOS reports. CTD casts with a high sampling rate were chosen for improved accuracy. Temperature profiles were plotted and divided into sections to derive linear equations to fit to bathymetric data. No stratification was assumed for temperature calculations, and therefore temperature inaccuracies may have been introduced at this point (Figure 3.3.9). 4 sets of temperature equations were used to calculate bottom water temperature, by dividing the study area into latitudinal and longitudinal bands (see section 3.1.2). By comparing the derived temperature gradients with original CTD cast temperature data it has been

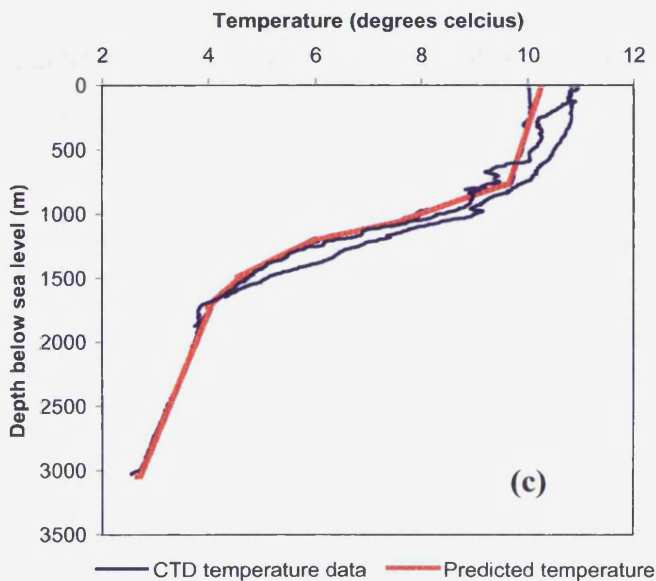
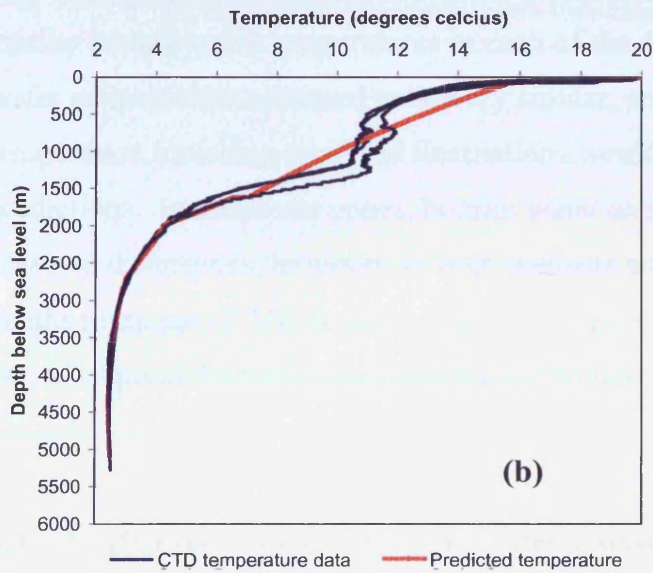
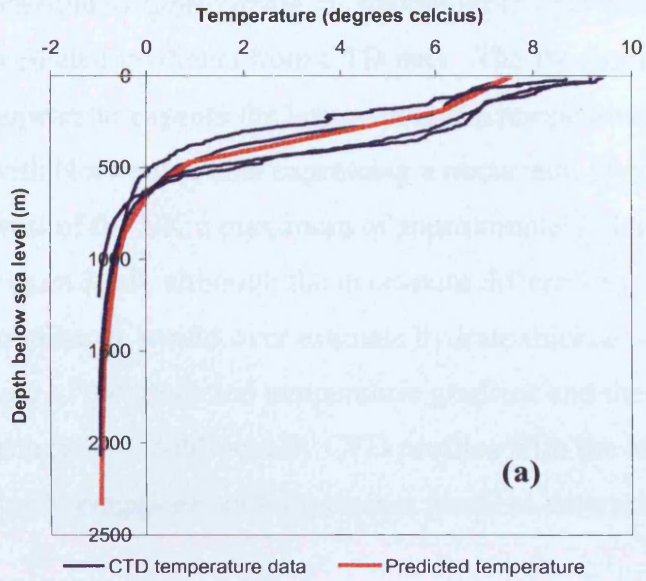


**Figure 3.3.9.** Temperature ( $^{\circ}\text{C}$ ) profiles for (a) Norwegian Sea and Baltic Sea (b) Iberian Basin, Bay of Biscay and offshore the Moroccan coast (c) Offshore the west of the British Isles ( $50^{\circ}\text{N} - 56^{\circ}\text{N}$ ). Blue profiles express actual CTD downcast temperature data, and red profiles express predicted temperature profiles used within the model from calculated gradients (see section 3.1.2). N.B. North Sea profiles have been excluded from this figure as any inaccuracies in these calculated temperatures would not influence hydrate stability predictions due to water depths being too shallow for hydrate formation.

possible to approximate the maximum temperature derivation introduced into the predicted gradients from CTD data. The Iberian/Bay of Biscay temperature gradient appears to express the largest possible temperature difference from CTD data of  $-2.4\text{ }^{\circ}\text{C}$ , with Norwegian data expressing a maximum of approximately  $-2.1\text{ }^{\circ}\text{C}$ , and data for the west of the UK a maximum of approximately  $-1.1\text{ }^{\circ}\text{C}$ . However, as can be seen in Figure 3.3.9, although the maximum differences appear to underestimate temperature (and hence would over estimate hydrate thickness), CTD cast temperatures lie either side of the predicted temperature gradient and therefore may average any under/over estimation. Additionally CTD profiles with the highest sampling rate were chosen to derive equations for temperature gradient determination, hence inaccuracies minimised.

The division of offshore regions into 4 areas to derive temperature gradients assumed similar bottom water temperatures in each of the 4 regions. Though localised bottom water temperatures appeared to be very similar, an accurate map of bottom water temperature including localised fluctuations would be necessary for highly accurate predictions. In shallower zones, bottom water temperatures may be subjected to seasonal differences; however, as both methane and carbon dioxide hydrate requires depths in excess of 300 m, inaccuracies as a result of such variations would be minimal. For other possible model inaccuracies see section 3.4.

### **3.3.5.2 Difference in $\text{CO}_2$ and $\text{CH}_4$ hydrate stability zone thickness**

In general predicted  $\text{CH}_4$  hydrate stability zones extend to greater depth than  $\text{CO}_2$  hydrate, 405 m greater at stability maxima in the Aegir Ridge; however  $\text{CO}_2$  hydrate stability zones appear to extend to greater depth in certain offshore regions. The most apparent region where  $\text{CO}_2$  hydrate is stable where  $\text{CH}_4$  hydrate is not is on the Voring Plateau, and in the Norwegian Deep Channel. These regions reach cold bottom water temperatures at relatively shallow water depths. For example, at  $9.86^{\circ}\text{E}$ ,  $64.49^{\circ}\text{N}$  water depths reach 304 m, and bottom water temperatures reach  $3.76\text{ }^{\circ}\text{C}$ , and at this point the  $\text{CO}_2$  hydrate stability zone extends to a depth of 158 m below the seafloor, where  $\text{CH}_4$  hydrate is not stable. This compares with  $3.75^{\circ}\text{E}$ ,  $60.18^{\circ}\text{N}$ , with a water depth of 299 m, bottom water temperature of  $3.84\text{ }^{\circ}\text{C}$ , a  $\text{CO}_2$  hydrate stability zone thickness of

148 m, and no CH<sub>4</sub> hydrate stability zone. Other regions expressing similar differences include the Rockall Plateau, the Porcupine Bank, and west of the Kolbeinsey Ridge, North of Iceland. This difference can be explained by the use of a P-T stability diagram (Figure 3.3.10).

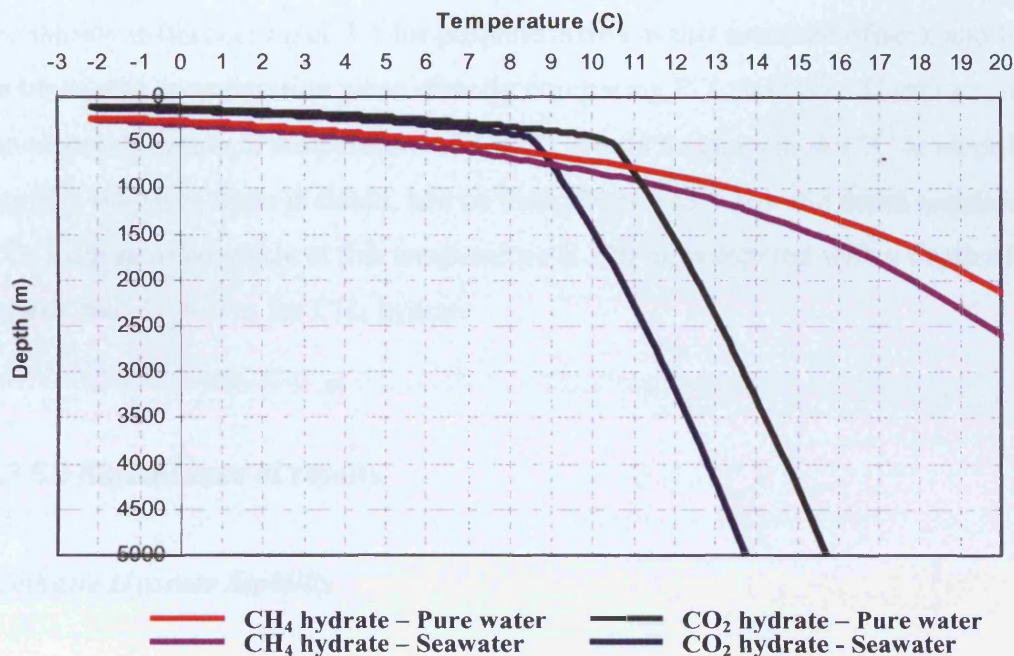


**Figure 3.3.10.** Depth-Temperature stability diagram for CO<sub>2</sub> hydrate and CH<sub>4</sub> hydrate in pure water and seawater (pressure represented as depth (m)) (Sloan, 1998).

Figure 3.3.10 shows the pressure-temperature stability differences between methane and carbon dioxide hydrate (the area under the curves represent conditions at which hydrate is stable). At shallower water depths (lower pressures) CO<sub>2</sub> hydrate can be more stable than CH<sub>4</sub> hydrate. For example, at a temperature of 3.85 °C, CO<sub>2</sub> hydrate is stable below approximately 195 m waters depth; however, at the same temperature CH<sub>4</sub> hydrate requires a depth of 380 m to be stable. The offshore regions with an absence of a CH<sub>4</sub> hydrate stability zone where CO<sub>2</sub> hydrate appears stable, such as in the Norwegian Deep Channel express this stability difference at shallower water depths, with bottom water temperatures of approximately 3.8 °C, and water depths of c.300 m in the Norwegian deep channel, west of the Kolbeinsey Ridge, and the Voring Plateau. Warmer bottom water temperatures of approximately 9 °C and water depths of around

550 m exist in the regions Porcupine Bank and the Rockall Plateau. A temperature of 9 °C would require a depth of approximately 620 m for CH<sub>4</sub> hydrate to be stable, in comparison with a depth of 370 m for CO<sub>2</sub> hydrate. These stability values are taken from stability data for hydrate formed in pure/distilled water, this differs in seawater. In the developed computer program a temperature offset of 1.1 °C is included to account for salinity differences (see 3.4 for possible errors in this assumed offset), and this must be taken into consideration when directly comparing P-T stability. Therefore, in the developed program, a temperature of 3.8 °C, would be taken as 4.9 °C to identify the depth at which hydrate is stable, and so using Figure (3.3.10), the depth required for CO<sub>2</sub> hydrate to be stable at this temperature is 220 m, compared with a depth of approximately 420 m for CH<sub>4</sub> hydrate.

### **3.3.5.3 Significance of results**

#### ***Methane Hydrate Stability***

The predicted depths to the base of the hydrate stability zone offshore western Europe indicate the potential for a very large hydrate reserve. However, although pressure and temperature conditions may be suitable for methane hydrate formation it doesn't mean other necessary conditions will be in place to initiate formation. Hydrate formation processes are still poorly understood, and hydrate formation seems to be dependant on a complicated range of factors. Porosity, gas availability, gas solubility, gas type, water availability and salinity are all key to whether natural hydrate reserves are present. Predictions assume a formation gas of pure methane; however, other gases are likely (Sloan, 1998), which would influence stability. Additionally, although hydrate stability predictions indicate a very thick hydrate layer, in reality natural hydrates have been discovered in shallow sediments (e.g. Sloan, 1998; Riedel et al., 2002; Ivanov et al., 2007) and their presence in sediments ranges from finely disseminated to distinct nodules (Holditch et al., 2006), and until formation processes are understood accurate volume estimates of methane hydrate reservoirs are impossible.

There is a general lack of data on natural hydrate for the NE Atlantic, and very few natural samples have been discovered. The only natural hydrate samples discovered in the study region appear to have been found in the Gulf of Cadiz (Figure 3.3.11). Hydrate samples were recovered from the central part of the Ginsburg and Bonjardim mud volcanoes (Kenyon et al, 2000; Gardner, 2001). Hydrates at these sites were present as small inclusions reaching up to 4cm in size. Other hydrate occurrences in the NE Atlantic have been inferred from the presence of BSRs (Bottom Simulating Reflectors), mud volcanoes or large coral reef structures and authigenic carbonate. Coral reefs and authigenic carbonate have been associated with hydrocarbon seepages and has been linked to the possible presence of hydrates in the Porcupine Bight area (Henriet et al., 1998). The Storegga Slide area offshore Norway is a well known massive submarine landslide area which has been linked to the dissociation of methane hydrate (Bunz et al., 2003), however more recently there have been doubts as to whether the slide can be attributed to methane hydrate (Westbrook, 2006). However, seismic surveys in the Storegga area offshore Norway would indicate some presence of natural hydrate (Figure 3.3.11) (Bugge et al, 1987; Mienert et al, 1998; Bunz et al, 2003). A BSR at 280 m below the seabed was determined from seismic data in this offshore region (Bunz et al, 2003), which would confer with stability predictions. Very recent sampling has revealed gas hydrate deposits on the Voring Plateau (Ivanov et al., 2007). Future research cruises and the increase of pressurised sample corers may aid to determine the true distribution of natural hydrate offshore western Europe.

Determining the distribution of natural methane hydrate reserves is extremely important to understand global carbon sources and sinks for climate change models as each  $\text{cm}^3$  of hydrate has the potential of releasing up to  $164 \text{ cm}^3$  (at standard temperature and pressure) of methane gas should destabilisation occur, or trapping the same volume on formation. As methane is much more effective than  $\text{CO}_2$  as a greenhouse gas large releases of methane gas into the atmosphere could adversely impact global climate. Natural hydrates also represent a possible future energy resource, and a full understanding of potential volumes and reserves would be necessary to calculate economic benefits of exploiting these carbon reservoirs.

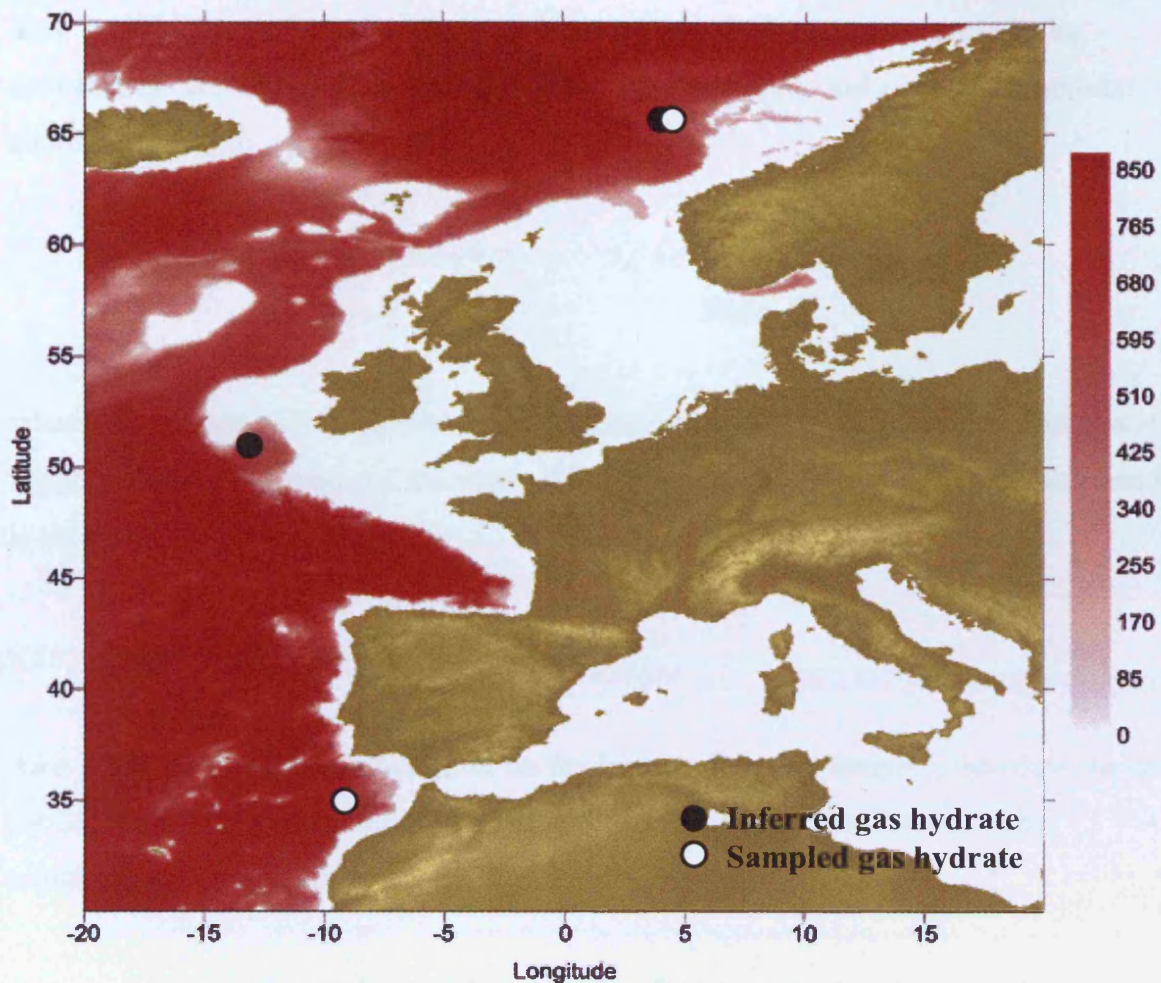


**Figure 3.3.11.** Predicted depth to the base of the methane hydrate stability zone (m) offshore western Europe with identified sites of natural methane hydrate occurrence (inferred and sampled). The Mediterranean has been omitted from this study.

### *Carbon dioxide density & hydrate stability: storage as a liquid and hydrate*

Model results have predicted large regions offshore the Western European continental shelf with suitable pressure and temperature conditions for storage as a liquid and hydrate. The predicted depth to the base of the hydrate stability zone reaches a maximum of 460 m below the seafloor, offering the potential of a very thick layer of carbon dioxide hydrate above a liquid carbon dioxide reservoir.

To fully comprehend this storage potential, latitude and longitude have been converted to distances in kilometres to approximate the volume of hydrate predicted in the study

area. To do so it was necessary to transform spherical coordinates to rectangular coordinates. If two points on the Earth are represented by  $x_1$  and  $x_2$ , their rectangular coordinates are:

$$x_1 = r \begin{matrix} \cos[a_1]\cos[b_1] \\ \cos[a_1]\sin[b_1] \\ \sin[a_1] \end{matrix} \quad x_2 = r \begin{matrix} \cos[a_2]\cos[b_2] \\ \cos[a_2]\sin[b_2] \\ \sin[a_2] \end{matrix}$$

where  $a$  = latitude,  $b$  = longitude and  $r$  = radius of the earth, which has been assumed to equal 6378km. To determine the angle  $\theta$  between  $x_1$  and  $x_2$  the dot product of  $x_1$  and  $x_2$  is used producing the equation:

$$x_1 \cdot x_2 = |x_1| |x_2| \cos\theta$$

Any vector pointing to another point on the Earth will have a length  $r$ , therefore the dot product creates  $r^2$  on both sides of the equation and can be cancelled out. The remaining dot product produces:

$$\cos\theta = \cos[a_1]\cos[b_1]\cos[a_2]\cos[b_2] + \cos[a_1]\sin[b_1]\cos[a_2]\sin[b_2] + \sin[a_1]\sin[a_2]$$

$$\cos\theta = \cos[a_1]\cos[a_2](\cos[b_1]\cos[b_2] + \sin[b_1]\sin[b_2]) + \sin[a_1]\sin[a_2]$$

$$\theta = \cos^{-1}(\cos[a_1]\cos[a_2](\cos[b_1]\cos[b_2] + \sin[b_1]\sin[b_2]) + \sin[a_1]\sin[a_2])$$

This is the angle between  $x_1$  and  $x_2$ , but to determine the length we use the equation:

$$Arclength = \theta / 360 * 2\pi * r$$

Producing the final equation for the distance between two points on Earth:

$$Distance = (\cos^{-1}(\cos[a_1]\cos[a_2](\cos[b_1]\cos[b_2] + \sin[b_1]\sin[b_2]) + \sin[a_1]\sin[a_2])) / 360 * 2\pi * r$$

Constructing a 1 by 1 degree grid for latitude, longitude, and converted distance, and matching each grid square with the predicted carbon dioxide hydrate thickness at that point, enabled calculation of the approximate volume of predicted carbon dioxide hydrate thickness for offshore western Europe within the 200 mile economic zone. These calculations provide a total volume of  $1.3 \times 10^9 \text{ km}^3$ .

This estimated carbon dioxide hydrate capacity is merely an estimated potential volume of sediment which may have suitable pressure and temperature conditions for the formation of carbon dioxide hydrate. It does not include potential sediment volume underlying the hydrate stability zone for the storage of liquid carbon dioxide, which would be dependant on the specific aquifer volume capacity. For a more detailed discussion on volume estimates see Chapter 7.

### **3.3.6 Conclusions**

- Computer models (see section 3.1 and 3.2) have been developed and used to calculate the predicted depth to the base of the CO<sub>2</sub> and CH<sub>4</sub> hydrate stability zones offshore the western European continental shelf.
- Calculations predict the CO<sub>2</sub> and CH<sub>4</sub> hydrate stability zones to be stable over large areas reaching a maximum depth of 460 m, and 867 m, respectively, where water depths exceed 3800 m and bottom water temperatures are at a minimum of approximately -0.9 °C in the Aegir Ridge, Norwegian basin.
- The predicted depths to the base of the CH<sub>4</sub> hydrate stability zone indicate the potential for a large natural hydrate reserve, however there appears to be a lack of confirmed natural hydrate occurrence below the NE Atlantic. Natural hydrate samples have been discovered in the Gulf of Cadiz (Gardner, 2001; Kenyon et al., 2000), and the Voring Plateau (Ivanov et al., 2007) with only other noted occurrences inferred from the presence of BSRs, submarine landslide scars, mud volcanoes, or coral reef structures and authigenic carbonate (Henriet et al., 1998; Long & Holmes, 1998; Bunz et al., 2003; Holmes et al., 2003).

- Large areas offshore the western European continental shelf appear to have suitable pressure and temperature conditions for CO<sub>2</sub> hydrate formation with an approximate CO<sub>2</sub> hydrate stability zone volume of 1.3 x 10<sup>9</sup> km<sup>3</sup>. Therefore predictions indicate considerable potential for storage as a liquid and hydrate.
- The offshore data set developed for predictive calculations of hydrate stability has also been applied for calculation of CO<sub>2</sub> density at the base of the CO<sub>2</sub> hydrate stability zone using an Excel function provided by Eric Lindeberg at SINTEF, and seawater density at the base of the CO<sub>2</sub> hydrate stability zone using the widely available Matlab function 'sw\_dens'.
- The maximum CO<sub>2</sub> density and seawater density is found to occur in the Iberian Basin, to the left of the Madeira-Tore Rise, at densities of 1092 kg/m<sup>3</sup> and 1052 kg/m<sup>3</sup> respectively, where water depth water depths reach their maximum of 5743 m. This offshore region also expresses the greatest negative density difference between liquid CO<sub>2</sub> and seawater (35‰), therefore possibly representing suitable conditions for a negatively buoyant liquid CO<sub>2</sub> store.
- Predictions assume an average geothermal gradient of 30 °C, and do not take into account the suitability of the sediment for hydrate formation and liquid CO<sub>2</sub> storage. These predictions could be greatly improved by more detailed temperature and geothermal gradient models.

### **3.4 Model and contouring errors**

The development of the hydrate stability zone thickness model and temperature and pressure datasets have unavoidably introduced some possible inaccuracies, which must be considered during interpretation of the results. Some of these have been considered in section 3.2.3 and 3.3.5.1. The following section will discuss possible errors introduced during the development of the models and contouring of the results, which apply to results presented in Chapter 3.

#### **3.4.1 Use of CSMHYD for pressure predictions**

The basis for Sloan's hydrate prediction model originates from the basic model produced by van der Waals and Platteeuw (1959), in which the phase equilibrium of gas hydrate was derived from statistical thermodynamics (later used for prediction of dissociation pressures of gas hydrates (Parrish and Prausnitz, 1972)). The Parrish and Prausnitz model was simplified by introducing universal reference properties for each type of hydrate structure (Holder et al, 1980). All models produced from these origins give relatively consistent results, and are comparable with experimental data (Sloan, 1998). Model assumptions may introduce some errors. For example, the model assumes spherical molecules, and although the model incorporates algorithms which provide better predictions for non-spherical molecules it tends to over estimate cage occupancy (Sun and Duan, 2005). Sloan predicts an average pressure prediction deviation of not less than  $\pm 7\%$  for hydrate results using CSMHYD, and any such inaccuracies are within an acceptable range for many calculations (Sloan, 1998). Figure 3.4.1 compares carbon dioxide hydrate P-T predictions using CSMHYD with experimental data from various sources. A degree of variation occurs, but true inaccuracy of model predictions cannot be fully determined, as experimental errors must also be taken into account.

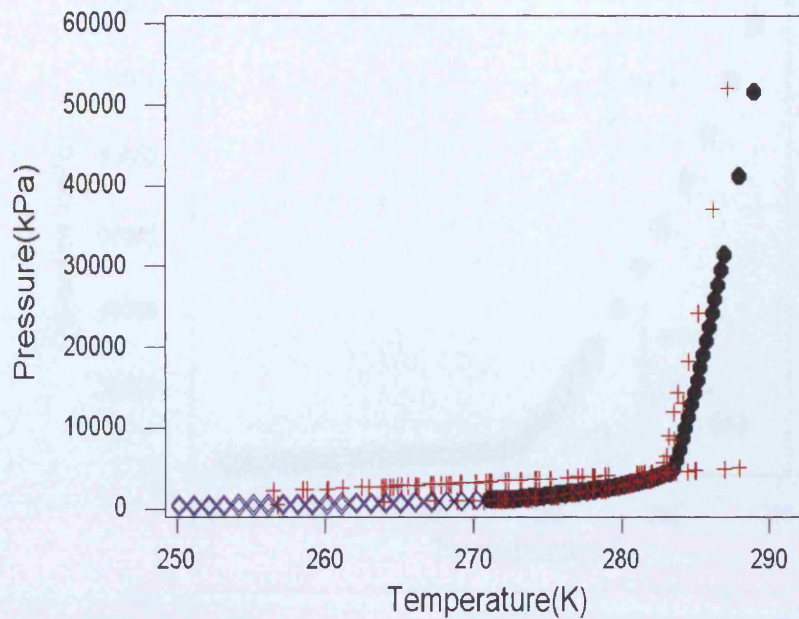


**Figure 3.4.1.** Graphical comparison of carbon dioxide P-T predicted using CSMHYD (●), experimental results (+) from various sources provided in Sloan (1998) and pressure predictions using HWHydrateGUI (◇).

### 3.4.2 Constants derived from CSMHYD

In order to use the JOIDES linear equilibrium equation data for the calculation of hydrate thickness, linear regression of the carbon dioxide hydrate logarithmic pressure predictions for a range of temperature reciprocals was necessary. The original methane constants used for hydrate thickness predictions were derived from two linear equations, as the logarithm of methane stability data provides values, which lie on a linear line of best fit. However, the logarithm of carbon dioxide hydrate pressure predictions is more complicated, and therefore linear regression more difficult (Figure 3.4.2).

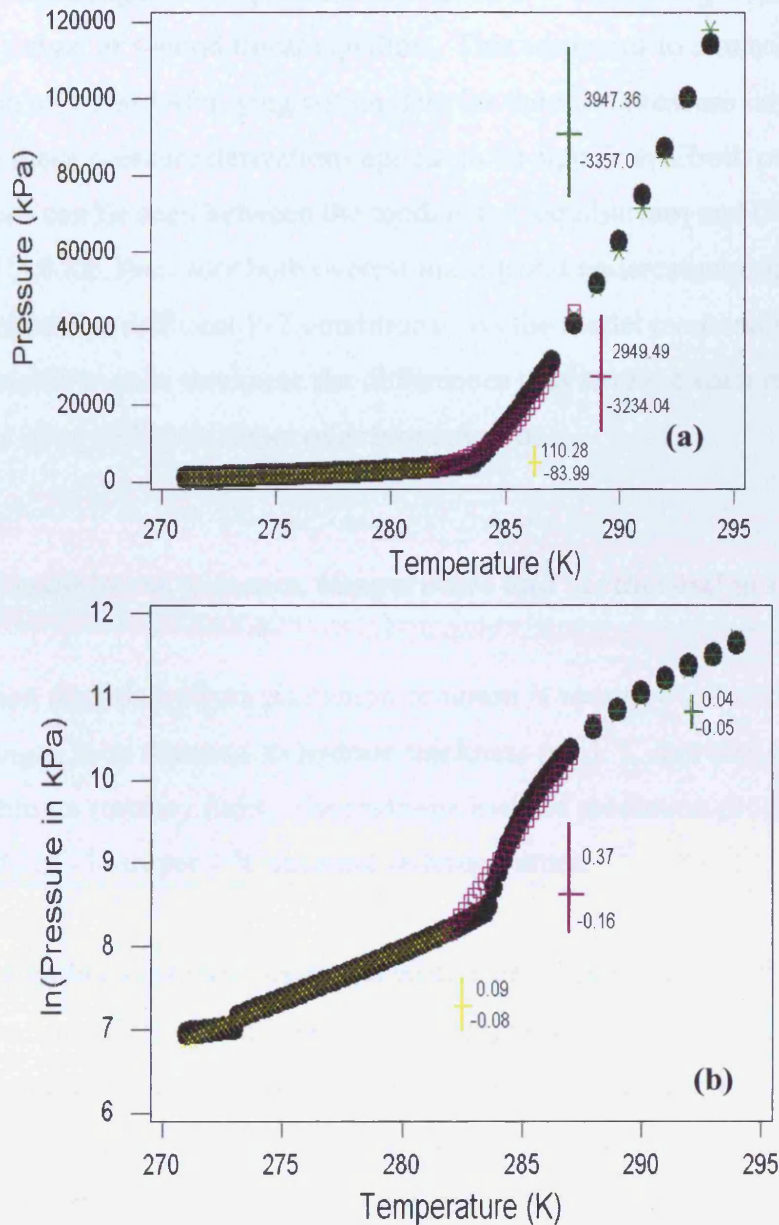


**Figure 3.4.2(a)** Pressure predictions for carbon dioxide hydrate results from Sloan's model (●) and their **(b)** comparison with constants derived from regression of such data (constants 1 (X), constants 2 (□), constants 3 (\*)). Error bars have been added to express the maximum and minimum pressure derivation of regressed equation data from original model predictions.

The hydrate stability data were divided into 3 pressure ranges, providing 3 linear regression equations (see section 3.1.1). As these linear equations were derived from lines of best fit it is possible that errors were introduced at this point. These have been plotted as error bars on pressure predictions derived from CSMHYD.exe (Figure 3.4.3).

The maximum logarithmic pressure derivation is + 0.37, lying within the middle pressure range, or second linear equation. This compares to a maximum pressure derivation of + 3947 kPa lying within data for the third pressure range. However, although these pressure derivations appear to be significant, both positive and negative differences can be seen between the models P-T equilibrium and that of CSMHYD.EXE, therefore both overestimating and underestimating hydrate stability zone thickness at different P-T conditions. As the model over and underestimates hydrate stability zone thickness the differences may average each other out, reducing the effect of equilibrium errors over large regions.

### **3.4.3 Sensitivity to pressure, temperature and geothermal gradient**

The carbon dioxide hydrate prediction program is sensitive to temperature changes; calculating a 36 m decrease in hydrate thickness per 1 °C increase in temperature, when well within its stability field. The methane hydrate prediction program shows a sensitivity of -38 m per 1 °C increase in temperature.

Hydrate stability sensitivity increases with decreasing pressure. If the pressure decreases from 3800 kPa to 3700 kPa the program predicts a 4 m decrease in carbon dioxide hydrate thickness. However, decreasing the pressure from 2200 kPa to 2100 kPa decreases the carbon dioxide hydrate thickness by 7 m. This compares with 7 m and 10 m, respectively, for methane hydrate.

The developed models show hydrates are highly sensitive to geothermal gradient and therefore any increase would significantly reduce the resulting thickness of the hydrate layer. However, the models' sensitivity is highly variable. For the original methane hydrate stability equation it was proposed there was an uncertainty of  $\pm 1\%$  in the total (water and sediment) depth estimate for  $\pm 0.1$  °C (JOIDES, 1992). Using `hydcalc.exe`, and altering the data file for the Faeroe-Shetland Channel to account for a 1 degree Celsius rise in geothermal gradient per kilometre, the average reduction in the methane hydrate stability zone would be 3%, with a standard deviation of 0.3. In this case, this reduction is the equivalent of an average 5.6 m, with a standard deviation of 7.7 m.

#### 3.4.4 1.1°C offset

The program incorporates a previously assumed temperature offset defined for methane hydrate stability in seawater as compared with pure water. This 1.1 °C offset was determined from the experimental dissociation pressure of methane hydrate in the pressure range of 2.75-10.0 MPa (Dickens and Quinby-Hunt, 1994). However, by using CSMHYD.exe (Sloan, 1998) to determine carbon dioxide hydrate stability in seawater (3.5% by weight) it has been found a variable temperature offset would be necessary to simulate the depression in dissociation temperature with the increase in salt content for carbon dioxide (Figure 3.4.3).

In the initial water-ice phase (I-H-V) / liquid-water (Lw-H-V) phase of pure water carbon dioxide hydrate, and liquid-water phase of seawater carbon dioxide hydrate, the difference in the dissociation temperature is minimal, but this increases as CO<sub>2</sub> hydrate reaches its liquid-water-liquid hydrocarbon phase. At this point (about 450 m depth), the temperature offset becomes fairly constant at approximately 1.9 °C.

Using previous estimates of program temperature sensitivity, this increase in temperature offset would account for an approximate decrease of 29 m in hydrate stability, at depths greater than 450 m (with presented results therefore overestimating hydrate thickness). Future model refinement should incorporate regression of data derived from carbon dioxide hydrate formation in seawater.

In addition the programs do not incorporate any influence of salinity increasing beyond seawater salinity as a consequence of the exclusion of salts during hydrate growth, assuming excluded salts can diffuse away. However, this assumption may be incorrect for rapid hydrate formation in natural and carbon dioxide hydrates (see chapters 5 and 6).

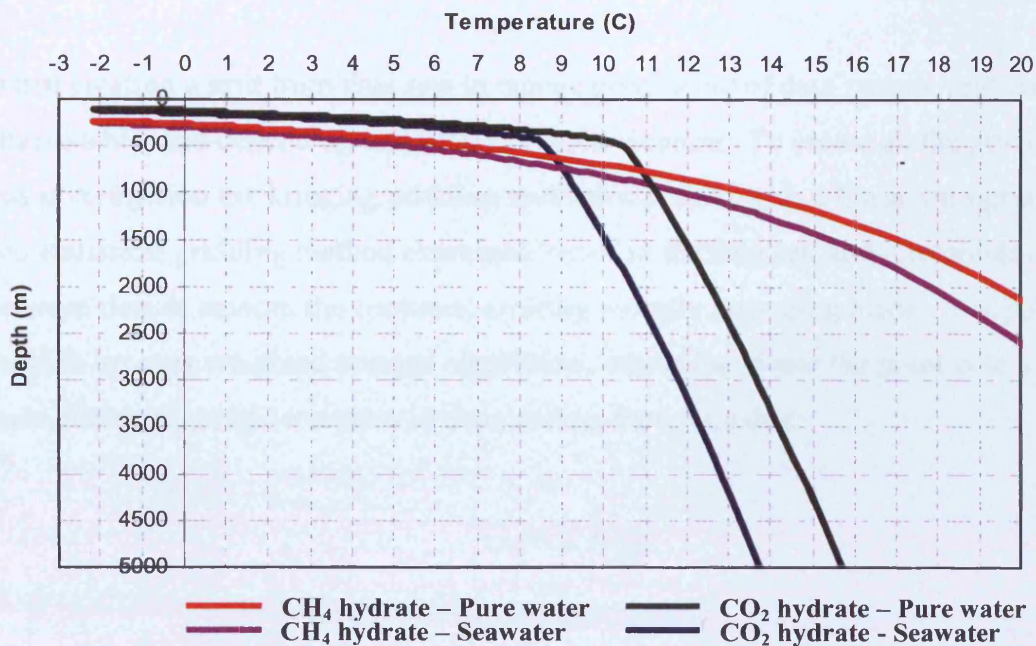


**Figure 3.4.3.** Depth-Temperature stability diagram for CO<sub>2</sub> hydrate and CH<sub>4</sub> hydrate in pure water and seawater (pressure represented as depth (m)), comparing the difference in P-T equilibrium with pure water and seawater, and the changing offset with pressure (Sloan, 1998). Repeat of Figure 3.3.10.

### 3.4.5 Density and solubility

The seawater density Matlab script is based upon the UNESCO equation of state for seawater, which is a complicated curve fit with extremely precise detailed calculations. As the program is used across the world by numerous oceanographers it is assumed the inaccuracies in the seawater density calculations are minimal. The carbon dioxide density excel function developed by Eric Lindeberg, is stated to be one of the most accurate programs for density calculations at present, though unfortunately no quantification of inaccuracies was available.

Solubility data has been taken from published scientific literature (see Rochelle & Camps, 2006), and hence further development of solubility calculations would require new experimental data or other models.

### 3.4.6 Contouring Grid errors

When creating a grid from data sets to enable contouring of data ranges, grid errors are unavoidable, and depend on the method of grid creation. To create all the grids used in this investigation the kriging gridding method was used with a linear variogram. This geo-statistical gridding method expresses trends in the data set, and interpolates between data to smooth the contours, creating visually appealing maps. Interpolation of the data set uses weighted average algorithms, where the closer the point is to a grid node, the more weight it carries in determining the grid value:

$$G_j = \sum_{i=1}^N W_{ij} Z_i$$

where  $G_j$  = the interpolated grid node value at  $j$ ,  $N$  is the number of points to interpolate at each node,  $Z_i$  = the  $Z$  value at the  $i$ th point; and  $W_{ij}$  = the weight associated with the  $i$ th data value when computing  $G_j$ .

Other methods were used during initial investigations for comparison, but the kriging method produced the most attractive contour plots. Grid errors vary with each data set, and have been calculated using the residuals command in the software package SURFER. The formula used in the residual command to compute grid errors is:

$$Z_{res} = Z_{dat} - Z_{grd}$$

where:  $Z_{res}$  = the residual value (grid error),  $Z_{dat}$  = the  $Z$  value in the data file, and  $Z_{grd}$  = the  $Z$  value of the surface of at the  $XY$  coordinate from the grid file.

The average residual value for the European  $CO_2$  hydrate grid is 0.042, with a standard deviation of -10.19, a minimum value of -272.48, and a maximum value of 271.72. A negative value indicates the data file  $Z$  value is less than the interpolated value. This compares with an average residual value of 0.051 for  $CH_4$  hydrate, with a standard deviation of 11.21, a minimum value of -467.04, and a maximum value of 421.82. The created grid for  $CO_2$  density has an average residual value of -0.034, with a standard deviation of 60.40, a minimum of -976.36, and a maximum of 963.45.

The minimum and maximum grid errors show a wide range and therefore indicate some grid points on the displayed maps may vary considerable from the actual data set. However, the average residual value is minimal, and any derivation from the original data set through the gridding process will not affect displayed general trends, and maximum, minimum and average values discussed have been calculated from the original data set, rather than created grids.

As discussed above, there are a number of modelling and contouring errors which need to be taken into consideration when analysing the described results. However, the majority of these are fairly unavoidable. Sloan's thermodynamic model for producing P-T equilibrium equations is an accurate model, and at present appears to be the most appropriate for this use. Contouring and gridding errors will always exist, but have been minimised by reducing the grid spacing. Due to sparse heat flow data, the geothermal gradient remains the greatest uncertainty, and results would be greatly improved by a geothermal gradient grid. Although the model could be improved by more accurate P-T equilibrium equation derivation and more detailed bottom water temperature grids, without heat flow data such would not improve the accuracy of the results significantly. The produced maps have shown pressure temperature conditions are favourable for this storage method offshore Western Europe, and rather importantly enable visualisation of the potential of storage as a liquid and hydrate which could be used to assist policy makers appreciate the possible future role Europe could play in CCS technologies.

### **3.5 Conclusions**

- Computer models have been developed to predict the depth to the base of the CO<sub>2</sub> hydrate and CH<sub>4</sub> hydrate stability zone.
- Initial investigations predict the CO<sub>2</sub> hydrate stability zone to extend to a depth of 346 m and 281 m below the seabed in the Faeroe-Shetland Channel and Rockall Trough, respectively. Calculations also predict the CH<sub>4</sub> hydrate

stability zone to extend to a depth of 682 m and 668 m below the seabed in the Faeroe-Shetland Channel and Rockall Trough, respectively.

- This preliminary investigation has been extended to predict the depth to the base of the CO<sub>2</sub> hydrate and CH<sub>4</sub> hydrate stability zones offshore the Western European continental shelf.
- Calculations predict the CO<sub>2</sub> and CH<sub>4</sub> hydrate stability zones to be stable over large areas reaching a maximum depth of 460 m, and 867 m, respectively, where water depths exceed 3800 m and bottom water temperatures are at a minimum of approximately -0.9 °C in the Aegir Ridge, Norwegian basin.
- The predictive depths to the base of the CH<sub>4</sub> hydrate stability zone indicate the potential for a large natural hydrate reserve, however there appears to be a lack of natural hydrates below the NE Atlantic.
- Large areas offshore the western European continental shelf appear to have suitable pressure and temperature conditions for CO<sub>2</sub> hydrate formation with an approximate CO<sub>2</sub> hydrate stability zone volume of  $1.3 \times 10^9 \text{ km}^3$ . Therefore predictions indicate considerable potential for storage as a liquid and hydrate.
- The offshore data set developed for predictive calculations of hydrate stability has also been applied for calculation of CO<sub>2</sub> density at the base of the CO<sub>2</sub> hydrate stability zone. The maximum CO<sub>2</sub> density and seawater density is found to occur in the Iberian Basin, to the left of the Madeira-Tore Rise, at densities of 1092 kg/m<sup>3</sup> and 1052 kg/m<sup>3</sup> respectively, where water depths reach their maximum of 5743 m. This offshore region also expresses the greatest negative density difference between liquid CO<sub>2</sub> and seawater (35‰), therefore possibly representing suitable conditions for a negatively buoyant liquid CO<sub>2</sub> store.
- The greatest level of uncertainty within these results is the geothermal gradient due to sparse heat flow data, and results would be greatly improved by a

geothermal gradient grid. Although the model could be improved by more accurate P-T equilibrium equation derivation and more detailed bottom water temperature grids, without heat flow data such alterations would not improve the accuracy of the results significantly.

- The produced maps have shown pressure temperature conditions are favourable for storage as a liquid and hydrate offshore Western Europe, and rather importantly enable visualisation of the potential this storage method which could be used to assist policy makers in appreciating the possible future role Europe could play in CCS technologies.

## **CHAPTER 4**

### **Experimental Procedures**

## **4. Experimental procedures**

The following chapter presents an overview of the experimental procedures conducted during this study for the investigations detailed in Chapters 5 and 6. For more specific procedures related to each individual experiment please see Appendix B.

### **4.1 Hydrate sample formation and preservation**

A number of experiments were conducted during the study ranging from initial simple batch experiments with water and CO<sub>2</sub> in stainless steel pressure vessels, to more complicated experiments with cooling coils inserted around sediment cores to freeze the sample before depressurisation, and others with the addition of magnetic stirrer beads to aid hydrate formation, totalling 29 experiments (see Appendix B for further details). However, the basic procedure remained the same for all CO<sub>2</sub> hydrate experiments. A known weight of sediment (natural, quartz rich sand, clay, pure minerals) was mixed with a known weight of water (pure distilled deionised water, or artificial seawater created in the laboratory (see Appendix B) and placed into a liner (polytetrafluoroethylene (PTFE) or aluminium). This liner was then placed into stainless steel pressure vessels, with various outlet and inlet tubes with connected pressure release valves (Figure 4.1a). A thermocouple was added to each experiment to monitor temperature changes. Pressure vessels were sealed with a Viton O-ring, and connected to CO<sub>2</sub> pressure lines within a cooled incubator to maintain temperature (Figure 4.1b). An ISCO 260D pressure pump was initially pressurised to the required pressure with CO<sub>2</sub>. CO<sub>2</sub> liquid at pressure was slowly bled into the batch pressure vessel to avoid temperature increases due to pressurisation. After pressurisation the ISCO pressure pump maintained the required pressure throughout the experiment.

Temperature and pressure could be altered for each specific experiment. Temperature changes were monitored throughout the experiments using Pico Log computer software. At the end of each experiment pressure valves connecting CO<sub>2</sub> lines were closed, the thermocouple disconnected, and the vessel was removed from the incubator. The vessel could then be rapidly depressurised, in a controlled manner, by opening an outlet valve and bleeding off the CO<sub>2</sub>. During depressurisation the samples underwent cooling due to CO<sub>2</sub> expansion and solid CO<sub>2</sub> ('dry ice') often formed inside the vessel helping to

maintain cooler temperatures and consequently aiding the preservation of the sample. Samples were then preserved by rapidly cooling to liquid nitrogen temperature (c.  $-180\text{ }^{\circ}\text{C}$ ), and these cooled samples were then wrapped in aluminium capsules for transport and storage. Samples were transferred to a cryogenic storage refrigerator where they were stored over liquid nitrogen until further analysis.

The time taken for each individual experiment varied between 3 days and 7 weeks, therefore unfortunately it has not been possible to study large numbers of samples. Additionally, time restrictions on the SEM limited the number of samples which could be analysed further.



**Figure 4.1(a).** Schematic diagram of a simple batch experiment; with water and sand in a PTFE liner inside a stainless steel pressure vessel, which when sealed was pressurised with  $\text{CO}_2$ . **(b)** Image of batch experiments inside the cooled incubator. Various pressure release valves and tubes are added to the experimental pressure vessels for connection and safety.

Throughout experimental procedures strict laboratory safety guidelines were adhered to, and a structured training programme was followed for working with high pressure equipment, including a Swagelok Installation Course for tube fitting and handling. The experimental sample formation procedures outlined are detailed step-by-step in Table 4.1. See Appendix B for specific procedures related to each experiment.

## **4.2 Visual observations**

After samples were removed from the pressure vessel, and further cooled to liquid nitrogen temperature, it was possible to make initial observations. These noted observations were augmented with detailed interpretation of photographs (Figure 4.2). Small sub-samples could also be taken to ensure presence of CO<sub>2</sub> hydrate before storage and analysis, through heating and observing dissociation and emission of gas. Other properties such as colour, lustre, texture, sediment disturbance, and volume changes could also be observed. Where images were not taken of samples initial visual observations are preserved in laboratory notebooks.

1.	<b>Weigh sediment and water, mix and place in liner.</b>
2.	<b>Secure pressure vessel base in a bench clamp, and place liner into vessel.</b>
3.	<b>Remove all inlets and outlets from vessel lid and fit Viton O-ring onto lid.</b>
4.	<b>Secure vessel lid onto the base and once sealed fit screw top the base of the vessel.</b>
5.	<b>Fit inlet, outlet tubes and valves onto the vessel, and insert thermocouple.</b>
6.	<b>Place vessel into cooled incubator and attach to pressure lines.</b>
7.	<b>Connect thermocouple and secure additional thermocouple to outside of the vessel.</b>
8.	<b>Load a new PICO log file and not experimental details into log book.</b>
9.	<b>Pressurise ISCO 260D pump to the required pressure, and once pressure has stabilized open valve to transfer pressure vessel.</b>
10.	<b>Once transfer vessel is fully pressurised, slowly bleed in CO<sub>2</sub> into experiment until required pressure is reached.</b>
11.	<b>Check for any leaks in the connections with soap solution, and tighten fittings if required.</b>
12.	<b>Set the incubator to the required temperature.</b>
13.	<b>Start temperature logging. Note the experiment start time, temperature and pressure.</b>
14.	<b>Monitor the experiment throughout.</b>
15.	<b>At the end of the experiment stop the logging trace, note the time, close all pressure valves into the experiment and stop the pressure pump.</b>
16.	<b>Disconnect the experiment from the incubator pressure lines.</b>
17.	<b>Secure vessel in bench clamp and with considerable control open valve to release pressure.</b>
18.	<b>When vessel is depressurised unscrew top and remove lid.</b>
19.	<b>Extract sample and cool in liquid nitrogen.</b>
20.	<b>Place cooled sample into a labelled aluminium foil capsule and store over liquid nitrogen until later analysis.</b>

**Table 4.1.** Step-by-step experimental procedures for CO<sub>2</sub> hydrate sample formation and preservation.



**Figure 4.2(a)** Image of pressure vessel containing 4 plastic tubes initially completely filled with seawater ice ball/sediment mixes at the start of the experiment. **(b)** Sediment/CO<sub>2</sub> hydrate sample with a domed base (top of sample in image) due to the lack of a firm base during the experiment (sediment and water placed on a fine mesh). Surface is uneven, and hydrate appears to fill pores and cement grains. **(c)** Pressure vessel containing sample with a very disturbed surface texture after depressurisation. **(d)** Sample from (c) with a surface water ice layer and some hoar frost. Some of the sample was completely un-cemented; hence some surface sediment has been lost. Natural sediment also appears fairly porous, and clay sediment appears very disturbed with a very porous texture.

### 4.3 Sample handling and SEM imaging

A series of development stages were undertaken to optimise efficiency and ensure minimal sample dissociation and damage in sub-sampling hydrate specimens for SEM imaging. A cryogenic sample preparation box was designed in house at the British Geological Survey by Tony Milodowski, Grenville Turner and the team in the BGS workshops, to maintain cryogenic temperatures and a nitrogen atmosphere to prevent the formation of hoar frost during sub-sampling. Attempts were made to polish samples

to produce a flat surface for BSEM. Polishing under liquid nitrogen in a small restricted space proved difficult however, and disturbed the samples considerably; therefore cleaving the samples was adopted as the most efficient technique for sub-sampling. Additionally, although used in initial investigations, the original SEM sample holders were too shallow for many suitably sized cleaved sub-samples. Therefore, a range of new sample holders were designed and constructed by BGS staff, and these were used during subsequent analysis.

Each sample for SEM analysis was transferred from a cryo-store into a controlled dry nitrogen atmosphere cryogenic sample preparation box (Figure 4.3). Within the sample preparation box the samples were cleaved into smaller pieces (typically 5-10 mm across and up to 5 mm thick) under liquid nitrogen, and placed in a cooled sample holder to insert into the SEM transfer chamber. All samples were left uncoated. Samples were then analysed using a Leo 435VP variable pressure SEM fitted with an Oxford CT1500 cryogenic gas-cooled sample handling cold stage facility (Figure 4.3). Backscatter electron imaging (BSEM) was used to enhance the contrast between ice and hydrate. The sample stage was maintained at approximately  $-160\text{ }^{\circ}\text{C}$  with typical nitrogen pressures of  $\sim 0.45$  Torr, with a typical working distance of 14 mm, and BSEM observations were made in variable pressure mode to prevent specimen charging.

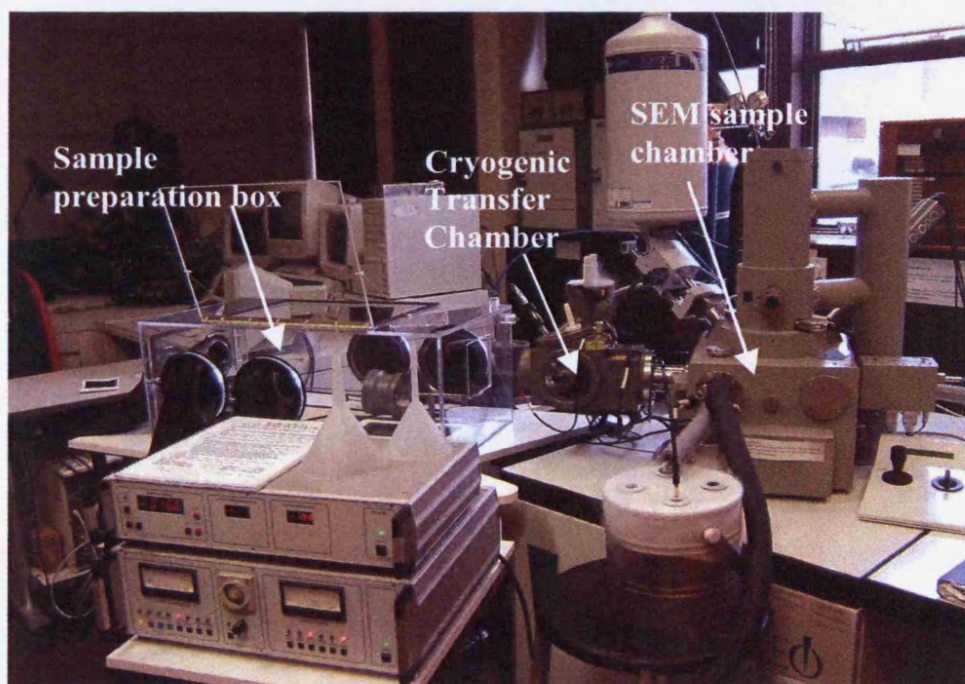


**Figure 4.3.** Image of the Leo 435VP SEM with a fitted cryogenic sample handling cold stage facility and the designed sample handling transfer box.

## Cryogenic scanning electron microscopy

Conventional scanning electron microscopy produces an image by rastering a focussed beam of electrons across the surface of a sample. The image is built by collecting the lower secondary electrons generated by interactions of the primary beam with electrons in the surface of the sample (Figure 4.4), and recording the intensity of secondary electron emission on a TV monitor scanned in synchronism with the electron beam raster (Goldstein et al., 1981; Reed, 2005).

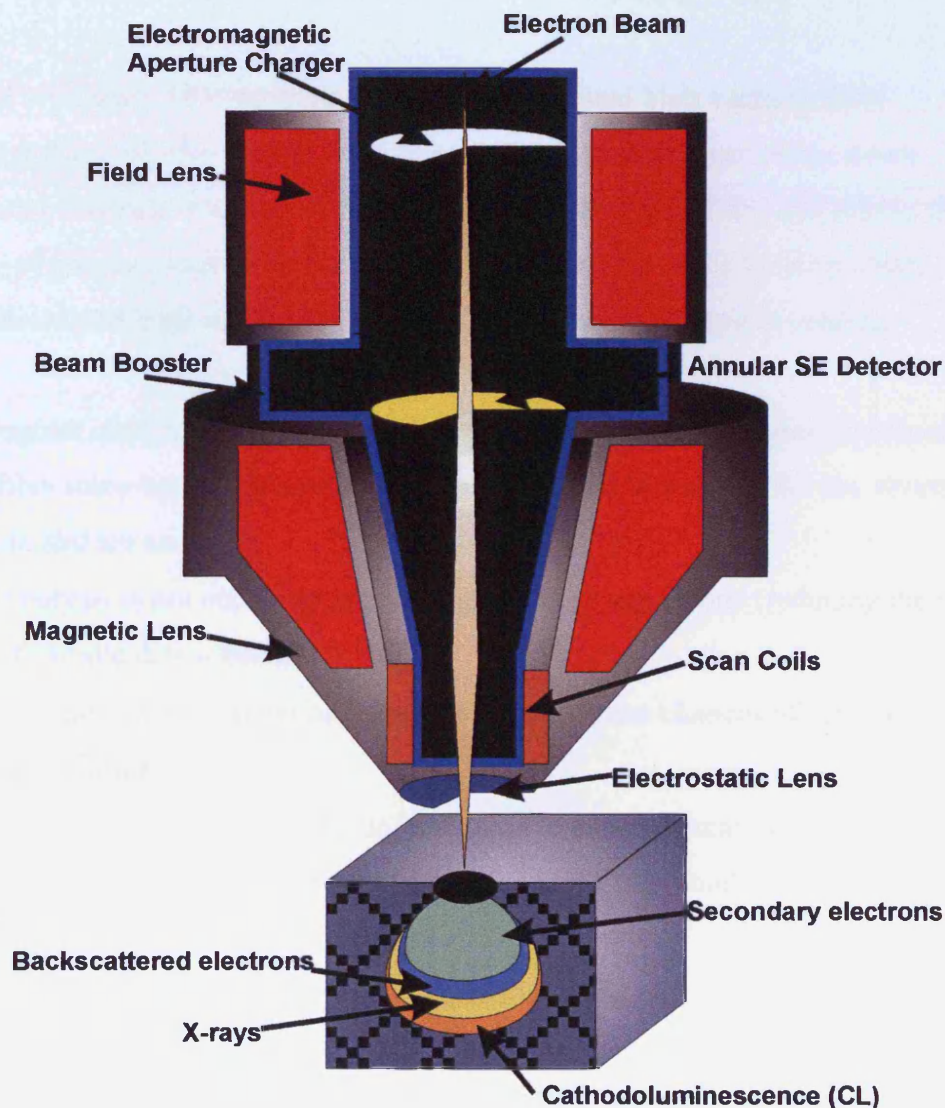


**Figure 4.4.** Diagram showing the interior construction of the BSEM and the sample/electron beam interaction with the sample, expressing the differing sample penetration depths of electrons used to construct sample images.

Uses of conventional SEM techniques for analysis of hydrate and ice samples raises various problems. These include:

- Analysis requires high vacuum conditions.
- Energy imparted by the primary electron beam can cause heating of the sample (and hence may dissociate the hydrate sample).
- The sample usually requires earthing to prevent image distortion as a result of sample charging under the electron beam (by coating with a thin layer of conductive carbon or metal). This again may cause warming of the sample which could cause partial dissociation of the hydrate sample.

Standard cryogenic SEM techniques use a conventional high vacuum SEM instrumentation, but the sample stage is cooled to liquid nitrogen temperature. The cold temperature reduces warming of the sample by the electron beam, and allows the imaging of phases (such as hydrate), which would not be stable under ambient temperatures and high vacuum. However, the sample still requires coating.

The cryogenic-BSEM technique used throughout analyses of samples discussed in this study offers some major advantages over conventional techniques for the investigation of hydrate and ice samples:

- Analysis is not conducted under high vacuum conditions (reducing the chances of sample dissociation).
- Samples do not require coating (also reducing the chances of sample dissociation).
- Imaging is achieved by the collection of reflected primary (backscattered) electrons from the sample surface (as opposed to secondary electrons).

The ionisation of a low-pressure gas (such as nitrogen), introduced into the sample chamber, by the passage of the primary electron beam, earths the negative charge, which would otherwise build up on the sample. This means samples do not require coating (although the introduction of a gas limits the maximum resolution due to the broadening of the electron beam by electron scattering). Backscattered scanning electron microscopy (BSEM) also has a lower spatial resolution than conventional secondary electron imaging, due to greater depth of sample penetration (Figure 4.4) and

interaction of backscattered electrons within the samples. However, BSEM produces additional information on phase distributions, as the image intensity is partly proportional to the average atomic number of the phases observed. This enables the identification of compositional differences, a major advantage for hydrate analysis (although images may be complicated with both compositional and topographical variations). An integrated Energy Dispersive X-ray Analysis (EDXA) system also allows detailed major elemental compositional information to be gathered, for the hydrate and the hosting sediment.

All samples were initially analysed at cryogenic temperatures (c. -170 °C), and areas were mapped to identify any changes during BSEM investigation. To fully appreciate the depth of the sample and to identify features, which may be present below surface layers, each sample was warmed slowly to gradually ablate the sample. Differential 'etching' of samples can reveal valuable information on fabric relationships within the materials and the stability of materials present. By using this approach the SEM effectively becomes an 'experimental reactor', enabling the investigation of dynamic processes by varying temperature during analysis (Camps et al., submitted 2007). This is a commonly used technique for removing unwanted hoar frost from samples during cryo-SEM observations. Images were taken throughout the warming phase showing sample changes during ablation. On occasions samples were refrozen at particular stages to ensure preservation of dynamic changes for imaging. During further and more rapid warming, dissociation of hydrate released gas trapped within the hydrate (lost into SEM vacuum system), and the release of this gas, as well as sample changes on dissociation, can cause a degree of image drifting within the chamber, and therefore returning to mapped locations can be difficult, and in such cases specific features, such as sediment grain shapes, are relied upon to return to previously imaged areas.

Please see Appendix B for specific details on each carbon dioxide hydrate experiment, with some further details documented within following Chapters 5 and 6.

## **CHAPTER 5**

### **Laboratory Investigation of Carbon Dioxide Hydrate**

## **5. Laboratory investigation of carbon dioxide hydrate**

### **Introduction**

Although research into clathrate hydrates has rapidly gained pace in more recent years their mineralogy and formation processes are still relatively poorly understood. Various imaging techniques have been used to study gas hydrates, such as Nuclear Magnetic Resonance (NMR; Kleinberg et al., 2003; Gao et al., 2005); Magnetic Resonance Imaging (MRI; Hirai et al., 2000; Gao et al., 2005); X-ray Computed Tomography (CT; Jin et al., 2004; Schultheiss et al., 2006), and have been proven to be very useful for non-invasive imaging of hydrate formation, dissociation and distribution. Scanning Electron Microscopy (SEM) at cryogenic temperatures offers an additional technique to study clathrate hydrates (Stern et al., 2000; Kuhs et al., 2004; Milodowski et al., 2004; Rochelle et al., 2004; Stern et al., 2004; Camps et al., submitted 2007) (see Chapter 4 for further details).

The following chapter presents and discusses findings from laboratory investigation of carbon dioxide hydrates and ices. Pore-scale BSEM imaging of CO<sub>2</sub> hydrate samples formed within a well-controlled laboratory environment has revealed detailed information on the growth of CO<sub>2</sub> hydrate within sediment, some of which, to my knowledge, have not been noted in previous research.

### **5.1 Different Ice morphologies**

Laboratory-grown hydrate samples are likely to also contain some residual water which will be preserved as ice during cryogenic-SEM observations, therefore it is important to be able to distinguish between different ice and hydrate morphologies present in the hydrate samples. A number of control experiments were conducted to help distinguish different morphologies of other ices, which may be present at cryogenic temperatures. Control samples included (see Appendix B for further details):

1. Pure distilled water mixed with quartz rich sand, frozen (-14°C).

2. Artificial seawater mixed with quartz rich sand, frozen (-14°C).
3. 1 and 2 repeated but pressurised with CO<sub>2</sub>, depressurised, frozen (-14°C).
4. Seawater ice balls (see Appendix B) prepared at cryogenic temperatures and mixed with sediment.

Imaging of control samples, in addition to hydrate samples enabled clearer distinction of ice, hydrate, and hydro-halite.

Water ice morphologies vary significantly, ranging from individual hexagonal plates (Figure 5.1c), to spherical balls (Figure 5.1b, d, e) and solid matrix filling masses (Figure 5.1a). Hexagonal water ice plates identified were approximately 20 µm deep and 50 µm wide, which are very similar in size to spherical ice balls with an approximate maximum diameter of 50 µm. A particularly interesting morphology appears as ice cones radiating from a common point (5.2b, c). This morphology in its more perfect form looks like a 'single flower in a vase'. With approximately six elongated hexagonal ice plates radiating from a single spherical ice ball, which is attached above a solid ice cone. Many examples of this particular ice morphology were seen in the imaged samples. Although samples were protected from the laboratory atmosphere, and the formation of hoar frost was generally prevented, Figure 5.1b shows the presence of hoar frost on one particular sample with spherical ice balls and fibrous ice crystals radiating away from the sample.

In addition to water ice morphologies, the presence of hydro-halite (NaCl·2H<sub>2</sub>O) in the samples (Figure 5.1f and Figure 5.2a, c, d, e) was determined from energy-dispersive X-ray microanalysis (EDXA) identifying different quantities of sodium and chlorine in different regions (Figure 5.3). Regions of bright white salt (largely halite with other minor salts) precipitated between crystals produced high sodium (7cps) and chlorine (16cps) peaks. Regions identified as hydro-halite produced reduced sodium (2cps) and chlorine (14cps) peaks, and CO<sub>2</sub> crystalline hydrate regions produced a higher carbon peak of 5cps, with much reduced sodium (2cps) and chlorine (3cps) peaks. There is some degree of scattering due to the width of the electron beam, and the different structures analysed were in very close proximity (<1 µm), explaining some similarity in composition.

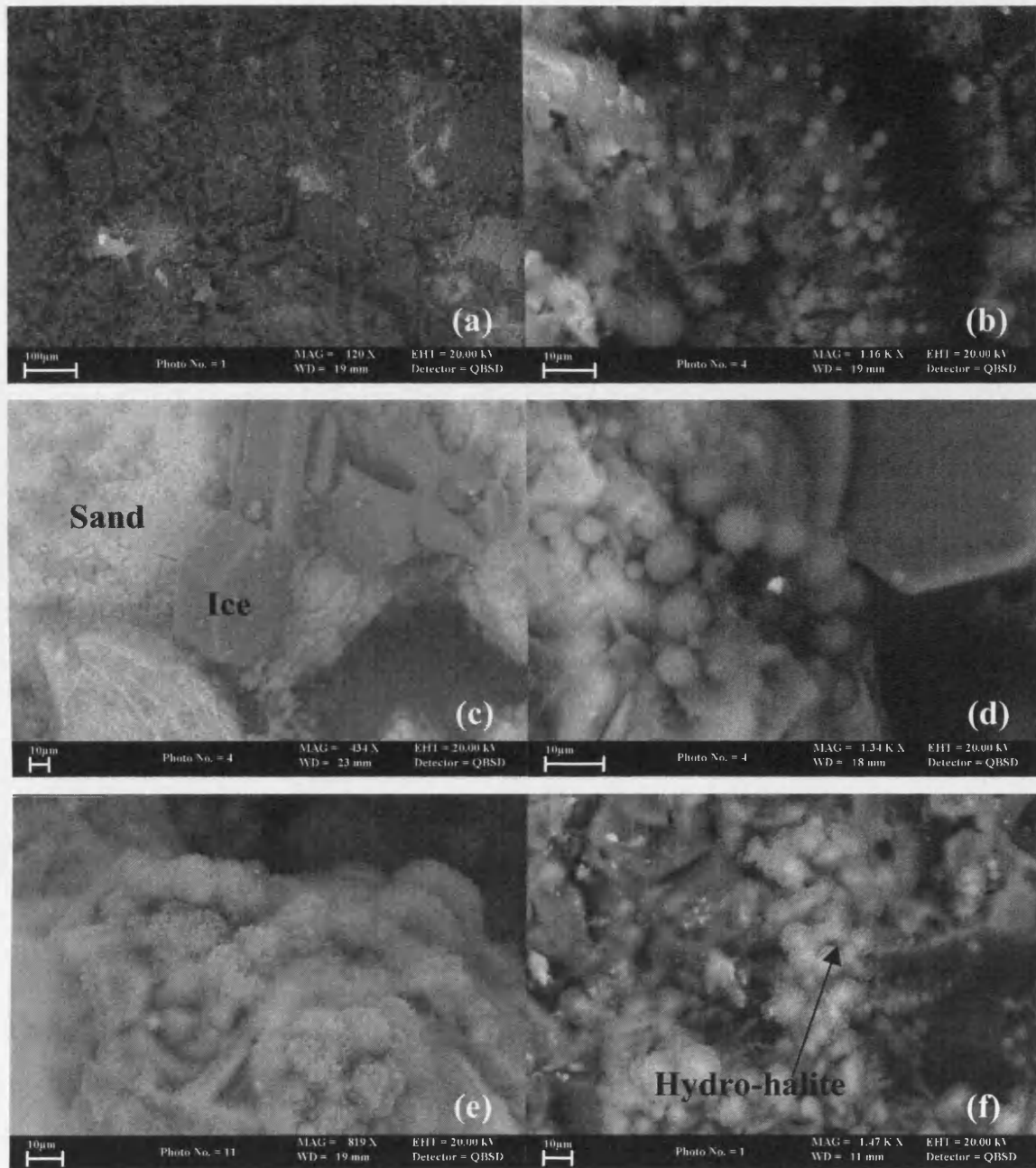


**Figure 5.1**(a) Quartz dominated sand matrix filled with water ice. (b) Spherical ice balls with radiating fibrous hoar frost ice crystals growing away from the sample. (c) Hexagonal ice plates formed between sediment grains. (d) Spherical ice crystals formed on the surface of a sand grain, and situated next to CO<sub>2</sub> hydrate crystals. (e) Spherical ice crystals, hydro-halite and CO<sub>2</sub> hydrate formed around a sediment grain. A degree of hoar frost can be seen covering the crystals. (f) Hydro-halite branching spherical globules within a CO<sub>2</sub> hydrate/ sediment matrix (see higher magnification image Figure 5.1.2a).

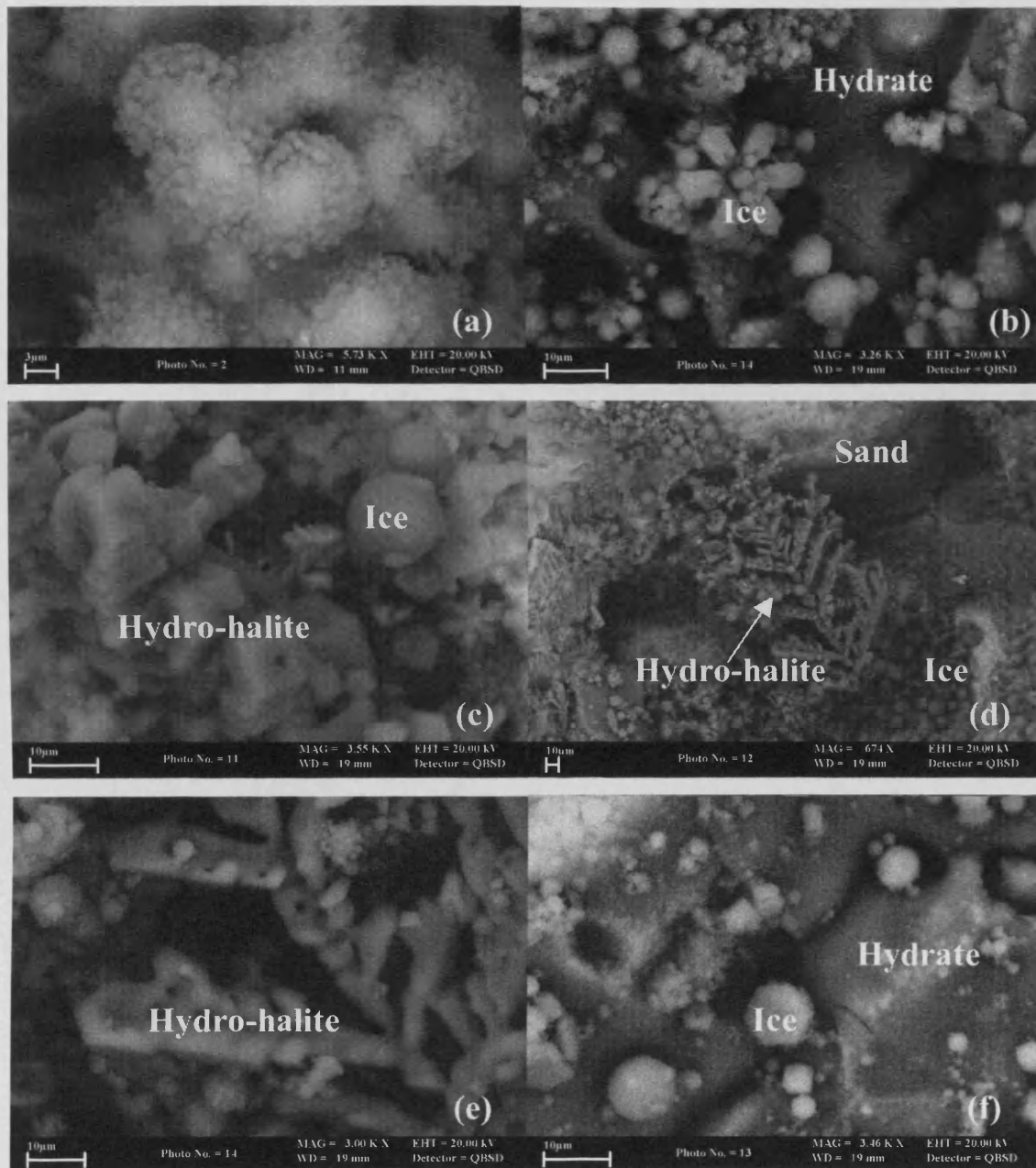


**Figure 5.2**(a) Hydro-halite branching spherical globules with 'furry' outer layer within a CO<sub>2</sub> hydrate/ sediment matrix (5.73kx magnification). During warming this 'furry' outer layer disappears at a lower temperature than the main branches (-110 °C), but at a higher temperature than hoar frost. **(b)** 'Flower bouquet' of ice crystals on the surface of CO<sub>2</sub> hydrate with surrounding ice balls and small salt globules. **(c)** Stacked hydro-halite crystals (left of image) with ice balls, flowers and plates (right of image). **(d)** Branches of stacked hydro-halite crystals (c) forming a skeletal leaf pattern within a sediment pore. **(e)** Higher magnification image of (d) showing branch-like nature of the hydro-halite crystals and surrounding ice balls. **(f)** Hexagonal ice plate (centre of image) lying on the surface of CO<sub>2</sub> hydrate with salt globules and ice balls nearby.

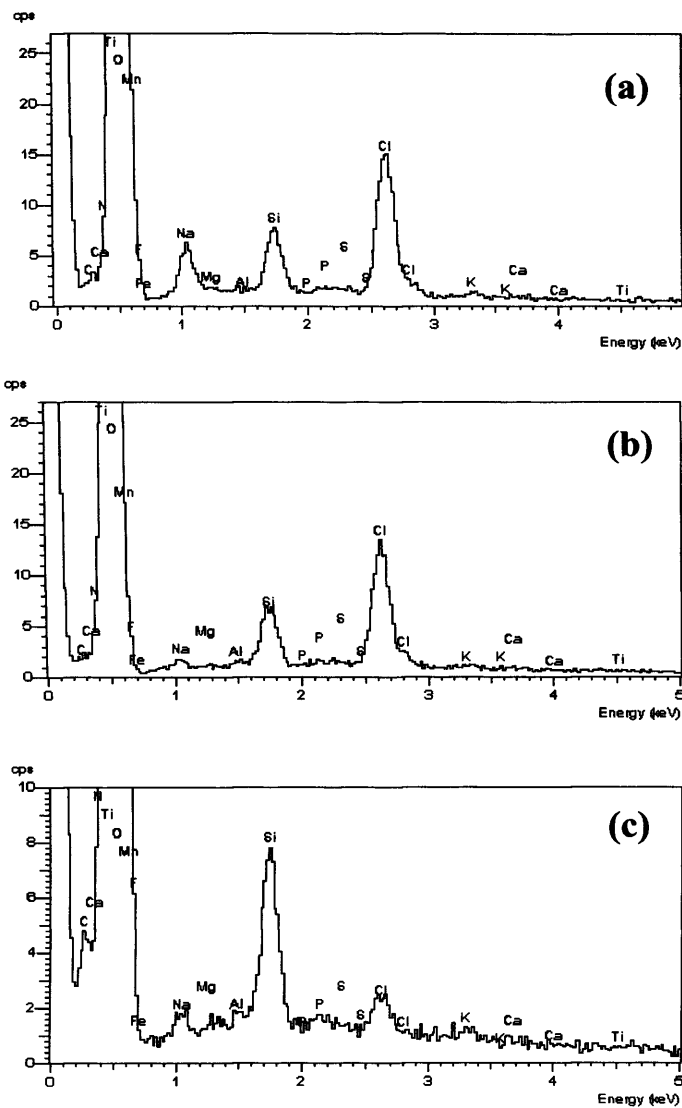


**Figure 5.3(a)** EDXA analysis of salt precipitated between hydrate and hydro-halite crystals showing strong sodium and chlorine peaks, with residual silicon peak from nearby quartz grains, and other residuals from nearby minerals. **(b)** EDXA analysis of hydro-halite crystals with greatly reduced sodium peak, and a reduced chlorine peak. **(c)** EDXA analysis of CO<sub>2</sub> hydrate crystals with a relatively strong carbon peak, background silica peak, and much reduced other residuals.

The same crystalline hydro-halite structures occurred in both hydrate samples, and in samples formed in a standard freezer with no hydrate present. The formation of hydro-halite ( $\text{NaCl}\cdot 2\text{H}_2\text{O}$ ) therefore appears to be a consequence of freezing at cryogenic temperatures, forming from water and halite remaining in the sample pore-waters at temperatures below  $-5\text{ }^\circ\text{C}$ . Below temperatures of  $-25.5\text{ }^\circ\text{C}$  (the eutectic temperature) an aqueous solution can no longer be in equilibrium with ice and salts, therefore, at this point; water ice, hydro-halite and halite co-exist as separate distinct phases. Cryogenic temperatures, as low as  $-180\text{ }^\circ\text{C}$ , are considerably lower than the eutectic temperature, hence; explaining the presence of water ice crystals, hydro-halite crystals, and salt within the samples.

## **5.2 $\text{CO}_2$ hydrate morphologies and salt inclusion during formation**

Carbon dioxide hydrate samples have been formed in a variety of sediments and water solutions, under variable pressure and temperature conditions. Each experiment was designed to investigate the influence of mineralogy, salinity, porosity, experimental technique, and the availability/quantity of formation components on the nature and formation of carbon dioxide hydrate (Figure 5.4). A selection of these samples were subsequently analysed using BSEM, and images from such are presented with detailed explanations for each image in underlying captions. After early experiments and consequent imaging to fully distinguish between ice phases and carbon dioxide hydrate, it has been possible to identify different carbon dioxide hydrate morphologies within the several experimental samples investigated. Experimental samples show different hydrate morphologies, resulting from different formation conditions with the primary supply of necessary components altering the rate of formation; hence each sample is described separately in the text. These samples include the following (for more detailed explanation of the experimental procedure for each sample, see Appendix B):

1. Coarse quartz rich sand ( $600\text{ }\mu\text{m} - 2\text{ mm}$ ) fully saturated with artificial seawater solution, with a thin surface layer of seawater lying above the sand. Pressure remained constant at 170 bar, and the temperature was varied between  $-3.8\text{ }^\circ\text{C}$  and  $3.1\text{ }^\circ\text{C}$  (Run 24).

2. Quartz rich sand (355 - 600  $\mu\text{m}$ ) mixed with seawater spherical ice balls used as a precursor for carbon dioxide hydrate formation. Both pressure (36 bar to 200 bar) and temperature (-8.2  $^{\circ}\text{C}$  to 1.8  $^{\circ}\text{C}$ ) were varied (Run 20).
3. Medium quartz rich sand (355  $\mu\text{m}$  – 600  $\mu\text{m}$ ) dampened with artificial seawater (approximately 5% by weight). Pressure remained constant at 200 bar, and temperature at 2  $^{\circ}\text{C}$  (<+0.4 variation) (Run 25).
4. Three different sediments used in one Teflon liner: Clay (Wyoming bentonite), Clean medium grained quartz rich sand (355  $\mu\text{m}$  – 600  $\mu\text{m}$ ), and natural mixed sand from Anglesey with a fine-medium size fraction, to investigate hydrate growth along sediment contact points. Variable temperature (12  $^{\circ}\text{C}$  to 2.2  $^{\circ}\text{C}$ ) and constant pressure at 200 bar (Run 31).
5. Medium quartz rich sand (355  $\mu\text{m}$  – 600  $\mu\text{m}$ ) fully saturated with deionised water. Pressure maintained at 200 bar, and temperature maintained at 2  $^{\circ}\text{C}$  (+/- 0.6 $^{\circ}\text{C}$ ) (Run 30).
6. Coarse quartz rich sand (600  $\mu\text{m}$  – 2 mm) dampened with deionised water. Pressure maintained at 200 bar, temperature varied (5.6  $^{\circ}\text{C}$  to -52  $^{\circ}\text{C}$ ). (Run 34).
7. Artificial seawater solution only, no sand. The aim was to investigate hydrate formation in an aqueous environment. Variable pressure (36 bar to 200 bar) and temperature (2  $^{\circ}\text{C}$  to 9  $^{\circ}\text{C}$ ) (Run 22).

CARBON DIOXIDE HYDRATE FORMATION WITHIN SEDIMENTS				
EXPERIMENTAL TECHNIQUES	POROSITY	SALINITY	MINERALOGY	AVAILABILITY OF CO <sub>2</sub> AND WATER
RUN 20				
RUN 21			RUN 21	
RUN 22				
		RUN 24		
		RUN 25		RUN 25
		RUN 28		
		RUN 29		
		RUN 30		
	RUN 31			
RUN 33				
RUN 34		RUN 34		RUN 34
RUN 35				
RUN 36				
RUN 38				

Figure 5.4. Chart to show the broad investigatory pathways followed for each experimental run. See appendix for further experimental details.

### 5.2.1 Investigated CO<sub>2</sub> hydrate samples

#### *Sample 1*

The sample contained carbon dioxide hydrate formed within and above a quartz dominated unconsolidated coarse sand (600 µm-2 mm) fully saturated with an artificial seawater solution (concentration of 3.5% by weight) (water-rich environment). BSEM images show carbon dioxide hydrate formed in the overlying water layer, which on initial visual inspection appeared as a homogenous white layer above a sand matrix with the latter having its porosity filled with white 'grains'. The sample degassed vigorously when warmed by hand suggesting a very high concentration of CO<sub>2</sub> hydrate

in the sample (although this could also indicate a large volume of trapped CO<sub>2</sub> within the sediment).

A cleaved sample of both the upper solid CO<sub>2</sub> hydrate layer and the hydrate filled sand was sub-sampled for BSEM analysis. However, what appeared as a pure white homogenous hydrate layer on initial inspection, appeared very differently under the BSEM. The sample stage of the SEM was maintained at -151.6 °C during analysis. White 'veins' of salts run throughout the sample, and at higher magnification these salt structures show very delicate salt fabrics, with radiating dendritic salt crystals (c. 15 µm) separating and included within the hydrate (Figure 5.5). Alongside these salt fabrics small holes puncture the hydrate (<20 µm), creating a slightly micro-porous structure. The hydrate itself appeared as acicular 'needles' (see 5.2.2) with a direction of growth visible by salt fronts within each needle, forming downwards into the sample towards the saturated sand layer (northeast in Figure 5.5c). Grey regions represent areas of CO<sub>2</sub> hydrate, bright white regions represent salt fabrics, and darker grey regions represent holes or gaps in the sample.

EDXA was used to assist in clarification of defining salt fabrics and hydrate, and the X-ray identified sodium, magnesium and chlorine peaks in bright regions, and a weak carbon peak in grey hydrate regions, indicating appreciable CO<sub>2</sub> and salt concentration within the sample. The dominating sodium and chlorine peaks indicate the majority of the salt fabrics within the sample are dominated by halite with other salts present in reduced concentrations.

To fully appreciate the depth of the sample and to ensure full analysis, the sample was warmed from -151.6 °C to -85 °C, at which point the CO<sub>2</sub> hydrate began to ablate, and the salt fabrics became more apparent. Figure 5.5d expresses the salt 'skeleton' remaining after raising the temperature to gradually ablate the CO<sub>2</sub> hydrate.

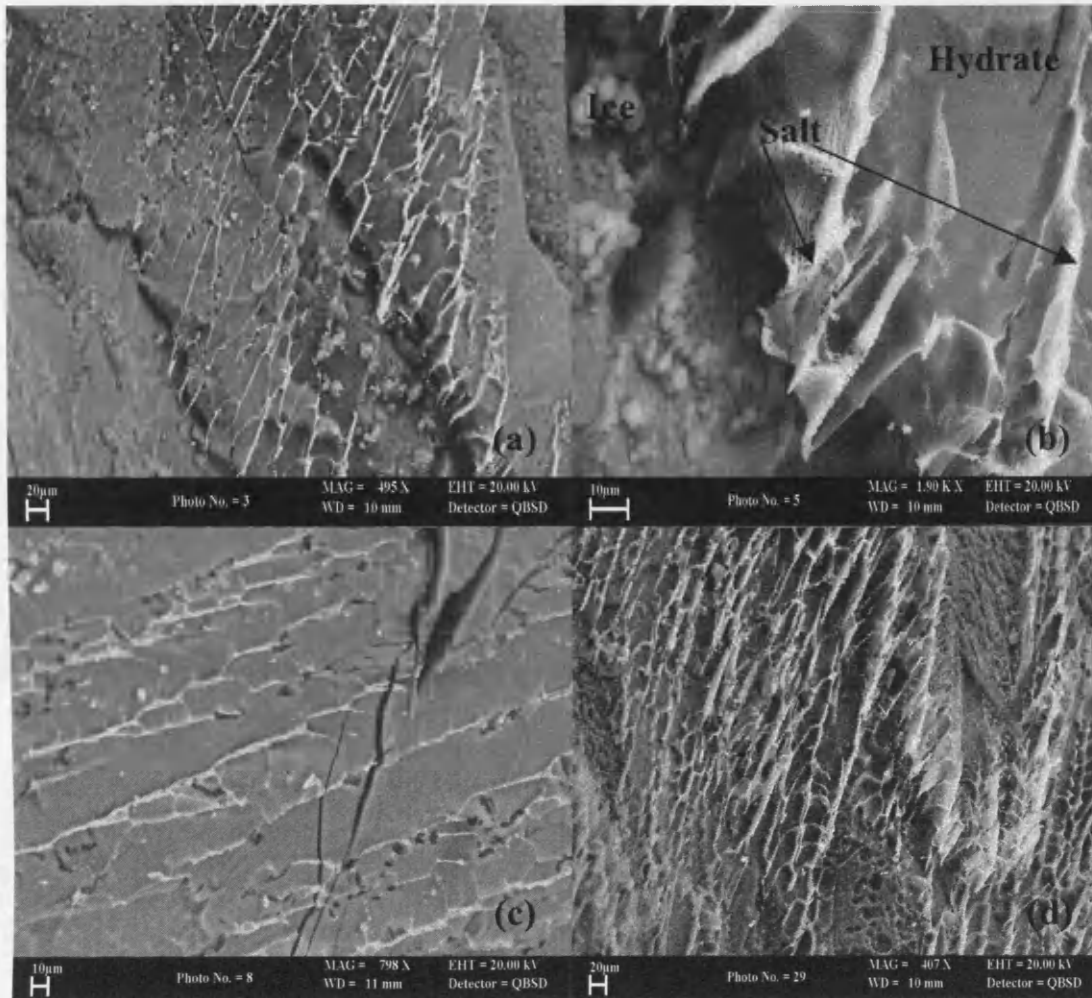


**Figure 5.5(a)** BSEM image of carbon dioxide hydrate needles forming downwards into Sample 1 with salt ‘veins’ separating and included within the formed hydrate. Grey regions represent CO<sub>2</sub> hydrate, bright white regions represent salts, and darker grey regions are holes (highlighting the porous nature of the hydrate). **(b)** BSEM image of a part of (a) at higher magnification identifying dendritic radiating salt needles forming a delicate ‘net-like’ salt fabric within the sample. **(c)** BSEM image of CO<sub>2</sub> hydrate needles with salt precipitated along grain boundaries and included within the hydrate, with salt ‘fronts’ identifying the direction of growth, towards the upper right of this image (or towards the underlying sediment). Dark cracks are visible in the sample, which are thought to have formed as a consequence of sample handling. **(d)** BSEM image of the same area as (a) after raising the temperature to -85 °C and ablating some of the hydrate sample. Grey regions represent CO<sub>2</sub> hydrate and ice, and lighter regions the delicate 3D salt ‘skeleton’ revealed after ablation.

## ***Sample 2***

Carbon dioxide hydrate formed within 50% quartz rich sand (355-600  $\mu\text{m}$ ) and 50% spherical ice balls (c. 500  $\mu\text{m}$  in diameter) made from artificial seawater. The use of seawater ice balls (see Appendix B for experimental procedures), or crushed ice, is an experimental technique to facilitate hydrate formation within a sample, with the ice acting as a precursor for hydrate growth (Stern et al., 2004). After depressurisation and preservation above liquid nitrogen the sample appeared as a light, slightly porous white and brown core. A degree of sample volume reduction (<27%) was also noted, either due to porosity reduction from melting ice balls and formation of  $\text{CO}_2$  hydrate, or contraction during cryogenic freezing. The porous nature of the sample on initial inspection became more apparent on BSEM investigation (Figure 5.6a). The sample stage was maintained at approximately  $-148\text{ }^\circ\text{C}$  throughout the investigation.

$\text{CO}_2$  hydrate surrounded sand grains and appeared within the pore spaces, in some areas forming pore-filling cement and in other areas connecting grains very weakly by fragile hydrate shells (Figure 5.6a). These textures represent the method used in the experiment to form the hydrate - using ice balls as a precursor, and using warming and cooling cycles to encourage hydrate growth. Shells of the outer regions of the original ice balls were initially replaced by hydrate, but maintained the spherical shell shape (Figure 5.6b, c), and have been seen in previous research (Stern et al., 2004). These 'shells' are thought to have formed as liquid water drained from the grain interior during melting cycles after initial hydrate formation around the exterior of the ice ball (Stern et al., 2004). Presumably further warming and cooling cycles would eventually remove this porous shell texture representative of the original seed material.

In some open pores well-formed euhedral carbon dioxide hydrate crystals can be seen (Figure 5.6b, c), but a large percentage of the hydrate present appears as 'melt structure' granoblastic hydrates (Figure 5.6d), representing secondary formation due to the melting and cooling cycles (see 5.2.2). Additional morphologies include 'coral-like' branching hydrates, which appear to be unique to this sample (Figure 5.6d).

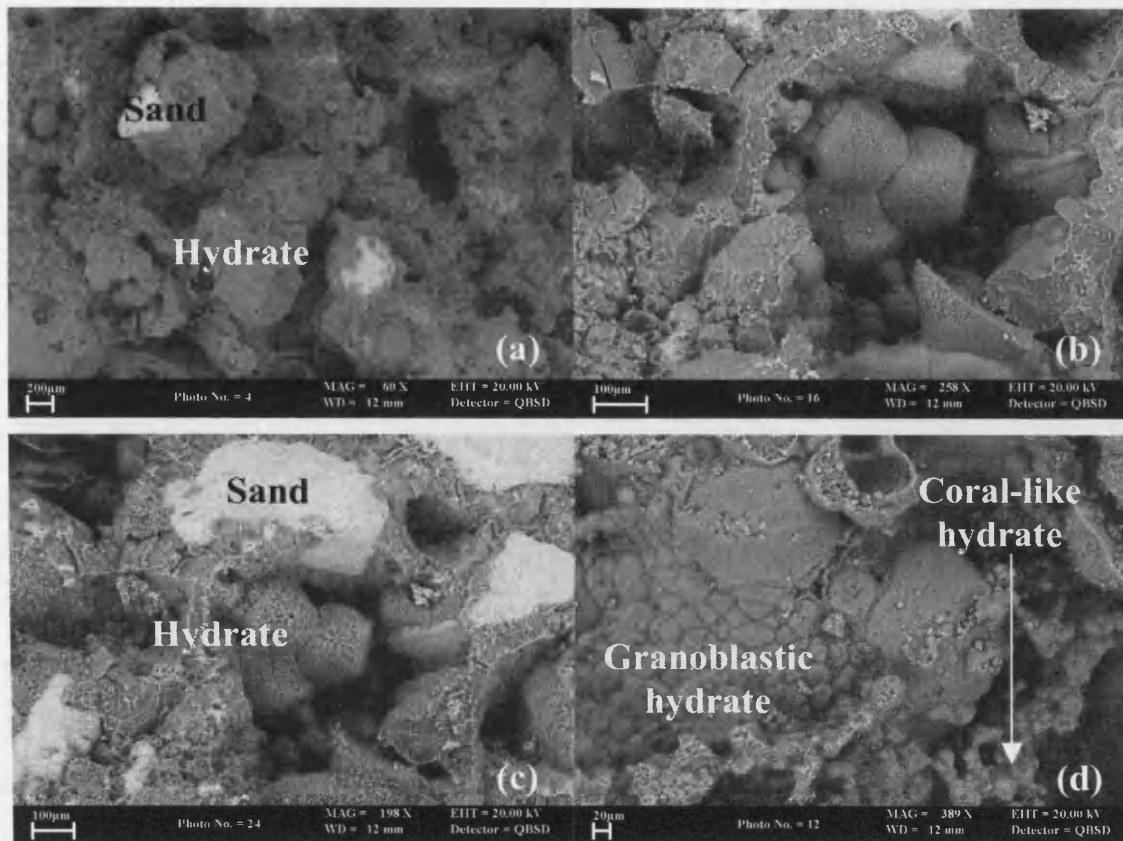


**Figure 5.6(a)** BSEM image of CO<sub>2</sub> hydrate formed within coarse quartz rich sand (355 – 600 µm) using seawater spherical ice balls (c. 500 µm in diameter) as a precursor. Grey regions represent CO<sub>2</sub> hydrate, white regions salt and sand grains, and darker grey regions are voids. **(b)** Higher magnification BSEM image of CO<sub>2</sub> hydrate crystals (c. 160 µm in diameter) formed within a void inside a CO<sub>2</sub> hydrate spherical ‘shell’ which was previously filled by seawater ice. **(c)** Lower magnification BSEM image of (b) after 30 minutes of ablation at -85 °C revealing halite networks within hydrate crystals. **(d)** BSEM image of granoblastic ‘melt structure’ CO<sub>2</sub> hydrate (c. 40 µm in diameter) surrounding larger hydrate crystals in the left hand side of the image. To the right hand side are ‘coral-like’ branching hydrates, unique to this sample.

Salt fabrics are not as clear as in other samples under discussion, but after ablation honeycomb salt structures appear to etch out of euhedral CO<sub>2</sub> hydrate crystals, and around the hydrate, which replaced the ice ball shells (Figure 5.6c).

Also imaged from this sample run was a white hydrate ‘curl’ which was discovered on the surface of the sample. This curl of hydrate, which on initial inspection looked a little like ‘pencil shavings’, expressed similar microscopic morphologies seen in other

hydrate samples ('holey' hydrate and 'vesicular' hydrate), but also an additional morphology not seen in any other sample – 'pea-pod' hydrate (see 5.2.2).



**Figure 5.7(a)** BSEM image of 'holey' hydrate within a CO<sub>2</sub> hydrate 'curl' found on the surface of sample 2. Sample stage was maintained at approximately -171 °C. **(b)** BSEM image of 'Pea-pod' hydrate with each pod (c. 40 μm) constructed by spherical and cubic polyhedral CO<sub>2</sub> hydrate 'peas' (<5 μm) surrounded by a layer of ice, another layer of hydrate and then an external ice/salt matrix. **(c)** BSEM image of (b) after etching at -140 °C. The CO<sub>2</sub> hydrate 'peas' have been ablated during warming, indicating a more unstable hydrate phase. **(d)** CL image of (b) showing the different phases which seem to be present. Saline regions appear white and water ice appears as darkest grey regions (between other phases).

The 'holey' hydrate contained trapped gas bubbles, as well as a 'crystalline mush' (Figure 5.7a) with very crystalline hydrate and salt precipitated along the crystal boundaries, as was also discovered in sample 5 (see 5.2.2). The pea-pod hydrate had a highly unusual structure (Figure 5.7b). More than one phase of hydrate and ice growth seemed to be present, with salt (or frozen brine) forming a skeleton around these

different phases (forming the pod or shell). Each pod appeared to be constructed by spherical and cubic polyhedral CO<sub>2</sub> hydrate ‘peas’ surrounded by a layer of ice, another layer of hydrate and then an external ice/salt matrix, the imaging of which appeared a little clearer using cathodoluminescence (CL) (Figure 5.7c). The direction of growth was not apparent, but some of these ‘pods’ did appear to spiral around a central point. There were also areas where a salt skeleton formed a branch-like network interconnecting the pea-pod hydrate. It is unclear as to how these salt networks form; but their growth could be connected to the spiral growth pattern observed in the pea-pod hydrate.

### ***Sample 3***

This sample contained carbon dioxide hydrate grown within medium grained (355-600 µm) unconsolidated quartz rich sand, dampened with an artificial seawater solution (35 ppm) (i.e. water poor sample with an interconnected open pore network to facilitate the access of liquid CO<sub>2</sub> to all the dampened sediment). Initial visual inspection identified a solid sediment ‘puck’ filled with intergranular white specs, which de-gassed when warmed. BSEM investigation noted very crystalline CO<sub>2</sub> hydrate cementing sediment grains, replacing the original water meniscus, which would have been present along sediment grain boundaries. Larger crystals of CO<sub>2</sub> hydrate appear to have formed within larger pore spaces, and reach up to 100 µm (Figure 5.8a). Small spherical ice balls are also present where some minor dissociation has occurred during sample cleaving, and hydro-halite crystals are present in the sample (identified though EDXA analysis, with high sodium and chlorine peaks in areas of high salt concentration and weaker signals in areas of hydro-halite). EDXA also identified a weak carbon peak in hydrate rich zones.

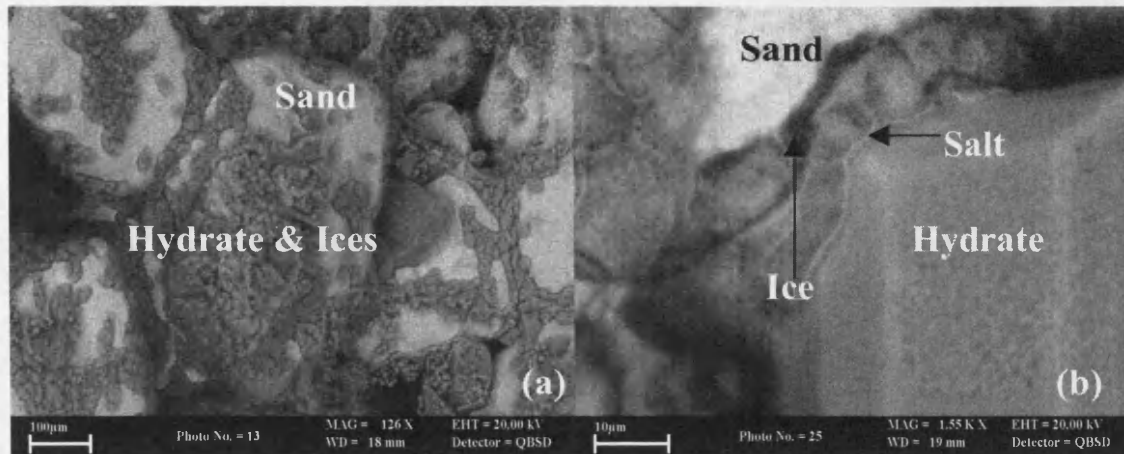


**Figure 5.8(a)** BSEM image at 126x magnification of crystalline CO<sub>2</sub> hydrate formed within medium quartz rich unconsolidated sand (355-600 μm) dampened with artificial seawater solution. Sample chamber maintained at -154 °C. Bright white regions are quartz sand grains, and grey regions are CO<sub>2</sub> hydrate (plus smaller amounts of hydro-halite and ice). **(b)** BSEM image at 1.55kx magnification of CO<sub>2</sub> hydrate crystals formed around quartz sand grains, with a larger crystal growing outwards into a gas filled pore space. Bright white regions represent a sand grain; duller white regions along crystal boundaries are precipitated salt, dark grey regions are open cavities and water ice, and lighter grey regions CO<sub>2</sub> hydrate.

Salt precipitate concentrations (halite dominated) within this sample are much lower than other samples discussed due to less seawater added initially in the experiment (although salinity was the same as for other seawater experiments). The majority of the salt present is along grain boundaries, separating hydrate crystals (Figure 5.8b). A degree of dissociation is also evident due to the presence of ice around hydrate grains, possibly as a consequence of electron beam damage from examining the same area for too long a period. Some of the larger crystals also appear to have some salt included within their structure as was present in other samples, but as very fine veins rather than obvious inclusions. Ablation of the sample etched some of the crystal boundaries further to enable clearer visualisation of salt present between grains, however; any fine salt fabrics were lost with further ablation due to their delicate nature.

#### ***Sample 4***

Carbon dioxide hydrate formed within three different sediments in a single Teflon liner: Clay (Wyoming bentonite), Clean medium grained quartz rich sand (355  $\mu\text{m}$  – 600  $\mu\text{m}$ ), and natural mixed sand from Anglesey with a fine-medium grained size fraction. On initial visual inspection the sand and clay appeared to be porous, with disseminated hydrate clearly visible in the sand matrix. The clay's texture was quite unusual with a highly porous (expanded) appearance, possibly as a result of degassing during depressurisation. A sub-sample was taken at the interface between the clean sand with a known size fraction and the bentonite clay. Unfortunately the SEM sample chamber accidentally vented while the sample was on the cold stage, and a considerable quantity of hoar frost covered the surface, which has impeded clear examination of the hydrate present.

Within the sand, hydrate appeared as both intergranular pore-filling cement and as discrete lenses. The hydrate forming lenses; within the sand; appeared as elongated flattened crystals, which seem to be have grown horizontally, diagonally and vertically (Figure 5.9a), with each crystal separated by a thin layer of precipitated mixed salt and clay (suggesting partial mixing of the sand and clay prior to, during, or, post hydrate growth). The pore-filling cement seems to have a smaller percentage of salt and clay present along crystal boundaries and the hexagonal shape of the crystals is more apparent (Figure 5.9b, c). Additionally, 'melt-structure' granoblastic (d) and acicular  $\text{CO}_2$  hydrates are also present (Figure 5.9e).

There are some salt globules present on the sample; but the majority of the salt in this sample has been precipitated along crystal boundaries. There appears to be no evidence for the presence of salt inclusions. On sample ablation, the precipitated salt became more apparent (Figure 5.9f), etching out into honeycomb salt fabrics within the sandy matrix. Salt structures within the clay are less clear as the majority of the hydrate within the clay formed as individual crystals and did not form the honeycomb structures which are easily distinguishable.

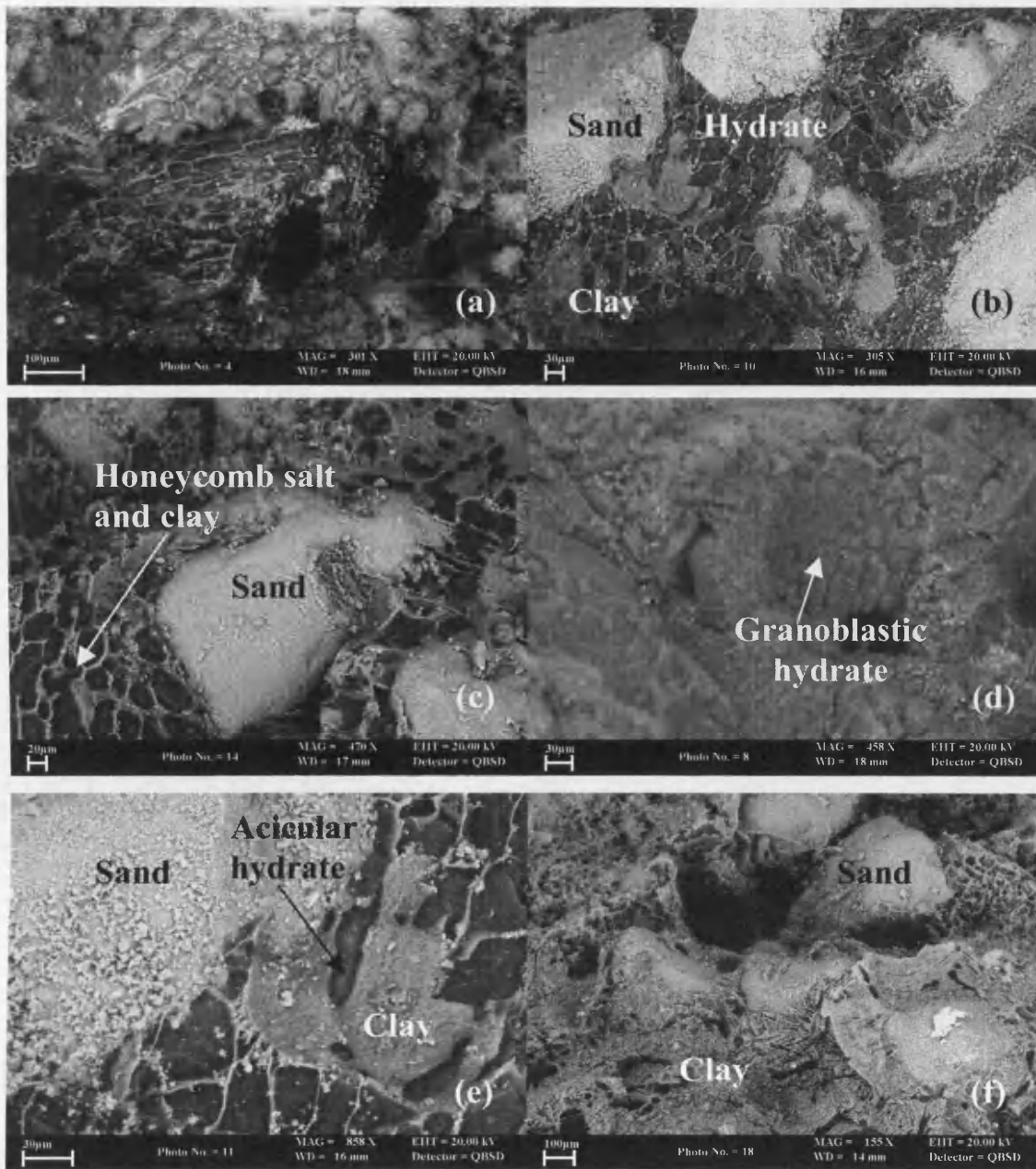


**Figure 5.9(a)** BSEM image of a CO<sub>2</sub> hydrate lens formed within medium grained quartz rich sand (355-600 μm) near the interface with Wyoming bentonite clay, showing flattened hydrate crystals grown vertically, diagonally and horizontally. Sample stage maintained at -171.6 °C. **(b)** BSEM image of pore-filling CO<sub>2</sub> hydrate cementing sand grains. White areas are sand grains, light grey regions represent intergranular clay and salt, and darker grey regions are hydrate. **(c)** BSEM image after ablating to -100 °C of pore-filling ice pseudomorphs after CO<sub>2</sub> hydrate enveloping a sand grain with pronounced intergranular honeycomb salt and clay fabrics between former hydrate crystals. **(d)** BSEM image of granoblastic CO<sub>2</sub> hydrate along the clay-sand interface. **(e)** BSEM image of acicular CO<sub>2</sub> hydrate formed away from a sand grain into surrounding the pore space. **(f)** BSEM image of the sand-clay interface after full ablation to 0 °C showing the nature of clay and salt fabrics within the sample.

### ***Sample 5***

Carbon dioxide hydrate formed within medium quartz rich sand (355  $\mu\text{m}$  – 600  $\mu\text{m}$ ) fully saturated with deionised water. The sample was depressurised a little too rapidly creating an expanded horizontal fracture in the sand. Within this fracture was a white hydrate lens; either formed during the experiment, or after cooling during depressurisation. A sub-sample was taken from this lens for BSEM investigation. The  $\text{CO}_2$  hydrate appeared micro-porous with a large percentage of surface ice crystals. There was some evidence for partial dissociation as ‘teeth-like’ ice crystals could be seen as the hydrate was actively being converted to ice (see Rochelle et al., 2004). Many trapped gas bubbles could also be seen in the sample, with some examples of hydrate growing around these gas bubbles (Figure 5.10a).

Three different hydrate morphologies appear within this sample. ‘Holey’ hydrate (Figure 5.10a, d), ‘Melt-structure’ hydrate (Figure 5.10b) and ‘Vesicular’ hydrate (Figure 5.10c, d) (see 5.2.2 morphological descriptions for more details). No salt is present in this sample as the hydrate was formed from deionised water

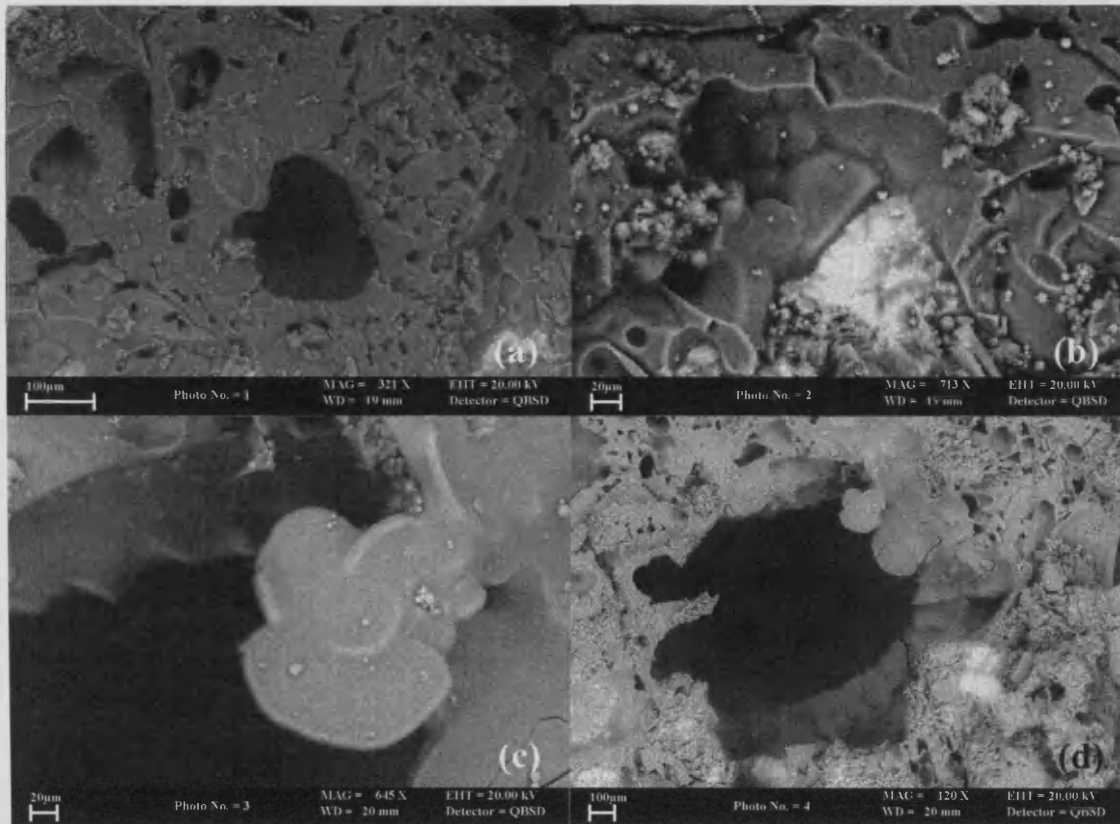


**Figure 5.10**(a) BSEM image of CO<sub>2</sub> hydrate formed as a lens within medium grained quartz rich sand (355-600 μm) fully saturated with deionised water. CO<sub>2</sub> hydrate crystals are shown to have formed around a gas bubble, with many trapped gas bubbles, expressing an example of the ‘Holey-hydrate’ morphology. Sample stage maintained at -150 °C. **(b)** ‘Melt-structure’ polyhedral CO<sub>2</sub> hydrate crystals formed alongside a sediment grain. **(c)** ‘Vesicular’ CO<sub>2</sub> hydrate which has grown into a large void within the sample. **(d)** Lower magnification image of (c) expressing the relationship between the ‘vesicular’ hydrate morphology grown into a large void and the ‘holey’ gas-rich hydrate.

### **Sample 6**

Carbon dioxide hydrate formed within coarse quartz rich sand (600 μm – 2 mm) dampened with deionised water. This sample was cryogenically frozen at pressure using a newly developed technique (see Appendix B), therefore eliminating the possibility of slight dissociation on depressurisation and transfer to liquid nitrogen temperatures. To my knowledge, this is the first noted attempt to preserve hydrate in-situ by freezing whilst at pressure. Additionally, the sample was immediately sub-

sampled in a nitrogen atmosphere and imaged using the BSEM, eliminating the possibility of sample breakdown during storage at liquid nitrogen temperatures. On analysis the sample was found to contain highly crystalline CO<sub>2</sub> hydrate, with well formed euhedral crystals  $\leq 70 \mu\text{m}$  in diameter and the largest crystals growing into large open pore spaces (Figure 5.11a). The sample was well cemented with all the sand grains coated with a thick layer of crystalline hydrate, but some pore spaces remained open due to water being the limiting factor for hydrate growth. No salt appears within this sample as deionised water was used to dampen the sand grains.

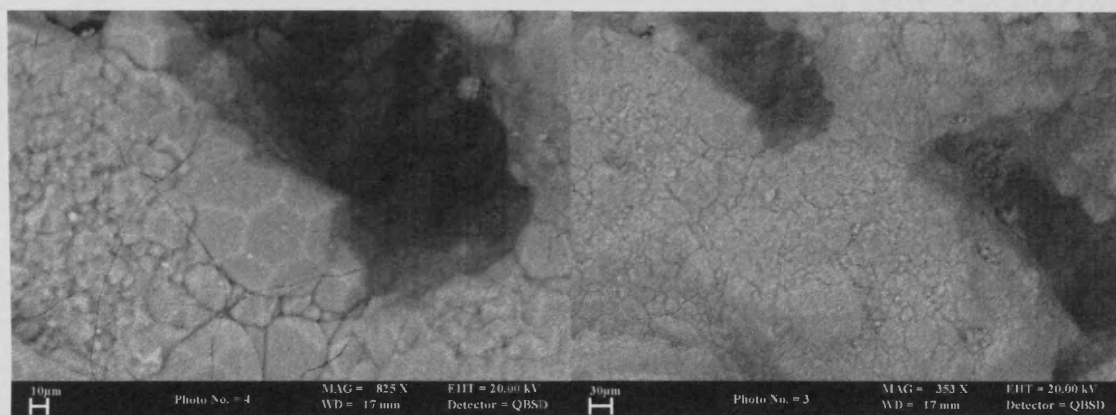


**Figure 5.11(a)** BSEM image of crystalline deionised water CO<sub>2</sub> hydrate cementing dampened quartz rich sand (600  $\mu\text{m}$ -2 mm) preserved in-situ at pressure, with larger hydrate crystals growing into open pore spaces. The sample stage was maintained at -169 °C. **(b)** Lower magnification image of (a) showing sand grains (beneath hydrate crystals) completely encrusted with euhedral CO<sub>2</sub> hydrate crystals.

### **Sample 7**

Carbon dioxide hydrate formed within artificial seawater solution (no sand). The sample appeared white on initial visual inspection, with a bubbly texture. BSEM images show euhedral CO<sub>2</sub> hydrate crystals which have grown downwards into the seawater solution, terminated by a growth front where hydrate formation ended and (frozen) seawater lay beneath (Figure 5.12a). As a consequence of sample handling there was very slight dissociation of this sample, and a degassing feature can be seen in Figure 5.12a in the right of the image. This degassing hole (dark grey pit) shows some 'teeth-like' ice along the bottom of the degassing feature, which formed as a

consequence of hydrate dissociation. However, it was possible to identify areas of pristine hydrate and ice from areas of slight hydrate dissociation. Small globules of salt appeared on the surface of the crystals and within the seawater ice, with some sheet-like salt structures disseminated on the surface of the seawater ice (Figure 5.12c). At higher magnification, the euhedral hydrate crystals showed salt inclusions (Figure 5.12b). These inclusions appear as brighter white zones, surrounded by dark grey zones. The included salt occurred as strings of crystals, which formed a ring around the crystal grain boundaries ( $<3 \mu\text{m}$  wide), near contact with other hydrate crystals, and as small single salt crystals included within the hydrate crystal faces ( $<2 \mu\text{m}$ ). The surrounding dark zones represent remaining frozen brine surrounding the hydrate crystals.

The sample was warmed very gradually from  $-151 \text{ }^\circ\text{C}$  to  $-44 \text{ }^\circ\text{C}$  for a period of 60 minutes, and at a temperature of  $-116 \text{ }^\circ\text{C}$  the sample began to ablate, slowly changing to ice, as the  $\text{CO}_2$  gas was lost into the vacuum of the SEM. As the sample was gradually etched the underlying salt fabrics in the frozen seawater became more visible, however; due to the very small scale of the salt inclusions within the hydrate crystals, these structures were lost. The fully etched sample revealed a large quantity of salt present within the frozen seawater solution, and very little within the crystalline hydrate region. On closer inspection the remaining salt structures formed a very fine honeycomb mesh within the seawater ice sample region (Figure 5.12d), at a finer scale than seen in previous images.

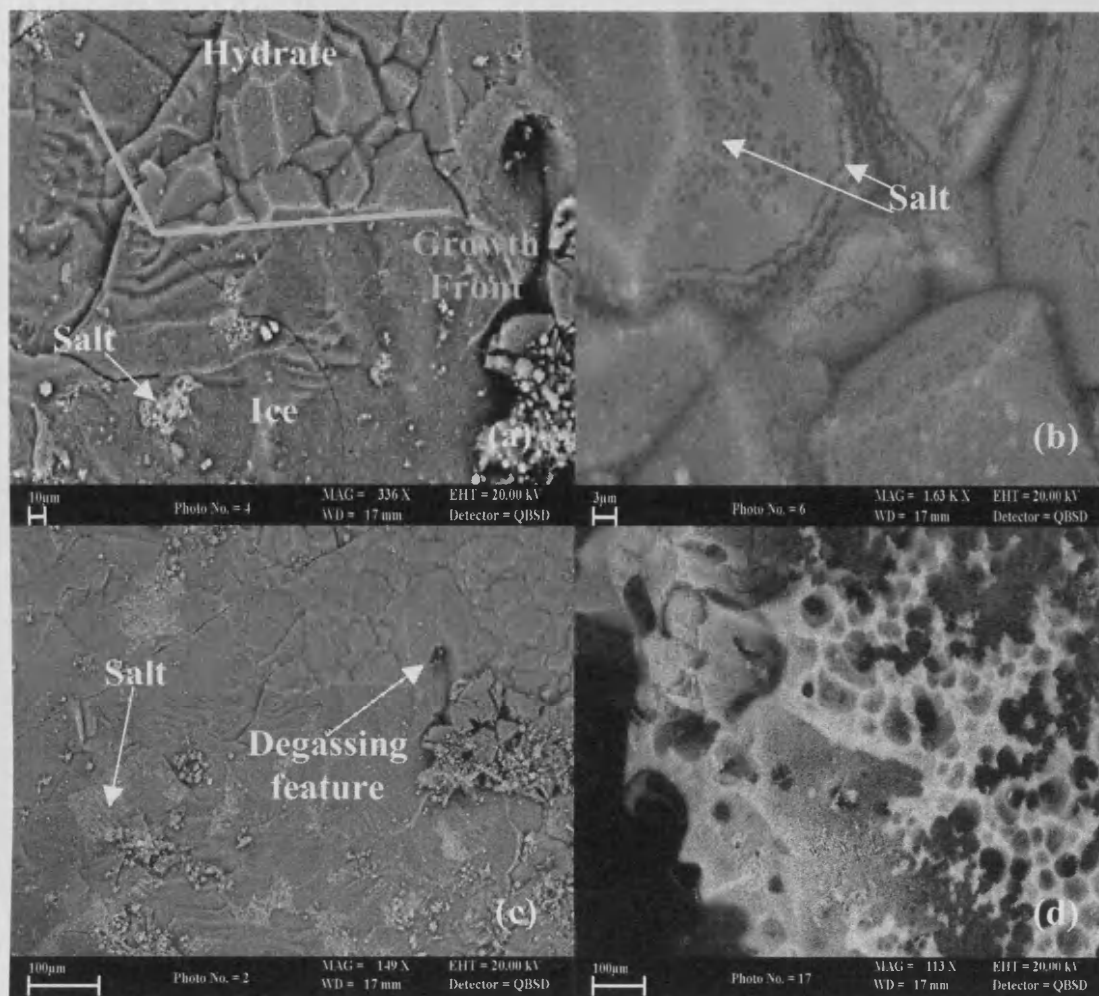


**Figure 5.12(a)** BSEM image of euheedral CO<sub>2</sub> hydrate crystals formed within artificial seawater, growing downwards into underlying seawater solution (now frozen) taken while the sample was at -151 °C. Globules of salt are present on the sample surface, with some delicate salt fabrics present in the frozen seawater solution. **(b)** Higher magnification BSEM image of part of (a) showing densely packed crystalline hydrate grains with small salt inclusions within the hydrate crystals. The salt was deposited as strings (<3 μm wide) and small crystals (<2 μm) in the hydrate with surrounding frozen brine. **(c)** Lower magnification BSEM image of (a) with hydrate crystals to the upper right of the image and underlying frozen seawater with salt fabrics in the rest of the image. **(d)** BSEM image of remaining salt fabric present within the sample (from frozen seawater region) after ablation for 60 minutes, with a final temperature of -44 °C.

### 5.2.2 Different CO<sub>2</sub> hydrate morphologies

The different hydrate morphologies present in the samples associated with the primary components and the rates of formation have been subdivided into the following categories to enable clearer comparison.

#### *Euhedral crystalline carbon dioxide hydrate*

Well-formed euhedral hydrate crystals appear in a number of the samples under investigation. This morphology appeared in samples formed within both pure deionised water (Figure 5.11) and artificial seawater (Figure 5.6, 5.8, 5.12), with the best-formed, largest crystals appearing in larger pore spaces. The morphology is not seen in samples formed within fully saturated sand. Polygonal crystal shape varies slightly, with some having sharper crystal edges and more easily identifiable faces than others, and some with slight distortion due to compression with surrounding crystals.

#### *Acicular carbon dioxide hydrate*

Two samples showed a morphology not seen in any of the others – acicular hydrate. In sample 1, acicular hydrate needles grew downwards from the overlying seawater into the underlying fully saturated sediment. Each acicular hydrate needle is separated by salt and sub-micron holes. There also appears to be a growth front visible in each needle, with each acicular needle forming in the same direction. It is assumed this form resulted from very rapid growth after rapid nucleation on the surface of the water layer, similar to other well known acicular crystal formation (see later section). Smaller and less distinctive acicular crystals were also seen within the clay layer in sample 4; however; the formation of these acicular crystal shapes may be associated with the most suitable growth method necessary to form within clay sediment due to formation difficulties within very fine-grained sediment (Clennel et al., 2000), rather than the rate of growth.

### ***Melt-structure carbon dioxide hydrate***

Within samples formed from using ice balls as a precursor for hydrate formation, there is an additional morphology formed from warming and cooling cycles to convert the ice balls into hydrate. Reaction rims can also be seen where parts of the ice balls have converted to hydrate. The hydrate crystals did not show such well-formed euhedral shapes as seen in other samples, but had more irregular shapes with a clearly visible layer separating each crystal, expressing a granoblastic-polygonal texture (Figure 5.6). These melt structure hydrates seem to be influenced by the formation processes. This hydrate form has also been seen within sample 4 (Figure 5.9d) and sample 5 (Figure 5.10b), both of which seem to have been affected by melting and cooling cycles. The experimental procedure used for these samples has produced this particular hydrate morphology, and evidence suggests it is a secondary crystal form.

### ***'Holey' or micro-porous carbon dioxide hydrate***

This morphology appeared in at least two of the samples under investigation, but forming under different experimental conditions. The first example can be seen in Figure 5.10a, which shows one central gas bubble, with other trapped gas bubbles to the left hand side of the image. Hydrate crystals can be seen to have grown into and around these gas bubbles, in some areas forming densely packed hydrate, and in others a crystalline 'mush' with each crystal separated by a distinct gas filled zone. The other example (Figure 5.7a) shows some branch-like hydrate, which appears to represent some degree of melting (possibly due to warming during sample preparation), and a similar crystal 'mush' fabric, but with much finer scale gas filled holes. This morphology seems to represent a secondary hydrate phase forming in a gas rich system after partial dissociation during depressurisation.

### ***'Vesicular' carbon dioxide hydrate***

This form appears in at least two of the samples under investigation (sample 2 and sample 5), and seems to grow into open pore spaces within the sediment (Figure 5.10c). The hydrate grew outwards into the free pore space, curving as it formed, yet seemingly 'blobbier' than in the acicular form. This hydrate morphology appears to result from a

gas rich environment, as both examples appear to have large quantities of trapped gas bubbles within the hydrate, with sample 5 possibly forming during depressurisation.

### ***'Pea-pod' carbon dioxide hydrate***

This morphology appears to be fairly unique and specific to hydrate formation in the CO<sub>2</sub> phase. At higher magnification the true complexity of this form can be appreciated. Each 'pod' seems to contain a number of layered 'peas' consisting of hydrate in the centre, surrounded by a shell of ice, surrounded by another layer of hydrate, and all contained in a 'pod' of ice, with each 'pod' separated by salt fabrics (with a small percentage of ice). At the end of some of these 'pods' are the remnants of some other form of crystalline structure, which are fairly angular and appear to grow from a pre-existing phase or crystal form at the edge of the 'pod'. This less stable form may also have existed between the salt networks present between some of these 'pods' (Figure 5.7). It is possible this morphology represents an early unstable hydrate phase which converts to a more stable phase with time.

### **5.2.3 Impact of hydrate formation on surrounding sediment**

The majority of the samples formed during this experimental investigation consisted of sediment-hosted carbon dioxide hydrate. In addition to the pressure, temperature, salinity, and host molecule, the sediment which the hydrate forms within also plays an important role in the formation of the hydrate. The impact hydrate formation has on the hosting sediment is extremely important in understanding any sediment instabilities which may occur. Natural mineralization often results in some disturbance in the host rock/sediment, and can lead to slope instabilities with consequent potential for landslides (Fletcher & Merino, 2001). Therefore, we need to understand the influence the host sediment has on hydrate formation, as well as the effects hydrate formation has on the host sediment. One key factor in understanding these interactions is where hydrate growth is initiated; for example, within the pore spaces of the sediment, or on the sediment grains; and whether or not hydrate growth pushes sediment grains apart or cements grains together. Although considerable research has been conducted to try to

answer some of these questions, there is a general lack of knowledge of these interactions.

Within this study, a variety of unconsolidated sediments have been used to form carbon dioxide hydrate samples, including clays (bentonite and kaolinite); clean, sorted quartz rich sand of different size fractions; and natural, unwashed sand, sorted into coarse, medium and fine grained fractions collected from Anglesey (OS reference SH 621 789, and/or 4°04' W 53°17.5' N). Unfortunately, due to time restrictions, not all of these samples have been analysed; however, analysis of a number of these samples (see section 5.2.1) has allowed a degree of comparison between sediment-hydrate relationships.

The carbon dioxide hydrate formed in sample 1 initially grew from rapid nucleation in the overlying seawater layer (water rich), forming as acicular needles rapidly advancing into the underlying quartz rich sand. These needles appear to have then formed sheets of hydrate (Figure 5.13a), which grew around the sand grains, enveloping the grains as the hydrate continued to grow. Further nucleation seems to have occurred within the fully water saturated pore spaces, with the carbon dioxide hydrate crystals growing around, and up to, sand grains, meeting one another, and in some cases stopping at a growth front (Figure 5.13b). The transition of a growth front seems to mark where one growth factor, such as CO<sub>2</sub>, water, or salinity, became limiting, and further hydrate formation could not occur.

Figure 5.13b shows hydrate crystals growing up to a layer of seawater (now preserved as ice), which appear to surround a sand grain. A strong growth front can also be seen in Figure 5.13c, following the same horizon along the sub-sample. This front represents a change from hydrate to seawater (preserved as ice), as diffusion of carbon dioxide was prevented from entering lower sand layers due to blocked pore networks. Prior to cryogenic freezing the pore spaces filled with ice would have been filled with free water, and this lower layer would have been un-cemented. Hydrate formation therefore appears to be self-limiting. As the hydrate forms it efficiently fills pore spaces, sealing the hydrate forming system and preventing further access of CO<sub>2</sub> necessary for hydrate

formation. In this case hydrate formation in the upper sediment layers blocked CO<sub>2</sub> diffusion pathways to underlying sediment and water.

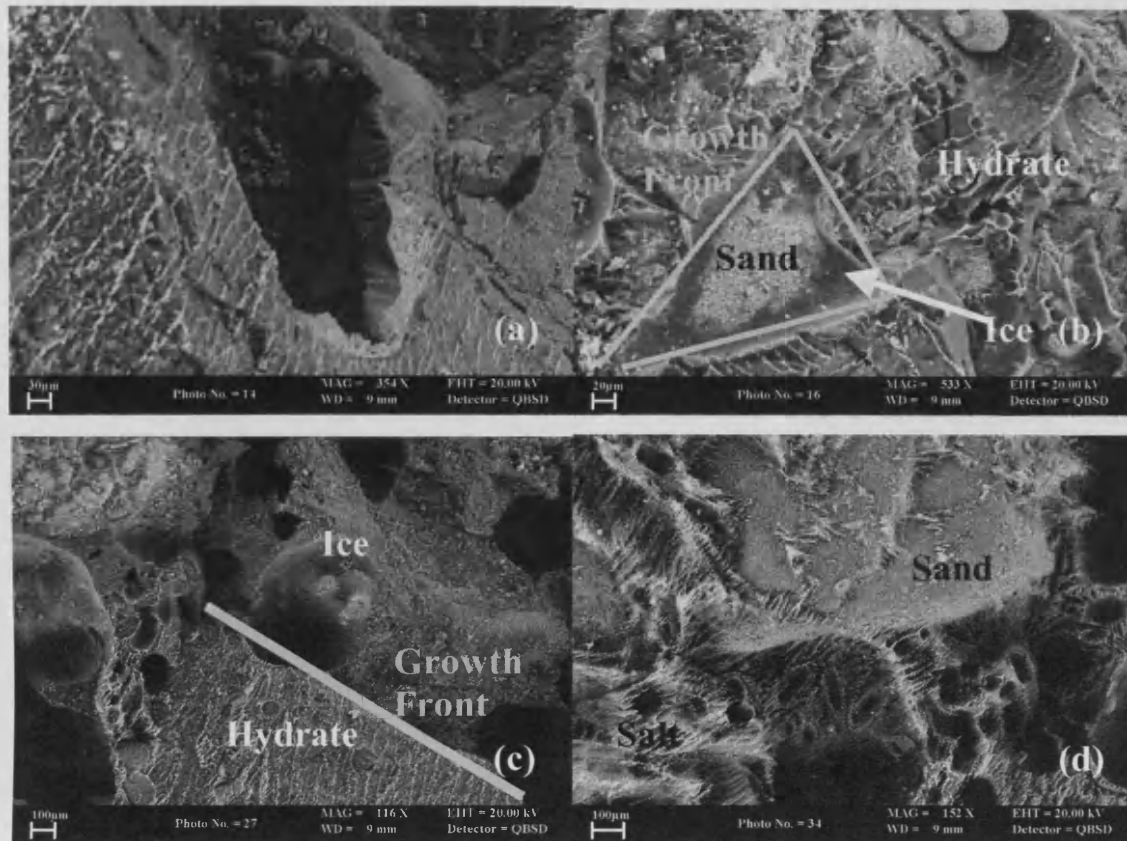


**Figure 5.13(a)** BSEM image of carbon dioxide hydrate needles forming hydrate sheets on contact with underlying quartz rich sand (600 µm-2 mm) (Sample 1). Grey regions represent CO<sub>2</sub> hydrate, bright white regions represent salts and darker grey regions are empty spaces. **(b)** BSEM image of CO<sub>2</sub> hydrate growing up to a sand grain separated by a layer of ice. The transition from hydrate to ice is marked by a strong growth front. **(c)** BSEM image of transition between hydrate and ice (formerly seawater) in the lower sediment layer marked by a growth front and represents the self-limiting nature of hydrate formation. **(d)** BSEM image revealing sand and salt fabrics after full ablation of hydrate and ice, with salt fabrics providing a supportive matrix for the sand grains in this ablated sample. Previously trapped gas bubble shapes are preserved within the salt fabric. Interesting salt ‘ladders’ are shown over the sand grains, possibly resulting from the meeting of hydrate crystals growing from two different directions around the sand grain.

In an initially fully water saturated system hydrate crystals completely fill the pore spaces, and therefore it is difficult to clearly distinguish between them. However, this is not the case in dampened sediment (CO<sub>2</sub> rich). In samples formed from sediment dampened with either seawater (Figure 5.14a, b) or deionised water (Figure 5.14d) the open pore networks allow CO<sub>2</sub> to rapidly access the water meniscus surrounding the grains, and even after initial hydrate formation some pore channels remain open enabling hydrate formation to occur throughout the sample. This water poor, CO<sub>2</sub> rich system, appears to form euhedral hydrate crystals indicating slower growth than in the water rich sediment-hosted system which formed acicular hydrate; although growth was still rapid. The water-limited system creating these well-formed euhedral crystals allowed clearer visualisation of their relationship with the host sediment. Hydrate crystals completely replace the water meniscus forming a cement between the sand grains, holding the sand grains together and strengthening the sediment. Larger crystals can be seen in larger pore spaces reaching 60 microns in diameter, with smaller crystals with less well-defined crystal faces forming the cement. The limiting factor in this system is water availability; hence, in the sample showing hydrate formation in sediment dampened with deionised water the hydrate content appears to be greater as there was a larger volume of water present initially. This greater volume of water allowed increased filling and cementation, but retained well-formed euhedral hydrate crystals.

Figure 5.14c shows Sample 4 ice pseudomorphs after hydrate ablation and ice replacement, retaining the original structure of the hydrate crystal. These pseudomorphs envelope the sand grains forming an intergranular supportive matrix cementing the grains. Separating each crystal and emphasising the crystal structure is an infilling matrix of both clay and salt. The direction of growth and the nature of the crystal texture indicate growth from within the pore spaces, growing towards and around the sand grain.

This sample also shows differences between growth textures in different sediments due to the design of the experiment to investigate hydrate growth along sediment contact points, in this case between clay and sand. The carbon dioxide hydrate appears to have preferentially grown within the sand, where porosity is high, forming pore-filling cement (Figure 5.14e), and in a few areas as discrete lenses (Figure 5.9d). In some

areas along the clay-sand interface, the hydrate had begun to grow into the clay, pushing the grains apart, either forming from the sandy zone (Figure 5.9e), or as discrete crystals or 'pods' within the clay formed from individual nucleation points (Figure 5.14e). After full ablation of hydrate and ice the different textures present within the sample became clearer. Distinguishable honeycomb salt/clay fabrics were seen in the sandy horizon with denser salt/clay structures beneath in the clay horizon, indicating a smaller percentage of hydrate present, and a different growth mechanism (Figure 5.14f). The quantity of hydrate seems to decrease into the clay away from the sand horizon, with hydrate restricted to the outermost 0.5mm clay adjacent to the sand interface. It is important to note hydrate formation within clay appears to be very difficult as this was the only clay sample seen to contain carbon dioxide hydrate, achieved by formation along a sand/clay interface (see Appendix B for experimental details).

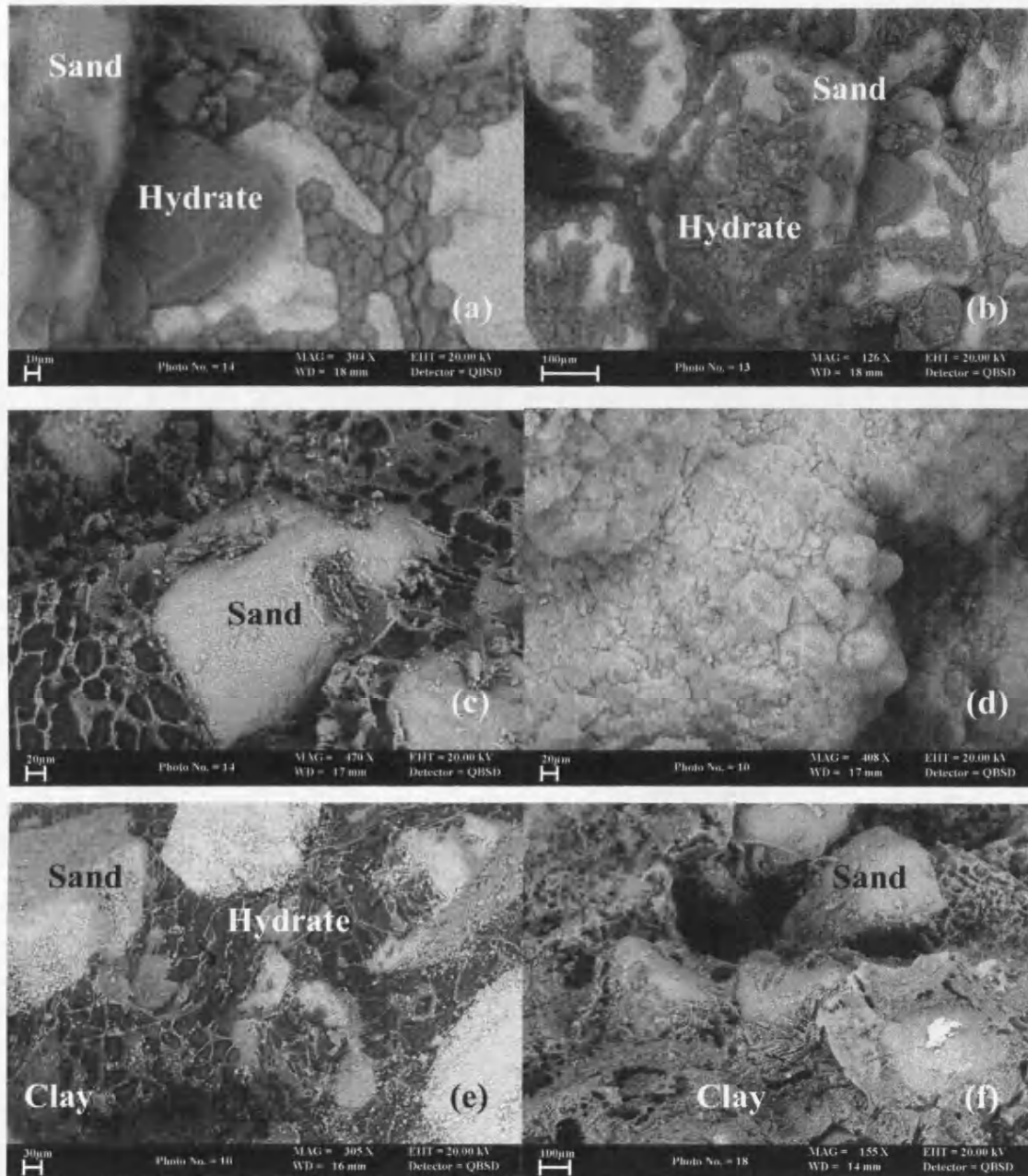


**Figure 5.14(a)** BSEM image of sample 3 euohedral crystalline pore-filling CO<sub>2</sub> hydrate cementing quartz rich sand grains (355-600 μm) formed within a CO<sub>2</sub> rich system. **(b)** Lower magnification BSEM image of (a). **(c)** BSEM image of sample 4 after partial ablation showing pore-filling ice pseudomorphs with pronounced intergranular honeycomb salt and clay fabrics, formed in a water rich system. **(d)** BSEM image of sample 6 euohedral, crystalline deionised water, CO<sub>2</sub> hydrate cementing quartz rich sand grains (600 μm-2 mm) formed in CO<sub>2</sub> rich system. **(e)** BSEM image of sample 4 hydrate formed as pore-filling cement within the sand horizon, as acicular crystals growing from the sand into the clay horizon, and discrete crystals formed from individual nucleation points within the clay. **(f)** BSEM image of the sand-clay interface after full ablation to 0 °C showing the nature of clay and salt fabrics within the sample.

## **5.3 Discussion**

### **5.3.1 CO<sub>2</sub> hydrate morphologies and salt fabrics**

The samples investigated have revealed different hydrate morphologies and different associated salt fabrics, seemingly as a consequence of different formation mechanisms (Table 1). Acicular CO<sub>2</sub> hydrate needles formed in a water saturated environment, growing above and into unconsolidated water saturated sand. The formation of needle-like shapes in minerals is well known to be a possible consequence of super-saturation and very rapid formation (Spry, 1969). Each needle would have formed from a single nucleation point and as each crystal grew, pure water would have been consumed from the surrounding solution, leaving the remaining solution between growing crystals more concentrated in solutes (Figure 5.15). Solute concentrations would have increased until the point of salt saturation, at this point salts would be precipitated out of solution. Due to the rapid formation of these hydrate crystals the hydrate continued to grow at salt saturation, therefore, not only were salt crystals precipitated between growing crystals, some were included within the hydrate crystal structure.

<b>Form and Occurrence of Hydrate</b>	<b>Form and Occurrence of Salt</b>	<b>Hydrate Formation Mechanism</b>
Acicular - needles formed within seawater solution above and growing into unconsolidated quartz rich sand fully saturated with artificial seawater.	Delicate salt sheets composed of dendritic salt crystals between the hydrate and included within it.	Very rapid hydrate formation and salt precipitation between advancing needles, and included within, as salt saturation reached. Water rich.
Euhedral – crystals formed within artificial seawater. No sand.	Strings of salt crystals and individual cubic salt crystals included within euhedral hydrate crystals.	Slightly slower hydrate formation – euhedral crystals with salt inclusions. Water rich.
Euhedral – crystals formed within unconsolidated quartz rich sand dampened with artificial seawater.	Very fine sheets of salt between hydrate grains and as needles within euhedral crystals of hydrate.	Slower hydrate formation – distinct euhedral crystals. CO <sub>2</sub> rich.
Euhedral – crystals formed within unconsolidated quartz rich sand dampened with deionised water.	None	Slower hydrate formation – well formed euhedral crystals. CO <sub>2</sub> rich.
Euhedral – crystals formed within unconsolidated quartz rich sand fully saturated with artificial seawater.	Honeycomb salt fabrics forming an intergranular pore-filling matrix.	Slow hydrate formation – euhedral hydrate crystals with excluded salt filling intergranular porosity. Water rich

**Table 5.1.** The range of carbon dioxide hydrate and salt fabrics seen during BSEM and EDXA analysis of laboratory formed samples. Explanations for these resulting fabrics are proposed to be different formation rates as a result of formation conditions.

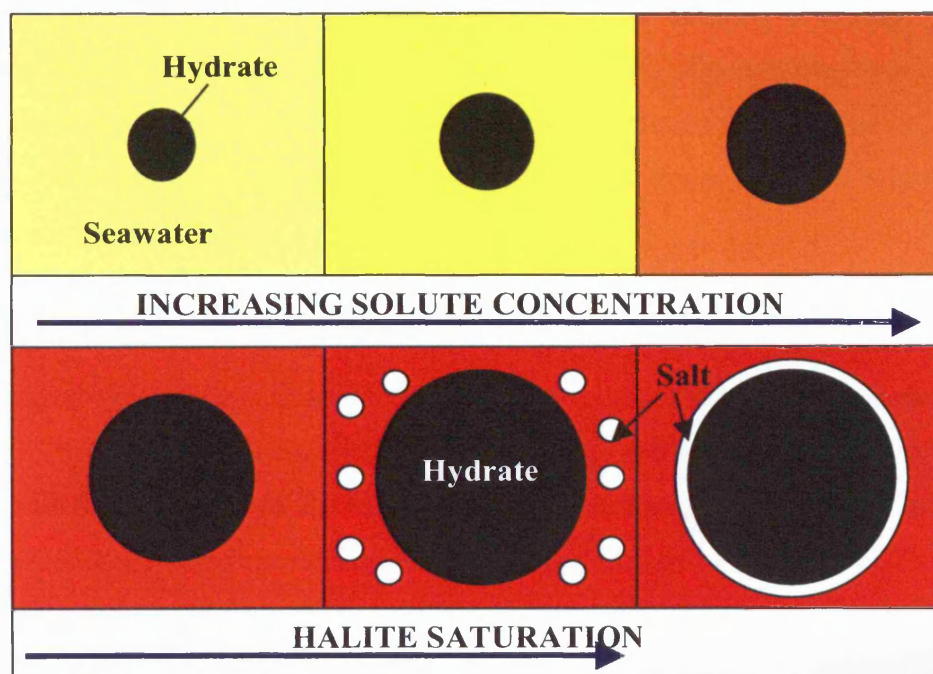


**Figure 5.15.** Diagram to show simplified version of the proposed hydrate growth model for the formation of imaged salt fabrics. Each acicular hydrate crystal starts as a single nucleation point and, as the hydrate grows, it consumes water excluding solutes, leaving the surrounding seawater more concentrated in solutes. Solute concentration increases until salt saturation is reached, at which point halite is precipitated. Hydrate continues to grow trapping the precipitated halite between hydrate crystals, and in some cases including halite within the hydrate crystal structure.

Slower formation allowed the hydrate to form well-defined euhedral crystals; in both water saturated, and CO<sub>2</sub> saturated, conditions. However, although slower formation allowed the growth of well-formed crystals, formation was still too rapid for diffusion processes to remove excess salinity between growing crystals, which would normally occur within the natural environment.

Within unconsolidated quartz-rich sand dampened with seawater, salt has been precipitated along crystal boundaries with a little included within the individual crystals. However, hydrate formation within a seawater solution led to the inclusion of strings of salt crystals and individual cubic salt crystals within the hydrate crystals, with very little along crystal boundaries. The inclusion of salt crystals indicates faster

formation than in the dampened sand samples where the majority of the salt appears to be concentrated along crystal boundaries. The exclusion of salt during hydrate formation is also highlighted in sample 1, as sample ablation revealed the majority of the salt within the sample appeared to be present in the frozen seawater below the hydrate zone.

The rapid rate of hydrate growth proposed for sample 1 and sample 7, formed in a water rich system, which differs from the apparent slow rate of formation in sample 4, also formed in a water rich system. This difference could perhaps be related to the effect of sediment interaction on hydrate formation, as sample 1 and 7 were formed in artificial seawater; and/or related to water access to CO<sub>2</sub> and efficient diffusion of CO<sub>2</sub>.

### **5.3.2 Salt inclusion during other mineralization processes**

#### ***5.3.2.1 High-temperature salt inclusion***

The precipitation, and/or inclusion of salts during crystallization are not uncommon natural processes. Solid halite inclusions have been identified in several major minerals crystallized during metamorphism, including within quartz, calcite and tremolite crystals (Trommsdorff et al., 1985). These inclusions have appeared as idiomorphic crystals and dendrites reaching up to 80 µm in size when observed under the petrographic microscope and SEM (Trommsdorff et al., 1985), considerably larger than the salt inclusions seen within samples presented in this thesis. The halite inclusions seen in these metamorphic minerals are thought to be early high temperature precipitates (forming at approximately 500 °C and >2000 bars derived from chloride compositions), forming independently of CO<sub>2</sub>-rich saline water fluid inclusions (Trommsdorff et al., 1985).

The existence of halite crystals enclosed within other minerals provides the best evidence for the existence of fluids saturated with salts prior to inclusion (Roedder, 1984; Trommsdorff et al., 1985). Many geological processes could lead to the development of super-saturated fluids, such as changes in pressure and temperature, or

escape of volatile components. Mineral reactions during prograde or retrograde metamorphism may also lead to the concentration of salts in fluids, including metamorphic reactions which consume water (Trommsdorff et al., 1985). Although the formation of hydrate is not considered as a metamorphic reaction, the crystallization of clathrate-hydrates consumes water, concentrating salts in the residual aqueous fluid, leading to super-saturation in this study. However, hydrate crystallization in this study has caused the formation of precipitates at low temperatures, rather than at the high temperatures seen in metamorphic minerals.

### ***5.3.2.2 Formation of sea ice***

The exclusion of salts during hydrate formation is similar to that observed during the formation of sea ice. Solutes present in seawater cannot enter the crystal structure of sea ice. However, although salts are excluded, young sea ice may still have a salinity of approximately 10 parts per thousand, reducing to approximately 1-3 in old sea ice (Wadhams, 2005). This salinity is due to the presence of trapped brine accumulated between parallel rows of dendritic ice crystals (Medjani, 1996; Wadhams, 2005). As the ice crystals continue to grow these brine pockets become very highly concentrated in salts, lowering the freezing point of ice and limiting further growth of ice crystals into the remaining brine. As the ice ‘ages’, these brine pockets eventually form a network of brine channels, which join together, allowing most of the brine to drain out into underlying water (Golden et al., 2005; Wadhams, 2005). The remaining sea ice is a porous composite of pure ice with brine and air inclusions (Golden et al., 2005).

### **5.3.3 Hydrate formation within sediment**

In addition to different hydrate morphologies and salt fabrics present within investigated samples, the influence of the formed CO<sub>2</sub> hydrate on the hosting sediment properties also differs. Within CO<sub>2</sub> rich environments, or dampened sediment with open pore networks, the hydrate always appears to form around the sand grains, replacing the water and cementing the grains together (Figure 5.16). Within water rich environments the sediment/hydrate interaction appears to be more complicated (Figure

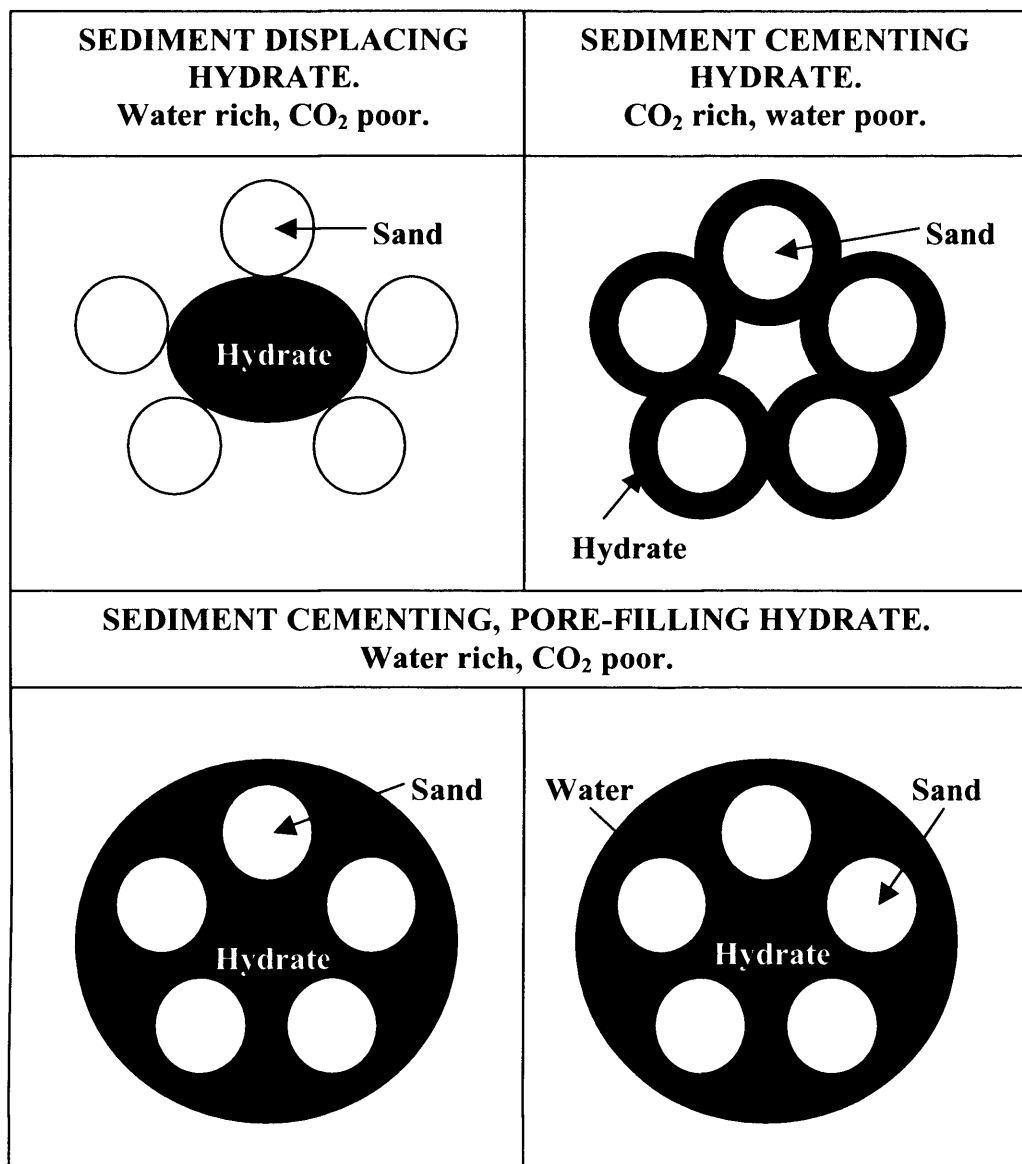


**Figure 5.16.** Proposed sediment-hosted hydrate pore growth models for CO<sub>2</sub> hydrate formed during the experimental investigations of this study.

5.16). In this situation hydrate is mainly seen to form as pore-filling cement, completely filling pore spaces sealing the system from further CO<sub>2</sub> access (see section 5.2.3). This pore-filling cementing hydrate appears as two forms, both of which are seen within sediment of a higher porosity: one growing from the pore spaces to the sand grains separated by a water layer around the sand grain, and one which contacts the sand grains (it is unclear as to where nucleation begins). The water film between the hydrate and the sand grain has been noted in previous in-situ and laboratory pore-scale investigations (Techmer et al., 2005; Kvamme et al., 2007). These have been

considered as possible distribution channels for the transport of gas or liquid formation components (Kvamme et al., 2007). However, images presented in this study show water films to be surrounded by hydrate, therefore their transport properties would be greatly reduced; although further investigation is required to fully determine the nature of these water layers. If these water layers were proven to be interconnected distribution pathways, they would need to be considered in physical property monitoring of potential CO<sub>2</sub> hydrate storage systems. Interestingly, research suggests these water layers are absent from clay sediment systems and clay minerals may actually stick directly to the hydrate (Odriozola et al., 2004; Titiloye & Skipper, 2005; Kvamme et al., 2007).

The water rich experimental environment has also produced another sediment-hosted hydrate growth form: sediment displacing hydrate. This hydrate appears to have formed from individual nucleation points within the sediment, pushing the sediment grains apart. Although there is some evidence of this hydrate formation mechanism within sandy sediment, this was mainly restricted to finer-grained clay sediment. Further investigation is required to quantify sediment displacement and determine any mechanical effect this growth mechanism has on the sediment and the subsequent effect of hydrate dissociation leaving a sediment framework in an unstable configuration. Hydrate formation within fine-grained clay sediments has proven difficult, with success in only one sample. Previous research has noted hydrate formation inhibition within fine-grained sediment (Clennell et al., 2000; Anderson et al., 2007), and our experiments certainly seem to support this conclusion.

### **5.3.4 Significance of experimental results**

#### ***5.3.4.1 Storage of CO<sub>2</sub>***

Precipitation of dissolved salts can occur in and near the well during the operation of natural gas storage aquifers and reservoirs if saline groundwater is present (Lorenz & Muller, 2003). This can reduce the performance of the well bore and cause considerable problems, and is usually solved by the injection of water down the well (Lorenz & Muller, 2003). The storage of CO<sub>2</sub> within aquifers and reservoirs would be

subject to similar problems, as injection procedures would rely upon the implementation of similar infrastructure. Storage conditions are likely to lie part way between those used for short-term laboratory studies, and those involved in natural long-term methane hydrate formation, therefore precipitation of salts may occur in some parts of the storage system. Should CO<sub>2</sub> storage as a liquid and hydrate be actively considered, it would be necessary to take into consideration the precipitation and inclusion of salt during rapid formation for further conceptual development. Hydrate formation in this type of artificial environment may be very rapid, and could lead to a brine rich system; therefore minerals associated with an evaporite basin may be present, such as gypsum, halite, and anhydrite. Mineral precipitation may also impede CO<sub>2</sub> fluid flow in the system, possibly resulting in the migration of CO<sub>2</sub> fluid in different directions, and should be considered in storage system models. In addition, the inclusion of salt during formation may influence the stability of the hydrate, possibly reducing the hydrate stability zone, therefore reducing the volume of predicted suitable storage sites.

Although salt inclusion may have an influence on stability, the precipitation of salt between hydrate crystals actually reduces permeability, filling interstitial pore spaces, effectively improving the potential sealing capacity of the CO<sub>2</sub> hydrate layer above the liquid CO<sub>2</sub> store.

This study has also shown pore-filling cementing sediment-hosted hydrate formed within water rich environments, blocking CO<sub>2</sub> transport, sealing the system and impeding further hydrate growth. The formation of hydrate in upper sediment layers prevented hydrate formation below, leaving the remaining sediment un-cemented. This supports previous research on CO<sub>2</sub> hydrate as an effective trapping mechanism (Kiode et al., 1997; Someya et al., 2006), although the evidence for this sealing capacity in this study is only qualitative and further quantitative investigations would add to results.

The proposed cool carbon dioxide storage method would consist of an underground store of liquid CO<sub>2</sub>, contained below a natural (clay) cap-rock with further sealing provided by a cap of overlying sediment-hosted CO<sub>2</sub> hydrate (see Chapter 2 for further details). Within this investigation CO<sub>2</sub> hydrate has been seen to have grown into clay sediment, from a higher porosity sand layer (sample 4). The hydrate appeared to have

displaced the clay sediment as it formed, which could have an effect on a clay cap-rock within a storage system. However, hydrate only seems to form within the first <5mm of the clay, and formation within fine-grained clay sediment appeared to have been relatively difficult (sample 4 is the only example, showing hydrate within clay) therefore this suggests any effects of hydrate formation in the cap-rock would be minimal.

#### **5.3.4.2 Desalination**

There are many desalination systems being researched to provide fresh drinking water from natural seawater. One such system involves the formation of CO<sub>2</sub> hydrate, believed to exclude salts during formation, and known to form relatively rapidly under relatively low pressure temperature conditions, reducing costs. However, in static CO<sub>2</sub> hydrate systems the desalination efficiency may be limited if salt is included within its structure, as shown within this study. Although there appears to be no reported high magnification imaging of hydrate produced during desalination to identify salt precipitation and inclusion, it has been noted that salt does appear to be trapped within the hydrate formed in static desalination systems (Tatro, 2006). During research at Marine Desalination Systems it was discovered on melting the formed CO<sub>2</sub> hydrate, what should have been pure melt-water was actually salty; with decreasing salinity as melting progressed towards the centre of the hydrate mass (Tatro, 2006). The images obtained during this study may aid the understanding of salt trapping during hydrate formation and influence the precise methodology adapted if using hydrate as a desalination agent.

#### **5.3.4.3 Natural hydrate**

Solute exclusion into surrounding pore waters during hydrate formation has been well documented, in both natural hydrates and artificially created laboratory hydrates (Torres et al., 2004; Teichert et al., 2005). However, in the natural environment, over time, diffusion and advection processes are generally believed to remove these excluded brines away from the localised point of hydrate formation. An exception to this rule is natural hydrate formation at Hydrate Ridge, Cascadia Margin, where there has been evidence of trapped brines from expedition data within the hydrate-forming zone

(Torres et al., 2004; Milkov et al., 2005). Salinity/Chlorinity determination from recovered sediment/hydrate cores is difficult as hydrate dissociation on warming samples results in the release of pure water trapped within the hydrate structure, causing the freshening of pore waters. Using geochemical mass-balance calculations, the pressure of initial gas release from a core retrieved during Cascadia Margin ODP Leg 204, and chlorinity measurements from the inner and outer barrel of the ODP Pressure Core Sampler (PCS), an in-situ salinity approaching or exceeding 105 g/kg has been estimated (Milkov et al., 2005). This would indicate an in-situ brine of 3x standard seawater salinity (35 g/kg). The observed increase in chlorinity at Hydrate Ridge, particularly in near surface sediments, has been explained by rapid gas hydrate crystallization (Torres et al., 2004; Milkov et al., 2004). Cascadia Margin represents an area of numerous active cold vent sites, with significant quantities of gas and fluids moving upwards through fault related conduits into the water column above (Riedel et al., 2006). Such geological processes cause intermittent rapid transport of gas and fluids into the hydrate-forming zone (Riedel et al., 2006), and with little overburden in near surface sediments this allows for rapid crystallisation of gas hydrates. See chapter 6 for further information on Cascadia Margin hydrates.

Within the well-controlled experiments of this study very rapid CO<sub>2</sub> hydrate formation can be clearly demonstrated. This very rapid formation caused interstitial pore water solutions to reach salt saturation. Therefore, rather than trapped brine pockets present within the hydrate, as in Cascadia Margin natural core samples, interstitial precipitated salt fabrics and salt inclusions were present. Under the experimental pressures and temperatures used to create these hydrate samples, salt saturation would occur when solute concentration reached approximately 26%w/w (as calculated from EQ3/6 based on a NaCl system). The seawater solution used in each experiment had a solute concentration of 3.5%w/w. If half of the water, surrounding growing hydrate crystals, was consumed (50%), the solute concentration would double to 7%w/w. With continuing hydrate growth, ~85.7% of water would need to be consumed to reach halite saturation of 26%w/w  $((87.5-75/14)*12)$ . However, this need not be the bulk water present, but the localised water present between surrounding growing hydrate crystals.

Assuming a halite saturation of 26%w/w it is possible to estimate whether it would be possible to form pure methane hydrate in the natural environment at salt saturation.

Using the thermodynamic computer program CSMHYD.EXE (Sloan, 1998) methane P-T stability conditions have been predicted for formation of gas hydrate in solutions of varying salinities (NaCl system) (Figure 5.17). A significant decrease in hydrate stability can be seen to occur with increasing salinity. However, at salinities of salt saturation (26%w/w) methane hydrate does still appear to be stable within P-T conditions seen in deep ocean sediments. Between c. 2000 m and 4000 m water depth, and temperatures between 0 °C to 4 °C methane hydrate could be stable with NaCl-saturated brine, therefore natural rapid hydrate formation may be possible at salt saturation, and so it seems plausible that similar salt structures forming as a consequence of rapid hydrate crystallization could occur naturally.

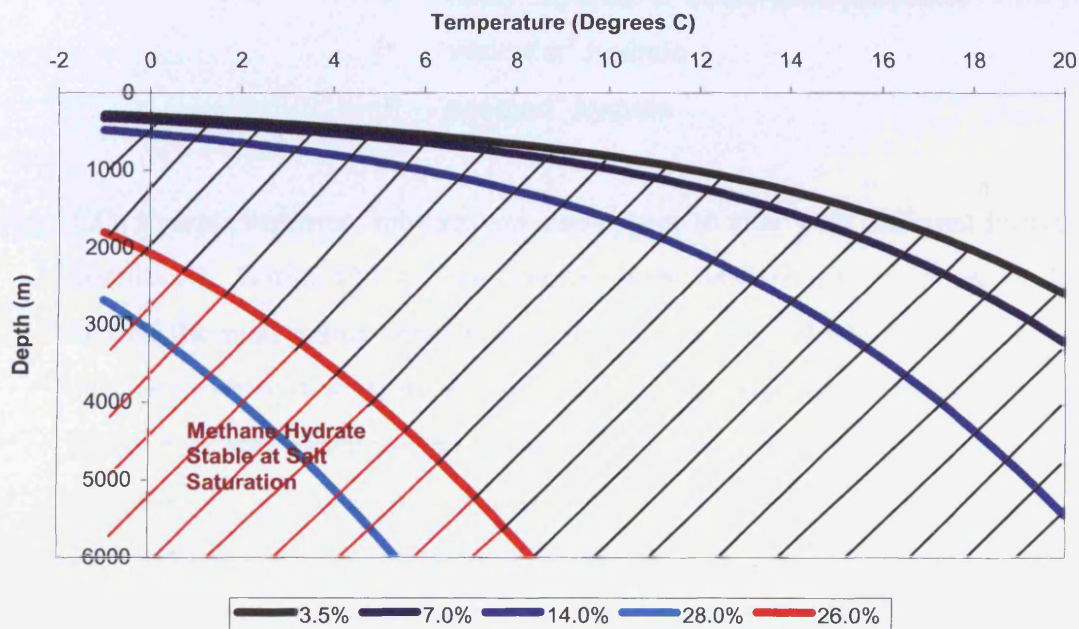


**Figure 5.17.** Pressure (depth) - Temperature pure methane hydrate stability plot derived from CSMHYD.exe (Sloan, 1998) for varying halite concentrations, highlighting the pressure temperature region where methane hydrate could be stable at halite saturation.

#### 5.4 Conclusions

- Carbon dioxide hydrate samples have been formed in a variety of sediments and water solutions, within a well-controlled laboratory environment and subsequently analysed by cryogenic-BSEM and EDXA.

- To help to distinguish between hydrate and ices, a number of control experiments have also been imaged revealing the presence of different morphologies of ice and hydro-halite.
- Experimental samples have shown different hydrate morphologies resulting from different formation conditions, with the primary supply of components altering the rate of formation. These morphologies include:
  - euhedral crystalline hydrate
  - acicular hydrate
  - ‘melt-structure’ or granoblastic hydrate
  - ‘holey’ hydrate or micro-porous hydrate
  - ‘vesicular’ hydrate
  - ‘pea-pod’ hydrate
- CO<sub>2</sub> hydrate/sediment interactions also appear to alter with different formation conditions. Within CO<sub>2</sub> rich environments the hydrate always appears to form around the sand grains cementing the grains together. Within water rich environments hydrate is mainly seen to form as pore-filling cement, completely filling pore spaces sealing the system from further CO<sub>2</sub> access, but is also seen as sediment displacing hydrate, pushing the sediment grains apart during formation though this form was mainly restricted to clay sediment.
- In addition to different hydrate morphologies and hydrate/sediment interactions these investigations have also revealed interesting salt (halite) fabrics differing with hydrate formation mechanisms, which to my knowledge have never before been recorded in previous research.
- Hydrate samples seem to show halite deposited along crystal boundaries and as solid inclusions within the hydrate crystals, with different salt fabrics and hydrate morphologies associated with different growth rates and conditions.

- Salt inclusion seems to have occurred as a consequence of very rapid hydrate formation, concentrating the surrounding solution until halite saturation was reached, and leading to salt precipitation.
- Salt inclusion during rapid hydrate formation may have important implications for carbon storage as a liquid and hydrate, static desalination systems and natural hydrate research.
- Further investigation of pore-scale formation processes and an increased number of samples formed under various known pressure and temperature conditions, within a variety of known sediments, and a range of water solutions, would greatly improve these results, with the aim of fully understanding the processes involved in the formation of different hydrate morphologies, salt fabrics, and the causes of different sediment/hydrate interactions.

## **CHAPTER 6**

### **Laboratory Investigation of Natural Methane Hydrate**

## **6. Laboratory investigation of natural methane hydrate**

### **6.1 Introduction**

Although the majority of this thesis is aimed at the study of carbon dioxide hydrates, to scope the suitability of CO<sub>2</sub> storage as a hydrate it is important to understand the formation of sediment-hosted CO<sub>2</sub> hydrates (see Chapter 5). Hydrate formation conditions and formation rates within the proposed storage system are likely to lie somewhere between the artificial laboratory conditions and those seen in the natural environment. It is difficult to reproduce an exact representation of the natural environment in the laboratory; therefore natural in-situ hydrates can provide pivotal information. Unfortunately, there are very few natural CO<sub>2</sub> hydrates on Earth, with the only known example in the Okinawa Trough, offshore Japan (Sakai et al., 1990); therefore natural methane hydrates provide a suitable alternative, although processes may be a little different. An excellent opportunity to study natural hydrates arose during this study and these results are presented in this chapter.

Natural sediment-hosted methane hydrate accumulations show different forms (see Chapter 2), ranging from layers and lenses, to veins and disseminated (Holditch et al., 2006), varying with the primary supply of components, and explained by the requirement of the hydrate system to minimize mechanical and surface energy (Clennell et al., 2000). Natural hydrates are known to form preferentially in sediments with higher porosity, larger pore-sizes, and high permeability, but have been found in sands, muds and clays (Makagon, 1981; Kvenvolden, 1993).

Though research into natural methane hydrates is extensive their formation within sediments remains poorly understood, and there is considerable debate on formation processes, such as whether hydrate forms within pores, or around sediment grains. CO<sub>2</sub> hydrate research within this study has certainly shown evidence for growth within pore-spaces, as well as around sediment grains (see Chapter 5). The SEM has been proven to be useful for non-invasive imaging of natural methane hydrate samples (Stern et al., 2004; Stern et al., 2005). This study of natural hydrates uses cryogenic-BSEM techniques previously used in CO<sub>2</sub> hydrate studies (which has been seen to be a

valuable investigatory tool for pore-scale analysis; Chapter 5) to investigate natural methane hydrate samples obtained from Cascadia Margin, offshore Oregon.

During the course of this PhD research Dr Peter Jackson of the BGS (British Geological Survey) was a participant on IODP Expedition Leg 311, which had a scientific goal of understanding the hydrate formation and fluid flow processes at Hydrate Ridge, Cascadia Margin, offshore Oregon. As a consequence of Dr Peter Jackson's participation the BGS successfully acquired two samples from the Expedition. After core retrieval the two core samples were cryogenically frozen on board ship and cryogenically dry-shipped from the US to the UK for further study.

This chapter introduces the oceanographic and geological setting for the Cascadia Margin, providing specific site location details for the two natural methane hydrate cores under investigation, and presents the findings from investigation of the two cores: U1327C and U1328B (conducted jointly with the BGS). The initial observations and sub-sampling of the hydrate cores were made by Dr Christopher Rochelle and Mr Anthony Milodowski from the BGS. Further sub-sampling and analysis were conducted jointly between me and the BGS.

## **6.2 Cascadia margin**

### **6.2.1 Oceanographic Setting**

The Cascadia Basin lies in the Northeast Basin of the North Pacific Ocean, off the continental slope of the mid-North Pacific US coastline, extending westward from the base of the Cascadia accretionary prism, offshore Oregon, to the edge of sediment onlap onto juvenile basement of the Juan de Fuca Ridge, reaching an approximate total surface area of 170,000 km<sup>2</sup> (IODP, 2006). The Strait of Juan de Fuca connects inland waters of western Washington and British Columbia to the Pacific Ocean, and the Strait of Georgia merges into the eastern end of the Strait of Juan de Fuca between Vancouver Island and mainland British Columbia. The maximum water depth in the Basin is 2930 m, and it widens and slopes to the south with a seafloor gradient of 1:1000.

The Cascadia Basin is affected by several currents, which influence regional patterns of sediment dispersal. In surface waters the North Pacific Current approaches North America from the central Pacific and splits into the north-flowing Alaskan Current and the south-directed California Current (IODP, 2006; Tomczak & Godfrey, 1994). During winter the Davidson Current also flows northward over the Oregon/Washington margin, and merges with the eastern edge of the Alaska gyre. The bottom water circulation within the region is still fairly poorly understood (IODP, 2006), but is known to be sluggish. Water masses in the area include Subarctic upper water, Arctic Intermediate water, and Eastern North Pacific Central Water (Tchernia, 1980; Open University, 1995; Tomczak & Godfrey, 1994), which fills the water column to the ocean floor.

### **6.2.2 Geological Setting**

Hydrate ridge is a 25 km long, 15 km wide accretionary ridge on the Cascadia Margin, approximately 100 km west of the Oregon coast (Milkov et al., 2004). This accretionary prism is part of the Cascadia subduction zone. The Juan de Fuca plate converges nearly orthogonally to the North American Plate at a rate of approximately 45 mm/year (IODP, 2006; Riddihough, 1984). To the seaward side of the deformation front the Cascadia basin consists of pre-Pleistocene hemi-pelagic sediments overlain by a rapidly deposited Pleistocene turbidite for a total sediment thickness of about 2500 m (IODP, 2006; Riedel et al, 2006). Most incoming sediment is scraped off the oceanic crust and folded and thrust upward to form elongated anticlinal ridges, with elevations as high as 700 m above the adjacent basin (IODP, 2006; Riedel et al, 2006). The thrust faults near the deformation front almost completely penetrate the entire sediment section (Davis and Hyndman, 1989; IODP, 2006). Active cold vent sites dominate hydrate ridge, with these vents associated with fault-related conduits for focussed fluid and/or gas migration (Riedel et al., 2006). Gas vents, authogenic carbonate build-ups, gas hydrate outcrops, and chemosynthetic communities on the seafloor attest to an area of gas-charged sediment where fluids and gases migrate in the subsurface (Milkov et al., 2004).

### 6.2.3 Specific site location details

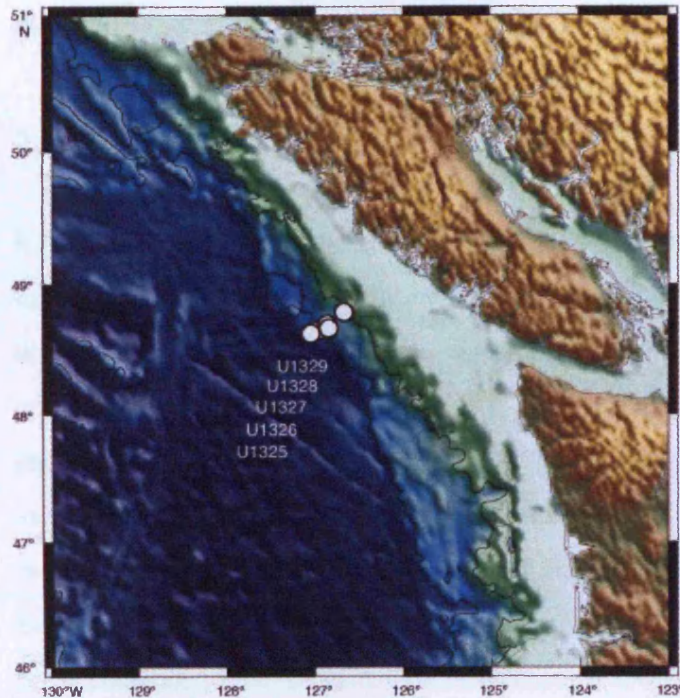


**Figure 6.1.** Map showing the locations of Expedition 311 Cascadia Margin hydrate investigation sites offshore Oregon. Taken from IODP, 2006.

#### 6.2.3.1 Site U1327

IODP site U1327 is located near ODP Leg 146 889/890 at  $48^{\circ}41.8889'N$ ,  $126^{\circ}51.9142'W$  (Figure 6.1; Westbrook, Caarson, Musgrave et al., 1994; IODP, 2006), at the mid-slope of the accretionary prism over a clearly defined BSR estimated at 223 mbsf (mbsf is meters below sea floor) (Riedel et al, 2006), in water depth of 1304.5 m. The site is characterized by  $\sim 90$  m thickness of slope-basin sediments underlain by a thick section of accreted sediments. In a 300 m thick recovered sediment section, mouse-like sediment textures related to the presence and dissociation of gas hydrate were detected to a maximum depth of 161.85 mbsf (Riedel et al, 2006). From 128 mbsf to the depth of the BSR the chlorinity and salinity profiles indicate freshening as a result of hydrate dissociation during the core recovery process (Riedel et al, 2006). Chlorinity values as low as 70 mM (salinity  $\sim 37$  ppm) correlated to individual sandy turbidite layers, and such values are predicted to be the equivalent of  $\sim 80\%$  gas hydrate concentration within pore spaces (Riedel et al, 2006).

The predominant hydrocarbon gas found in the cores from this site was methane, although there was an increase in ethane concentrations from the stratigraphic section overlying the predicted depth of the BSR (Riedel et al, 2006).

#### **6.2.3.2 Site UI328**

IODP site 1328 is located within a seafloor cold vent field, consisting of at least four vents associated with near-surface faults, at 48°40.0479'N, 126°51.0564'W (Figure 6.1), water depth 1267.8 m. The cold vents are characterized by seismic blank zones, between 80 m and several 100 m wide, and show an east-west trend identified by 3D seismic imaging (Riedel et al., 2002). The most prominent vent in the field, referred to as the Bullseye vent, was the target of this site, and has been the subject of intensive research (Riedel et al, 2006). The site is different from all the other sites visited during Leg 311 expedition, as it represents an area of active, focussed fluid flow. Five holes were cored at 1328. Hole A was dedicated to LWD/MWD (Logging While Drilling/Measuring While Drilling) measurements, Hole E was used to carry out a VSP (Vertical Seismic Profiling). A 300 m thick sequence of Quaternary (0 to <1.6Ma) slope and slope basin sediments was recovered at B, C, and D, and divided into 3 lithostratigraphic units (Riedel et al, 2006).

Massive gas hydrate was recovered from near the seafloor, and evidence for hydrate was found in the recovered cores. The chlorinity profile for this site shows four distinct zones. In the upper ~40 mbsf, a significant increase in chlorinity is seen, with maximum values exceeding 850 mM (Riedel et al, 2006). This increase has been interpreted to imply salt exclusion during in situ gas hydrate formation, which has not been removed by advective or diffusive processes (Riedel et al, 2006). The second zone (~40 mbsf - ~150 mbsf) show linearly decreasing chlorinity values (ranging from 538 to 570 mM). The third zone (~150 - 250 mbsf) shows fresher values (as low as 348 mM) suggesting gas hydrate presence and dissociation immediately prior to analysis. In the deepest zone, below 250 mbsf, the chlorinity values remain relatively constant at 493 mM ( $\pm 3$  mM) (Riedel et al, 2006).

The predominant hydrocarbon gas found in the cores from this site was methane, although concentrations of ethane, propane, and isobutene were also found, increasing in cores cross-cutting the predicted depth of the BSR (Riedel et al, 2006).

### **6.3 Initial observations of hydrate cores**

The deeply frozen hydrate cores were cut part way along their full length using a circular saw with a reciprocating action, and then split in half using a hammer and chisel. Images of the two cores and initial visual observations are provided in the following sub-sections.

#### **U1328B**

This core, from a hydraulic piston corer, was 16.5 cm in length and cutting revealed hydrate masses lying below the surface layers of frozen sediment. Spherical voids were also present along the edges of the core, presumed to be in situ gas bubbles, or degassing sites on sample recovery. Splitting the core lengthways identified the sediment and hydrate distribution (Figure 6.2). The outer 1 cm of each half showed signs of disruption from initial coring and subsequent core cutting. The top 3 cm consisted of green/grey silt, within which very little hydrate was identified. The remaining length of the core consisted of an organic/sulphur rich black mud. Between 3 and 8.5 cm lay a hydrate rich zone, containing brecciated hydrate and hydrate pods up to 2.5 cm wide. Thinner brecciated hydrate layers were present below this hydrate rich zone, with the exception of a few larger hydrate pods present at approximately 13 cm (c.1.5 cm thick).

Sub-samples taken along the core were representative of each different hydrate zone, 5 from the hydrate rich zone, 3 from the central brecciated sheet zone, and 1 from the larger pods present in the bottom layer (Figure 6.2).

## U1327C

This core came from a rotary sampler approximately 162-171 m below the seafloor at site 1327. The core was 18.5 cm in length and when cut there was no easily identifiable hydrate present. There was some evidence of disruption along the edges of the core, up to approximately 2 cm of the total diameter. The top of the core (<4.8 cm) consisted of contorted silty/sandy clay laminae fining upwards. Lying below this zone (>4.8 cm<6.5 cm) was more uniform muddy green sandy sediment with a coarse sand base consisting of dark laminations between 1 and 2 millimetres thick (Figure 6.3). Directly below this coarse base consisted of massive fine olive clay. Sub-samples were taken from each of these horizons, with a total of three.

On warming small chips of this core, very few bubbles were seen, suggesting there was a possibility of no hydrate being present in the core at the time of observation, which has been confirmed by subsequent SEM imaging (see section 6.4)

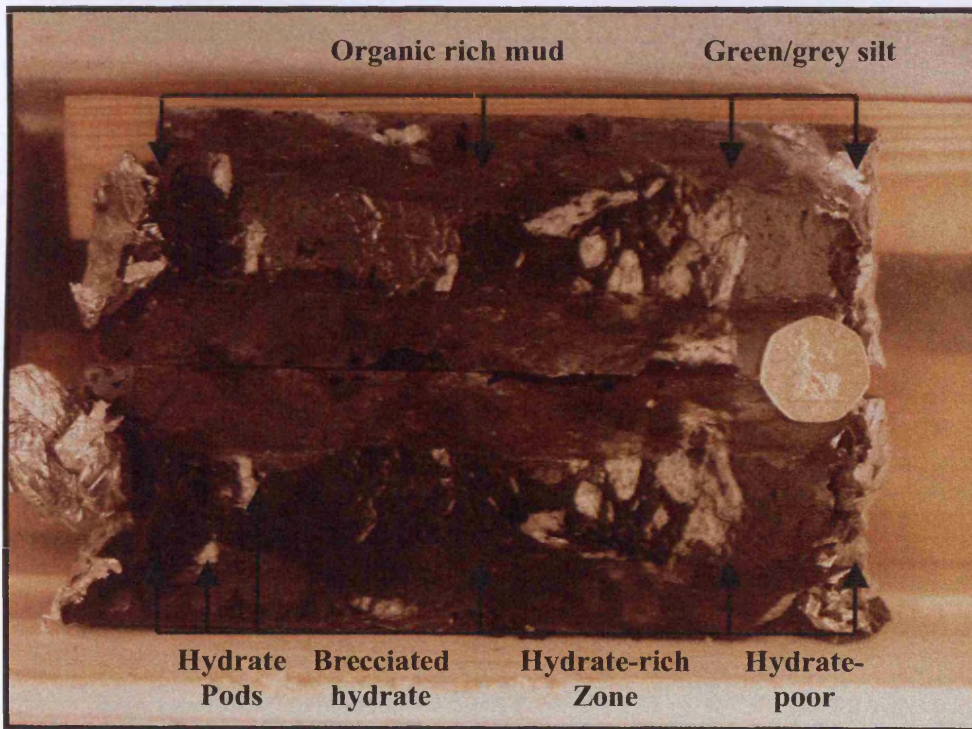


**Figure 6.2(a)** Digital image of the split 1328B core. BGS copyright. **(b)** Annotated digital image of the split 1328B core, showing the 2 halves used for sub-sampling. Well preserved white hydrate pods and lenses can be seen throughout the core, separated by muddy and silty sediment.

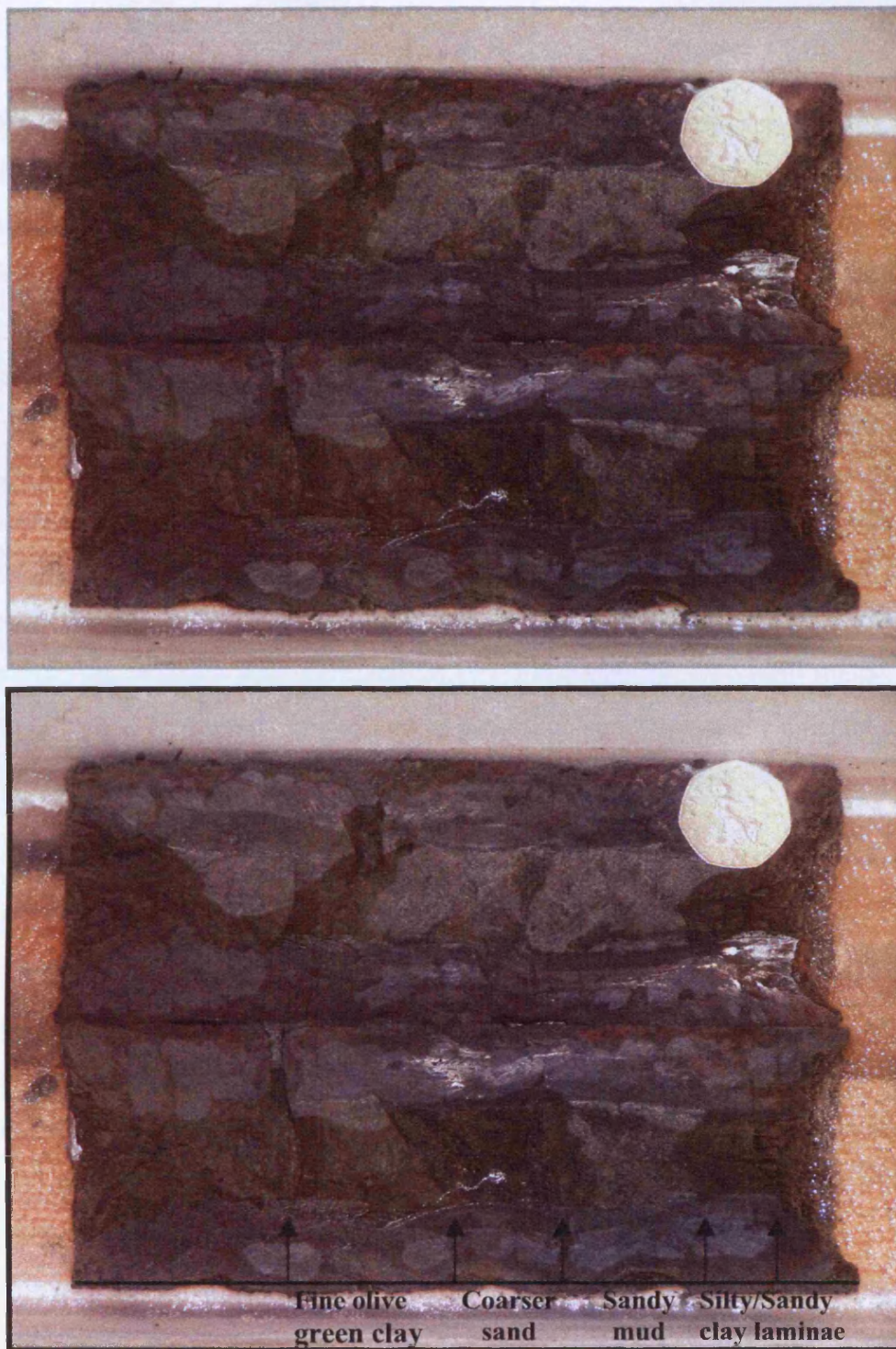


**Figure 6.3(a)** Digital image of the split 1327C core. BGS copyright. **(b)** Annotated digital image of the split 1327C core, showing the 2 halves used for sub-sampling. No easily identifiable hydrate could be found in the core, with silty/sandy clay laminae forming the top of the core and more uniform sandy mud below, with a coarse sandy base.

## **6.4 SEM imaging**

As with laboratory grown carbon dioxide hydrate samples (see chapter 4 for methods used for analysis), the Cascadia Margin natural methane hydrate samples have been cryogenically frozen, cleaved to form sub-samples, and analysed using a cryogenic BSEM. Imaging and analysis under the BSEM has revealed fascinating detailed results about these natural hydrate samples. Comparison with previous understanding of the processes involved in the formation of laboratory grown carbon dioxide hydrates in a controlled environment, has allowed greater understanding of active natural hydrate formation at Cascadia Margin.

Four samples from core 1328B have been analysed (2, 4, 6, 9) representing different hydrate bearing zones, and one sample from core 1327C (2). The sub-samples from 1328B show very similar hydrate morphologies and structures, with each subsequent SEM sample confirming the same resulting formation patterns and textures; therefore each sample has not been described separately as in the previous chapter.

### **6.4.1 Natural methane hydrate morphologies and related salt fabrics**

There appears to be three major different morphologies present in the natural methane hydrate samples: ‘micro-porous’ or ‘holey’ hydrate with very little salt present, ‘dense’ or solid hydrate with no precipitated salt, and ‘crystalline hydrate’ with a larger quantity of interstitial precipitated salt. Additionally, within the clay rich sediment there are other morphologies present including ‘acicular’ hydrate (Figure 6.4c), hydrate ‘laminae’ (Figure 6.4d), hydrate ‘pods’ (Figure 6.5b), and ‘vesicular’ hydrate (Figure 6.5c). Similar morphologies have been seen previously in imaged samples of laboratory grown carbon dioxide hydrate (see chapter 5).

One of the dominant morphologies – ‘micro-porous’ hydrate also appears to have two slightly different forms. A gas rich form, where there appears to be many trapped gas bubbles within the hydrate (Figure 6.4a; 6.5a), and a crystalline ‘mush’ with gas filled intergranular pore spaces created by euhedral hydrate crystal contact points (Figure

6.4b; 6.5d). These two forms may represent different stages of growth and dissociation (see discussion 6.5).

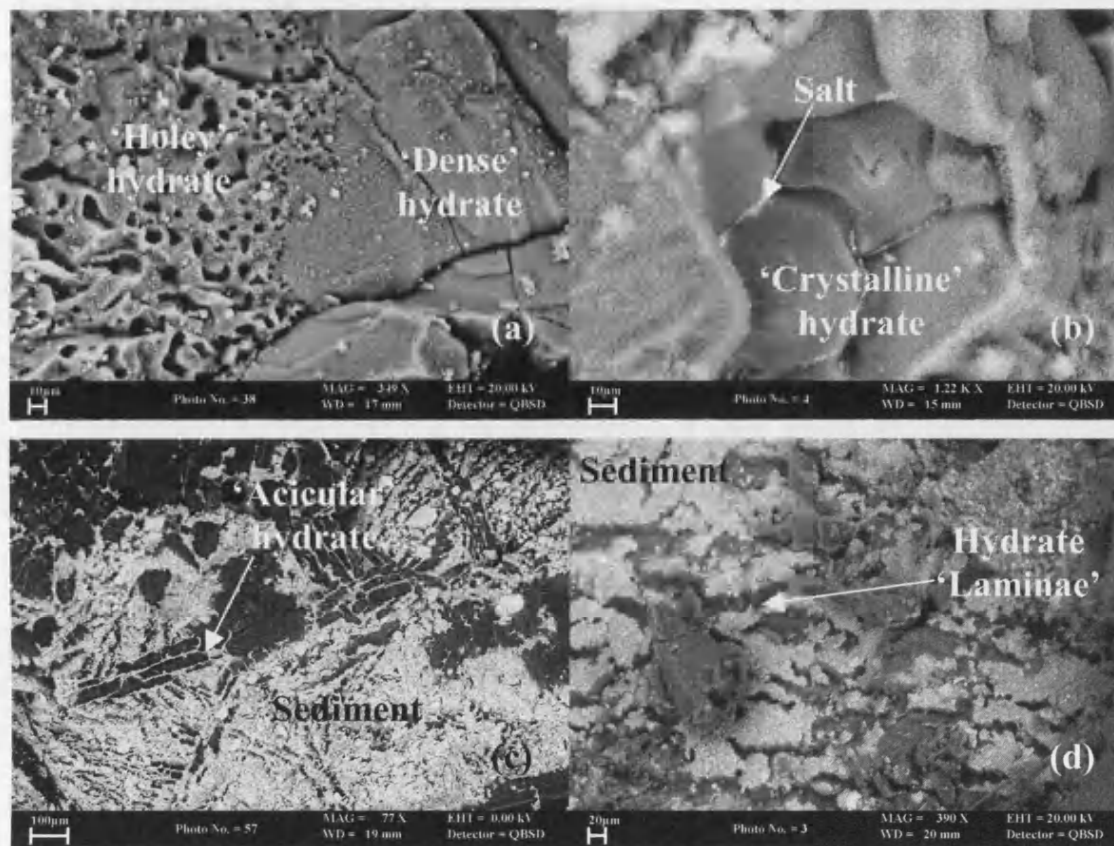


**Figure 6.4** (a) BSEM image showing a contact zone between ‘dense’ methane hydrate and gas-rich ‘micro-porous’ methane hydrate, with increasing trapped gas bubble size away from the contact zone. (b) BSEM image of ‘crystalline’ methane hydrate showing interstitial precipitated salt along grain boundaries. (c) BSEM image of ‘acicular’ methane hydrate formed within fine-grained sediment. (d) BSEM image showing methane hydrate ‘laminae’ within fine-grained sediment.

The micro-porous hydrate appears to be layered with the dense hydrate. The dense hydrate appearing as nodules with very little microstructure surrounded by the highly micro-porous hydrate. Additionally, the trapped gas pockets or ‘bubbles’ appear to increase in diameter away from the dense hydrate nodules (Figure 6.4a), with a series of very fine rounded gas bubbles on the contact between these two forms, growing and elongating away from the contact.

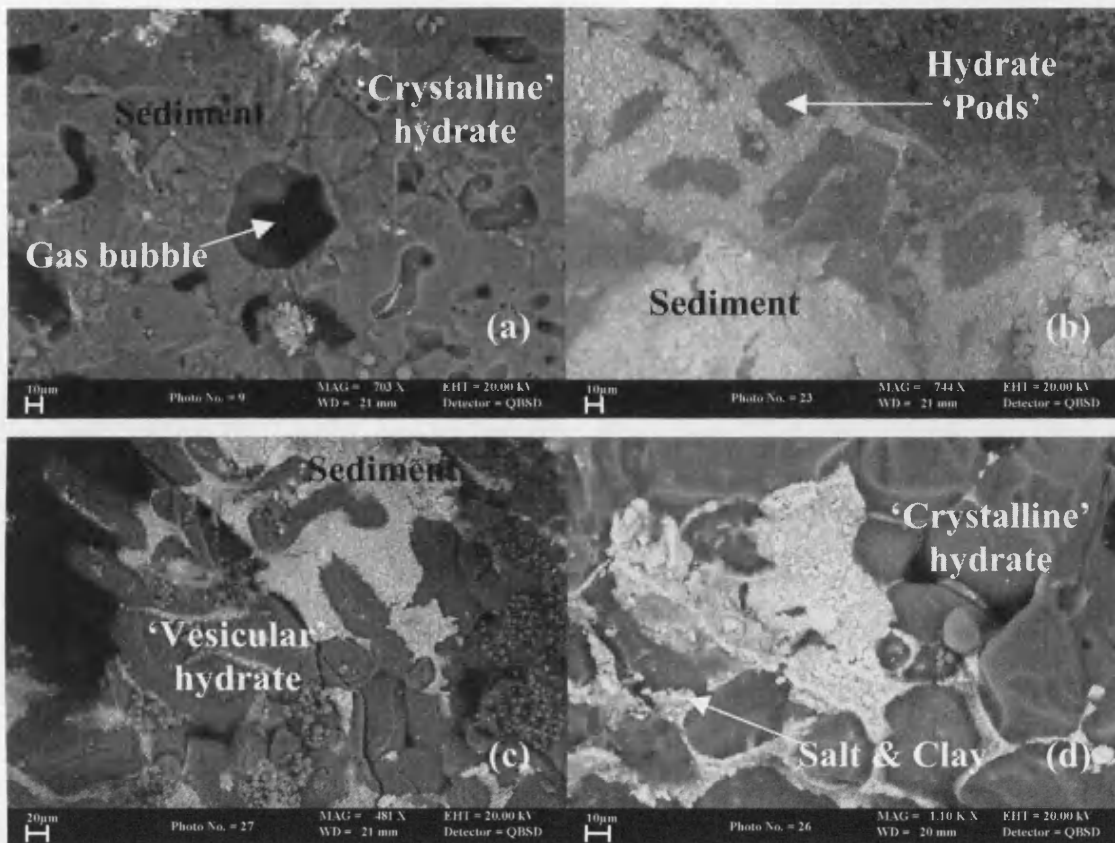


**Figure 6.5(a)** BSEM image of gas-rich ‘micro-porous’ methane hydrate formed around a gas bubble. Euhedral crystal faces can be seen to line the inside of the central gas bubble. **(b)** BSEM image of methane hydrate ‘pods’ formed within fine-grained sediment. **(c)** BSEM image of ‘vesicular’ hydrate growing within fine-grained sediment and into an open gas-filled pore space. **(d)** BSEM image of ‘crystalline’ hydrate with inter-granular pore spaces filled with precipitated salt and clay.

Within the samples are a series of crosscutting gas filled channels, some annealed, some partially annealed and some fully open. Surrounding these channels is a larger crystalline hydrate form, separated by precipitated salt filling the inter-granular porosity. This larger crystalline form, the micro-porous form, and the dense form create repeating patterns throughout the hydrate samples, all of which appear to be well preserved. This repetition in addition to the nature of the salt precipitated within the hydrate samples has allowed formulation of a picture of hydrate formation and growth processes at this particular natural site (see discussion 6.5).

Within the sediment rich zones in the samples there are various other hydrate forms. Rapid growing acicular hydrate can be seen to enter the sediment (Figure 6.4c), and hydrate laminae (Figure 6.4d) appears to brecciate the clay-rich sediment, forcing the sediment apart as it forms. 'Pods' of hydrate also appear to force the sediment apart forming from isolated crystals (Figure 6.5b). Vesicular hydrate appears to be present in open pore spaces growing into gas filled cavities (Figure 6.5c), which is similar to a form seen within laboratory grown carbon dioxide hydrate.

No hydrate has been discovered in the imaged sub-sample from the second core acquired from IODP 311. This sample contained a sandy matrix with frozen interstitial water filled pores. This frozen water ice forms cement supporting the sandy sediment grain matrix, and takes the form of 'bubbly ice' consisting of many trapped gas bubbles frozen within the ice (Figure 6.6a, b). Interestingly there appears to be a considerable quantity of pyrite within this sample (approximately 5%), which although seen in the other core, seems to be clearer in the second core.

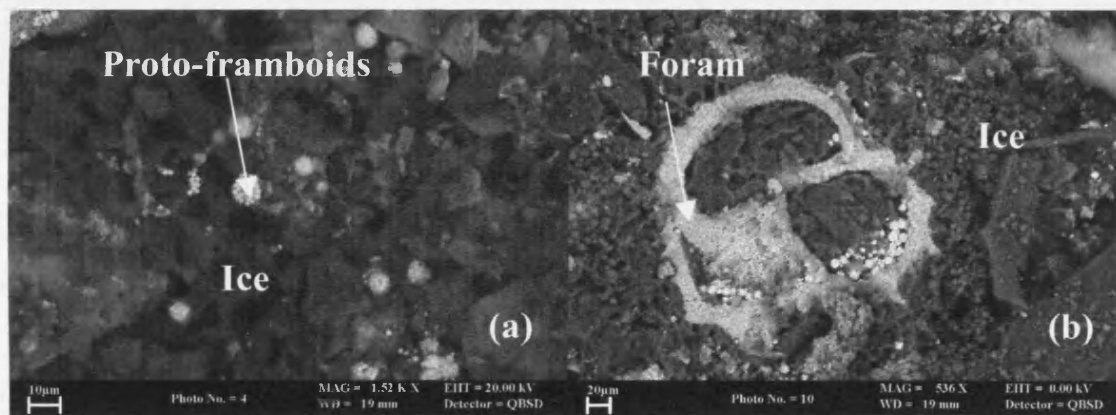


**Figure 6.6(a)** BSEM image of 'bubbly' ice from 1327C. Small proto-pyrite-framboids can be seen within the sample. **(b)** BSEM image of 'bubbly' ice, from 1327C, surrounding and filling a foraminifera.

#### **6.4.2 Natural methane hydrate salt fabrics.**

Before describing the salt fabrics within the samples, it is important to note that these salt fabrics are not believed to have formed in-situ. These salt fabrics represent cryogenically-frozen brine and result from the sampling and preservation processes deployed. This differs from the in-situ precipitated salt interpreted during analysis of laboratory formed carbon dioxide hydrate due to the inclusion of salts during hydrate growth (see Chapter 5).

As previously mentioned the sub-samples show well preserved hydrate with a series of channels running through the hydrate, some open and some partially annealed. These channels are surrounded by salt (Figure 6.7), shown in the image as bright white areas, darker areas represent empty spaces, and lighter grey areas are methane hydrate. These salt fabrics appear to line the channels and exist within the hydrate surrounding the channels filling inter-granular pore spaces between the hydrate crystals. X-ray analysis (EDXA) of these fabrics identify Na, Cl and K peaks, as well as Ca, therefore providing evidence for a range of salts and clays present in the fabrics. In the area surrounding the channel the hydrate appears fairly dense, with larger crystals, as we move down into the sample the hydrate becomes porous, and the salt concentration decreases. Lying below the micro-porous hydrate is a very dense hydrate, with no visible salt present.

The sample was gradually ablated under the BSEM by slowly warming the sample stage (see Chapter 4 and 5) to reveal hidden information below surface layers, and as the hydrate began to dissociate salt structures become clearer and their distribution more apparent (Figure 6.8). Salts are seen to form a complex salt fabric, identifying a complicated pore network between hydrate grains. The hydrate lying near the main open micro-channel contained the greatest concentration of salts, which surrounded each hydrate grain. Further away from the channel the salt concentration decreases and the salt fabric changes, from a well-structured 'honeycomb' network to a more fibrous structure in the porous hydrate, to a very minimum concentration in the dense hydrate. This may indicate some relationship between the salt structures present and the formation of the hydrate, or possibly just how well the brine pore-waters could access intergranular spaces between the hydrate.

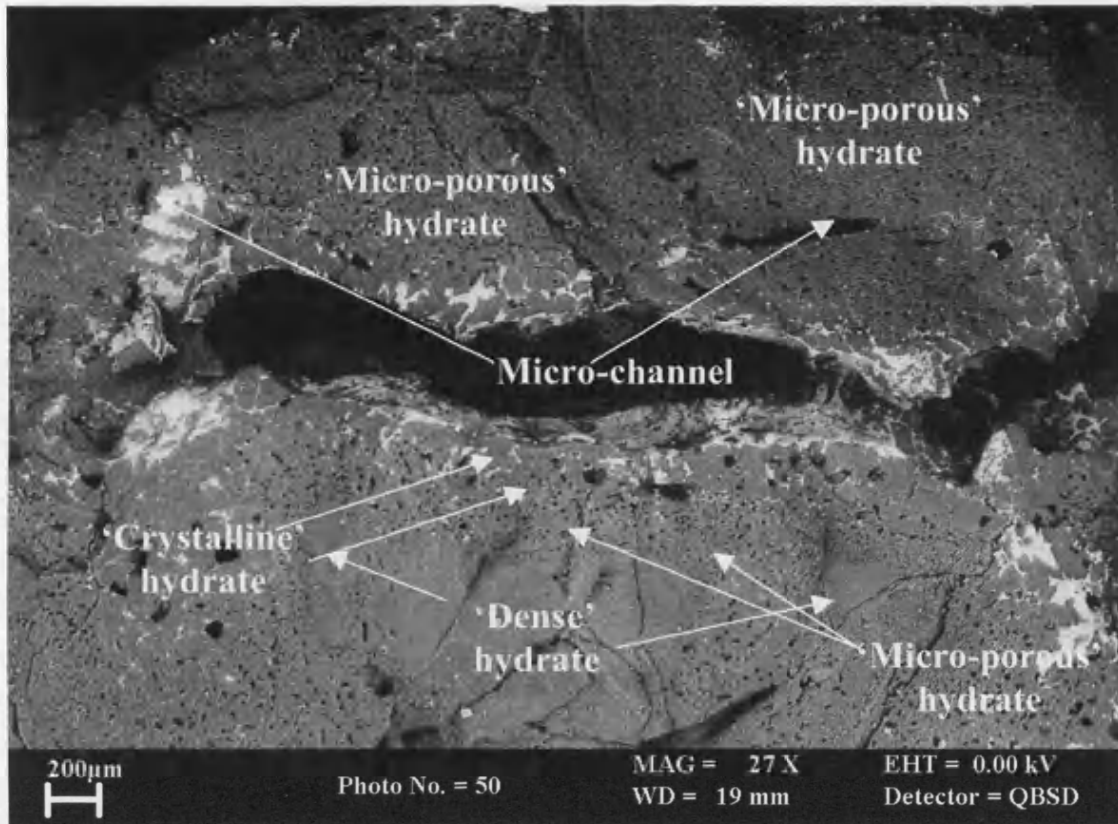


**Figure 6.7.** BSEM of methane hydrate sub-sample from 1328B, showing the distribution of different hydrate morphologies present within the sample, formed around micro-channels (some open and some partially annealed).

To gain a better understanding of the structure of these salt fabrics clearly visible after gas hydrate dissociation, a series of 3D images were taken. By tilting the sample stage at known incremental angles, composite images were taken to construct stereoscopic images. These were then imported into a freeware software Callipygian 3D to create red and green 3D images visible through standard 3D viewers (supplied at the back of this thesis). Visualisation in 3D allows full understanding of the depth of the sub-samples and the intricate, delicate salt fabrics present. Figure 6.9(a) highlights an area with dendritic salt crystals surrounding spaces once filled with methane hydrate crystals. Additional images show low magnification images of the remaining sample after full ablation (Figure 5.9b, c). These 3D images allow easier visualisation of different salt fabrics present in the sample, relating to the distribution of the various forms of hydrate and the sediment distribution.

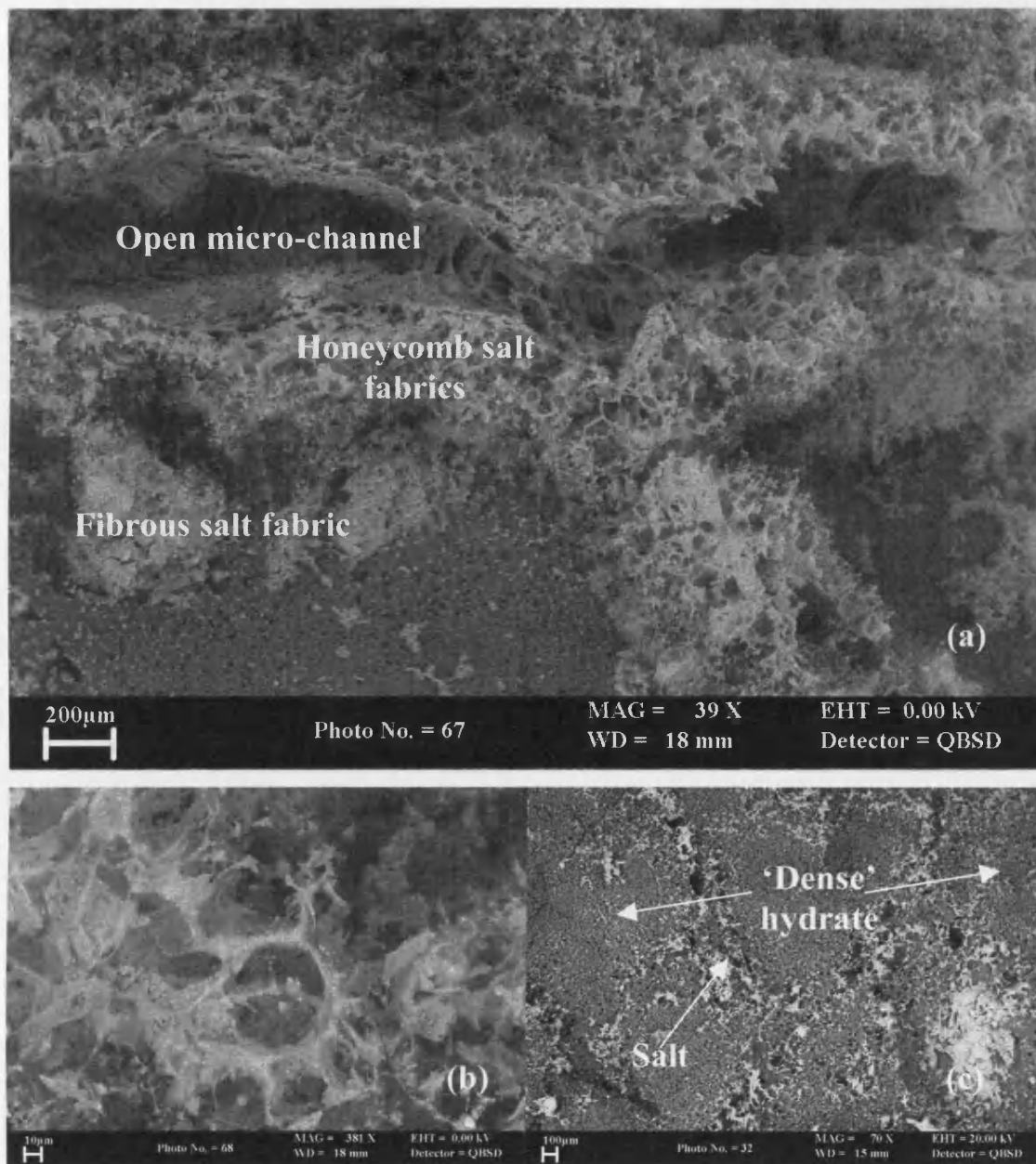


**Figure 6.8 (a)** BSEM of sample area shown in Figure 6.7 after partial sample ablation revealing inter-granular salt (brine) filled pore networks, and different salt concentrations and distributions present within the sample. **(b)** BSEM higher magnification image of the inter-granular pore networks. **(c)** BSEM image showing revealed salt between 'dense' hydrate after partial sample ablation. Higher salt concentrations can be seen around micro-channels between nodules of 'dense' hydrate.

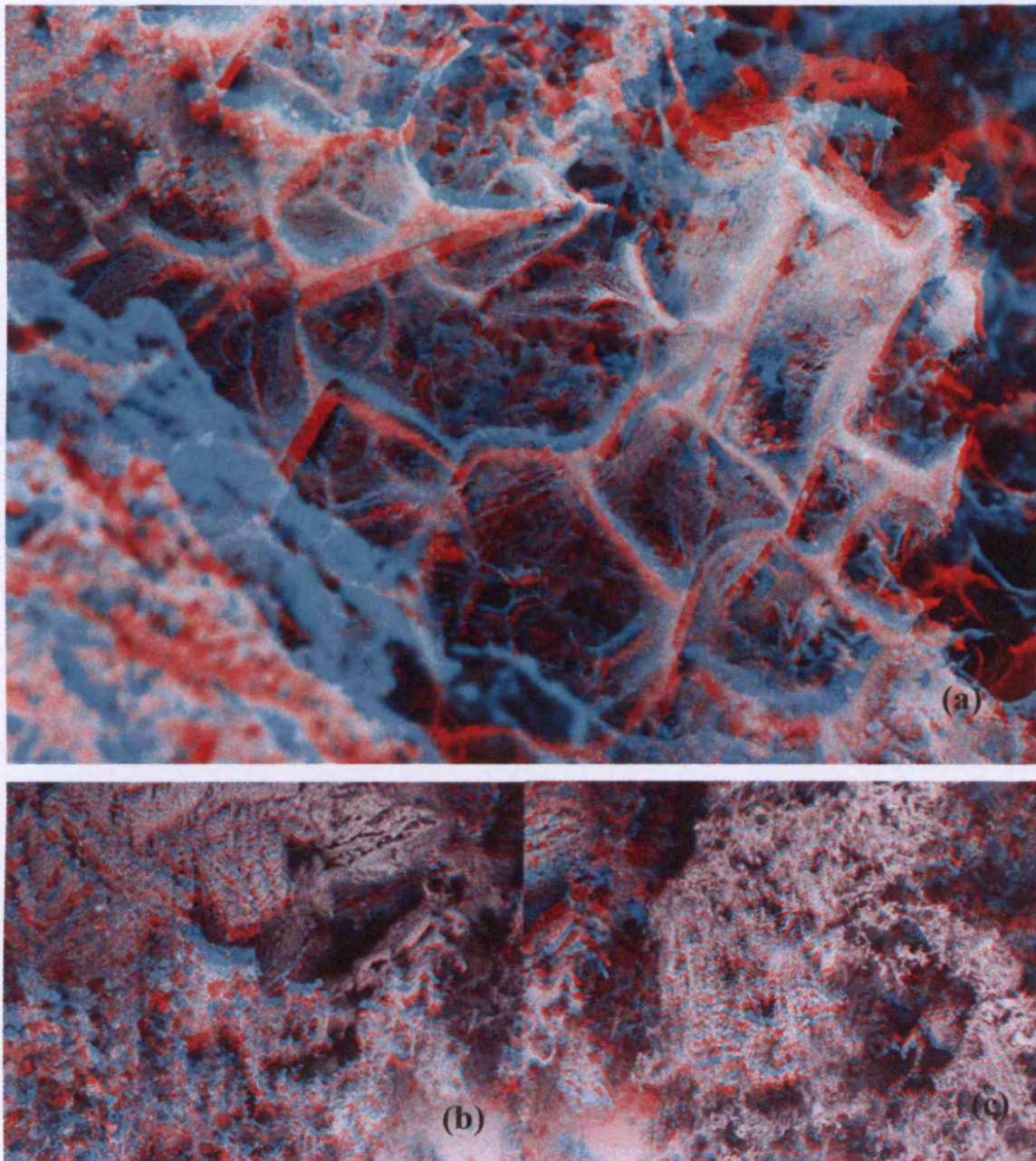


**Figure 6.9** (a) 3D BSEM of dendritic salt crystals which have formed 'honeycomb' salt fabrics representing brine filled inter-granular pore-networks between euhedral and subhedral methane hydrate crystals. (b) Lower magnification 3D BSEM image showing 'honeycomb' salt fabrics (lower half of image) and their relation to the underlying fine-grained sediment (upper half of image). (c) Lower magnification 3D BSEM image showing different salt fabrics revealed after sample ablation.

## 6.5 Discussion

There appears to be three main forms of distinguishable hydrate forms present in the sub-samples from the 1328B core, each expressing different quantities/relationships with the precipitated salt (brine) fabrics present: massive hydrate with no salt present, micro-porous hydrate with very little precipitated salt present and dense crystalline hydrate with considerable quantities of precipitated salt crystals filling intergranular interconnected pore spaces. Running throughout the hydrate samples are cross-cutting micro-channels, some open (now gas filled), some partially annealed, which seem to be lined with water ice and precipitated salt. The position of these hydrate forms in relation to one another, appears to create a repeating pattern (Figure 6.10). The densely packed crystalline hydrate with large quantities of pore-filling salt is present on either side of the micro-channels. Directly surrounding the crystalline hydrate is the micro-porous hydrate giving the appearance of a crystalline 'mush'. The furthest away from the micro-channels, lying beneath and within the micro-porous hydrate, is the massive hydrate found to contain no salt after ablation.

The delicate salt structures seen represent brines present in the recovered samples. Subsequent cryogenic freezing causes the formation of ice, or hydrate, further concentrating the brines present, causing the precipitation of salts at saturation.

There has been some debate about the formation of highly saline pore waters during hydrate formation, and the hydrate formation processes causing a positive chloride anomaly measured at Cascadia Margin (Haeckel et al, 2004; Torres et al., 2004; Milkov & Xu., 2005). It is understood the formation of hydrate and ice, causes salt exclusion into surrounding waters, creating highly saline waters surrounding the zone of hydrate formation. However, Cascadia Margin represents a natural region of very rapid hydrate formation, and we appear to have captured recently formed well preserved hydrate, with trapped brine fluids within the hydrate mass. Although it is assumed natural diffusion will remove the brine fluids over time, the hydrate captured appears to have formed recently and rapidly, and the process of natural diffusion has not had time to remove these fluids. However, it is possible that these brines present within the samples have entered the inter-granular matrix after hydrate formation, though this is less likely due to the seemingly well-preserved nature of the natural methane hydrate.

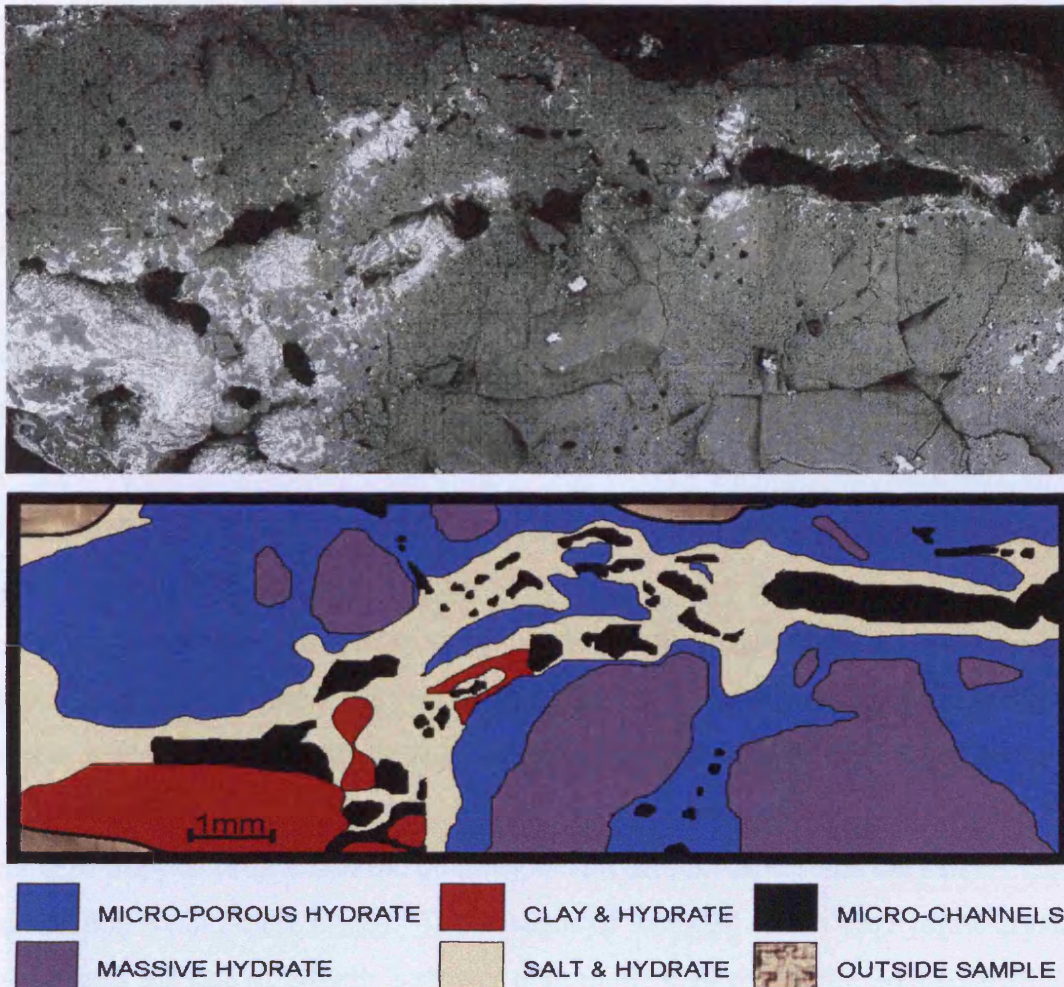


**Figure 6.10(a)** Combined panoramic BSEM image showing a full c.12 mm methane hydrate sample (part of which has been seen previously in Figure 6.7). **(b)** Annotated full scale sketch of (a) showing the distribution of different methane hydrate morphologies, different salt fabrics and the fine-grained sediment. ‘Micro-porous’ hydrate can be seen to surround ‘dense’ hydrate, and ‘crystalline’ hydrate with inter-granular salt fabrics can be seen to surround the main micro-channels which almost run across the full length of the sample.

Very similar salt fabrics have been seen in laboratory grown carbon dioxide hydrates formed within pressure vessels under controlled pressure and temperature conditions (Chapter 5). These carbon dioxide hydrates formed very rapidly, and due to the static formation conditions, any brine fluids present could not diffuse away. When cryogenically frozen and imaged these hydrates show complicated salt fabrics, which differ according to formation conditions. Figure 6.11a shows ice pseudomorphs replacing CO<sub>2</sub> hydrate on sample ablation (darker areas) surrounding quartz grains in

natural sediment (large, bright areas). Honeycomb salt structures appear etched out of the sample as ice replacement occurs. These distinct salt structures are associated with slightly slower hydrate formation, with well defined crystal boundaries. However, Figure 6.11b shows salt structures associated with very rapid hydrate formation, with hydrate crystals growing as acicular needles including salt/brine within its structure, as growth is too quick for adequate exclusion, and hence forming at salt saturation. These hydrate needles formed within a water layer above sediment, and the needles formed rapidly advancing into sediment directly below.

The salt; included within the hydrate in the formation of these carbon dioxide hydrate samples, indicate hydrate formation at salt saturation. However, there is no evidence to suggest formation at salt saturation in the natural methane hydrate samples, as no salt can be seen to be included within the hydrate crystals. The salt precipitated in the Cascadia Margin samples only appears along crystal boundaries, therefore leading to the conclusion that the precipitation of salt is simply a consequence of cryogenic freezing of trapped brines, and the quantity of salt present represents the salt concentration within these brines. The absence of included salt in the hydrate crystals also indicates the rate of growth is slower than in the majority of the imaged artificially formed carbon dioxide hydrate samples (see Chapter 5) (though slower grown 6.11a expresses very similar salt fabrics to those seen in the Cascadia Margin samples).

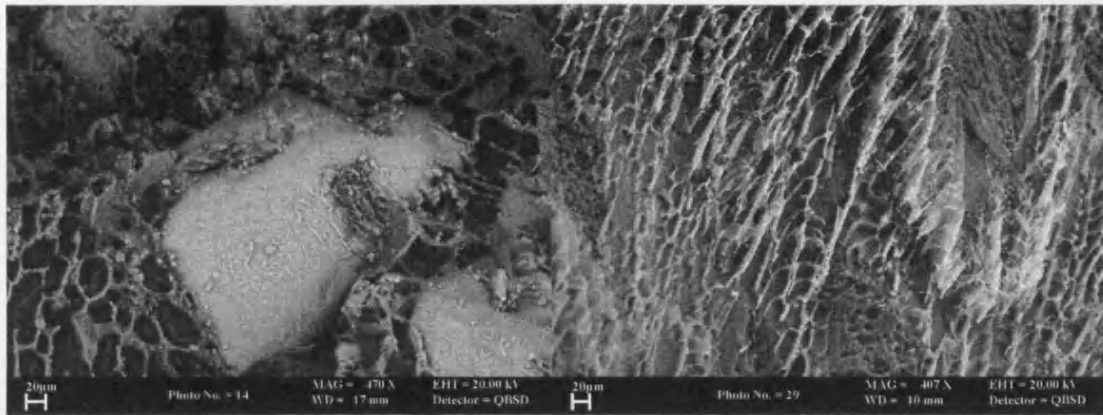


**Figure 6.11(a)** BSEM image of pore-filling ice pseudomorphs of CO<sub>2</sub> hydrate enveloping a sand grain with pronounced intergranular honeycomb salt and clay fabrics between hydrate crystals after ablating to -100 °C. **(b)** BSEM image of acicular carbon dioxide hydrate formed within a water-rich environment after raising the temperature to -85 °C and ablating some of the hydrate sample. Grey regions represent CO<sub>2</sub> hydrate and ice, and white regions the delicate 3D salt skeleton revealed after ablation.

The comparison with artificial samples, which were formed under controlled laboratory conditions, allows us to understand the natural system as well as reaffirming conclusions made for carbon dioxide hydrate samples, and they do show comparable salt fabrics.

In addition a second natural hydrate core sample, U1327C, from Hydrate Ridge, Cascadia Margin, has been imaged, which on core recovery was assumed to contain disseminated hydrate throughout due to the presence of ‘mouse-like’ textures (often associated with hydrate dissociation). When imaged the sample contained ice (see Figure 6.6 and 6.12), presumably due to subsequent handling of the samples after recovery, causing the finely disseminated hydrate to dissociate. However, the ice present in sub-samples from this core did not show any evidence of salt being present (Figure 6.12). The absence of salt in this core provides evidence for the conclusion that hydrate was present, and has dissociated, flushing the sediment with fresh water. The absence of salt also indicates the finely disseminated hydrate was a slower forming older morphology, allowing diffusion to take effect and remove brines from the pore waters.

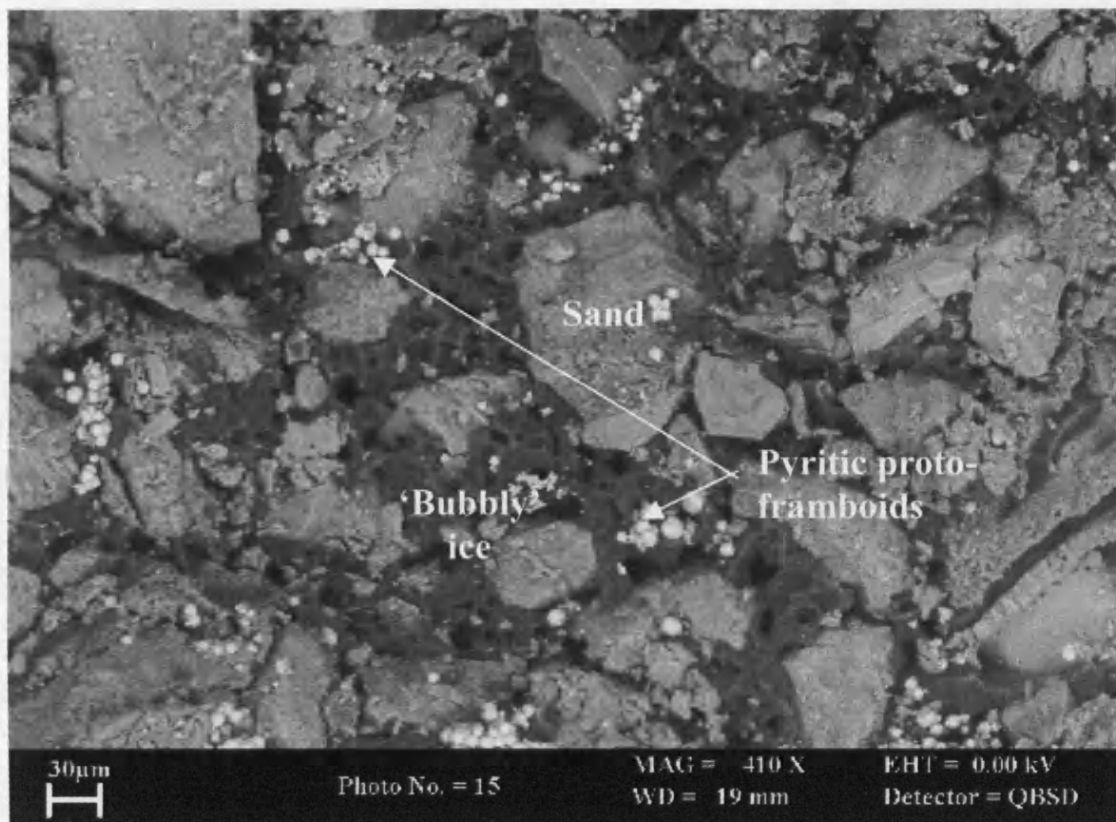


**Figure 6.12.** BSEM image of a sub-sample from U1327C, showing a sandy matrix filled with gas-rich 'bubbly' ice thought to represent disseminated methane hydrate prior to sample handling during recovery. Pyritic proto-framboids are seen to be dispersed throughout the sample. There is no evidence for the presence of salts.

The distribution of salts (principally halite) in relation to the micro-channels and the different natural methane hydrate morphologies within the sub-samples of 1328B, allows the formulation of a hypothesis to explain the formation of hydrates at this particular site. The absence of salts in the more massive 'dense' hydrate suggests this is an older, slower forming morphology, where excluded salt has been removed by natural advection and diffusion processes. Images show evidence for a reaction front along the edges of this massive hydrate where it contacts the 'micro-porous' form (see Figure 6.4a). This contact zone shows trapped gas bubble frozen within the hydrate, increasing in size away from the more massive 'dense' hydrate. This gas rich hydrate zone indicates partial dissociation. The 'micro-porous' hydrate surrounds the 'dense' hydrate, and contains very little precipitated salts, which can only be seen on sample ablation. This appears to be a secondary, younger, hydrate morphology formed after

partial dissociation of the massive 'dense' hydrate. The 'crystalline' hydrate directly surrounding the existing open micro-channels appears to be the youngest, rapidly forming morphology, with concentrated trapped brines between the crystals.

The open micro-channels are, as previously discussed, lined with water ice and precipitated salt filigree. This provides evidence that suggests these channels have been filled with seawater, or brine at some point in the recent past. It is highly plausible that these channels were in fact filled with gas charged saline fluid, acting as feeder channels to the growing hydrate pods and lenses. On recovery of the sample, the force of depressurisation could have ejected these fluids out of the sample, leaving only trapped brine pockets between crystals. The open feeder channels may have been active at the time of recovery, 'feeding' the dense crystalline morphology, with partially annealed channels being their older, inactive counterparts.

The interpretation of these micro-channels being feeder channels may help to explain the relationships between the different morphologies of hydrate present. These different morphologies may represent periods of activity and inactivity of the micro-channels supplying the necessary formation components:

1. Primary methane hydrate formation components are supplied to a sediment horizon via gas-charged fluids within micro-channels, allowing the formation and continued growth of methane hydrate.
2. The supply of necessary methane hydrate formation components stops. This is followed by a brief period of inactivity allowing brines (formed by salt exclusion processes during hydrate formation) to diffuse away from the methane hydrate. The hydrate ages, and forms massive 'dense' hydrate.
3. The micro-channels become active again transporting deeper warm, saline fluids into the massive hydrate zone, either through the same micro-channel as before or through one nearby. These warm fluids cause the dissociation of some of the massive hydrate. Dissociation is an endothermic reaction, which consequently leads to a decrease in

temperature, re-creating suitable conditions for hydrate formation, and the methane hydrate reforms rapidly, in some cases trapping gas between the hydrate crystals. These conditions lead to the formation of 'Holey' or 'micro-porous' hydrate. Micro-channels may then become partially annealed by methane hydrate.

4. The primary supply of components necessary for hydrate formation is re-activated, supplied through micro-channels to the hydrate bearing zone, allowing the rapid formation of methane hydrate. This leads to the formation of 'crystalline' hydrate, which is proposed to be the youngest hydrate form.

This hypothesis assumes active dissociation and formation of hydrate in-situ. The Cascadian Margin represents numerous active vent sites where gas-charged fluids and free gas are frequently released into the water column. Rapid transport of methane to near-surface sediments, with suitable pressure and temperature conditions leads to the formation of methane hydrates very near to the ocean floor, where conditions are highly variable. The known rapid passage of fluids and gas bubbles to the ocean floor would support the above hypothesis, creating a variable, active environment for hydrate growth. However; it is also possible; the dissociation front seen within this sample represents sample breakdown during sampling and recovery, and subsequent cryogenic freezing reformed the secondary hydrate morphology seen. This is believed to be unlikely, as pressure conditions on board ship are unsuitable for hydrate formation.

The interpretation of the fascinating detailed information about rates of formation and processes involved in the formation of these natural methane hydrates has been aided by previous examination of salt fabrics discovered in synthetic carbon dioxide hydrate samples. The understanding of hydrate formation at salt saturation has enabled the examination of these natural methane hydrate samples in greater depth and with improved understanding. It is the salt distribution (brine) which provides us with information on the rates of growth, and therefore, it is proposed that salt *distribution* (brine) be considered in future investigations of hydrate samples (rather than simply the total salt concentration). Although the site these samples have been recovered from is an active, rapidly forming hydrate region, it is quite possible similar sites exist

elsewhere. Additionally, the examination of these samples and the direct comparison with artificial samples created in the laboratory also supports the use of artificial carbon dioxide hydrates as an effective medium to investigate hydrate formation and dissociation, and the validity of using laboratory investigations as analogies for the natural world.

## 6.6 Conclusions

- Two natural methane cores (1328B and 1327C) have been sub-sampled and imaged from Cascadia Margin, offshore Oregon during IODP expedition 311. Massive methane hydrate was recovered from site 1328, and chlorinity values obtained on board ship supports the presence of methane hydrate within 1328 samples on recovery. ‘Mouse-like’ textures (often associated with hydrate dissociation) were observed within 1327 after core recovery, and this observation was assumed as evidence to support the presence of disseminated methane hydrate.
- Cryogenic BSEM imaging has revealed a number of different well preserved methane hydrate morphologies and complex precipitated salt fabrics in 1328B
- The salt fabrics seen in the samples are not believed to have formed in-situ, and represent cryogenically frozen brines resulting from the sampling and preservation processes deployed.
- No hydrate or salt fabrics have been observed in 1327C.
- There appears to be three main forms: massive hydrate with no salt present, micro-porous hydrate with very little precipitated salt present and dense crystalline hydrate with considerable quantities of precipitated salt crystals filling intergranular interconnected pore spaces.

- The absence of salts in the massive hydrate indicates this is an older, slower forming morphology, where excluded salts have been removed by natural advection and diffusion processes. The micro-porous hydrate surrounds the massive hydrate, and contains very little precipitated salt. This appears to be a secondary, younger, hydrate morphology formed after partial dissociation of the massive hydrate. The densely crystalline hydrate directly surrounding the open micro-channels appears to be the youngest, rapidly forming morphology, with concentrated trapped brines between the crystals.
- Open micro-channels cross-cut the samples. It is possible these channels were filled with gas charged saline fluid, acting as feeder channels to the growing hydrate pods and lenses. Interpreting these micro-channels as feeder channels may help to explain the relationships between the different morphologies of hydrate present. These different morphologies may represent periods of activity and inactivity of the micro-channels supplying the necessary formation components.
- Interpretation of detailed information about the rate of formation and processes involved has been aided by previous examination of salt fabrics discovered in synthetic carbon dioxide hydrate samples. It is the salt (brine) distribution which provides us with information on the rate of growth, and therefore, it is proposed that salt (brine) distribution be considered in future interpretation of hydrate samples.
- Additionally, the examination of these samples and the direct comparison with artificial samples created in the laboratory also supports the use of artificial carbon dioxide hydrates as an effective medium to investigate hydrate formation and dissociation.

## **CHAPTER 7**

### **Discussion**

## 7. Discussion

The rationale behind this PhD study is to understand key scientific aspects underpinning the feasibility of carbon storage as liquid CO<sub>2</sub> and CO<sub>2</sub> hydrate within sub-seabed sediments (see Chapter 2). This has been considered by dividing the research into a number of aims to answer specific problems:

- *Are there suitable sites offshore Western Europe for carbon storage as liquid CO<sub>2</sub> and CO<sub>2</sub> hydrate?*
- *What short-term effects will hydrate formation have on the hosting sediment?*
- *How do sediment-hosted hydrates form?*
- *Is carbon storage as CO<sub>2</sub> hydrate within sub-seabed sediments a feasible storage method?*

Two main investigatory pathways have been followed during this project to meet these aims: the study of hydrate stability through computer modelling (Chapter 3), and the study of hydrate formation within sediments, both in CO<sub>2</sub> hydrates formed within the laboratory (Chapter 4, 5) and in natural in-situ methane hydrates (Chapter 6). The investigation of liquid CO<sub>2</sub> has been limited to computer modelling to scope the potential of this storage approach.

This discussion chapter considers the results from these investigations (reported in previous chapters) and identifies remaining gaps in our knowledge, which could be addressed in further research.

### 7.1 Are there suitable sites offshore Western Europe for carbon storage as a liquid and hydrate, and if so where are they?

The definitive answer to this question appears to be yes. The collection of pressure and temperature data off the western European continental shelf, and the application of the carbon dioxide hydrate stability model – `hydcalcCO2.exe` – developed during this project, has determined large regions offshore Western Europe with suitable pressure and temperature conditions for the storage of carbon dioxide as a liquid and hydrate

(see Chapter 3). The model predicts the base of the CO<sub>2</sub> hydrate stability zone could reach a maximum depth of 460 m below the seafloor where water depths exceed 3800 m and temperatures reach a minimum of -0.9 °C in the Aegir ridge, Norwegian basin (assuming a 30 °C/km geothermal gradient). This would mean liquid CO<sub>2</sub> could be injected at a depth of greater than 460 m below the seafloor, and a very thick zone above this liquid store (<460 m) would have suitable conditions for the formation of a solid hydrate 'cap'.

Simple volume calculations predict the carbon dioxide hydrate stability zone to have a total volume of  $1.3 \times 10^9 \text{ km}^3$  within the Western European 200 mile economic zone (within the mapped area between 20°W, 30°N to 20°E, 30°N and 20°W, 70°N to 20°E, 70°N). To convert this sediment volume into a potential estimate of carbon dioxide, which could be stored as a hydrate within this zone, it is necessary to make several assumptions (the second and fourth assumptions do not have any physical basis, and have only been estimated to reduce the volume of the hydrate stability zone into a more realistic figure):

- CO<sub>2</sub> hydrate density of 1.1kg/l
- Only 0.1% of the available sediment volume with suitable pressures and temperatures is viable.
- A total of 10% of the sediment volume is available for hydrate formation (10% porosity; assuming 100% hydrate saturation within this volume).
- Only 1% of the CO<sub>2</sub> hydrate stability zone is filled by a hydrate cap (assuming 100% hydrate saturation within this volume).

Using these assumptions the total volume potentially filled hydrate reduces to  $1.3 \times 10^3 \text{ km}^3$ , equivalent to  $1.43 \times 10^{12}$  tonnes of hydrate which could be deposited offshore Western Europe (within the contoured area). If 30% by weight of this hydrate volume is carbon dioxide, then  $4.29 \times 10^{11}$  tonnes of carbon dioxide could be stored within this volume, or 429 Gt (gigatonnes) of carbon dioxide. Therefore, even if only  $1/1000000^{\text{th}}$  (0.1% = 1/1000, 10% = 1/10, 1% = 1/100) of the hydrate stability zone within this area was to be filled with carbon dioxide hydrate, as much as 429 Gt of carbon dioxide could be locked away as a hydrate. This represents over 400 years of European emissions from point sources (Holloway et al., 1996).

This estimate is the volume of carbon dioxide, which could potentially be stored as a hydrate, assuming all sites within the hydrate stability zone had suitable sediments for storage. It does not include the storage potential of the underlying liquid carbon dioxide beneath this hydrate 'cap', which would be dependant on the specific aquifer volume capacity and the sealing properties of the hydrate 'cap'. However, the storage capacity of CO<sub>2</sub> in its liquid phase would be considerably larger than for CO<sub>2</sub> in its hydrate phase. Therefore, there seems to be enormous potential for this storage method. These estimates should however be used with caution as many simplistic assumptions have been used for the calculations used to generate these volumes.

As can be seen in Figure 7.1, the carbon dioxide hydrate stability reaches great depths below the ocean floor (>200 m), very close to shore near Spain, Portugal, and Norway. These offshore regions appear to offer the most suitable conditions for storage as a liquid and hydrate for Western Europe when considering their proximity to the shore. Around the UK the CO<sub>2</sub> hydrate stability zone is a considerable distance away from the coast due to shallow seas around the UK, and therefore pipeline cost from onshore CO<sub>2</sub> sources may be relatively high.

The physical trapping mechanism of hydrate formation offers many benefits to permanently store this greenhouse gas, however, to fully appreciate the storage methods' benefits, density must also be considered. Model calculations also predict the density of liquid CO<sub>2</sub> to increase rapidly off the continental margin of Spain and Portugal. Within the Biscay Abyssal Plain, the Iberian Basin, the Tagus Basin, and the Seine Abyssal Plain, liquid CO<sub>2</sub> below the hydrate stability zone becomes denser than seawater (Figure 3.3.7, Chapter 3). In these regions if liquid CO<sub>2</sub> was to be injected into sediments beneath the CO<sub>2</sub> hydrate stability zone, the stored liquid CO<sub>2</sub> would no longer experience any buoyancy driven upward vertical migration, sinking deeper into the sediments and descending further underground. In this case the formation of hydrate would be dependent on the possibility of CO<sub>2</sub> dissolving into the formation pore-waters and rising into cooler sediments via diffusion, acting as a secondary 'back-up' trapping mechanism, with dense liquid storage being the primary storage trapping mechanism. Storage as a dense descending liquid plume and as a liquid and solid hydrate appears to offer many benefits over conventional supercritical storage, where CO<sub>2</sub> is in a free, highly mobile phase.

Not only does this density increase offer potential benefits over supercritical storage, but storage at lower temperatures than used in conventional warm, deep supercritical storage, would also increase CO<sub>2</sub> viscosity and solubility. For example at a pressure of 100 bar, and a temperature of 30 °C, previous research indicates a CO<sub>2</sub> viscosity of approximately 70 μPa s<sup>-1</sup>, but at 10 °C this increases to approximately 110 μPa s<sup>-1</sup> (Vesovic et al, 1990, Rochelle et al, 2006). This increased viscosity at lower temperatures may slow CO<sub>2</sub> migration, should any occur. CO<sub>2</sub> is relatively soluble in water. Once dissolved in pore-waters CO<sub>2</sub> will no longer be susceptible to buoyancy-driven vertical migration. CO<sub>2</sub> solubility increases with decreasing temperature up to the point of hydrate formation. Therefore, pore-waters underlying the hydrate stability zone may be able to store large quantities of CO<sub>2</sub>, as increased solubility could potentially increase the storage capacity of the reservoir (Rochelle et al., 2006). For example, at seawater salinities (35‰) and a pressure of 100 bar (1000 m depth) the solubility is approximately 25% greater at 10 °C than at 30 °C. The solubility of CO<sub>2</sub> also increases with increasing pH, therefore storage in, or near, systems which have the potential to increase pore-water pH by CO<sub>2</sub> fluid-rock interactions would further enhance the storage capacity of the carbon storage reservoir (Gunter et al, 1993; Rochelle et al, 2004; Rochelle et al, 2006). This research study has not investigated the effects of solubility, viscosity, or the longer-term effects on this storage method

In terms of an efficient trapping mechanism, there appear to be considerable benefits of this storage method over current supercritical storage, and calculations have predicted large regions close to shore with significant CO<sub>2</sub> hydrate stability zone thickness and high liquid CO<sub>2</sub> density. As with all storage concepts economics play a pivotal role in further development. Transport and pipeline costs can be extensive, however some of the regions which appear to have the most suitable conditions for this storage method offshore Western Europe, also appear to have large CO<sub>2</sub> sources located along the coastline. Figure 7.1 shows some of the major CO<sub>2</sub> sources around the coast of Western Europe (Holloway et al., 1996; IEA, 2002). These major CO<sub>2</sub> sources include cement factories, power stations, refineries, ammonia producers and iron, steel and other metal manufacturers. CO<sub>2</sub> emissions are represented as filled circles decreasing in size with decreasing CO<sub>2</sub> emissions (measured in tonnes). Spain and Portugal have many major CO<sub>2</sub> emitters close to the coast where water depths rapidly increase to

depths suitable for storage as a liquid and hydrate. Denmark, Sweden and Norway also have major CO<sub>2</sub> sources close to the Norwegian Deep Channel where suitable conditions exist. Along the west coast of Norway CO<sub>2</sub> sources exist offshore and onshore, very close to or within offshore regions where CO<sub>2</sub> hydrate is stable. These offshore sources mean infrastructure is already in place for initial storage testing, development of the storage method and active storage as a liquid and hydrate.

It is also within the offshore region along the west coast of Norway that CO<sub>2</sub> hydrate is stable yet where methane hydrate is not. Therefore, should this offshore region be considered for this novel CO<sub>2</sub> storage method, there would be no contamination of methane hydrate reserves, which is extremely important if methane hydrate is to be exploited in the future as an energy resource. The quantity of carbon dioxide which could be stored in this offshore region would of course be dependant upon localised geothermal gradient and sediment characteristics. Full exploration of the area would be necessary before injection.

This investigation of hydrate stability zone thickness offshore Western Europe has not considered sediment characteristics. These are extremely important for site selection, as a reservoir with a relatively high porosity, such as a sandstone reservoir would be preferred to maximise the storage potential. It is also important to consider possible errors during predictive calculations of the hydrate stability zone thickness, with the major discrepancy lying in the geothermal gradient used for calculations (see Chapter 3 for details of modelling and contouring errors). A 30 °C geothermal gradient is often used as a global average value determined from many years of research; however, geothermal gradients vary widely, and as this model is highly sensitive to geothermal gradient this is where the largest errors could occur (reducing the hydrate stability zone in areas with a high geothermal gradient and increasing the hydrate stability zone in areas of low geothermal gradient). A detailed map of geothermal gradients for the studied region would greatly improve the calculations; however there appears to be a lack of geothermal gradient data so this may be implausible at this time, and has certainly not been possible within the timeframe of this project.

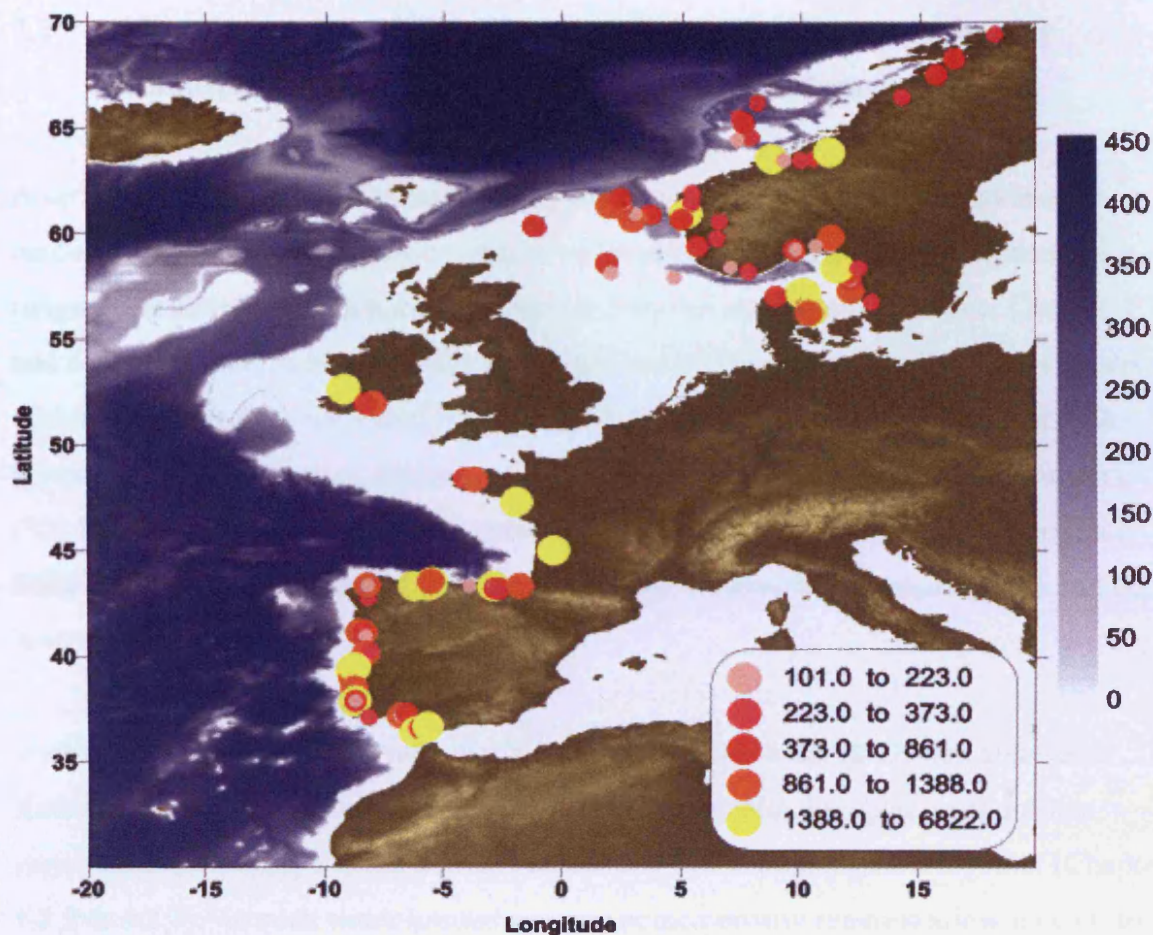


**Figure 7.1.** The predicted base to the hydrate stability zone (m) with posted major CO<sub>2</sub> sources along the Western European coastline within close proximity to the CO<sub>2</sub> hydrate stability zone. CO<sub>2</sub> source emissions are in tonnes per year and sourced data was collected between 1996 and 2002 (Holloway et al., 1996; IEA, 2002).

Although the developed model predicts suitable storage sites offshore Western Europe, this does not answer the feasibility of storage as a liquid and hydrate. It appears to offer many benefits over conventional supercritical storage including, increased density, viscosity and solubility; however, the suitability of hydrate as a storage medium within sediments has not yet been considered in this discussion.

Experimental investigation of carbon dioxide hydrate at the micro-scale (see Chapter 5) has been necessary to research hydrate formation within sediments to attempt to comprehend its suitability as a solid trapping mechanism, such as the effect of hydrate formation on the hosting sediments (see section 7.2).

## **7.2 What short-term effects will hydrate formation have on the hosting sediment? and how do sediment-hosted hydrates form?**

A series of laboratory experiments have been conducted in this study to investigate carbon dioxide hydrate formation within sediments. These experiments represent a range of conditions which may be present in a forced storage situation (see Chapter 4 and 5) and include; formation within fine-grained and coarse-grained sediment matrix, within sediment fully-saturated with water; within sediment partially-saturated with water, and within water of different salinity (deionised water and artificial seawater). CO<sub>2</sub> hydrate samples formed in the laboratory have been analysed under a cryogenic SEM and images show very detailed relationships between the formed hydrate and the hosting sediment.

Hydrate formed within sediment partially saturated with water (CO<sub>2</sub> rich and water limited) appears very crystalline under the BSEM, completely replacing the water meniscus surrounding sediment grains cementing the sediment grains together (Chapter 5.2.2 & 5.2.3). In such water limited systems some porosity remains allowing CO<sub>2</sub> to continue to pass through the sediment after hydrate formation with all the water present is replaced by hydrate. This would be unfavourable for a storage situation as open connected porosity may also allow upward vertical migration. The depth of liquid CO<sub>2</sub> injection, below the hydrate stability zone, could mean however, that if liquid CO<sub>2</sub> was to pass through such open porosity it would simply enter a zone higher into the stability zone and form hydrate. This could impede the escape of CO<sub>2</sub>, though the system may remain permeable eventually allowing CO<sub>2</sub> seepage. Experiments show this is not the case for sediment fully saturated with water (water rich). In a fully saturated system hydrate appears to be completely pore filling, cementing the sediment grains and apparently sealing the system (see Chapter 5). Hydrate is seen to form a solid layer within the upper sediment horizon, stopping any further CO<sub>2</sub> from entering sediment and water below this layer, therefore leaving the remaining lower sediment horizon uncemented with seawater filled pores (see Chapter 5.2.3). Someya et al (2006) discovered even a thin sealing hydrate 'cap' can maintain its sealing capacity after withstanding as much as 10MPa of pressure, and the sealing ability of the hydrate layer is mainly dependant on the availability of water in the system. The qualitative observations from experimental results within this study seem to be in agreement with

Someya et al (2006), adding support for the sealing nature of hydrate within sediment, and therefore the suitability of hydrate as a trapping mechanism for carbon storage. Further quantitative studies of the seal capacity of hydrate would however be necessary.

In these two systems (water rich and, CO<sub>2</sub> rich, water poor) the hydrate formed as pore-filling cement within high porosity sands, and hence as disseminated hydrate. In finer grained sediment there is evidence to suggest hydrate preferentially forms as veins, nodules, and other such forms (Clennell et al., 2000; Holditch et al., 2006). It is important to understand hydrate formation in finer grained sediment should these sedimentary conditions be present in a storage environment.

It has proven extremely difficult to form hydrate within clays and muddy sediments during this study, with very few successes in achieving this goal, seemingly due to impeded formation in low porosity, fine-grained sediment (see Clennell et al., 2000). Hydrate formation within clay sediment was achieved by formation along a sand/clay interface. In this sample the hydrate grew into the clay, pushing the clay grains apart, either forming from the sandy interface, or as discrete 'pods' within the clay (Chapter 5.2.3). Another example of this grain displacing hydrate formation has been seen in a natural mixed sediment sample, where the hydrate formed a lens along a horizontal fracture within the muddy sediment (see Appendix B). Therefore, formation processes involved within finer sediment appears to be different than that observed in sandy sediment. There appears to be a degree of sediment grain displacement during hydrate formation within finer sediment (clay), and should certainly be considered for storage developments (see Chapter 5).

It is only possible to investigate a limited number of variables in the laboratory at one time and of course the natural environment is considerably more complex than those created during the formation of synthetic samples. As there are no known natural occurrences of sediment-hosted carbon dioxide hydrate, no samples are available for investigation. Consequently natural methane hydrate samples provide the obvious and nearest analogue. Methane and carbon dioxide hydrate formation processes appear to be very similar (Chapter 5, 6; Stern et al., 2004) (and they are both structure I hydrates); therefore it may be possible to apply knowledge gained from investigation of one to the other. Also natural methane hydrate is being considered as a possible future energy

resource, and should storage as a liquid and hydrate be actively considered in the future it will be necessary to avoid contamination of these natural methane gas reserves, therefore knowledge of the stability of methane hydrate is important.

Fortunately it has been possible to include the investigation of natural methane hydrate samples as a part of this project due to timely coincidence of BGS involvement with an IODP hydrate research expedition (311) along the Cascadia Margin, offshore Oregon (see Chapter 6). Analysis of these samples has yielded detailed results about in-situ natural hydrate formation. Some of the natural methane hydrate within this active vent field appears to have formed very rapidly, seemingly similar to the formation of carbon dioxide hydrate created within the laboratory (see Chapter 6), and experiments conducted within the laboratory have proved to be extremely useful, and directly applicable to these natural rapidly forming sediment-hosted hydrates. There has been concern about the relevance of artificially created laboratory hydrates for research into processes of natural hydrate formation; however in this case, artificially created samples appear to show close comparison with natural samples, helping to justify investigation in a controlled laboratory environment.

An interesting discovery of these investigations has been the formation of a wide variety of hydrate morphologies, which appear to reflect different formation conditions, and these resulting hydrate morphologies appear to affect the hosting sediment differently (see Chapters 5 and 6). A thorough understanding of these morphologies and their sedimentary effects is an important area of research to investigate further.

### **7.3 Is carbon storage as CO<sub>2</sub> hydrate within sub-seabed sediments a feasible storage method?**

The proposed method of carbon storage as a liquid and hydrate into cool sub-seabed sediments is still in its infancy, and to date no initial field studies to test the method have been undertaken. However, there are natural systems where methane hydrate forms a seal above a porous rock stratum creating an effective gas trap (Kvenvolden, 1994; IEA GHG, 2000), for example the Messoyakha gas field. In such natural examples hydrate forms at the junction between a free gas zone and a water rich zone within the hydrate stability zone, sealing the system and trapping free gas beneath it.

No known examples are recorded for natural sediment-hosted carbon dioxide hydrate. The rarity of carbon dioxide hydrate samples in nature may be due to microbial reduction of CO<sub>2</sub> into CH<sub>4</sub>, and if this is the case biological activity may, over time, reduce the stored CO<sub>2</sub>, naturally replenishing the methane we have been extracting for energy production. CO<sub>2</sub> storage as a liquid and hydrate can use the same systems as are seen in these methane traps. The CO<sub>2</sub> hydrate trap or 'cap' would not exist prior to injection, and would have the potential to be self-sealing should any rupture occur. The impermeable, sealing/trapping mechanism introduced by the use of hydrate in the storage method is one area, which has been examined qualitatively within this project, and only a thin hydrate layer appears to restrict CO<sub>2</sub> transport into water-saturated sediments below. However, this impermeable hydrate 'cap' should only be considered as an additional sealing layer to a natural cap-rock present at the storage site.

There are a number of factors to consider when selecting suitable storage sites, including physical, chemical and geological properties of the area. Physical conditions include temperature, pressure, and geothermal gradient. A simplified general investigation of these conditions has been undertaken during this study, and maps generated to provide an initial assessment of suitable offshore areas for storage as a liquid and hydrate. A similar, more detailed investigation would be required on a site-to-site basis to ensure accuracy. Additional knowledge would be required on host sediment properties, particularly porosity, permeability, geo-chemistry and geo-mechanical strength, on pore-water chemistry and reservoir fluid dynamics, as well as detailed knowledge on the presence of any overlying natural cap-rock, which would be critical for site selection. The most suitable structures for storage of carbon dioxide will be permeable aquifers or reservoirs with an impermeable seal. Such structures are similar to those sought in petroleum exploration; therefore, the identification of a suitable site would use similar exploration techniques.

As well as finding a site with suitable conditions for this storage method, site selection is also highly dependent on the safety of the site, and the costs involved. The cost of deep sea drilling and the laying of underwater pipelines for CO<sub>2</sub> transport to the storage site would be one major cost, as well as the development of infrastructure, site management and monitoring. A detailed assessment of the economics involved in the storage practice is outside the scope of this project, however pipeline costs are usually

calculated by length (Holloway et al., 1996) and the vertical pipelines drilled for CO<sub>2</sub> storage as a liquid and hydrate would be a similar length to those used for supercritical CO<sub>2</sub> storage (though presumably deep water drilling is more costly). Other costs involved including the development of infrastructure, management and monitoring is presumably similar to those of offshore supercritical storage schemes. Safety considerations would be similar to those in the petroleum industry and conventional CO<sub>2</sub> storage installations, but I will discuss these in more detail in section 7.4.

A possible offset for the costs of storage as a hydrate could be to convert natural methane hydrate to carbon dioxide hydrate by injecting CO<sub>2</sub> into natural hydrate reservoirs, releasing methane gas in the process, which could then be used for energy production (IEA GHG, 2000; Kvamme et al., 2007). There is considerable uncertainty about the efficiency of this process. Laboratory experiments indicate the conversion of CH<sub>4</sub> hydrate to CO<sub>2</sub> hydrate is a very slow process, and in sub-seabed environments mass transport limitations will ensure very limited access of the injected CO<sub>2</sub> to the existing hydrate deposits (IEA GHG, 2000). Natural methane hydrate deposits appear to be sporadic, and their formation in the natural environment is still poorly understood, therefore it would be difficult to identify a site with suitable volumes of methane for extraction. Additionally, any gas stream produced is likely to be contaminated by the injected CO<sub>2</sub>, and gas separation would add to the cost of recovery. The storage of CO<sub>2</sub> combined with the extraction of methane may also create a moral dilemma, as the extracted methane could be used as a source of energy, which in turn would produce more CO<sub>2</sub>.

Although there are a number of practical issues to solve, these issues are very similar to those faced by proven conventional underground CO<sub>2</sub> storage schemes, which are currently storing considerable quantities of CO<sub>2</sub> as a supercritical phase. This project has shown there are large areas offshore Western Europe which may have the potential to store considerable volumes of CO<sub>2</sub> as a liquid and hydrate, and hydrate appears to form rapidly and relatively easily in sandy sediments, cementing the sediment grains together and adding to the sediments' stability. Hydrate formation also appears to restrict further gas flow into underlying sediments, creating a solid layer, which may add to the sealing capacity of a natural cap-rock. These preliminary investigations

show CO<sub>2</sub> storage as a liquid and hydrate to be a possible feasible storage method, which should be investigated further as an additional CO<sub>2</sub> mitigation strategy.

#### **7.4 What potential problems could be encountered?**

Although successful conventional underground carbon dioxide storage has already been administered for a number of years, there remains the possibility of something going wrong and therefore it is important to consider potential problems. Potential problems for storage as a liquid and hydrate share similarities with those considered for supercritical storage with the addition of a few specific problems relating to the stability of hydrate in sub-seabed sediments.

Injection of fluid into a sediment layer or fractured rock modifies its mechanical state and high pore pressure gradients in and/or around the reservoir may induce micro-earthquakes, and possibly larger seismicity as a result of injection (Holloway et al., 1996). Additionally the Earth's surface may sink or rise (subsidence or uplift) due to a change in pore space, depending on factors such as formation thickness, the extent of the formation, the characteristics of the overburden and the level of compaction. Such geo-mechanical problems are not predicted to occur in conventional carbon storage schemes (Holloway et al., 1996), but should be considered as potential problems particularly as hydrate formation effects on the hosting sediment are still poorly understood.

There is always the possibility of some leakage of CO<sub>2</sub> from the storage site. Leakage from pipelines can occur due to corrosion (on older sites), ground movement, bad connections, and external damage of the pipelines (Holloway et al., 1996). Natural geological instabilities, such as geothermal or seismic activity near a CO<sub>2</sub> store could introduce a risk of leakage, and a fault, or permeable pathway through the reservoir cap-rock could provide another route for CO<sub>2</sub> to escape. The chances of leakage through such events would be greatly reduced by accurate surveying and site selection, to ensure an efficient cap-rock and a stable environment for storage. Storage as a liquid and hydrate also introduces a potential solid impermeable trapping mechanism beneath the natural cap-rock, adding to the sealing capacity of the system, and significantly reducing the potential of any leakage from the underlying store of CO<sub>2</sub>. This storage

technique would be dependent on deep-water sub-seabed sediments; therefore if any leakage occurred the CO<sub>2</sub> would escape into deep waters and be absorbed into the ocean before it could escape into the atmosphere.

The potential environmental impact of CO<sub>2</sub> escaping into onshore ground waters must be considered, influencing water-rock reactions and the effects of pH reduction by acidic CO<sub>2</sub> in formation waters. The reduction of pH could adversely effect any bacterial populations present in or near the storage site, and therefore site-specific biological impact assessments would be necessary.

From the investigation of laboratory formed CO<sub>2</sub> hydrate samples this project has also observed that in a forced system (such as a man-made storage site) rapid CO<sub>2</sub> hydrate formation can occur at salt saturation. Hydrate formation at salt saturation leads to the inclusion of salts (principally halite) within the hydrate crystals. This inclusion of salt within the hydrate may influence the stability of the hydrate, and would need to be considered in a storage scenario. During hydrate formation salts are usually excluded from the crystals, concentrating the surrounding pore-waters, as has been observed in nature. In Chapter 6 there is discussion that in some areas of rapid natural methane hydrate formation these brine pore-waters have been seen between hydrate crystals, as they have not had time to diffuse away. In many of the CO<sub>2</sub> samples these brines have been concentrated to the point of salt precipitation in-situ, with the precipitated salt filling any inter-crystalline porosity which may have existed during early stages of growth, adding to the sealing capacity of the hydrate.

The stability of the hydrate is an important issue, and therefore any influence on temperature, pressure, geothermal gradient and salinity needs to be addressed as a potential problem. Global warming may be an influence on these conditions. As global temperatures continue to rise, a warming of the oceans has been noted. The effect of this temperature increase is negligible at the seafloor under deep waters, and a very large temperature difference would be required to warm a sub-seabed sediment layer. Additionally, global sea levels are rising in parallel to temperature increase, which increases pressures at the seafloor, possibly offsetting some of the warming influence on hydrate stability. However, catastrophic temperature increase would have a major influence on hydrate stability; for example due to submarine volcanic eruption, or due

to the collapse of the thermohaline circulation system. In the North Atlantic, deep water formation creates dense cold waters, with temperatures reaching as low as  $-0.9^{\circ}\text{C}$ . If this deep water formation was to collapse much warmer waters would entrench sub-seabed sediments. This could reduce the depth to the base of the hydrate stability zone (Figure 7.2) and could create mass dissociation of any hydrate present in near surface sediments potentially leading to slope instabilities. Although these temperature increases do have implications for this storage scenario, effects would be minimised by injection beneath a thick hydrate stability zone, ensuring the  $\text{CO}_2$  hydrate 'cap' was well within its stability regime. Such major temperature increases would also be a concern for natural methane hydrate deposits, whose massive dissociation in Earth's history has been seen to cause the warming of global temperatures, especially as it has a greater radiative forcing (x16) than  $\text{CO}_2$ . Natural hydrate deposits would be largely unmonitored and so dissociation could go unseen until dramatic consequences are unavoidable; whereas stored  $\text{CO}_2$  hydrate is likely to have a stringent monitoring procedure in place.

Though realistically implausible, if any  $\text{CO}_2$  did escape into the atmosphere in large quantities a major risk would be suffocation of humans (though minimal in offshore environments) and animals. Under atmospheric conditions  $\text{CO}_2$  is heavier than air, and it therefore tends to pool in topographic depressions driving away oxygen.  $\text{CO}_2$  is a colourless, odourless gas and initially would go unnoticed. A rare natural disaster in 1986 killed more than 1700 people from a sudden release of large quantities of volcanic  $\text{CO}_2$  from Lake Nyos in Cameroon, which demonstrates how hazardous  $\text{CO}_2$  can be (Kling et al., 1987). In terms of the environmental potential risk of  $\text{CO}_2$  entering the atmosphere, should any leakage cause an increase in atmospheric concentrations, this increase would still be less than that caused from direct emissions by point sources, as the chances of all the stored  $\text{CO}_2$  escaping into the atmosphere is extremely slim.

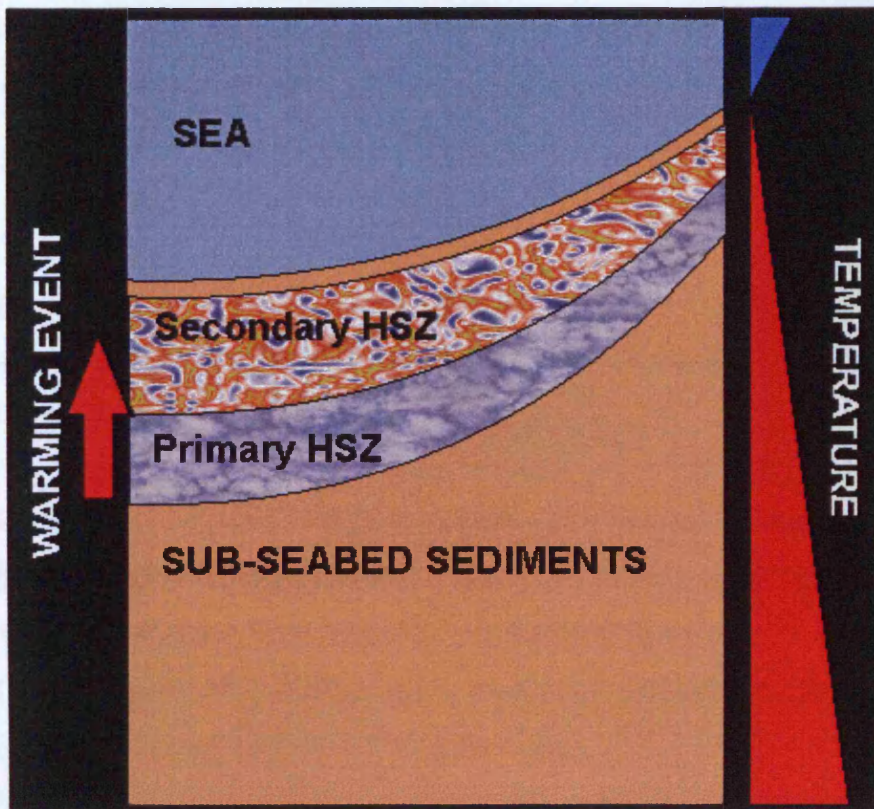


**Figure 7.2.** Schematic diagram of the sub-sea hydrate stability zone (HSZ). Ocean temperatures decrease with increased depth, and sub-seabed sediment temperatures increase with increased depth according to the geothermal gradient, and these temperature and pressure conditions determine the depth to the base of the HSZ. If there were considerable warming of sub-seabed sediments within this zone, the base of the HSZ would rise into shallower sediments, reducing the volume of the HSZ.

With research, surveying and modelling for site selection, effective risk assessment, site management and monitoring, this novel storage technique should prove a safe underground carbon dioxide storage method. It has been shown very large volumes of CO<sub>2</sub> could be trapped within its hydrate phase and its liquid phase within deep-water cool sub-seabed sediments. Increased solubility, viscosity, density and the precipitation of solid impermeable hydrate appears to be advantageous for long-term storage, supporting the use of this method in addition to conventional supercritical storage. However; although we have gained considerable knowledge through the investigatory pathways followed during this project, there are many details which need clarification

and further research; and filling these knowledge gaps is extremely important to advance this storage technique.

## **7.5 What gaps remain in our knowledge?**

This project has highlighted a number of research areas which need addressing through further research, from both modelling stability and hydrate formation experiments, including:

- Geothermal gradient data collection to generate detailed geothermal gradient maps for hydrate stability predictions.
- The effect of halite inclusion on the stability of CO<sub>2</sub> hydrate.
- Geo-mechanical effects of hydrate formation in sediments and the quantitative sealing capacity of sediment-hosted hydrates.
- The effect of the rate and extent of the supply of hydrate forming components on hydrate formation.
- The formation and effect of different hydrate morphologies on salt exclusion/inclusion and sediment geo-mechanical properties.
- Technology and costs required for CO<sub>2</sub> storage as a liquid and hydrate.

To select a site for storage of CO<sub>2</sub> as a liquid and hydrate the conditions under which hydrate forms must be clearly distinguished. There appears to be a general lack of detailed geothermal gradient data for sub-seabed sediments, and unless these are determined, further improvement of the stability model could not reduce the level of uncertainty. With maps of geothermal gradient the CO<sub>2</sub> hydrate model could be refined by altering the equilibrium constants for a change in equilibrium in seawater, and improving the regression of equilibrium data for the determination of model constants. Additionally more refined temperature gradients may improve the stability results. The contouring of the hydrate stability zones may be improved by the use of ArcGIS for comparison with geological data. Seafloor sediment data would also help to narrow down specific suitable sites.

Additionally hydrate formation within sediments remains to be relatively poorly understood, and this is critical to evaluate the potential of this storage method. The supply of hydrate forming components, the hosting sediment and the rate of formation seems to influence the hydrate morphology of the hydrate, the exclusion of salts and the effect the hydrate formation has on the hosting sediment. The complex amalgamation of causes and effects has been difficult to distinguish, but with a series of highly controlled experiments (ensuring repeatability) investigating one parameter at a time, and more detailed petrography, it may be possible to understand these complex formation processes. The inclusion of halite in CO<sub>2</sub> hydrate crystals is another important area of interest to follow up, and investigations into the effect this has on the stability and permeability of the hydrate may prove necessary to fully scope the efficiency of this storage approach.

Neither technology nor costs for storage as a liquid a hydrate have been considered during this preliminary study. However, these factors are still important to investigate to produce a complete picture of the potential of this approach.

## **7.6 Are there any further implications to the research?**

In addition to the carbon storage community the hydrate formation and stability research presented within this project have implications for many research communities. Interest in natural methane hydrates on Earth is wide and varied, including its role in sub-marine slope stability, in past and present climate change, in the global carbon cycle, and its potential role as a future energy resource, and carbon dioxide hydrate investigations have been seen to assist in understanding natural methane hydrate formation. There is the possibility of both carbon dioxide and methane hydrate existence elsewhere in the solar system; therefore the space science community are showing an increasing interest in their formation and stability. Additionally, carbon dioxide hydrate is being researched as a possible desalination agent, and salt inclusion studies within this project may be extremely relevant in static desalination systems.

Interest in hydrates appears to be growing and hopefully with further research we can answer questions posed within this thesis.

## **CHAPTER 8**

### **Conclusions**

## 8. Conclusions

- The motivation for this PhD research study has been to understand key scientific aspects underpinning the feasibility of carbon storage as CO<sub>2</sub> hydrate within sub-seabed sediments.
- Rising CO<sub>2</sub> emissions are contributing to climate change and rising global temperatures. If no action is taken to reduce these emissions the effects of global warming such as droughts, floods and extreme weather could be exacerbated.
- Other than a major change in human lifestyle, no current single technology or process is believed to be able to achieve the emissions reduction required to stabilise atmospheric CO<sub>2</sub> concentrations at a predicted level of 550 ppmv to ensure a global temperature rise of no more than 2 °C. However, one proven method which could help to reduce these greenhouse emissions is Carbon Capture and Storage (CCS).
- CCS involves capturing CO<sub>2</sub> at the point source and storing it within another domain of our planet. Conventional underground storage has been practised since 1996 in the North Sea Sleipner gas field, where CO<sub>2</sub> is stored in its supercritical phase within deep, warm rocks.
- An additional underground storage method receiving relatively little attention, CO<sub>2</sub> storage as a liquid and hydrate. This would involve the injection of CO<sub>2</sub> into cool, deep water, sub-seabed sediments below the hydrate stability zone. Under these pressure and temperature conditions CO<sub>2</sub> would be in its slightly buoyant liquid phase. As the CO<sub>2</sub> rises into cooler sediments and enters the hydrate stability zone it may form a solid hydrate phase ‘capping’ the underlying store of liquid CO<sub>2</sub>. This method has several potential advantages including increased CO<sub>2</sub> density, viscosity and solubility at lower temperatures, all of which have the potential to aid long-term storage.

- Hydrates are crystalline ice-like solids built of a cage of ‘host’ water molecules and one or more hydrate ‘guest’ molecules. The majority of natural hydrates are primarily composed of methane and can be found worldwide along continental margins and in permafrost settings including Lake Baikal, Cascadia Margin, Gulf of Mexico and offshore Norway. They have received wide and varied research interest ranging from their role in the carbon cycle to their potential as a future energy resource.
- The aims of this project to assist in understanding scientific aspects of this more novel storage method have been to help to answer the following questions:
  - Are there suitable CO<sub>2</sub> storage sites offshore Western Europe for storage as a liquid and hydrate?
  - What short-term effects will hydrate formation have on the hosting sediment, and how do sediment-hosted hydrates form?
  - Is carbon storage as CO<sub>2</sub> hydrate within sub-seabed sediments a feasible storage method?

These have been addressed by two main investigatory pathways: hydrate stability computer modelling, and hydrate formation within sediments (in synthetic CO<sub>2</sub> hydrates and natural in-situ methane hydrates).

- Computer models have been developed to successfully predict the depth to the base of the CO<sub>2</sub> hydrate and CH<sub>4</sub> hydrate stability zones, and have been applied to regions offshore Western Europe.
- These preliminary investigations have determined large regions offshore Western Europe with suitable pressure and temperature conditions for the storage of CO<sub>2</sub> as a liquid and hydrate. Models predict the base of the CO<sub>2</sub> hydrate stability zone could reach a maximum of 460 m below the seafloor, in comparison with the maximum depth to the base of the CH<sub>4</sub> hydrate stability zone of 867 m below the seafloor (assuming a 30 °C/km average geothermal gradient).

- Simple calculations predict the CO<sub>2</sub> hydrate stability zone to have a total volume of  $1.3 \times 10^9 \text{ km}^3$  within the Western European 200 mile economic zone, which may have the potential to store as much as 429 Gt of CO<sub>2</sub> in its hydrate phase.
- Although predicting areas with suitable pressure and temperature conditions; sediment characteristics, such as porosity and permeability, have not been taken into consideration. It is also important to consider possible errors within the calculations (see Chapter 3 for further details), with the largest uncertainty lying in the geothermal gradient used. The models are highly sensitive to geothermal gradient, and detailed assessments of geothermal gradients for the studied region would greatly improve the calculations.
- The investigation of CO<sub>2</sub> hydrate manufactured in the laboratory and naturally occurring CH<sub>4</sub> hydrate, at the micro-scale, has been an important component of this study to research hydrate formation within sediments to attempt to comprehend its suitability as a solid trapping mechanism.
- A series of laboratory experiments have been conducted to represent CO<sub>2</sub> hydrate formation over a range of conditions, including formation within fine-grained and coarse-grained sediment, within fully-water-saturated and partially-water-saturated sediment, and within water of different salinity. These laboratory samples were then analysed with a cryogenic-Backscattered Scanning Electron Microscope (BSEM) and Energy Dispersive X-ray Analysis (EDXA).
- Experimental samples showed different hydrate morphologies resulting from different formation conditions: euhedral crystalline hydrate, acicular hydrate, ‘melt-structure’ or granoblastic hydrate, ‘holey’ or micro-porous hydrate, ‘vesicular’ hydrate, and ‘pea-pod’ hydrate.
- CO<sub>2</sub> hydrate/sediment interactions also appear to alter with formation conditions. Within CO<sub>2</sub>-rich environments the hydrate appeared to form around the grains, cementing them together. Within water-rich environments hydrate was mainly seen to form as pore-filling cement sealing the system from further CO<sub>2</sub> access, but is

also seen as sediment displacing hydrate pushing the grains apart during formation (though this form was largely restricted to clay-rich sediment).

- The pore-filling (apparently sealing) hydrate which forms within water-rich environments would be advantageous for CO<sub>2</sub> storage, allowing a hydrate 'cap' to aid the trapping of an underlying liquid CO<sub>2</sub> store. The sealing ability of a hydrate 'cap' has been found to be dependent on the availability of water in the system in previous research (Someya et al., 2006), and observations from this study appear to be in agreement.
- Hydrate formation within clay sediments appears to be different than that observed within sandy sediments, forming as sediment-displacing hydrate. This sediment displacement could create weaknesses, and should be considered for storage developments.
- Investigations also revealed interesting salt (mainly halite) fabrics within the hydrate samples that varied with hydrate formation mechanisms, which to my knowledge have never before been documented. Samples show halite deposited along crystal boundaries and as solid inclusions within hydrate crystals. This salt inclusion seems to be a consequence of rapid hydrate formation, with CO<sub>2</sub> hydrate formation at salt saturation. Salt inclusion during rapid hydrate formation may have important implications for natural hydrate research, static desalination systems, and should be considered during the development of the CCS method of storage of CO<sub>2</sub> as a hydrate.
- Only a limited number of variables can be investigated within the laboratory, and the natural environment is considerably more complex. As there are no known natural occurrences of sediment-hosted CO<sub>2</sub> hydrate, there are no samples available, and natural methane hydrate samples provide the nearest analogue.
- Natural methane hydrate cores (U1328B and U1327C) have been sub-sampled and analysed from the Cascadia Margin, offshore Oregon, yielding detailed results. Cryogenic BSEM imaging revealed a number of well preserved methane hydrate

morphologies, similar to those formed in synthetic CO<sub>2</sub> hydrate samples. These include crystalline hydrate, micro-porous hydrate, ‘dense’ or massive hydrate, acicular hydrate, granoblastic hydrate and ‘vesicular’ hydrate. In addition analysis revealed complex brine filled pore networks between hydrate crystals preserved as salt fabrics. No hydrate or salt fabrics have been observed in core 1327C.

- The three main forms of hydrate present within the imaged natural methane hydrate samples appear to represent different stages of formation. ‘Dense’ or massive hydrate, containing no salt fabrics (brine), appears to be an older, primary, slower forming morphology. This is surrounded by a secondary, younger, micro-porous form, containing very little salt (brine), formed after partial dissociation of the massive hydrate. The tertiary, overlying crystalline form, surrounding micro-channels appear to be the youngest, rapidly forming morphology with concentrated brine-filled pore-networks. Micro-channels within the samples may have been ‘feeder’ channels supplying the hydrate with necessary formation components.
- The interpretation of these natural methane hydrate samples has been aided by previous investigation of synthetic CO<sub>2</sub> hydrates which revealed similar morphologies and salt (brine) fabrics (although CO<sub>2</sub> samples differs as they also appeared to show salt inclusion during hydrate formation). Therefore, it is proposed that salt distribution (cryogenically frozen brine) could be considered in the investigation of hydrate samples under cryogenic-BSEM. The similarity between natural and synthetic samples also supports the use of laboratory formed CO<sub>2</sub> hydrates to investigate hydrate formation.
- Research into carbon storage as CO<sub>2</sub> liquid and CO<sub>2</sub> hydrate is still in its infancy, and this project has only studied a small number of factors which need to be investigated. Costs, safety, biological implications, the physical, chemical and geological properties, and the effects of liquid CO<sub>2</sub> storage on the storage system, would all need to be studied prior to field testing stages.
- This project has shown large regions offshore Western Europe which may have the potential to store considerable volumes of CO<sub>2</sub> as a hydrate. CO<sub>2</sub> hydrate also

appears to form rapidly and relatively easily in sandy sediments, cementing the sediment grains. In water-rich environments hydrate appears to create pore-filling cement that may impede further CO<sub>2</sub> flow to underlying sediments, which may add to the sealing capacity of a natural cap-rock. These preliminary investigations support CO<sub>2</sub> storage as a hydrate as a potential feasible storage method, and this method should be pursued further as an emissions reducing mitigation strategy.

- A number of research areas have been highlighted within this project, which need to be addressed through further modelling and laboratory investigations. These include:
  - Improvement of geothermal gradient data and hydrate stability models for stability predictions.
  - The effect of halite inclusion on the stability of CO<sub>2</sub> hydrate.
  - Geo-mechanical effects of hydrate formation in sediments.
  - The effect of rate and extent of the supply of hydrate forming components on hydrate formation.
  - The formation and effect of different hydrate morphologies on salt exclusion/inclusion and sediment geo-mechanical properties.
  - The technology and costs required for CO<sub>2</sub> storage as a liquid and hydrate.
  
- Research results from this project not only have implications for the storage community, but also for static desalination systems, the space community for research on hydrates elsewhere in the solar system, and for research into the roles natural hydrates have on sub-marine slope stability, past and present climate change, the global carbon cycle, and its potential as a future energy resource.

## **References**

## References

- Anderson, R., Tohidi, B. & Webber, J. B. W. 2007. Gas hydrate growth and dissociation in narrow pore networks: Capillary inhibition and hysteresis phenomena. *Geological Society Special Edition*, In press.
- Andreasson, K., Mienert, J., Berteussen, K. A., Sognnes, H., Henneberg, K., Langhammer, J., & Anonymous. 2000. Multi-component seismic data in gas hydrate investigations. *Annual Meeting Expanded Abstracts, American Association of Petroleum Geologists*, 7.
- Ashi, J., Tokuyama, H & Taira, A. 2002. Distribution of methane hydrate BSRs and its implication for the prism growth in the Nankai Trough. *Marine Geology*, **187** (1), 177-191.
- Atreya, S. K. 2007. The Mystery of Methane on Mars & Titan. *Scientific American*, May 2007, 24-33.
- Austvik, T & Loken, K. P. 1992. Deposition of CO<sub>2</sub> on the seabed in the form of hydrates. *Energy Conversion Management*, **33** (5-8), 659-666.
- Bachu, S., Gunter, W. D. & Perkins, E. H. 1994. Aquifer disposal of CO<sub>2</sub>: hydrodynamic and mineral trapping. *Energy Conversion Management*, **35**, 269-279.
- Baines, S. J. & Worden, R. H. 2004a. Geological Storage of Carbon Dioxide. *Geological Society Special Publication*, **233**, 255p.
- Baklid, A., Korbøl, R. & Owren, G. 1996. Sleipner Vest CO<sub>2</sub> disposal, CO<sub>2</sub> injection into a shallow underground aquifer. *Society of Petroleum Engineers*, **36600**, 269-277.
- Berecz, E. & Balla-Achs, M. 1983. Gas hydrates. *Elsevier Science Publishing Co., Inc, New York, NY*, pp344.

BGS. 2004. Information regarding borehole sediment records offshore the North and West of Scotland. Personal communication.

Booth, J. S., Winters, W. J., Dillon, W. P., Clennell, M. B. & Rowe, M. M. 1998. Major occurrences and reservoir concepts of marine clathrate hydrates: implications of field evidence. In *Gas Hydrates, Geological Society Special Publications*, **137**, 113-128.

Brewer, P. G., Friederich, G., Peltzer, E. T. & Orr, F. M. Jr. 1999. Direct experiments on the ocean disposal of fossil fuel CO<sub>2</sub>. *Science*, **284**, 943-945.

Buenz, S., Mienert, J. & Berndt, C. 2003. Geological controls on the Storegga gas-hydrate system of the mid-Norwegian continental margin. *Earth and Planetary Science Letters*, **209**, 291-307.

Buffet, B. & Archer, D. 2004. Global inventory of methane clathrate: sensitivity to changes in the deep ocean. *Earth and Planetary Science Letters*, **227**, 185-199.

Bugge, T., Befring, S. & Belderson, R. H. et al. 1987. A giant three-stage submarine slide off Norway. *Geo-marine Letters*, **7**, 191-198.

Bunz, S., Mienert, J. & Berndt, C. 2003. Geological controls on the Storegga gas-hydrate system of the mid-Norwegian continental margin. *Earth and Planetary Science Letters*, **209** (3), 291-307.

Camps, A. P., Rochelle, C. A., Milodowski, A. E., Sims, M. R., Pullan, D. & Lovell, M. A. 2007. The potential for applying cryogenic SEM imaging to help understand ices and hydrates under conditions of the Martian cryo-sphere. Submitted to *Astrobiology*.

Camps, A. P., Rochelle, C. A., Milodowski, A., Long, D., Lovell, M. A., Bateman, K., Gunn, D., Jackson, P. & Rees, J. 2006. The underground storage of CO<sub>2</sub> at low temperatures and its trapping in solid phases. *Abstract within the proceedings of the 8<sup>th</sup> International Conference on Greenhouse Gas Control Technologies (GHGT-8), Trondheim, Norway, 19-22 June 2006.*

Chatti, I., Delahaye, A., Fournaison, L. & Petitet, J-P. 2004. Benefits and drawbacks of clathrate hydrates: a review of their areas of interest. *Energy Conservation and Management*, **46** (9-10), 1333-1343.

Clennell, M. B., Henry, P., Hovland, M., Booth, J. S., Winters, W. J. & Thomas, M. 2000. Formation of Natural Gas Hydrates in Marine Sediments: Gas Hydrate Growth and Stability Conditioned by Host Sediment Properties. *Annals of the New York Academy of Sciences*, **912**, 887-896.

Clennell, M. B., Hovland, M., Booth, J. S., Henry, P. & Winters, W. J. 1999. Formation of natural gas hydrates in marine sediments; 1, Conceptual model of gas hydrate growth conditioned by host properties. *Journal of Geophysical Research B*, **104** 22,985-23,003.

Collett, T. S., Lewis, R & Uchida, T. 2000. Oilfield Review: Growing Interest in Gas Hydrates.

Collett, T. S., Lewis, R. E., Dallimore, S. R., Lee, M. W., Mroz, T. H. & Uchida, T. 1999. Detailed evaluation of gas hydrate reservoir properties using JAPEx/JNOC/GSC Mallik 2L-38 gas hydrate research well downhole well-log displays. *In: Dallimore, S. R., Uchida, T. & Collett (eds), Scientific Results from JAPEx/JNOC/GSC Mallik 2L-38 Gas Hydrate Research Well, Mackenzie Delta, Northwest Territories, Canada. Bulletin of the Geological Survey of Canada*, **544**, 295-311.

Colwell, F., Matsumoto, R. & Reed, D. 2004. A review of the gas hydrates, geology, and biology of the Nankai Trough. *Chemical Geology*, **205**, 391-404.

Corthay, J. E. II. 1998. Delineation of a massive seafloor hydrocarbon seep, over pressured aquifer sands and shallow gas reservoirs, Louisiana Continental Slope. *Proceedings of the Offshore Technology Conference*, OTC **8594**, 37-56.

Craig, H., Shoji, H., & Langway, C. C, Jr. 1993. Nonequilibrium air clathrate hydrates in Antarctic ice: A paleopiezometer for polar ice caps. *Proceedings of the National Academy of Science, USA*, 11416-11418.

Dallimore, S. R., Collett, T. S., Uchida, T., Weber, M., Takahashi, H. & Team MGHR. 2002. Overview of the 2002 Mallik gas hydrate production research well program. In: *Fourth international conference on gas hydrates*, 36-9.

Davies, R. J. & Cartwright, J. 2002. A fossilized Opal A to Opal C/T transformation on the northeast Atlantic margin: support for a significantly elevated Palaeogeothermal gradient during the Neogene? *Basin Research*, **14**, 467-486.

Davis, E. E. & Hyndman, R. D. 1989. Accretia and recent deformation of sediments along the northern Cascadia subduction zone. *Geological Society of America Bulletin*, **101**, 1465-1480.

Dickens, G.R. & Quinby-Hunt, M.S. 1994. Methane hydrate stability in seawater. *Geophysical Research Letters*, **21** (19), 2115-2118.

DTI. 2003. Energy White Paper: Our energy future-creating a low carbon economy. *TSO (The Stationary Office)*.

Durham, W. B., Kirby, S. H., Stern, L. A. & Zheng, W. 2003. The strength and rheology of methane clathrate hydrate. *Journal of Geophysical Research*, **108** (B4), 2182-2193.

Duxbury, N. S., Abyzov, S. S., Romanovsky, V. E. & Yoshikawa, K. 2004. A combination of radar and thermal approaches to search for methane clathrate in the Martian subsurface. *Planetary and Space Science*, **52** (1-3), 109-115.

Duxbury, N. S., Nealon, K. H. & Romanovsky, V. E. 2001. On the possibility of clathrate hydrates on the Moon. *Journal of Geophysical Research*, **106**(E11), 27, 811-827.

Falkowski, P., Scholes, R. J., Boyle, E., Candell, J., Canfield, D., Elser, J., Gruber, N., Hibbard, K., Hogberg, P., Linder, S., MacKenzie, F. T., Morre, B, Pedersen, T, Rosenthal, Y, Seitzinger, S, Smetacek, V, Steffen, W. 2000. The Global Carbon Cycle: A Test of Our Knowledge of Earth as A System. *Science*, **290**, 291-296.

- Fletcher, R. C. & Merino, E. 2001. Mineral growth in rocks: kinetic-rheological models of replacement, vein formation, and syntectonic crystallization. *Geochimica Cosmochimica Acta*, **65**, 3733-3748.
- Gao, S., House, W. & Chapman, W. G. 2005. NMR/MRI Study of Clathrate Hydrate Mechanisms. *Journal of Physical Chemistry B*, **109** (41), 19090-19093.
- Gardner, J. M. 2001. Mud volcanoes revealed and sampled on the Western Moroccan continental margin. *Geophysical Research Letters*, **28**, 339-342.
- Genov, G., Kuhs, W. F., Stayakova, D. K., Goreshnik, E. & Salamatin, A. N. 2004. Experimental studies on the formation of porous gas hydrates. *American Mineralogist*, **89**, 1228-1239.
- GESAMP. 1997. Report of the twenty-seventh session of GESAMP, Nairobi, Kenya, 14-18 April 1997. *GESAMP Reports and Studies*, **63**, 45pp.
- Ginsburg, G. D., Milkov, A. V., Soloviev, V. A., Egorov, A. V., Cherkashev, G. A., Vogt, P. R., Crane, K., Lorenson, T. D. & Khutorskoy, M. D. 1999. Gas hydrate accumulation at the Hakon Mosby Mud Volcano. *Geo-Marine Letters*, **19**, 57-67.
- Ginsburg, G. D. & Soloviev, V. A. 1997. Methane migration within the submarine gas-hydrate stability zone under deep-water conditions. *Marine Geology*, **137**, 49-57.
- Ginsburg, G., Kremlev, A., Grigor'ev, M., et al. 1990. Filtrogenic gas hydrates in the Black Sea. *Soviet Geology and Geophysics*, **31** (3), 8-16.
- Gipe, P. 2004. Wind Power – Renewable Energy for Home, Farm, and Business. *Chelsea Green Publishing*, pp512.
- Golden, K. M., Heaton, A. L., Eicken, H. & Lytle, V. I. 2005. Void bounds for fluid transport in sea ice. *Mechanics of Materials*.

Goldstein, J. I., Newbury, D. E., Echlin, P., Joy, D. C., Fiori, C. & Lifshini, E. 1981. Scanning Electron Microscopy and X-ray Microanalysis: A text for Biologists, Materials Scientists, and Geologists. *Plenum Press, New York*.

Golomb, D. 1993. Ocean disposal of CO<sub>2</sub>: Feasibility, economics and effects. *Energy Conversion Management*, **34** (9-11), 967-976.

Golomb, D. S., Zemba, S. G., Dacey, J. H. & Micheals, A. F. 1992. The fate of CO<sub>2</sub> sequestered in the deep ocean. *Energy Conversion Management*, **33** (5-8), 675-683.

Greenpeace International. 2003. Ocean disposal/sequestration of carbon dioxide from fossil fuel production and use: An overview of rationale, techniques and implications.

Gunter, W. D., Perkins, E. H. & McCann, T. J. 1993. Aquifer disposal of CO<sub>2</sub>-rich gases: reaction design for added capacity. *Energy Conversion Management*, **34**, 941-948.

Haeckel, M., Suess, E., Wallman, K. & Rickert, D. 2004. Rising methane gas bubbles form massive hydrate layers at the seafloor. *Geochimica Et Cosmochimica Acta*, **68** (21), 4335-4345.

Harrison, W. J., Wendlandt, R. F & Sloan, E. D. 1995. Geochemical interactions resulting from carbon dioxide disposal on the sea floor. *Applied Geochemistry*, **10**, 461-475.

Haugan, H.A. & Eide, L. I. 1996. CO<sub>2</sub> Capture and Disposal: The realism of large scale scenarios. *Energy Conversion Management*, **37** (6-8), 1061-1066.

Haugan, P. M & Drange H. 1992. Sequestration of CO<sub>2</sub> into the deep ocean by shallow injection. *Nature*, **357**, 318-319.

Heggland, H. D. & Nygaard, E. 1998. Shale intrusions and associated surface expressions-examples from Nigerian and Norwegian deepwater areas. In: *Proceedings of the Offshore Technology Conference, Houston, TX*, **1**, 111-124.

Henning, R. W., Schultz, A. J., Thieu, V. & Halpern, Y. 2000. Neutron Diffraction Studies of CO<sub>2</sub> Clathrate Hydrate: Formation from Deuterated Ice. *Journal of Physical Chemistry A*, **104**, 5066-5071.

Henriet, J. -P., De Mol, B., Pillen, S., Vaneste, M., Van Rooij, D., Versteeg, W., Croker, P. F., Shannon, P. M., Unnithan, V., Bouriak, S., Chachkine, P., & the Porcupine Belgica 97 shipboard party. 1998. Gas hydrate crystals may help build reefs. *Nature*, **391**, 648-649.

Henriet, J.-P. & Mienert, J. 1998. Gas Hydrates: the Gent debates. Outlook on research horizons and strategies. In *Gas Hydrates: Relevance to World Margin Stability and Climate Change*, Geological Society, Special Publications, **137**,1-8.

Herzog, H. & Golomb, D. 2004. Carbon capture and storage from fossil fuel use. In: *Encyclopedia of Energy*, Elsevier Science Inc., New York, 277-287.

Hesse, R. 2003. Pore water anomalies of submarine gas hydrate zones as tool to assess hydrate abundance and distribution in the subsurface. *Earth Science Reviews*, **61**, 149-179.

Hirai, S., Tabe, Y., Kuwano, K., Ogawa, K. & Okazaki, K. 2000. MRI Measurement of Hydrate Growth and an Application to Advanced CO<sub>2</sub> Sequestration Technology. In *Gas Hydrates: Challenges for the Future*, Annals of the New York Academy of Sciences, **912**, 246-253.

Holder, G. D., Corbin, G. & Papadopoulos, K. D. 1980. Thermodynamic and Molecular Properties of Gas Hydrates from Mixtures Containing Methane, Argon and Krypton. *Industrial and Engineering Chemical Fundamentals*, **19**, 282-286.

Holditch, S., Patzek, T., Moridis, G. & Plumb, R. 2006. Geomechanical performance of hydrate-bearing sediments in offshore environments. *Semi-Annual Report DOE Award Number DE-FC26-05NT42664*, Department of Energy, July 2006.

Holloway, S. 1997. An overview of the underground storage of carbon dioxide. *Energy Conversion Management*, **38**, S193-S198.

Holloway, S, Heederik, J. P., van der Meer, L. G. H., Czernichowski-Lauriol, I, Harrison, R., Lindeberg, E., Summerfield, I. R., Rochelle, C., Schwarzkopf, T., Kaarstad, O. & Berger, B. 1996. The Underground Disposal of Carbon Dioxide: Summary Report. *British Geological Survey, Keyworth*.

Holmes, R., Hobbs, P.R.N., Leslie, A.B., Wilkinson, I.P., Gregory, F.J., Riding, J.B., Hoult, R.J., Cooper, R.M. And Jones, S.M. 2003. DTI Strategic Environmental Assessment Area 4(SEA4): Geological evolution of Pilot Whale Diapirs and stability of the seabed habitat. *British Geological Survey Commercial Report CR/03/082*, 19pp.

Holmes, R., Alexander, S. A., Ball, K., Bulat, J., Evans, R., Long, D., MacBeth, C., McCormac, M. & Sankey, M. 1995. The issues surrounding a shallow gas database in relation to offshore hazards. *British Geological Technical Report WB 95/13C*.

Houghton, J. 1999. Global Warming: The complete briefing. *Cambridge University Press*, 251pp.

House, K. Z., Schrag, D. P., Harvey, C. F. & Lackner, K. S. 2006. Permanent carbon dioxide storage in deep-sea sediments. *Proceedings of the National Academy of Science, USA*, **103** (33), 12291-12295.

Hovland, M. & Svenson, H. 2006. Submarine pingoes: Indicators of shallow gas hydrates in a pockmark at Nyegga, Norwegian Sea. *Marine Geology*, **228**, 15-23.

Howe, J.A., Stoker, M.S., Masson, D.G., Pudsey, C.J., Morris, P., Larter, R.D. And Bulat, J. 2006. Seabed morphology and the bottom-current pathways around Rosemary Bank seamount, northern Rockall Trough, North Atlantic. *Marine and Petroleum Geology*, **23** (2), 165-181.

Huo, Z., Eaton, M., Miller, K. T. & Sloan, E. D. 2005. Design and Construction of an X-ray Diffraction Cell for Hydrate Studies at Elevated Pressures. *International Journal of Thermophysics*, **26** (1), 107-114.

IEA GHG. 2004. Gas Hydrates for Deep Ocean Storage of CO<sub>2</sub>. *IEA Greenhouse Gas R&D Programme Report*, **PH4/26**.

IEA. 2002. CO<sub>2</sub> Emissions from Fuel Combustion 1971-2000. *IEA, Paris*.

IEA. 2001. Putting the carbon back into the ground. *IEA Greenhouse Gas R&D Programme*.

IEA GHG. 2000. Natural gas and methane hydrates. *IEA Greenhouse Gas R&D Programme Report*, **PH3/27**.

IEA GHG, 2000. Issues underlying the feasibility of storing CO<sub>2</sub> as hydrate deposits. *IEA Greenhouse Gas R&D Programme Report*, **PH3/25**.

IEA GHG. 1998. Sleipner aquifer storage of CO<sub>2</sub>. *Greenhouse Issues*, **34**, 4.

Inaba, H. 2000. New challenge in advanced thermal energy transportation using functionally thermal fluids. *International Journal of Thermal Science*, **39**, 9-11.

IOC et al. IOC, IHO, BODC. 2003. Centenary Edition of the GEBCO Digital Atlas. Published on CD-ROM on behalf of the Intergovernmental Oceanographic Commission and the International Hydrographic Organization as part of the General Bathymetric Chart of the Oceans. *British Oceanographic Data Centre, Liverpool*.

IODP. 2006. Geologic and Oceanographic Setting. [http://www-odp.tamu.edu/publications/168\\_SR/chap\\_05/c5\\_3.htm](http://www-odp.tamu.edu/publications/168_SR/chap_05/c5_3.htm)

IPCC. 2007. Climate Change 2007: The Physical Science Basis. IPCC WGI Fourth Assessment Report.

IPCC. 2005. IPCC Special Report on Carbon Dioxide Capture and Storage. Prepared by Working Group III of the Intergovernmental Panel on Climate Change [Metz, B., O. Davidson, H. C. de Coninck, M. Loos, and L. A. Meyer (eds.)]. *Cambridge University Press, Cambridge, United Kingdom and New York, NY, USA*, 442 pp.

IPCC. 2001. Climate Change 2001: the Scientific Basis. Contribution of Working Group I to the third assessment report of the Intergovernmental Panel on Climate Change. [J. T. Houghton, Y. Ding, D. J. Griggs, M. Noguer, P. J. van der Linden, X. Dai, K. Maskell, and C. A. Johnson, (eds.)]. *Cambridge University Press, Cambridge, UK*.

Ivanov, M., Blinova, V., Kozlova, E., Pinheiro, L., van Werring, T. & Stadnitskaia, A. 2007. Natural gas hydrates from mud volcanoes in the Gulf of Cadiz. *Geophysical Research Abstracts*, **9**, 05495.

Ivanov, M., Blinova, V., Kozlova, E., Westbrook, G. K., Mazzini, A., Minshull, T. A. & Nouzé, H. 2007. First sampling of Gas Hydrate From the Vøring Plateau. *EOS, Transactions American Geophysical Union*, **88** (19), p209.

Javanmardi, J. & Moshfeghian, M. 2003. Energy consumption and economic evaluation of water desalination by hydrate phenomenon. *Applied Thermal Engineering*, **23**, 845-857.

Jaworowski, Z. 2007. CO<sub>2</sub>: The Greatest Scientific Scandal of Our Time, *EIR*, March 16<sup>th</sup> 2007, 38-53.

Jin, S., Takeya, S., Hayashi, J., Nagao, J., Kamata, Y., Ebinuma, T. & Narita, H. 2004. Structure Analyses of Artificial Methane Hydrate Sediments by Microfocus X-ray Computed Tomography. *Japanese Journal of Applied Physics*, **43** (8A), 5673-5675.

Johnston, P & Santillo, D. 2004. Carbon Capture and Sequestration: Potential Environmental Impacts. Produced for IPCC workshop on carbon dioxide capture and storage.

JOIDES. 1992. Ocean Drilling Program Guidelines for Pollution Prevention and Safety. *JOIDES Journal*, **18** (7).

Kaya, Y. 1995. The role of CO<sub>2</sub> removal and disposal. *Energy Conservation and Management*, **36** (6-9) pp.375-380.

Kemp, D., Coe, A. & Cohen, A. 2005. Burps that warmed the world. *Planet Earth*, p25.

Kennett, J. P., Cannariato, K. G., Hendy, I. L. & Behl, R. J. 2000. Carbon Isotopic Evidence for Methane Hydrate Instability During Quaternary Interstadials. *Science*, **288**.

Kenyon, N. H., Ivanov, M. K., Akhmetzhavanov, A. M. & Akhmanov, G. G. 2000. Multidisciplinary study of geological processes on the North East Atlantic and Western Mediterranean margins. Preliminary results of geological and geophysical investigations during the TTR-9 cruise of R./V Professor Logachev, June – July. *IOC Technology Series* **56**, UNESCO, Paris.

Kessler, J. D., Reeburgh, W. S. & Tyler, S. C. 2006. Controls on methane concentration and stable isotope ( $\delta^2\text{H-CH}_4$  and  $\delta^{13}\text{C-CH}_4$ ) distributions in the water columns of the Black Sea and Cariaco Basin. *Global Biogeochemical Cycles*, **20**, GB4004.

Kiode, H, Takahashi, M, Shindo, Y, Tazaki, Y, Ijiima, M, Ito, K, Kimura, N & Omata, K. 1997. Hydrate formation in sediments in the sub-seabed disposal of CO<sub>2</sub>. *Energy*, **22** (273), 279-283.

Kleinberg, R. L., Faum, C., Griffin, D. D., Brewer, P. G., Malby, G. E., Peltzer, E. T. & Yesinowski, J. P. 2003. Deep sea NMR: Methane hydrate growth habit in porous media and its relationship to hydraulic permeability, deposit accumulation, and submarine slope stability. *Journal of Geophysical Research*, **108** (B10), 2508.

Kling, G. W., Clark, M. A., Wagner, G. N., Compton, H. R., Humphrey, A. M., Devine, J. D., Evans, W. C., Lockwood, J. P., Tuttle, M. L. & Koenigsberg, E. J. 1987. The 1986 Lake Nyos Gas Disaster in Cameroon, West Africa. *Science*, **236** (4798), 169-175.

Koh, C. A., Westacott, R. E., Hirachand, K., Zugic, M., Zhang, W. & Savidge, J. L. 1998. Low dosage natural gas hydrate inhibitor evaluation. *Proceedings of the International Gas Research Conference, San Diego, U. S. A, 8-11<sup>th</sup> November, I*, 194-200.

Krauskopf, K. B. 1982. Introduction to Geochemistry. *McGraw-Hill Book Co.*, p263.

Kuhs, W. F., Genov, G., Stayakova, D. K. & Hansen, T. 2004. Ice perfection and onset of anomalous preservation of gas hydrates. *Physical Chemistry Chemical Physics*, **6**, 4917-4920.

Kuzmin, M. I., Kalmychkov, G. V., Geletij, V. F., Gnilusha, V. A., Goreglyad, A. V., Khakhaev, B. N., Pevzner, L. A., Kawai, T., Ioshida, N., Duchkov, A. D., Ponomarchuk, V. A., Kontorovich, A. E., Bazhin, N. M., Mahov, G. A., Dyadin, Yu. A., Kuznetsov, F. A., Larionov, E. G., Manakov, A. Yu., Smolyakov, B. S., Mandelbaum, M. M., Zheleznyakov, N. K. 1998. First find of gas hydrates in sediments of Lake Baikal. *Dokl. Akad. Nauk*, **362**, 541-543.

Kvamme, B., Graue, A., Buanes, T., Kuznetsova, T. & Ersland, G. 2007. Storage of CO<sub>2</sub> in natural gas hydrate reservoirs and the effect of hydrate as an extra sealing in cold aquifers. *International Journal of Greenhouse Gas Control*, **I**, 236-246.

Kvenvolden, K. A. & Lorenson, T. D. 2001. The Global Occurrence of Natural Gas Hydrates. In: *Paull, C. K. & Dillon, W. P. (eds) Natural Gas Hydrates: Occurrence, Distribution, and Detection, American Geophysical Union, Geophysical Monograph*, **124**, 3-18.

- Kvenvolden, K. A. 1998. A primer on the geological occurrence of gas hydrate. *In Gas Hydrates: Relevance to World Margin Stability and Climate Change, Geological Society, Special Publications*, **137**, 9-30.
- Kvenvolden, K. A. 1994. *Annals of the New York Academy of Science*, **715**, 232.
- Kvenvolden, K. A, Ginsburg, G. & Soloviev, V. 1993. Worldwide distribution of subaquatic gas hydrates. *Geo-Marine Letters*, **13**, 32-40.
- Langeland, K & Wilhelmsen, K. 1993. A study of the costs and energy requirement for carbon dioxide disposal. *Energy Conversion Management*, **34** (9-11), 807-814.
- Lapidus, D. F. 1990. Collins Dictionary of Geology. HarperCollins Publishers, pp565.
- Lee, S-Y. & Holder, G. D. 2001. Methane hydrates as a future energy source. *Fuel Processing Technology*, **71**, 181-186.
- Long, D., Jackson, P.D., Lovell, M.A., Rochelle, C.A., Francis, T.J.G. & Schultheiss, P.J. 2005. Methane hydrates: problems in unlocking their potential. *In Petroleum Geology: North-West Europe and Global Perspectives - Proceedings of the 6th Petroleum Geology Conference*, **1**, 723-730
- Long, D. 2000. The Methane Hydrate Stability Zone north and west of Scotland. *WFA hydrates report, British Geological Survey*, **69**.
- Long, D. & Holmes, R. 1998. Methane hydrates in the Faeroe-Shetland Channel?. Abstract volume, *Geoscience*, **98**, Geological Society, p28.
- Long, D. 1996. Hydrates and their potential existence in the Faeroe-Shetland Channel. *British Geological Survey Technical Report WB/96/34*, 80pp.
- Lorenz, S. & Muller, W. 2003. Modelling of halite formation in natural gas storage aquifers. *Proceedings of the Tough Symposium 2003, Berkeley, California, May 12-14, 2003*.

- MacDonald, G. J. 1990. Role of methane clathrates in past and future climates. *Climate Change*, **16**, 247-281.
- Makagon, Y. F. 1997. Hydrates of Hydrocarbons. *Penn Well, Tulsa, OK*.
- Makagon, Y. F. 1981. Hydrates of natural gas. *Penn Well, Tulsa*, pp237.
- Malik, Q. M. & Islam, M. R. 2000. CO<sub>2</sub> injection in the Weyburn field of Canada: Optimization of enhanced oil recovery and greenhouse gas storage with horizontal wells. *Society of Petroleum Engineers*, **59327**, 16p.
- Marchetti, C. 1977. On Geoengineering and the CO<sub>2</sub> problem. *Climatic Change* **1**, 59-68.
- Maslin, M., Owen, M., Day, S. & Long, D. 2004. Linking continental-slope failures and climate change: Testing the clathrate gun hypothesis. *Geology*, **32** (1), 53-56.
- Max, M. D. & Clifford, S. M. 2000. The state, potential distribution, and biological implications of methane in the Martian crust. *Journal of Geophysical Research*, **105** (E2), 4165-4171.
- Max, M. D., Pellanbarg, R. E. & Hurdell, B. G. 1997. Methane hydrate, a special clathrate: its attributes and potential (Report). *Naval Research Laboratory, February 28, 1997*.
- Mazurenko, L. L., Soloviev, J. M., Gardner, J. M. & Ivanov, M. K. 2003. Gas hydrates in the Ginsburg and Yuma mud volcano sediments (Moroccan margin): results of chemical and isotopic studies of pore water. *Marine Geology*, **195**, 201-210.
- McCormack, R. A. & Anderson, R. K. 1995. Clathrate desalination plant preliminary research study. *Water Treatment Technology Program Report No. 5, June 1995, Thermal Energy Storage, Inc, California*, pp 94.

Medjani, K. 1996. Numerical simulation of the formation of brine pockets during the freezing of the NaCl-H<sub>2</sub>O compound from above. *International Communication of Heat Mass Transfer*, **23** (7), 917-928.

Meincke, J. 1978. On the distribution of low salinity intermediate water around the Faroes. *Deutsche Hydrographische Zeitschrift*, **31**, 50-64.

Mienert, J., Posewang, J. & Baumann, M. 1998. Gas hydrates along the northeastern Atlantic Margin: possible hydrate bound margin instabilities and possible release of methane. In *Gas Hydrates: Relevance to World Margin Stability and Climate Change*, Geological Society, *Special Publications*, **137**, 275-291.

Mikami, J., Masuda, Y., Uchida, T., Satoh, T. & Takeda, H. 2000. Dissociation of Natural Gas Hydrates Observed by X-ray CT Scanner. In: *Gas Hydrates – Challenges for the future*, *Annals of the New York Academy of Sciences*, **912**, 1011-1021.

Miles, P. R. 1995. Potential distribution of methane hydrate beneath the European continental margins. *Geophysical research letters*, **22**, 23, 3179-3182.

Milkov, A. V. & Xu, W. 2005. Comment on “Gas hydrate growth, methane transport, and chloride enrichment at the southern summit of Hydrate Ridge, Cascadia margin off Oregon” by Torres et al. [*Earth Planet. Sci. Lett.* 226 (2004) 225-241]. *Earth and Planetary Science Letters*, **239**, 162-167.

Milkov, A. V., Dickens, G. R., Claypool, G. E., Lee, Y.-J., Borowski, W. S., Torres, M. E., Xu, W., Tomaru, H., Trehu, A. M. & Schultheiss, P. 2004. Co-existence of gas hydrate, free gas, and brine within the regional gas hydrate stability zone at Hydrate Ridge (Oregon margin): evidence from prolonged degassing of a pressurized core. *Earth and Planetary Science Letters*, **222**, 829-843.

Milkov, A. V. 2000. Worldwide distribution of submarine mud volcanoes and associated gas hydrate. *Marine Geology*, **167**, 29-42.

Milkov, A. V. & Sassen, R. 2000. Thickness of the gas hydrate stability zone, Gulf of Mexico continental slope. *Marine and Petroleum Geology*, **17**, 981-991.

Miller, S. L. & Smythe, W. D. 1970. Carbon Dioxide Clathrate in the Martian Ice Cap. *Science*, **170**, 531-533.

Milodowski, A.E., Rochelle, C.A., Bateman, K., Gunn, D.A, Jackson, P.D., Nelder, L.M., Rees, J.G. and Lovell, M.A. 2004. Mineralogical observations of CO<sub>2</sub> hydrate as resolved by cryo-SEM. *Proceedings of the 11th International Symposium on Water-Rock Interaction WRI-11, 27 June-2 July 2004, Saratoga Springs, New York, USA (R.B. Wanty and R.R. Seal 2<sup>nd</sup> eds)*, Balkema, Rotterdam, **2**, 1043-1047.

Mork, M., Schel, G. & Larsen, R. 2000. NMR Imaging of Hydrates in Sediments. In: *Gas Hydrates – Challenges for the future, Annals of the New York Academy of Sciences*, **912**, 897-905.

Moudrakovski, I. L., Ratcliffe, C. I., McLaurin, G. E., Simard, B. & Ripmeester, J. A. 1999. Hydrate layers on ice particles and superheated ice: a <sup>1</sup>H NMR microimaging study. *Journal of Physical Chemistry A*, **103**, 4969-4972.

Murray, C. N, Visintini, L, Bidoglio, G & Henry, B. 1996. Permanent storage of carbon dioxide in the marine environment: The solid CO<sub>2</sub> penetrator. *Energy Conversion Management*, **37**(6-8), 1067-1072.

Nakano, S., Yamamoto, K. & Ohgaki, K. 1998. Natural gas exploitation by carbon dioxide from gas hydrate fields – high pressure phase equilibrium for an ethane hydrate system. *Proceedings of the Institution of Mechanical Engineers*, **212**(A), 159-163.

NETL. 2004. All About Hydrates. *National Energy Technology laboratory, U.S. Department of Energy*. [www.netl.doe.gov](http://www.netl.doe.gov).

Odriozola, G., Aguilar, J. F. & Lopez-Lemus, J. 2004. Namontmorillonite hydrates under ethane rich reservoirs: NPzzT and mPzzT simulations. *Journal of Chemical Physics*, **121**.

Open University. 1995. Ocean Circulation. *Pergamon Press*, pp238.

Parrish, W. R. & Prausnitz, J. M. 1972. Dissociation pressures of gas hydrates formed by gas mixtures. *Industrial and Engineering Chemistry Process Design and Development*, **11**, 26-35.

Paull, C. K., Matsumoto, R., Wallace, P. J., et al. 1996. Proceedings of the Ocean Drilling Program, Initial Reports. *Ocean Drilling Program, TX*, **164**, pp623.

Paull, C. K., Ussler, W. III. & Dillon, W. P. 1991. Is the extent of glaciation limited by marine gas-hydrates? *Geophysical Research Letters*, **18** (3), 432-434.

Peterson, C. J., Papenburg, C. & Klaeschen, D. 2007. Local seismic quantification of gas hydrates and BSR characterization from multi-frequency OBS data at northern Hydrate Ridge. *Earth and Planetary Science Letters*, **255** (3-4), 414-431.

Powell, H. J. M. 1948. The structure of molecular compounds. Part IV, clathrate compounds. *Journal of the Chemical Society of London*, **61**.

Press, F. & Siever, R. 1998. Understanding Earth. *W H Freeman, N. Y.*, pp682.

Prieto-Ballesteros, O., Kargel, J. S., Fernandez-Sampedro, M., Selsis, F., Martinez, E. S. & Hogenboom, D. L. 2006. Evaluation of the possible presence of clathrate hydrates in Europa's icy shell or seafloor. *Icarus*, **177** (2), 491-505.

Randerson, J. 2007. UK plans to cut CO<sub>2</sub> doomed to fail – scientists. *The Guardian*, March 5.

Rao, Y. H. *et al.* 2001. Estimates of geothermal gradients and heatflow from BSRs along the western continental margin of India. *MGR*, **29** (2), 355-358.

Reed, S. J. B. 2005. Electron Microprobe Analysis and Scanning Electron Microscopy in Geology. *Cambridge University Press, UK*, pp189.

Riedel, M., Long, P. E. & Collett, T. S. 2006. Estimates of in situ gas hydrate concentration from resistivity monitoring of gas hydrate bearing sediments during temperature equilibration. *Marine Geology*, in press.

Riedel, M., Collett, T., Malone, M. J. & IODP Expedition 311 Scientists. 2006. IODP Expedition 311 establishes drilling transect across northern Cascadia margin to study gas hydrate. *Geological Society Special Publications*. In press.

Riedel, M., Spence, G. D., Chapman, N. R. & Hyndman, R. D. 2002. Seismic investigations of a vent field associated with gas hydrates, offshore Vancouver Island. *Journal of Geophysical Research*, **107**, 1-16.

Rochelle, C. & Camps, A. 2006. Underground storage of CO<sub>2</sub> as a Liquid and Solid Hydrate. *Greenhouse Issues*, **82**, June 2006, 8-9. *Published by the IEA Greenhouse Gas R&D Programme*.

Rochelle, C.A., Camps, A.P., Bateman, K., Gunn, D., Jackson, P., Long, D., Lovell, M.A., Milodowski, A. & Rees, J. 2006. Can CO<sub>2</sub> hydrate assist in the underground storage of carbon dioxide? *Geological Society Special Publications*. In press.

Rochelle, C.A., Milodowski, A.E., Bateman, K., Gunn, D.A., Jackson, P.D., Nelder, L.M., Rees, J.G. and Lovell, M.A. 2004. An experiment frozen in time - cryo-SEM imaging of rapidly-formed CO<sub>2</sub> hydrate. *Proceedings of the 11th International Symposium on Water-Rock Interaction - WRI-11, 27 June-2 July 2004, Saratoga Springs, New York, USA (R.B. Wanty and R.R. Seal 2<sup>nd</sup> eds) Balkema, Rotterdam*, **1**, 579-583.

Roedder, E. 1984. Fluid Inclusions. *Geological Society of America, Reviews in Mineralogy*, **12**.

Ruddihough, R. P. 1984. Recent movements of the Juan de Fuca plate system. *Journal of Geophysical Research*, **89**, 6980-6994.

Ruddiman, W. F. 2001. Earth's climate past and future. *W. H. Freeman and Co.*, 465pp.

Ruppel, C. 2007. Trapping Methane Hydrates for Unconventional Natural Gas. *Elements*, **3**, 193-199.

Sakai, A. et al. 1999. Velocity analysis of vertical seismic profile (VSP) survey at JAPEX/JNOC/GSC Mallik 2L-38 gas hydrate research well, and related problems for estimating gas hydrate concentration. *In: Scientific Results EPM 1-10 GUERIN AND GOLDBERG: SONIC ATTENUATION IN HYDRATED SEDIMENTS from JAPEX/GNOC/GSC Mallik 2L-38 Gas Hydrate Research Well, Mackenzie Delta, Northwest Territories, Canada, edited by S. R. Dallimore, T. Uchida, and T. S. Collett, Bulletin of the Geological Survey of Canada*, **544**, 323-340.

Sakai, H., Gamo, T., Kim, E-S, Tsutsumi, M., Tanaka, T., Ishibashi, J., Wakita, H., Yamano, M. & Oomori, T. 1990. Venting of Carbon Dioxide-Rich Fluid and Hydrate Formation in Mid-Okinawa Trough Backarc Basin. *Science*, **248**, 1093-1095.

Schultheiss, P. J., Francis, T. J. G., Holland, M., Roberts, J. A., Amann, H., Thjunjoto, Parkes, R. J., Martin, D., Rothfuss, M., Tyunder, F. & Jackson, P. D. 2006. Pressure coring, logging and subsampling with the HYACINTH system. *Geological Society, London, Special Publications*, **267**, 151-163.

Sherwin, T. J. & Turrell, W. R. 2005. Mixing and advection of a cold water cascade over the Wyville Thomson Ridge. *Deep-Sea Research I*, **52**, 1392-1413.

Sloan, E. D. JR. 1998. Physical/chemical properties of gas hydrates and application to world margin stability and climatic change. *In Gas Hydrates: Relevance to World Margin Stability and Climate Change, Geological Society, Special Publications*, **137**, 31-50.

Sloan, E. D. JR. 1998. Clathrate Hydrates of natural gases. *Marcell Dekker inc*, 359pp.

Smelik, E. A. & King, H. E. JR. 1997. Crystal-growth studies of natural gas clathrate hydrates using a pressurized optical cell. *American Mineralogist*, **82**, 88-98.

Soloviev, V. A. 2002. Global estimation of gas content in submarine gas hydrates accumulations. *Russian Geology and Geophysics*, **43**, 648-661.

Someya, S., Saito, K., Nishio, M. & Tsutsui, K. 2006. CO<sub>2</sub> sequestration under a sealed layer with clathrate hydrate in sediments. *Abstract in: Sediment-hosted Gas Hydrates: New Insights on Natural and Synthetic Systems Conference Program, 25<sup>th</sup>-26<sup>th</sup> January, 2006, UK*, p34.

Spry, A. 1969. *Metamorphic Textures*. Pergamon Press, pp350.

Stern, N. 2007. *The Economics of Climate Change: The Stern Review*. Cambridge University Press, UK, pp712.

Stern, L. A., Kirby, S. H. & Durham, W. B. 2005. Scanning electron microscope imaging of grain structure and phase distribution within gas-hydrate-bearing intervals from JAPEX/JNOC/GSC et al. Mallik 5L-38: what can we learn from comparisons with laboratory-synthesized samples?; in *Scientific Results from the Mallik 2002 Gas Hydrate Production Research Well Program, MacKenzie Delta, Northwest Territories, Canada* (ed.) S. R. Dallimore and T. S. Collett; Geological Survey of Canada, Bulletin **585**, pp19.

Stern, L. A., Kirby, S. H., Circone, S. & Durham, W. B. 2004. Scanning Electron Microscopy investigations of laboratory-grown gas clathrate hydrates formed from melting ice, and comparison to natural hydrates. *American Mineralogist*, **89**, 1162-1175.

Stern, L. A., Kirby, S. H., Durham, W. B., Circone, S. & Waite, W. 2000. Synthesis of pure methane hydrate suitable for measurement of physical properties and decomposition behaviour. In *Natural Gas Hydrate: In Oceanic and Polar Subaerial Environments*, Kluwer: Dordrecht, 323-349.

- Stoll, R. D. & Bryan, G. M. 1979. Physical Properties of Sediments Containing Gas Hydrates. *Journal of Geophysical Research*, **84** (B4), 1629-1634.
- Subramanian, S, Kini, R. A., Dec, S. F. & Sloan, E. D. JR. 2000. Structural Transition Studies in Methane + Ethane Hydrates Using Raman and NMR. In: *Gas Hydrates – Challenges for the future, Annals of the New York Academy of Sciences*, **912**, 873-885.
- Suga, H., Matsuo, T. & Yamamuro, O. 1992. Thermodynamic study of ice and clathrate hydrates. *Pure & Applied Chemistry*, **64** (1), 17-26.
- Sun, R. & Duan, Z. 2005. Prediction of CH<sub>4</sub> and CO<sub>2</sub> hydrate phase equilibrium and cage occupancy from ab initio intermolecular potentials. *Geochemica et Cosmochimica Acta*, **69** (18), 4411-4424.
- Taira, A., Hill, I., Firth, J. V. et al., 1991. Proceedings of the Ocean Drilling Program, Initial Reports, Leg 131. *Ocean Drilling Program*, College Station, TX.
- Takeya, S., Hori, A., Hondoh, T. & Uchida, T. 2000. Freezing-Memory Effect of Water on Nucleation of CO<sub>2</sub> Hydrate Crystals. *Journal of Physical Chemistry B*, **104**, 4164-4168.
- Tanaka, S. et al. 1996. Investigation on disposal of CO<sub>2</sub> in aquifers. *Engineering Advancement Association of Japan Journal (In Japanese) for the Ministry of International Trade and Industry (MITI)*.
- Tanasawa, I. & Takao, S. 2002. Low-temperature storage using clathrate hydrate slurries of tetra-n-butylammonium bromide: thermophysical properties and morphology of clathrate hydrate crystals. In: *Fourth international conference on gas hydrates, Yokohama, Japan*, 963-7.
- Tatro, S. 2006. Personal communication.
- Tchernia, P. 1980. Descriptive Regional Oceanography. *Pergamon Press*, pp253.

- Techmer, K. S., Henrichs, T. & Kuhs, W. F. 2005. Cryo-electron microscopic studies of structures and composition of Mallik gas-hydrate-bearing samples. *Geological Survey of Canada Bulletin*, **585**, 12.
- Titiloye, J. O. & Skipper, N. T. 2005. Monte Carlo and molecular dynamics simulations of methane in potassium montmorillonite clay hydrates at elevated pressures and temperatures. *Journal of Colloid Interfacial Science*, **282**, 422-427.
- Teichert, B. M. A., Gussone, N., Eisenhauer, A., Bohrmann, G. 2005. Clathrites: Archives of near-seafloor pore-fluid evolution ( $\delta^{44/40}\text{Ca}$ ,  $\delta^{13}\text{C}$ ,  $\delta^{18}\text{O}$ ) in gas hydrate environments. *Geology*, **33** (3), 213-216.
- Tohidi, B., Anderson, R., Clennell, M. B., Burgass, R. W. & Biderkab, A. B. 2001. Visual observation of gas-hydrate formation and dissociation in synthetic porous media by means of glass micromodels. *Geology*, **29** (9), 867-870.
- Tomczak, M. & Godfrey, J. S. 1994. Regional Oceanography: An Introduction. *Pergamon Press*, pp 422.
- Tomutsa, L., Freifield, B., Kneafsey, T. J. & Stern, L. A. 2002. X-ray computed tomography observation of methane hydrate dissociation. **SPE 75533**. *SPE Gas Technology Symposium*, Calgary, Alberta, Canada, April.
- Torres, M. E., Wallmann, K., Trehu, A. M., Bohrmann, G., Borowski, W. S. & Tomaru, H. 2004. Gas hydrate growth, methane transport, and chloride enrichment at the southern summit of Hydrate Ridge, Cascadia margin off Oregon. *Earth and Planetary Science Letters*, **226**, 225-241.
- Tréhu, A. M., Long, P. E., Torres, M. E., Bohrmann, G., Rack, F. R., Collett, T. S., Goldberg, D. S., Milkov, A. V., Riedel, M., Schultheiss, P., Bangs, N. L., Barr, S. R., Borowski, W. S., Claypool, G. E., Delwiche, M. E., Dickens, G. R., Gracia, E., Guerin, G., Holland, M., Johnson, J. E., Lee, Y. -J., Liu, C. -S., Su, X., Teichert, B., Tomaru, H., Vanneste, M., Watanabe M. and Weinberger, J. L. 2004. Three-dimensional

distribution of gas hydrate beneath southern Hydrate Ridge: constraints from ODP Leg 204. *Earth and Planetary Science Letters*, **222** (3-4), 845-862.

Trommsdorf, V., Skippen, G. & Ulmer, P. 1985. Halite and sylvite as solid inclusions in high-grade metamorphic rocks. *Contributions to Mineralogy and Petrology*, **89**, 24-29.

Turner, D. J., Kumar, P. & Sloan, E. D. 2005. New technique for hydrate thermal diffusivity measurements. *International Journal of Thermophysics*, **26** (6), 1681-1691.

Turrell, W. R., Slessor, G., Adams, R. D., Payne, R. & Gillibrand, P. A. 1999. Decadal variability in the composition of Faroe Shetland Channel bottom water. *Deep-Sea Research I*, **46**, 1-25.

Uchida, T., Ebinuma, T. & Narita, H. 2000. Observations of CO<sub>2</sub>-hydrate decomposition and reformation processes. *Journal of Crystal Growth*, **217**, 189-200.

USGS. 2007. India Project. <http://energy.usgs.gov/other/gashydrates/india.html>.

Van Der Waals, J. H. & Platteeuw, J. C. 1959. Clathrate solutions. In *Advances in Chemical Physics*, 1-57, Interscience.

Vanneste, M., De Batist, M., Golmshtok, A., Kremlev, A. & Versteeg, W. 2001. Multi-frequency seismic study of gas hydrate-bearing sediments in Lake Baikal, Siberia. *Marine Geology*, **172** (2001), 1-21.

Vesovic, V., Wakeham, W. A., Olchoway, G. A., Sengers, J. V., Watson, J. T. R. & Millat, J. 1990. The transport properties of carbon dioxide. *Journal of Physics and Chemistry Reference Data*, **19** (3), 763-808.

Wadhams, P. 2005. How does Arctic Sea Ice Form and Decay?  
[www.arctic.noaa.gov/essay\\_wadhams.html](http://www.arctic.noaa.gov/essay_wadhams.html), 1-6.

Westbrook, G. K. 2006. Hydratech. *Presentation at the 5<sup>th</sup> International Workshop on Methane Hydrate Research and Development, Edinburgh, 9<sup>th</sup> -12<sup>th</sup> October.*

Westbrook, G. K., Caarson, B., Musgrave, R. J. & Suess, E. 1994. *Proceedings of the Ocean Drilling Program, Initial Reports*, **146**, pp477.

Wilson, P. W., Lester, D. & Haymet, A. D. J. 2005. Heterogeneous nucleation of clathrates from supercooled tetrahydrofuran (THF)/water mixtures, and the effect of an added catalyst. *Chemical Engineering Science*, **60**, 2937-2941.

Wilson, M. & Monea, M. 2004. IEA GHG Weyburn CO<sub>2</sub> Monitoring and Storage project Summary Report 2000-2004. *Proceedings of the 7<sup>th</sup> International Conference on Greenhouse Gas Control Technologies*, September 5-9, 2004, Vancouver, Canada, **3**, p273.

Wong, C. S. & Hirai, S. 1997. Ocean Storage of Carbon Dioxide: A Review of Oceanic Carbonate and CO<sub>2</sub> hydrate chemistry. *Pub. International Energy Agency Greenhouse Gas R&D Programme, Cheltenham, UK*, 90pp.

World Energy Assessment. 2004. A study of the role of end-of-pipe technologies in reducing CO<sub>2</sub> emissions. *Waste Management*, **17** (5-6), 295-302.

Zheng, L., Wang, S., Liao, Y. & Feng, Z. 2001. CO<sub>2</sub> gas pools in Jiyang sag, China. *Applied Geochemistry*, **16**, 1033-1039.

## UNITS

<b>nm</b> = nanometre	$1 \times 10^{-9}$ m
<b>µm</b> = micron or micrometre	$1 \times 10^{-6}$ m
<b>mm</b> = millimetre	$1 \times 10^{-3}$ m
<b>cm</b> = centimetre	$1 \times 10^{-2}$ m
<b>m</b> = metre	
<b>km</b> = kilometre	$1 \times 10^3$ m
<b>mbsf</b> = metres below sea floor	
<b>kg</b> = kilogram	$1 \times 10^3$ g
<b>kg/m<sup>2</sup></b> = kilograms per squared metre	
<b>g/cm<sup>3</sup></b> = grams per cubic centimetres	
<b>kg/m<sup>3</sup></b> = kilograms per metre cubed	
<b>mol/m<sup>3</sup></b> = moles per metre cubed	
<b>kg/l</b> = kilograms per litre	
<b>°C</b> = degrees celcius	K - 273.15
<b>°C/km</b> = degrees celcius per kilometre	
<b>K</b> = kelvin	°C + 273.15
<b>bar</b> = pressure in bars	$1 \times 10^{-5}$ Pa
<b>Torr</b> = pressure in Torrs	$7.5006 \times 10^{-3}$
<b>Pa</b> = pascal	$1 \times 10^5$ bar
<b>kPa</b> = kilopascal	$1 \times 10^3$ Pa
<b>MPa</b> = megapascals	$1 \times 10^6$ Pa
<b>µPa s<sup>-1</sup></b> = micropascals per second	$1 \times 10^{-6}$ Pa s <sup>-1</sup>
<b>‰</b> = parts per thousand	
<b>ppmv</b> = parts per million by volume	
<b>%w/w</b> = weight by weight percentage	
<b>t</b> = tonne	
<b>Gt</b> = gigatonne	$1 \times 10^9$ tonnes
<b>MWh<sup>-1</sup></b> = milliwatt per hour	$1 \times 10^6$ watts/hour
<b>GW</b> = gigawatt	$1 \times 10^9$ watts/hour
<b>US\$</b> = US dollars	
<b>US\$/t</b> = US dollars per tonne	

## PUBLICATIONS

1. **Camps, A. P.**, Long, D., Rochelle, C. & Lovell, M. A. (\*\*\*\*). Mapping Hydrate Stability Zones Offshore Scotland. *Geological Society Special Publications. Accepted 2007.*
2. Rochelle, C. A., **Camps, A. P.**, Long, D., Milodowski, A., Bateman, K., Gunn, D., Jackson, P., Lovell, M. A. & Rees, J. (\*\*\*\*). Can CO<sub>2</sub> hydrate assist in the underground storage of carbon dioxide? *Geological Society Special Publications. Accepted 2007.*
3. **Camps, A. P.**, Rochelle, C. A., Milodowski, A. E., Sims, M. R., Pullan, D. & Lovell, M. A. 2007. The potential for applying cryogenic SEM imaging to help understand ices and hydrates under conditions of the Martian cryo-sphere. *Submitted to Journal of Astrobiology.*
4. **Camps, A. P.**, Milodowski, A. E., Rochelle, C. A., Lovell, M. A., Brewer, T. S., Jackson, P. D., & Williams, J. F. 2007. Salt inclusion during rapid CO<sub>2</sub> hydrate formation. *European Geosciences Union, Vienna, April 2007.*
5. **Camps, A. P.**, Lovell, M. A., Brewer, T. S., and Williams, J. F. 2007. Putting our heads together: Physprops.net. *European Geosciences Union, Vienna, April 2007.*
6. **Camps, A. P.** 2007. Putting our heads together: Physprops.net. *Earth Science Teaching Association (ESTA) Magazine, Volume 32, No. 1.*
7. **Camps, A. P.**, Rochelle, C. A., Milodowski, A., Long, D., Lovell, M. A., Bateman, K., Gunn, D., Jackson, P. & Rees, J. 2006. The underground storage of CO<sub>2</sub> at low temperatures and its trapping in solid phases. *Proceedings of 8<sup>th</sup> International Conference on Greenhouse Gas Technologies, Trondheim, 19-22 June 2006.*
8. **Camps, A. P.**, Rochelle, C. A., Milodowski, A. and Lovell, M. A. 2006. Salt inclusion during rapid CO<sub>2</sub> hydrate formation. Abstract in the proceedings of a Geological Society international conference entitled '*Sediment-hosted gas hydrates: new insights on natural and synthetic systems*', London, 25-26 January 2006.
9. **Camps, A. P.**, Long, D., Rochelle, C. A. and Lovell, M. A. 2006. Mapping hydrate stability zones offshore Scotland. Abstract in the proceedings of a Geological Society international conference entitled '*Sediment-hosted gas hydrates: new insights on natural and synthetic systems*', London, 25-26 January 2006.
10. Rochelle, C. A., **Camps, A. P.**, Long, D., Milodowski, A., Bateman, K., Gunn, D., Jackson, P., Lovell, M. A. & Rees, J. 2006. Can CO<sub>2</sub> hydrate assist in the underground storage of carbon dioxide? Abstract in the proceedings of a Geological Society international conference entitled '*Sediment-hosted gas hydrates: new insights on natural and synthetic systems*', London, 25-26 January 2006.

11. Rochelle, C. & **Camps, A.** 2006. Underground storage of CO<sub>2</sub> as a Liquid and Solid Hydrate. *Greenhouse Issues*, No. **82**, June 2006, p8-9. *Published by the IEA Greenhouse Gas R&D Programme.*
12. **Camps, A. P.** 2006. Trapped in Ice. *Planet Earth*, Autumn 2006. *Published by the Natural Environment Research Council.*
13. Rochelle, C. A. & **Camps, A. P.** (2006). Potential for storing CO<sub>2</sub> underground as a gas hydrate. *Earthwise*. *Published by the British Geological Survey.*
14. **Camps, A. P.**, Long, D., Rochelle, C. A. and Lovell, M. A. 2005. Mapping hydrate stability zones off the Scottish Coast. Abstract in the proceedings of the VIII International conference on Gas in Marine Sediments, Vigo, Spain, 5-10 September 2005.

## PRESENTATIONS

1. Oral presentation of 'Frozen experiments to solve a crisis: me and my little hydrate crystals!' at the BGS sponsored fieldtrip on the Volcanology of Milos, Greece, 27<sup>th</sup> April – 6<sup>th</sup> May 2007.
2. Poster presentation of 'Salt inclusion during rapid CO<sub>2</sub> hydrate formation' at the European Geosciences Union (EGU) General Assembly, Vienna, 15<sup>th</sup>-20<sup>th</sup> April 2007.
3. Oral presentation of 'Putting our heads together: Physprops.net' at the European Geosciences Union (EGU) General Assembly, Vienna, 15<sup>th</sup>-20<sup>th</sup> April 2007.
4. Poster presentation of 'Trapping Carbon Dioxide' at the 9<sup>th</sup> Great British Research and R&D Show evening reception, **House of Commons**, 19<sup>th</sup> March 2007.
5. Poster presentation of 'Hydrate Stability Zones offshore Western Europe' at Fiery Ice from the Seas – 5<sup>th</sup> International Workshop on Methane Hydrate Research and Development, Edinburgh, 9-12<sup>th</sup> October 2006.
6. 2<sup>nd</sup> poster presentation of 'Carbon Storage – Mapping offshore hydrate stability zones' at the **UKGRAD Midlands Hub Regional Poster Competition**, Warwick Arts Centre, 3<sup>rd</sup> July 2006. Won the runners up prize for the best presentation.
7. Poster 'The underground storage of CO<sub>2</sub> at low temperatures and its trapping in solid phases' presented at the **8<sup>th</sup> International Greenhouse Gas Technologies conference**, Trondheim, Norway, 19-22 June 2006.
8. Presentation of the poster 'Carbon Storage – Mapping offshore hydrate stability zones' at the **University of Leicester's Festival of Postgraduate Research**, 13<sup>th</sup> June 2006. Won award of the best presentation in the science and engineering category.
9. Oral presentation 'Salt inclusion during rapid CO<sub>2</sub> hydrate formation' 23<sup>rd</sup> February 2006, University of Leicester, Department of Geology.

10. An oral presentation entitled 'Salt inclusion during rapid CO<sub>2</sub> hydrate formation' was given at the **Sediment Hosted Gas Hydrates international conference**, London, 25-26 January 2006.
11. Poster presentation of 'Mapping hydrate stability zones offshore Scotland' given at the **Sediment Hosted Gas Hydrates international conference**, London, 25-26 January 2006.
12. Poster presentation of 'Mapping Hydrate Stability Zones off the Scottish Coast' was given at the **VIII International Conference of Gas in Marine Sediments**, Vigo, Spain, 5-10 September 2005.
13. Oral presentation 'Carbon dioxide storage within sediments: Mapping hydrate stability zones off the Scottish Coast', 10<sup>th</sup> March 2005, University of Leicester, Department of Geology.
14. Oral presentation 'Frozen experiments to solve a crisis? CO<sub>2</sub> hydrates and future climate change', 5<sup>th</sup> November 2004, University of Leicester, Department of Geology. Poster 'Carbon Storage & Sequestration: A solution to a global crisis?' presented at the
15. **ES4 Earth System Science School**, 13-24 September 2004, Reading University Meteorology Department.

## PRESS RELEASES

**Cold Storage Solution for Global Warming?** – Sent by the University of Leicester press office on 05/02/2007, officially released 08/02/2007. Release based upon published Planet Earth article.

- **BBC East Midlands Today Special Feature – Scientists study CO<sub>2</sub> storage.** Aired 07/02/2007, including interviews & filming of me and Prof. Mike Lovell.
- **Worldwide media coverage**

# **APPENDIX**

## APPENDIX A

<b>1.</b>	<b>Hydcalc.exe script</b>	<b>1-4</b>
<b>2.</b>	<b>HydcalcCO2.exe script</b>	<b>5-8</b>
<b>3.</b>	<b>Temperature gradient Matlab scripts</b>	<b>9-12</b>
<b>3.1</b>	<b>North Sea temperature calculation script</b>	<b>9</b>
<b>3.2</b>	<b>Norwegian Sea temperature calculation script</b>	<b>9-10</b>
<b>3.3</b>	<b>Rockall Trough temperature calculation script</b>	<b>10-11</b>
<b>3.4</b>	<b>Iberian temperature calculation script</b>	<b>11-12</b>
<b>4.</b>	<b>Data files on CD used to construct offshore Western European maps presented in Chapter 3.3.</b>	<b>CD</b>

See CD enclosed on the inside of the back cover. Unfortunately, hydrate stability calculation programs have not been included on this CD due to BGS copyright. See 4.1 for data description.

- 4.1**    **Appendix\_A4\_data.doc**
- 4.2.**    **europe\_co2\_hsz\_30.txt**
- 4.3.**    **europe\_methane\_hsz\_30.txt**
- 4.4.**    **europe\_sw\_co2dens\_basehsz.txt**

## 1. Hydcalc.exe script

```
VERSION 5.00
Object = "{F9043C88-F6F2-101A-A3C9-08002B2F49FB}#1.2#0"; "COMDLG32.OCX"
Begin VB.Form frmHcalc
  BackColor = &H00FFC0C0&
  Caption = "Hydrate Calculation Application"
  ClientHeight = 4710
  ClientLeft = 1260
  ClientTop = 1485
  ClientWidth = 7455
  LinkTopic = "Form1"
  ScaleHeight = 4710
  ScaleWidth = 7455
  Begin VB.CommandButton cmdStart
    Caption = "Start"
    BeginProperty Font
      Name = "Arial Black"
      Size = 9.75
      Charset = 0
      Weight = 400
      Underline = 0 'False
      Italic = 0 'False
      Strikethrough = 0 'False
    EndProperty
    Height = 615
    Left = 5880
    TabIndex = 0
    Top = 2880
    Width = 1455
  End
  Begin VB.CommandButton cmdExit
    Caption = "Quit"
    Height = 615
    Left = 5880
    TabIndex = 1
    Top = 3600
    Width = 1455
  End
  Begin MSComDlg.CommonDialog CommonDialog1
    Left = 120
    Top = 6600
    _ExtentX = 847
    _ExtentY = 847
    _Version = 393216
  End
  Begin VB.Image Image1
    Height = 495
    Left = 0
    Picture = "hydcalc.frx":0000
    Stretch = -1 'True
    Top = 4200
    Width = 1095
  End
  Begin VB.Label lblFinish
    Alignment = 2 'Center
    BackColor = &H00C0E0FF&
    BorderStyle = 1 'Fixed Single
    Caption = " "
    BeginProperty Font
```

```

Name      = "Arial Black"
Size      = 9.75
Charset   = 0
Weight    = 400
Underline = 0 'False
Italic    = 0 'False
Strikethrough = 0 'False
EndProperty
ForeColor = &H00FF00FF&
Height    = 1095
Left      = 1920
TabIndex  = 4
Top       = 3600
Width     = 3255
End
Begin VB.Label Label1
Alignment = 2 'Center
BorderStyle = 1 'Fixed Single
Caption    = $"hydcalc.frx":1EA2E
BeginProperty Font
Name      = "Times New Roman"
Size      = 9.75
Charset   = 0
Weight    = 700
Underline = 0 'False
Italic    = 0 'False
Strikethrough = 0 'False
EndProperty
Height    = 2055
Left      = 2280
TabIndex  = 3
Top       = 1080
Width     = 2535
WordWrap  = -1 'True
End
Begin VB.Label lblDescr
Alignment = 2 'Center
BackColor = &H00C0C0FF&
BorderStyle = 1 'Fixed Single
Caption    = "Application to calculate the pressure needed for hydrate formation."
BeginProperty Font
Name      = "Times New Roman"
Size      = 12
Charset   = 0
Weight    = 700
Underline = 0 'False
Italic    = 0 'False
Strikethrough = 0 'False
EndProperty
Height    = 375
Left      = 120
TabIndex  = 2
Top       = 360
Width     = 7095
WordWrap  = -1 'True
End
Begin VB.Menu mnuFile
Caption    = "&File"
Begin VB.Menu mnuFileOpen
Caption    = "&Open"

```

```

End
Begin VB.Menu mnuFileSaveAs
    Caption    = "&Save As"
End
Begin VB.Menu mnuFileExit
    Caption    = "&Exit"
End
End
End
Attribute VB_Name = "frmHcalc"
Attribute VB_GlobalNameSpace = False
Attribute VB_Creatable = False
Attribute VB_PredeclaredId = True
Attribute VB_Exposed = False
Private Sub cmdExit_Click()
End
End Sub

Private Sub cmdStart_Click()
Dim WD As Integer          'water depth
Dim Infile As String
Dim Outfile As String
Dim BWT, BWT2 As Single   ' bottom water temp
Dim GT As Single         ' geothermal grad
Dim PRES As Double
Dim Startstr As String   ' start input str
Dim Inpstring As Variant 'input str array
Dim HSZ As Integer
Dim CnSta As Double
Dim CnStb As Double
'
'
CommonDialog1.ShowOpen    'standard dialogue file open
Infile = CommonDialog1.FileName
Open Infile For Input As #1
CommonDialog1.ShowSave    ' standard dialogue file save as
Outfile = CommonDialog1.FileName
Open Outfile For Output As #2
'
'
Do While (Not EOF(1))
Line Input #1, Startstr    ' get input line; comma separated
Inpstring = Split(Startstr, ",", -1, 1) ' sep out into 5 element array
WD = CInt(Inpstring(2))    ' convert to numeric
BWT = CSng(Inpstring(3))  ' ditto with offset
BWT2 = BWT + 1.1
GT = CSng(Inpstring(4))   ' ditto
'
'      start loop
For HSZ = 0 To 2500
PRES = Log(10.17 * (WD + HSZ))
If PRES > 9.355001 Then
    CnSta = 46.7
    CnStb = 10748.1
Else
    CnSta = 38.53
    CnStb = 8386.8
End If
Temp = (CnSta - (CnStb / ((BWT2 + (HSZ * GT / 1000)) + 273.15)))
If PRES < Temp Then

```

```
Write #2, Cdbl(Inpstring(0)); Cdbl(Inpstring(1)); WD; BWT; GT; HSZ
GoTo zz          'get next rec
End If
Next HSZ
zz: Loop
lblFinish.Caption = "Processing ended ...press Quit to exit"
Close #1
Close #2
End Sub
```

```
Private Sub mnuFileExit_Click()
End
End Sub
```

```
Private Sub mnuFileOpen_Click()
Dim Infile As String
CommonDialog1.ShowOpen
Infile = CommonDialog1.FileName
End Sub
```

```
Private Sub mnuFileSaveAs_Click()
Dim Outfile As String
CommonDialog1.ShowSave
Outfile = CommonDialog1.FileName
End Sub
```

## 2. HydcalcCO2.exe script

```
VERSION 2.00
Object = "{F9043C88-F6F2-101A-A3C9-08002B2F49FB}#1.2#0"; "COMDLG32.OCX"
Begin VB.Form frmHcalc
    BackColor = &H00FFC0C0&
    Caption = "CO2 Hydrate Calculation Application"
    ClientHeight = 4710
    ClientLeft = 1260
    ClientTop = 1485
    ClientWidth = 7455
    LinkTopic = "Form1"
    ScaleHeight = 4710
    ScaleWidth = 7455
    Begin VB.CommandButton cmdStart
        Caption = "Start"
        BeginProperty Font
            Name = "Arial Black"
            Size = 9.75
            Charset = 0
            Weight = 400
            Underline = 0 'False
            Italic = 0 'False
            Strikethrough = 0 'False
        EndProperty
        Height = 615
        Left = 5880
        TabIndex = 0
        Top = 2880
        Width = 1455
    End
    Begin VB.CommandButton cmdExit
        Caption = "Quit"
        Height = 615
        Left = 5880
        TabIndex = 1
        Top = 3600
        Width = 1455
    End
    Begin MSComDlg.CommonDialog CommonDialog1
        Left = 120
        Top = 6600
        _ExtentX = 847
        _ExtentY = 847
        _Version = 393216
    End
    Begin VB.Image Image1
        Height = 495
        Left = 0
        Picture = "hydcalc.frx":0000
        Stretch = -1 'True
        Top = 4200
        Width = 1095
    End
    Begin VB.Label lblFinish
        Alignment = 2 'Center
        BackColor = &H00C0E0FF&
        BorderStyle = 1 'Fixed Single
        Caption = " "
        BeginProperty Font
```

```

Name      = "Arial Black"
Size      = 9.75
Charset   = 0
Weight    = 400
Underline = 0 'False
Italic    = 0 'False
Strikethrough = 0 'False
EndProperty
ForeColor = &H00FF00FF&
Height    = 1095
Left      = 1920
TabIndex  = 4
Top       = 3600
Width     = 3255
End
Begin VB.Label Label1
Alignment = 2 'Center
BorderStyle = 1 'Fixed Single
Caption    = $"hydcalc.frx":1EA2E
BeginProperty Font
Name      = "Times New Roman"
Size      = 9.75
Charset   = 0
Weight    = 700
Underline = 0 'False
Italic    = 0 'False
Strikethrough = 0 'False
EndProperty
Height    = 2055
Left      = 2280
TabIndex  = 3
Top       = 1080
Width     = 2535
WordWrap  = -1 'True
End
Begin VB.Label lblDescr
Alignment = 2 'Center
BackColor = &H00C0C0FF&
BorderStyle = 1 'Fixed Single
Caption    = "Application to calculate the pressure needed for CO2 hydrate formation."
BeginProperty Font
Name      = "Times New Roman"
Size      = 12
Charset   = 0
Weight    = 700
Underline = 0 'False
Italic    = 0 'False
Strikethrough = 0 'False
EndProperty
Height    = 375
Left      = 120
TabIndex  = 2
Top       = 360
Width     = 7095
WordWrap  = -1 'True
End
Begin VB.Menu mnuFile
Caption    = "&File"
Begin VB.Menu mnuFileOpen
Caption    = "&Open"

```

```

End
Begin VB.Menu mnuFileSaveAs
    Caption    = "&Save As"
End
Begin VB.Menu mnuFileExit
    Caption    = "&Exit"
End
End
End
Attribute VB_Name = "frmHcalc"
Attribute VB_GlobalNameSpace = False
Attribute VB_Creatable = False
Attribute VB_PredeclaredId = True
Attribute VB_Exposed = False
Private Sub cmdExit_Click()
End
End Sub

Private Sub cmdStart_Click()
Dim WD As Integer           'water depth
Dim Infile As String
Dim Outfile As String
Dim BWT, BWT2 As Single    ' bottom water temp
Dim GT As Single          ' geothermal grad
Dim PRES As Double
Dim Startstr As String    ' start input str
Dim Inpstring As Variant  'input str array
Dim HSZ As Integer
Dim CnSta As Double
Dim CnStb As Double
'
'
CommonDialog1.ShowOpen      'standard dialogue file open
Infile = CommonDialog1.FileName
Open Infile For Input As #1
CommonDialog1.ShowSave     ' standard dialogue file save as
Outfile = CommonDialog1.FileName
Open Outfile For Output As #2
'
'
Do While (Not EOF(1))
Line Input #1, Startstr    ' get input line; comma separated
Inpstring = Split(Startstr, ",", -1, 1) ' sep out into 5 element array
WD = CInt(Inpstring(2))    ' convert to numeric
BWT = CSng(Inpstring(3))  ' ditto with offset
BWT2 = BWT + 1.1
GT = CSng(Inpstring(4))   ' ditto
'
'      start loop
For HSZ = 0 To 2500
PRES = Log(10.17 * (WD + HSZ))
'
Select Case PRES
Case PRES > 11.647733
    CnSta = 60.566
    CnStb = 14372
Case PRES > 10.626279
    CnSta = 129.31
    CnStb = 34161
Case Else

```

```

    CnSta = 40.495
    CnStb = 9114.3
End Select
'
Temp = (CnSta - (CnStb / ((BWT2 + (HSZ * GT / 1000)) + 273.15)))
If PRES < Temp Then
    Write #2, CDbI(Inpstring(0)); CDbI(Inpstring(1)); WD; BWT; GT; HSZ
    GoTo zz          ' get next rec
End If
Next HSZ
zz: Loop
lblFinish.Caption = "Processing ended ...press Quit to exit"
Close #1
Close #2
End Sub

Private Sub mnuFileExit_Click()
End
End Sub

Private Sub mnuFileOpen_Click()
Dim Infile As String
CommonDialog1.ShowOpen
Infile = CommonDialog1.FileName
End Sub

Private Sub mnuFileSaveAs_Click()
Dim Outfile As String
CommonDialog1.ShowSave
Outfile = CommonDialog1.FileName
End Sub

```

### 3. Temperature gradient Matlab scripts

#### 3.1 North Sea temperature calculation script

```
function[out]=depth(North_Sea_Norway)
%
load North_Sea_Norway.txt
depth=North_Sea_Norway(:,3).*-1;
%
[r,c]=size(depth);          %start of temperature calculations
temp=ones(r,c);
%
D0=depth<0;
temp(D0==1)=50;
D40=depth<=40 & depth>0;
temp(D40==1)=13.055;
D80=depth<=80 & depth>40;
temp(D80==1)=-0.0889*depth(D80==1)+16.451;
D200=depth<=200 & depth>80;
temp(D200==1)=-0.0156*depth(D200==1)+10.602;
D201=depth>200;
temp(D201==1)=-0.007*depth(D201==1)+9;
%
out=[North_Sea_Norway temp];
csvwrite('NorthSeaTemp2.csv',out)
%
load NorthSeaTemp2.csv;
lat=NorthSeaTemp2(:,1);
long=NorthSeaTemp2(:,2);
temp=NorthSeaTemp2(:,4);
depth=NorthSeaTemp2(:,3);
%
[r,c]=size(depth);          %Creating a new depth, which makes all depths positive so doesn't effect
hydcalc
newdepth=ones(r,c);
D0=depth<0;
newdepth(D0==1)=depth(D0==1).*-1;
D1=depth>=0;
newdepth(D1==1)=depth(D1==1).*1;
%
[r,c]=size(depth);          %adds geothermal gradient column
geothermal=ones(r,c);
D30=geothermal;
geothermal(D30==1)=30;
%
northsea_2input=[lat long newdepth temp geothermal]
csvwrite('northsea_2input.csv',northsea_2input)
```

#### 3.2 Norwegian Sea temperature calculation script

```
function[out]=depth(Norway_Temp)
%
load Norway_Temp.txt
depth=Norway_Temp(:,3).*-1;
%
[r,c]=size(depth);          %start of temperature calculations
temp=ones(r,c);
%
D0=depth<0;
```

```

temp(D0==1)=50;
D190=depth<=190 & depth>0;
temp(D190==1)=-0.0071*depth(D190==1)+7.3515;
D470=depth<=470 & depth>190;
temp(D470==1)=-0.0202*depth(D470==1)+9.9008;
D630=depth<=630 & depth>470;
temp(D630==1)=-0.0048*depth(D630==1)+3.0371;
D890=depth<=890 & depth>630;
temp(D890==1)=-0.0022*depth(D890==1)+1.4271;
D1010=depth<=1010 & depth>890;
temp(D1010==1)=-0.0011*depth(D1010==1)+0.4977;
D1550=depth<=1550 & depth>1010;
temp(D1550==1)=-0.0005*depth(D1550==1)-0.1489;
D2210=depth<=2210 & depth>1550;
temp(D2210==1)=-0.0001*depth(D2210==1)-0.6399;
D2211=depth>2210;
temp(D2211==1)=-0.93;
%
out=[Norway_Temp temp];
csvwrite('NorwayTemp.csv',out)
%
load NorwayTemp.csv;
lat=NorwayTemp(:,1);
long=NorwayTemp(:,2);
temp=NorwayTemp(:,4);
depth=NorwayTemp(:,3);
%
[r,c]=size(depth);          %Creating a new depth, which makes all depths positive so doesn't effect
hydcalc
newdepth=ones(r,c);
D0=depth<0;
newdepth(D0==1)=depth(D0==1).*-1;
D1=depth>=0;
newdepth(D1==1)=depth(D1==1).*1;
%
[r,c]=size(depth);          %adds geothermal gradient column
geothermal=ones(r,c);
D30=geothermal;
geothermal(D30==1)=30;
%
norway_2input=[lat long newdepth temp geothermal]
csvwrite('norway2input.csv',norway_2input)

```

### 3.3 Rockall Trough temperature calculation script

```

function[out]=depth(Rockall_Temp)
%
load Rockall_Temp.txt
depth=Rockall_Temp(:,3).*-1;
%
[r,c]=size(depth);          %start of temperature calculations
temp=ones(r,c);
%
D0=depth<0;
temp(D0==1)=50;
D773=depth<=773 & depth>0;
temp(D773==1)=-0.0008*depth(D773==1)+10.26;
D1043=depth<=1043 & depth>773;
temp(D1043==1)=-0.007*depth(D1043==1)+14.981;
D1197=depth<=1197 & depth>1043;

```

```

temp(D1197==1)=-0.0112*depth(D1197==1)+19.463;
D1499=depth<=1499 & depth>1197;
temp(D1499==1)=-0.0049*depth(D1499==1)+11.863;
D1726=depth<=1726 & depth>1499;
temp(D1726==1)=-0.0027*depth(D1726==1)+8.6371;
D3047=depth<=3047 & depth>1726;
temp(D3047==1)=-0.001*depth(D3047==1)+5.7682;
D3048=depth>3047;
temp(D3048==1)=-0.00008*depth(D3048==1)+2.8945;
%
out=[Rockall_Temp temp];
csvwrite('RockallTemp.csv',out)
%
load RockallTemp.csv;
lat=RockallTemp(:,1);
long=RockallTemp(:,2);
temp=RockallTemp(:,4);
depth=RockallTemp(:,3);
%
[r,c]=size(depth);          %Creating a new depth, which makes all depths positive so doesn't effect
hydcalc
newdepth=ones(r,c);
D0=depth<0;
newdepth(D0==1)=depth(D0==1).*-1;
D1=depth>=0;
newdepth(D1==1)=depth(D1==1).*1;
%
[r,c]=size(depth);          %adds geothermal gradient column
geothermal=ones(r,c);
D30=geothermal;
geothermal(D30==1)=30;
%
rockall_2input=[lat long newdepth temp geothermal]
csvwrite('rockall2input.csv',rockall_2input)

```

### 3.4 Iberian temperature calculation script

```

function[out]=depth(spainmorroco)
%
load spainmorroco.txt
depth=spainmorroco(:,3)*-1

[r,c]=size(depth);
temp=ones(r,c);

D0=depth<0;
temp(D0==1)=50;
D62=depth<=62 & depth>0;
temp(D62==1)=-0.0533*depth(D62==1)+20.765;
D92=depth<=92 & depth>62;
temp(D92==1)=-0.0603*depth(D92==1)+20.714;
D1615=depth<=1615 & depth>92;
temp(D1615==1)=(0.0000009*(depth(D1615==1)).^2)-(0.0071*depth(D1615==1))+16.205;
D1979=depth<=1979 & depth>1615;
temp(D1979==1)=-0.0062*depth(D1979==1)+16.626;
D2730=depth<=2730 & depth>1979;
temp(D2730==1)=-0.0018*depth(D2730==1)+7.9157;
D2836=depth<=2836 & depth>2730;
temp(D2836==1)=-0.0009*depth(D2836==1)+5.4982;
D3672=depth<=3672 & depth>2836;

```

```
temp(D3672==1)=-0.0005*depth(D3672==1)+4.3412;
D4440=depth<=4440 & depth>3672;
temp(D4440==1)=-0.00007*depth(D4440==1)+2.7625;
D5070=depth<=5070 & depth>4440;
temp(D5070==1)=0.0001*depth(D5070==1)+2.0;
D5071=depth>=5071;
temp(D5071==1)=2.507;
%
out=[spainmorroco temp];
csvwrite ('spainmortemp.csv',out)
```

## APPENDIX B

<b>1.</b>	<b>Artificial seawater solution composition</b>	<b>1</b>
<b>2.</b>	<b>CO<sub>2</sub> hydrate experiments</b>	
<b>2.1</b>	<b>Run 20 (Sample 2)</b>	<b>2-4</b>
<b>2.1.1</b>	<b>Seawater ice ball formation</b>	<b>2</b>
<b>2.1.2</b>	<b>Sample construction and experimental procedures</b>	<b>3-4</b>
<b>2.2</b>	<b>Run 21</b>	<b>5</b>
<b>2.3</b>	<b>Run 22 (Sample 7)</b>	<b>5-6</b>
<b>2.4</b>	<b>Run 24 (Sample 1)</b>	<b>6</b>
<b>2.5</b>	<b>Run 25 (Sample 3)</b>	<b>6</b>
<b>2.6</b>	<b>Run 28</b>	<b>7</b>
<b>2.7</b>	<b>Run 29 and 30 (Sample 5)</b>	<b>7</b>
<b>2.8</b>	<b>Run 31 (Sample 4)</b>	<b>7-8</b>
<b>2.9</b>	<b>Run 33</b>	<b>8-9</b>
<b>2.10</b>	<b>Run 34 (Sample 6)</b>	<b>9-10</b>
<b>2.11</b>	<b>Run 35</b>	<b>11</b>
<b>2.12</b>	<b>Run 36</b>	<b>11-12</b>
<b>2.13</b>	<b>Run 28</b>	<b>12</b>
<b>3.</b>	<b>Ice experiments</b>	<b>13</b>
<b>4.</b>	<b>Laboratory run sheets</b>	<b>14-31</b>

## 1. Artificial seawater solution composition

Using Krauskopf (1982) as a guide to seawater composition the following salt compositions were used to produce an artificial seawater solution (35 ‰) for CO<sub>2</sub> hydrate and ice experiments.

Salt	Ion	Quantity of salt needed (g/kg)	Quantity of Na <sup>+</sup> or Cl <sup>-</sup> (mol/kg)
NaHCO <sub>3</sub>	HCO <sub>3</sub> <sup>-</sup>	0.19275	2.294 x 10 <sup>-3</sup> Na <sup>+</sup>
NaBr	Br <sup>-</sup>	0.086284	8.386 x 10 <sup>-4</sup> Na <sup>+</sup>
SrCl <sub>2</sub> .6H <sub>2</sub> O	Sr <sup>2+</sup>	0.02434	2 x (9.1303 x 10 <sup>-5</sup> ) Cl <sup>-</sup>
MgCl <sub>2</sub> .6H <sub>2</sub> O	Mg <sup>2+</sup>	10.788	2 x (0.05306) Cl <sup>-</sup>
Na <sub>2</sub> SO <sub>4</sub>	SO <sub>4</sub> <sup>2-</sup>	4.01456	2 x (2.8264 x 10 <sup>-2</sup> ) Na <sup>+</sup>
KCl	K <sup>+</sup>	0.7245	9.7187 x 10 <sup>-3</sup> Cl <sup>-</sup>
CaCl <sub>2</sub> .2H <sub>2</sub> O	Ca <sup>2+</sup>	1.5112	2 x (1.0279 x 10 <sup>-2</sup> )

The solution required a total of 18,800 mg/kg of Cl<sup>-</sup> (Krauskopf, 1982); therefore the final stage was to calculate the quantity of NaCl needed to complete the solution. As Cl<sup>-</sup> is relatively un-reactive the quantity of Na<sup>+</sup> ions was calculated as follows:

$$\begin{aligned} \text{Na}^+ &= 10770 \text{ mg/kg} \\ &= 10.77 \text{ g/kg} \end{aligned}$$

$$1 \text{ mole of Na} = 10.77/22.99 = 0.4685 \text{ mol/kg}$$

$$\begin{aligned} \text{Deduct total Na used (from table above)} &= 0.4685 - 0.0596606 = 0.4088394 \\ &= 0.4088394 \times (22.99 + 35.45) \\ &= 23.89258 \text{ g/kg NaCl} \end{aligned}$$

To make 8 litres of artificial seawater solution the above salts were added to 8 litres of distilled water in the following quantities (all salts used were Analar reagents):

1. 191.141g of NaCl
2. 0.6938g of NaBr
3. 5.9592g of KCl
4. 12.0898g of CaCl<sub>2</sub>.2H<sub>2</sub>O
5. 86.303g of MgCl<sub>2</sub>.6H<sub>2</sub>O
6. 0.1952g of SrCl<sub>2</sub>.6H<sub>2</sub>O
7. 1.5429g of NaHCO<sub>3</sub>
8. 32.1167g of Na<sub>2</sub>SO<sub>4</sub>

## 2. CO<sub>2</sub> hydrate experiments

### 2.1 Run 20 (Sample 2)

This experiment was designed to obtain the maximum quantity of hydrate for SEM analysis using seawater ice balls as a precursor for hydrate growth. To examine the effect of varying pore sizes / sediment grain sizes 4 plastic tubes were placed within a stainless steel pressure vessel to allow the formation of more than one hydrate sample during the same experimental run.

#### 2.1.1 Seawater ice ball formation

Using an ISCO 260D pressure pump artificial seawater solution was injected through 1/16<sup>th</sup> inch tubing at continuous flow rate into a vat of 'bubbling' liquid nitrogen (due to the injection of nitrogen gas; Figure 2.1a). This procedure formed fine (sub-millimetre) frozen seawater ice 'balls' (Figure 2.1b).

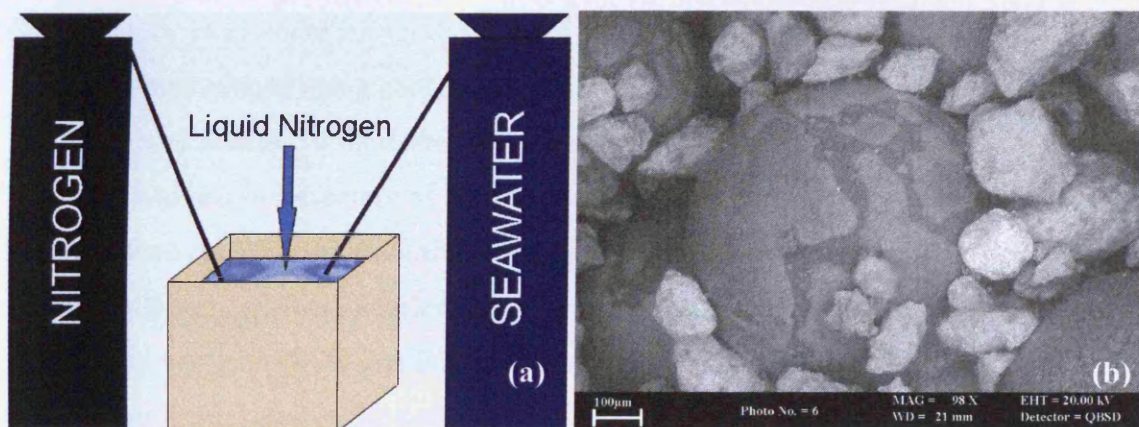


**Figure 2.1(a)** Schematic diagram showing seawater ice balls formation procedure. **(b)** BSEM image of seawater ice ball/quartz rich sediment mix for Run 20. The ice balls can be seen to be surrounded by a crust of salts excluded during ice formation.

### 2.1.2 Sample construction and experimental procedures

Internal plastic sample vessels were constructed using 25mm plastic tubing cut into 4.2cm lengths. A ridge was then etched 2mm from the base of each plastic vessel, and a fine mesh was attached to the base of each vessel using gold wire (Figure 2.2). Each tube was labelled from A to D for sample identification. A known quantity of sediment was weighed into Teflon pressure vessel liners, and this sediment was cooled to liquid nitrogen temperatures by placing in an aluminium coated tray of liquid nitrogen. The previously made seawater ice balls were then sieved from the liquid nitrogen and mixed into the cooled sediment, forming a 50:50 sediment/ice ratio. Inner plastic sample vessels were also cooled to liquid nitrogen temperature, and these were filled with the different sediment and ice mixtures:

Tube A = Seawater ice balls

Tube B = 63-212 $\mu$ m quartz rich sand and seawater ice balls.

Tube C = 150-400 $\mu$ m pure cleaned quartz and seawater ice balls.

Tube D = 355-600 $\mu$ m quartz rich sand and seawater ice balls. **Sample 2.**

Each tube was placed into a cooled stainless steel pressure vessel, and the pressure vessel lid was attached after defrosting the screw threads and ensuring the CO<sub>2</sub> inlet tube was situated in the centre of the experiment. Samples of each sediment/ice ball mixture were placed in aluminium capsules to store for later analysis. The pressure vessel containing all four samples was then placed into a cooled incubator, and slowly pressurised using an ISCO 260D pressure pump filled with liquid CO<sub>2</sub>. A record of the experiment is provided in Section 4, laboratory sheets 1a and 1b.

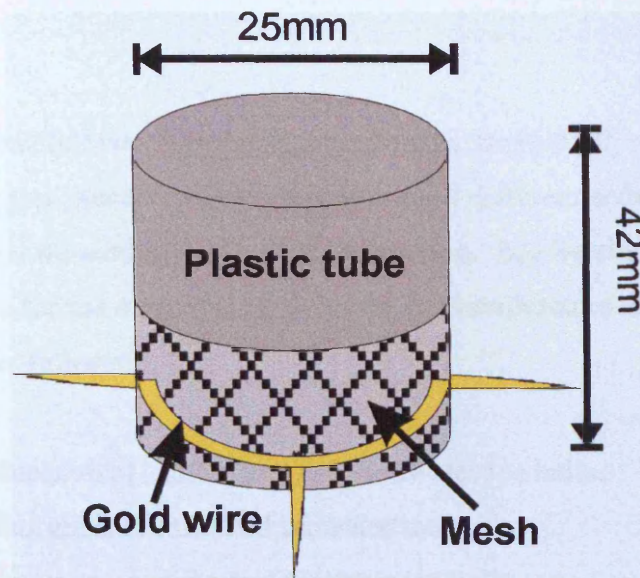


**Figure 2.2.** Schematic diagram of the inner plastic vessels constructed using plastic tubing, fine mesh and gold wiring.

The vessel was depressurised at the end of the experiment using the procedure noted in Chapter 4, and the samples were preserved for later BSEM analysis. Some hydrate/sand fragments were noted in the base of the pressure vessel and on the surface of sample B after depressurisation (Figure 2.3), some of which appeared curved. A few of these curved hydrate fragments were preserved and imaged (see Chapter 5).

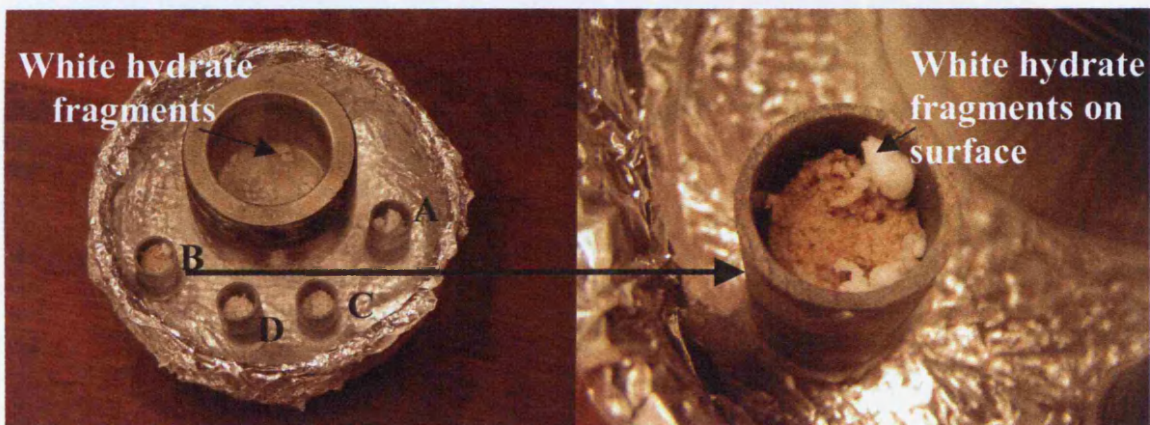


**Figure 2.3 (a)** Stainless steel pressure vessel and plastic sample vessels within aluminium lined tray of liquid nitrogen after depressurisation. The small white hydrate fragments can be seen at the bottom of the pressure vessel. **(b)** Higher magnification image of sample B showing the white hydrate fragments on the surface of the sample.

## 2.2 Run 21

This experimental run followed the same procedure as for Run 20, with four experiments within one pressure vessel; however used different sediments to investigate the effect of different mineralogy on hydrate formation. See Section 4, laboratory sheets 2a, 2b and 2c for the experiments pressure and temperature record. The four experiments were as follows:

Tube E = Muscovite (125-250 $\mu$ m) and seawater ice balls.

Tube F = Georgia Kaolinite and seawater ice balls.

Tube G = Precipitated silica and seawater ice balls.

Tube H = Wyoming Bentonite and seawater ice balls.

## 2.3 Run 22 (Sample 7)

Again this experimental run followed the same experimental technique of producing 4 experimental samples in one vessel, as for Run 20 and Run 21, however the four experiments designed for this run used seawater solution rather than seawater ice balls. The aim of these experiments was to compare the use of seawater ice balls as a precursor for hydrate formation with the formation of CO<sub>2</sub> hydrate in different fully saturated sediments. Sediments fully mixed and saturated with seawater solution were placed into the constructed plastic tubes. These un-cooled inner vessels were placed into a stainless steel pressure vessel at room temperature. Therefore, no liquid nitrogen was used to construct the samples. At the end of the experimental run the pressure vessel was depressurised and the samples preserved as detailed in Chapter 4. The four experimental samples produced during this laboratory run were as follows:

Tube A = Seawater (no sediment). **Sample 7.**

Tube B = Quartz rich sand (355-600 $\mu$ m) fully saturated with seawater.

Tube C = Pure cleaned quartz (150-400 $\mu$ m) fully saturated with seawater.

Tube D = Wyoming bentonite fully saturate with seawater.

See Section 4, laboratory sheet 3 for pressure and temperature conditions throughout the experiment.

#### **2.4 Run 24 (Sample 1)**

This sample was generated using 35.2g of coarse quartz rich sand (600µm-2mm) mixed and fully saturated with 14.1g of seawater solution, with an aim to investigate the effect of salinity, mineralogy and availability of CO<sub>2</sub> and water on hydrate formation (to compare with other samples on analysis). A layer of seawater remained on the surface of the sand (see Chapter 4, Figure 4.1 for schematic diagram). Standard pressurisation and depressurisation procedures were followed, as detailed in Chapter 4. See Section 4, laboratory sheet 4 for pressure and temperature conditions.

#### **2.5 Run 25 (Sample 3)**

This sample was generated using 44.4g of quartz rich sand (355-600µm) mixed with 13.1g of seawater solution. After placing the mixed seawater and sand into a Teflon liner, seawater was extracted using a paper towel; absorbing seawater and removing it from the sediment pores. The paper towel was weighed before and after seawater extraction to enable calculation of the quantity of seawater remaining in the sediment. Approximately 2.3g of seawater remained in the sediment; therefore leaving the sample partially saturated, with 4.9% seawater and 95.1% sand. This sample was then placed into a stainless steel pressure vessel. Standard pressurisation and depressurisation procedures were followed, as detailed in Chapter 4

The main aim of this experiment was to investigate sediment-hosted hydrate formation in a partially water saturated environment. See Section 4, laboratory sheet 5 for pressure and temperature conditions.

## **2.6 Run 28**

An experiment to investigate hydrate formation in natural sediment. Natural unsorted sandy sediment from Anglesey (see Chapter 5) was washed in de-ionised water, and 71.7g of this sediment was mixed with 19.7g of seawater solution and placed in a Teflon liner. Standard experimental laboratory procedures were followed. See Section 4, laboratory sheet 6 for pressure and temperature conditions.

## **2.7 Run 29 and 30 (Sample 5)**

Both sample Run 29 and sample Run 30 (Sample 5) were generated at the same time using two separate pressure vessels in one incubator. Run 29 was composed of 50.4g of natural sandy sediment (used in Run 28) mixed and fully saturated with 16.7g of deionised water. Run 30 was composed of 50.4g of quartz rich sand (355-600 $\mu$ m) mixed and fully saturated with 17.5g of deionised water. These experiments were designed to compare pure water systems with seawater systems and hence, the effect of salinity on sediment-hosted CO<sub>2</sub> hydrate formation. Standard experimental laboratory procedures were followed. See Section 4, laboratory sheet 7 for pressure and temperature conditions.

## **2.8 Run 31 (Sample 4)**

This experiment was designed to investigate CO<sub>2</sub> hydrate formation along different sediment contact points. A cardboard 3 face divider was constructed and inserted into a Teflon liner (Figure 2.4) to separate 3 different fully saturated sediments. Quartz rich sand (355-600 $\mu$ m), natural sandy sediment, and Wyoming bentonite were fully saturated and mixed with seawater solution. These fully saturated sediments were then placed into separate compartments in the Teflon liner. After applying slight compression to each sample to remove any voids, the cardboard divider was removed, allowing the sediments to come into contact with one another. The sample was pressurised and depressurised using standard procedures. There was a pressure relief valve failure at the beginning of the experiment, causing a temperature reduction, but

this did not affect the remainder of the experimental run. See Section 4, laboratory sheet 8 for experimental run pressure and temperature conditions.

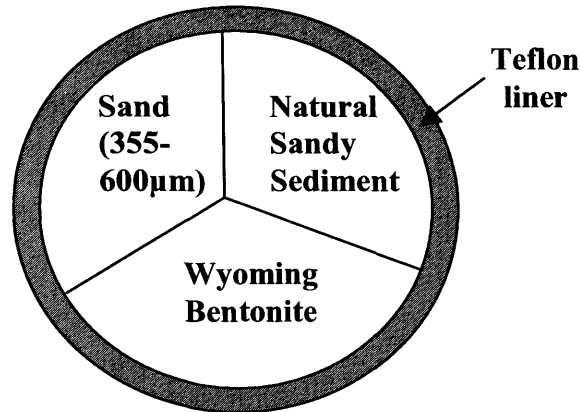


**Figure 2.4.** Schematic diagram showing the relationship between the three different sediments used to form sample run 31.

## 2.9 Run 33

This experiment was designed to try and maximise the quantity of CO<sub>2</sub> hydrate within a sediment sample, by placing a magnetic stirrer bead underneath the sample to aid CO<sub>2</sub> diffusion into the pore waters. 21.3g of quartz rich sand (355-600µm) fully saturated and mixed with 7.1g of seawater was placed within an inner plastic vessel (same as that used in Run 20, 21, and 22). A magnetic stirrer bead was placed within a shallow hollow tube with semi-circular cut out sections to allow water to escape. This shallow tube was then placed beneath the inner plastic vessel (Figure 2.5). Semi-circular sections of tubing were placed around this centrally positioned inner plastic vessel to prevent sample movement. The pressure vessel lid was carefully placed onto the vessel base to ensure the CO<sub>2</sub> inlet tube and thermocouple was positioned into the sample. Standard pressurisation and depressurisation procedures were followed, with the vessel placed onto a magnetic stirrer plate to turn the internal magnetic stirrer bead. See Section 4, laboratory sheet 10 for pressure and temperature conditions.

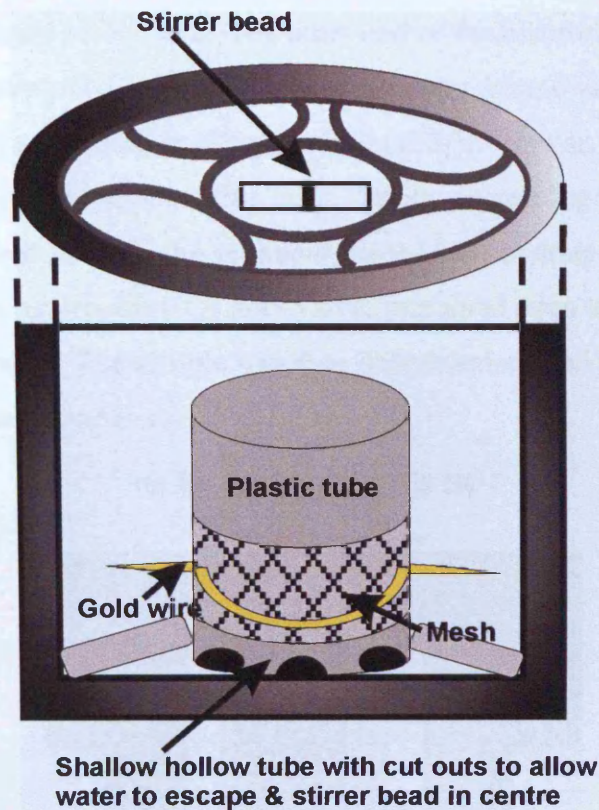


**Figure 2.5.** Schematic diagram showing the relative internal experimental structure inside the stainless steel pressure vessel used for run 33.

### 2.10 Run 34 (Sample 6)

This sample was generated using coarse quartz rich sand (600 $\mu$ m-2mm) fully saturated and mixed with seawater solution. After placing the sand and seawater mix into an aluminium liner, seawater was extracted using a paper towel; absorbing seawater and removing it from the sediment pores (the same technique used in Run 25). The paper towel was weighed before and after seawater extraction to enable calculation of the quantity of seawater remaining in the sediment. The remaining sample was partially saturated with 8.1% seawater. This sample was then placed inside a coil of steel tubing attached to a stainless steel pressure vessel lid through inlet and outlet valves. The lid was then placed onto the pressure vessel base (see Figure 2.6). Standard pressurisation procedures were followed, as detailed in Chapter 4. At the end of the experiment the sample was depressurised using a newly developed technique. A cooling coil made of steel tubing was attached to the sample pressure vessel by connecting the tubing to the

inlet valve of the internal vessel coil. The other end of the external cooling coil was then attached to a bottle of Helium with a fitted pressure release valve. This external cooling coil was then submersed in a liquid nitrogen filled Dewar. Helium was injected through the external and internal cooling coils, rapidly decreasing the temperature of the pressure vessel, and freezing the sediment-hosted CO<sub>2</sub> hydrate sample in-situ. Throughout this cooling process CO<sub>2</sub> inlet valves remained open to maintain the internal sample pressure. The sample was then depressurised and preserved using standard experimental procedures.

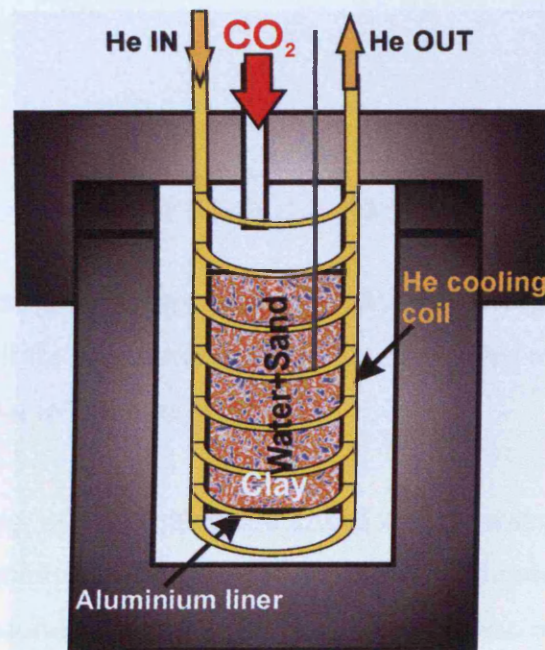


**Figure 2.6.** Schematic diagram of Run 34 batch experiment with an added Helium cooling coil surrounding an aluminium liner encasing the partially water saturated sand. The Helium coil allowed sample preservation in-situ, at pressure.

The main aims of this experiment were to investigate sediment-hosted hydrate formation in a partially deionised water saturated environment, and to minimise any effects of experimental depressurisation techniques. See Section 4, laboratory sheet 11 for pressure and temperature conditions.

## **2.11 Run 35**

The aim of this experiment was to form a solid seawater CO<sub>2</sub> hydrate sample (no sand), optimising the quantity of CO<sub>2</sub> hydrate in the sample by the use of a magnetic stirrer bead. A Teflon liner was filled with 78.2g of seawater solution and a magnetic stirrer bead was placed into the seawater. Standard pressurisation and depressurisation techniques were used during the experiment, with the addition of the use of a magnetic stirrer plate (as used in Run 33). See Section 4, laboratory sheet 12 for pressure and temperature conditions.

## **2.12 Run 36**

This experiment was designed to represent a CO<sub>2</sub> hydrate storage system, and was the most complicated of all the experiments conducted during this research project. The basic design was similar to that used in Run 34.

Wyoming bentonite clay fully saturated and mixed with seawater solution was pressed into the base of an aluminium liner. The remainder of the aluminium liner was completely filled by natural sandy sediment fully saturated and mixed with seawater solution. This liner was then inserted inside a steel tube cooling coil attached to a stainless steel pressure vessel lid (Figure 2.7). This cooling coil was the same used in Run 34. A CO<sub>2</sub> inlet tube could then be inserted into the centre of the filled aluminium liner, ensuring the tube ended just above the clay layer, to enable the formation of a liquid CO<sub>2</sub> 'bubble' beneath a clay layer representing a caprock (after sample inversion). The experiment was sealed by fitting the pressure vessel lid to its base.

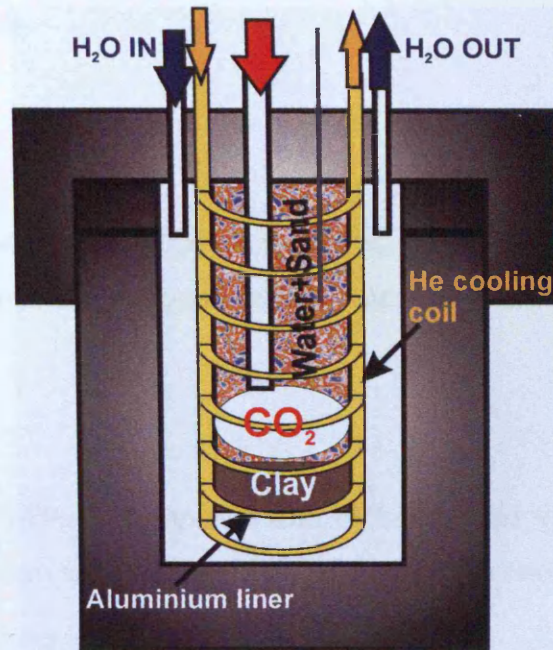


**Figure 2.7.** Schematic diagram of Run 36 batch experiment with an added Helium cooling coil surrounding an aluminium liner encasing the fully seawater saturated sand and clay. The experiment was inverted and pressurised with seawater. Liquid CO<sub>2</sub> was then injected beneath the clay 'cap'. The Helium cooling coil allowed sample preservation in-situ, at pressure.

and CO<sub>2</sub> gas reservoirs, see how, and reproduced using standard procedure.

The sample was inverted, pressurised to 200 bar with seawater solution, and then 9ml of liquid CO<sub>2</sub> was injected into the sample. The temperature and pressure were monitored throughout the experiment (see laboratory sheet 13a, 13b).

On depressurisation the sample was cooled in-situ using the technique described for Run 34.

### 2.13 Run 28

This experiment was a repeat of Run 33. See Section 4, laboratory sheet 14 for pressure and temperature conditions.

### **3. Ice experiments**

#### **Fridge 1**

Quartz rich sand (355-600 $\mu$ m) dampened with 18% seawater solution. The sample was slowly cooled to sub-zero temperatures and then placed in a chest freezer at -18°C.

#### **Fridge 2**

Quartz rich sand (355-600 $\mu$ m) dampened with 18% deionised water. The sample was slowly cooled to sub-zero temperatures and then placed in a chest freezer at -18°C.

#### **Run 32**

Quartz rich sand (355-600 $\mu$ m) fully saturate with seawater solution. A Teflon liner was filled with 65.5g of quartz rich sand fully saturated and mixed with seawater solution, and placed into a stainless steel pressure vessel. The experiment was pressurised with liquid CO<sub>2</sub> for approximately one hour, and depressurised using standard procedures described in Chapter 4. The sample was seen to contain CO<sub>2</sub> hydrate after depressurisation; however this sample was then placed into a chest freezer at -18°C and all CO<sub>2</sub> hydrate present dissociated before analysis. See Section 4, laboratory sheet 9 for pressure and temperature conditions.

4. Laboratory run sheets

Laboratory Sheet 1a

HYDRATE Laboratory Run Sheet

Whole Run in BS7

Run No. 20

Experiment 4 internal tubes forming hydrate with seawater ice.  
 Cubicle Incubator  
 Vessel B45 018

Initial Solid + capsule wt (g)  
 Initial capsule wt (g)  
 Initial Solid wt (g)  
 Initial Fluid volume (ml)  
 Fluid : Solid ratio  
 Solid Area  
 Weight after welding (g)  
 Final Solid + capsule wt (g)  
 Final Solid wt (g)  
 Solid weight loss/gain (g)

Thermocouple # Added  
 Run Temperature Variable  
 Rupture disc

Applicable Procedures:-

Notes:- Vary temp to melt + reform ice > to form masses of hydrate.  
 A, B, C, D - internal tubes. A - pure seawater, B - coarse sand, C - pure quartz sand, D - fine

on 1500 controller

Sample	Date	Time	Elaps. Time		T °C	P (psig) (bar)	Volume			Flow Rate	pH	Comments
			Total	t			Flush	Samp	Left			
	29/10/04	14:25			-5					100 set to -5°C		ON
	11/1/04	11:40			-3.3	36				Raised pressure slowly to 36 bar by blanking CO <sub>2</sub> slowly to the valves from the pump.		
										Note - seem to have pump controller set +5.0 bar relative to separate transducer. - have had inside seal thermocouple at +0.1°C above other two. Wiggled the connections to see if this helps.		
	"	11:50			-2.9	45.3				Set programmed gradual increase in pressure at 0.2 bar/min to go to 200 bars		
	"	11:55			-2.6	46.3				Stopped pressure increase for a few minutes as the gas > liquid transition was making the temperature rise too rapidly		
	"	12:10			-2.6	47.3				As above but left on land		
	"	14:05			-3.0	48.0				Restarted pressure increase Set incubator to -7.0°C		
	2/11/04	13:30			-5.1	168				Increased pressure manually to 200 bar Incubator reading 2.0°C low Set <del>incubator</del> temp to read by 1°C.		

# Laboratory Sheet 1b

AF

## HYDRATE Laboratory Run Sheet

Whole run in (BST)

Run No. 20 CONT.

Experiment 4 internal tubes forming hydrate with seawater ice  
Cubicite ~~BS-018~~ Incubator

Vessel BS-018

Thermocouple # Added

Run Temperature Variable

Rupture disc —

Applicable Procedures: —

Initial Solid + capsule wt (g)  
Initial capsule wt (g)  
Initial Solid wt (g)  
Initial Fluid volume (ml)  
Fluid : Solid ratio  
Solid Area  
Weight after welding (g)  
Final Solid + capsule wt (g)  
Final Solid wt (g)  
Solid weight loss/gain (g)

Notes:- Vary temp to melt + reform ice → form large quantities of hydrate.  
A, B, C, D - internal tubes  
A = pure seawater ice balls  
B = coarse sand  
C = fine quartz sand  
D = fine sand.

Sample	Date	Time	Elaps. Time		T °C	P (psig)	Volume			Flow Rate	pH	Comments
			Total	t			Flush	Samp	Left			
	4/11/04	12:37			-4.1	200						Increased temp to -5 on incubator hence to -5 inside vessel incubator out by 2°C
	"	"										Temp on comp not changed for winter
	"	"										Need to change temp before next
	5/11/04	10:32			-3.3	200						Increased temp to -2°C -4 on incubator to be left over weekend
	"	"										just below -2°C
	9/11/04	15:22			-2.4	200						Change temp to +3°C on incubator
	10/11/04	12:00			-1.6	200						Change incubator to -10°C
	12/11/04	10:40			-8	200						Change incubator to -1°C
	"	15:25			-0.4	200						Change temp on incubator to -1°C
	"	<del>10:25</del>			-	200						Power off so triggered up exp
	17/11/04	11:25			-9.2	200						increase incubator temp to -1°C
	"	10:50			-0.2	200						Decrease temp on incubator to -1°C
	19/11/04	11:05			1.8	200						increase? OFF

Laboratory Sheet 2a

APC

HYDRATE Laboratory Run Sheet

Run No. 21

Experiment 4 internal tubes containing bentonite, muscovite, kaolinite + silica with seawater ice.

Cubicle

Vessel BGS018

Thermocouple # Added

Run Temperature Variable

Rupture disc -

Applicable Procedures: -

Initial Solid + capsule wt (g)  
 Initial capsule wt (g)  
 Initial Solid wt (g)  
 Initial Fluid volume (ml)  
 Fluid : Solid ratio  
 Solid Area  
 Weight after welding (g)  
 Final Solid + capsule wt (g)  
 Final Solid wt (g)  
 Solid weight loss/gain (g)

Notes: - Vary temp to melt + reform ice/hydrate  
 M = Muscovite (HTL 100)  
 F = Coarse Kaolinite (HTL 53)  
 G = Silica (HTL 82)  
 H = Bentonite (Bentonite) (HTL 11)

lac  
x

Sample	Date	Time	Elaps. Time		T °C	P (psig) (bar)	Volume			Flow Rate	pH	Comments
			Total	t			Flush	Samp	Left			
	26/11/04	15:55			-10	0						Put in incubator ready for pressuring to 200 bar after weekend.
	29/11/04	11:10			-9	0						Coverts switched on
	"	13:00			-6	40						Started to pressurise slowly by manually opening valves.
	"	13:15			-4	40						Pump + vessels connected, leave to stabilize temperature
	"	13:20			-4	40						Shut valve to pump, temp rise was too fast (high CO <sub>2</sub> formation in vessel?). Leave overnight to settle.
	30/11/04	09:35			-8.2	31						Manually started to add more CO <sub>2</sub> to vessel.
	"	09:50			-6.7	48.7						Raised pressure with pump very slowly via a programmed gradient. To 50 bar in 1 hour. Should all be full of liquid.
	"	12:25			-7.8	55.8						P seems to have gone > 50 bar! But all seems OK. Set P to increase to 100 bar at 0.2 bar/min
	"	14:00			-7.9	74.4						Increased rate to 0.5 bar/min as temp staying low and flow rate has come down. Re-filled now.

Laboratory Sheet 2b

HYDRATE Laboratory Run Sheet

Run No. Run 21 cont

Experiment *Internal tubes filled with fines + seawater, ice balls.*

Cubicle

Vessel *865018*

Thermocouple # *Added*

Run Temperature *Variable*

Rupture disc

Applicable Procedures:-

- Initial Solid + capsule wt (g)
- Initial capsule wt (g)
- Initial Solid wt (g)
- Initial Fluid volume (ml)
- Fluid : Solid ratio
- Solid Area
- Weight after welding (g)
- Final Solid + capsule wt (g)
- Final Solid wt (g)
- Solid weight loss/gain (g)

Notes:- *Vary temp to melt + reform ice*

Sample	Date	Time	Elaps. Time		T °C	P (psig)	Volume			Flow Rate	pH	Comments
			Total	t			Flush	Samp	Left			
	1/12/04	12:26			-8.15	200						increase temp to -
	"	"			-10.10	200						on incubator
	04/12/04	17:27			-5.05	200						increase temp to -
	"	"			-6.00	200						leave at -5 overnight
	02/12/04	10:30			-4.87	200						increase temp to -
	"	14:40			-3.2	200						-4.5°C on incubator
	03/12/04	10:40			-3.04	200						leave overnight
	"	"			-4.50	200						increase to -1
	"	15:30			-1.0	200						-2.2°C on incubator
	"	"			"	200						Remove to -10 on
	"	"			"	200						leave for weekend
	07/12/04	11:30			-8.0	200						increase temp to 0
	"	"			"	200						(-1 on incubator)
	"	16:34			-0.17	200						decrease to -2°C
	08/12/04	12:50			-4.03	200						-5.8°C on incubator
	"	"			"	200						increase to -1 on
	17/12/04	14:38			0.22	200						decrease day but to
	"	15:00			0.0°C	200						(stand left in pump)
	21/12/04	16:20			0.16	200						Refilled pump w/
	"	"			-1.1 on incubator	200						
	22/12/04	15:27			0.27	200						
	"	"			-1.1 on incubator	200						
	24/12/04	10:20			0.25	250 on pump						← But other transducer + gauge read ~
	"	"			-1.1 on incubator	200						bar. Calibration seems to have gone
												off. Treat g mechanical gauges
												re-set pump to 210 bar.
												To give gauges at ~200 bar

*Handwritten signature and notes at the bottom of the page.*



# Laboratory Sheet 3

A

## HYDRATE Laboratory Run Sheet

Run No. 22

Experiment 4 mm tubes with seawater

Cubicle 845018 Inshore

Vessel ↓

Thermocouple # Aided

Run Temperature 2°C

Rupture disc

Applicable Procedures:-

Initial Solid + capsule wt (g)  
 Initial capsule wt (g)  
 Initial Solid wt (g)  
 Initial Fluid volume (ml)  
 Fluid : Solid ratio  
 Solid Area  
 Weight after welding (g)  
 Final Solid + capsule wt (g)  
 Final Solid wt (g)  
 Solid weight loss/gain (g)

Notes:- Using black BOX gas cylinder under desk  
 as need new one for outside.

Sample	Date	Time	Elaps. Time		T °C	P (psig) bar	Volume			Flow Rate	pH	Comments
			Total	t			Flush	Samp	Left			
	26/10/05	15:12			2°C	200						ON
	28/11/05	10:10			3.4	35.9						No CO <sub>2</sub> left in pipe. Possible leaks - odd temp trace ~ 13.00 x 100 bar day
	"	17:10			8.9	200						Back at pressure, but found some remaining inside vessel when compressed the CO <sub>2</sub>
	"	18:10			6.8	200						Gas going down in pipe too fast - suspect a leak, sealed off all valves
	31/10/05	9:45			3.2	140						Some dip in pressure over weekend
	"	9:50	4.4		<del>3.2</del>	200						Back at pressure
	"	15:00			-	-						<del>Back at pressure</del> Finished on temp traces/long due to working on Run 23 which is on the same line and x the same water
	9/2/05	10:56			2.35	200						OFF

# Laboratory Sheet 4

## HYDRATE Laboratory Run Sheet

A. Lamp.

Run No. 24

Experiment Supply of 18

Cubicle

Vessel BGS018

Thermocouple # Added

Run Temperature Variable

Rupture disc

Applicable Procedures:-

- Initial Solid + capsule wt (g)
- Initial capsule wt (g)
- Initial Solid wt (g)
- Initial Fluid volume (ml)
- Fluid : Solid ratio
- Solid Area
- Weight after welding (g)
- Final Solid + capsule wt (g)
- Final Solid wt (g)
- Solid weight loss/gain (g)

Notes:- Seawater + coarse sand (600µm - 2mm) in large teflon liner. Repeat of 18.

Sample	Date	Time	Elaps. Time		T °C	P (psig)	Volume			Flow Rate	pH	Comments
			Total	t			Flush	Samp	Left			
	11/02/05	3:50pm			-3.5	170						ON
	17/02/05	3:45pm			-3.5	170						refilling pump + change receptacle
	15/02/05	4:19pm			-2.1	170						check temp - 3
	16/02/05	3:10pm			-2.1	170						22.67 ml left in
	17/02/05	12:09pm			-3.5	170						29.38 ml left
	"	16:18			-3.5	170						14.48 ml left
	18/02/05	14:57			-3.5	170						
	21/2/05	11:55			-3.7	76.9						Pump empty, but still 4g. 20% in expt.
	"	12:15			-2.6	170						Repressured.
	22/2/05	14:30			-3.6	170						Refill pump
	"	11:45			-3.8	170						
	23/2/05	12:46			-3.7	170						Refill
	1/3/05	10:45			-3.5	170						(No Temp to 2)
			(New Pico file opened 85.2 change name after exp)									
	3/3/05	17:45			+3.1°	170						* Pico log generated so no data file
	1/3/05	09:59			+2.0°	170						- Mini file Run-2.4pwr 3
												Refilled pump
	"	10:50			+2.2	170						OFF



# Laboratory Sheet 6

## HYDRATE Laboratory Run Sheet

Run No. 28

Experiment *CO<sub>2</sub> hydrate in natural sediment*  
 Cubicle *Incubator*  
 Vessel *β GFS 018*  
 Thermocouple # *Added*  
 Run Temperature *2°C (incubator)*  
 Rupture disc  
 Applicable Procedures:-  
 Initial Solid + capsule wt (g)  
 Initial capsule wt (g)  
 Initial Solid wt (g)  
 Initial Fluid volume (ml)  
 Fluid : Solid ratio  
 Solid Area  
 Weight after welding (g)  
 Final Solid + capsule wt (g)  
 Final Solid wt (g)  
 Solid weight loss/gain (g)  
 Notes:-

Sample	Date	Time	Elaps. Time		T °C	P (psig)	Volume			Flow Rate	pH	Comments
			Total	t			Flush	Samp	Left			
	10/06/05	13:36			2°C	200						on
	"	17:31			2°C	200						438m
	18/06/05	15:58			2.01	200						As the thermocouples reading correct Reduced to 1°C 1% of incubator
	"	"			"	"						337.7ml (0.5ml/h)
	18/06/05	16:18			2.17	200						296.57ml
	"	"			"	"						
	16/06/05	17:23			2.26	200						274.53ml
	"	"			"	"						187.98ml
	19/06/05	14:59			2.35	200						dec temp applied 311ml
	"	"			"	"						
	24/06/05	14:09			2.08	200						193.88 (0.72ml)
	"	"			"	"						refilled to 4.03ml
	"	14:24			1.99	200						flow data set Run 25 part
	"	15:48			2.08	200						389.67ml
	28/06/05	12:27			2.03	200						286.82ml (0.8ml)
	"	18:09			2.26	200						242.48ml
	8/07/05	11:47			1.94	200						213.82ml
	"	18:00			2.08	200						212.86ml
	9/07/05	13:21			1.85	200						145.76ml (0.7ml)
	"	13:27			1.78	200						refilled pump (4.3ml)
	"	15:50			1.89	200						4.21 ml
	10/07/05	10:53			2.05	200						278.73ml
	13/07/05	13:44			2.15	200						230.10ml
	"	"			"	"						CF

# Laboratory Sheet 7

## HYDRATE Laboratory Run Sheet

Run No. 29 & 30

Experiment  $CO_2$  hydrate in natural  
Cubicle incubator Sediment & 30 =  
Vessel BG5018 + BG5022 *artificial*

Thermocouple # Added

Run Temperature 2°C (incubator) <sup>0.8°C</sup>

Rupture disc

Applicable Procedures:-

*Demin water used*

Initial Solid + capsule wt (g)  
Initial capsule wt (g)  
Initial Solid wt (g)  
Initial Fluid volume (ml)  
Fluid : Solid ratio (Run-26. PLW)  
Solid Area  
Weight after welding (g)  
Final Solid + capsule wt (g)  
Final Solid wt (g)  
Solid weight loss/gain (g)

Notes:-

Sample	Date	Time	Elaps. Time		T °C	P (psig)	Volume			Flow Rate	pH	Comments
			Total	t			Flush	Samp	Left			
	13/07/05	17:37			200	200						ON
	"	"			18.9°	200						refilled pump
	"	18:09			19.6°	200						380ml.
	17/07/05	12:41			1.96	200						Refilled 423ml
	"	13:21			1.39	200						hydrocarbon slight
	"	16:51			2.17	200						4.0978
	19/07/05	16:57			1.96	200						351.81ml
	24/07/05	11:21			1.78	200						335.70ml
	25/07/05	10:23			1.89	200						
	26/07/05	14:18			1.92	200						213.61ml
	27/07/05	15:42			2.01	200						189.59ml
	27/07/05	16:08			2.03	200						140.64ml
	"	"			1.92	200						Refilled 405.
	"	"			"	"						New PLW - Run 21
	11/08/05	15:47			2.01	200						319.88ml
	31/08/05	12:28			1.94	200						272.74ml
	5/08/05	15:32			2.01	200						223.24ml
	"	"			1.83	200						refilled to 397.19ml
	10/08/05	15:54			2.01	200						260.36ml
	11/08/05	11:24			1.89	200						255.37ml
	"	11:27			1.83	200						refilled to 431ml
	15/08/05	16:28			1.99	200						320.68ml
	"	"			"	"						started Run 26 - p
	7/08/06	15:28			2.05	200						OFF

# Laboratory Sheet 8

## HYDRATE Laboratory Run Sheet

Run No. **31**

Experiment **CO<sub>2</sub> in 3 diff sediments for contact points**

Cubicle **Hubarr**

Vessel **BGS 018**

Thermocouple # **Added**

Run Temperature **Variable**

Rupture disc

Applicable Procedures:- **Seawater**

Initial Solid + capsule wt (g)  
 Initial capsule wt (g)  
 Initial Solid wt (g)  
 Initial Fluid volume (ml)  
 Fluid : Solid ratio  
 Solid Area  
 Weight after welding (g)  
 Final Solid + capsule wt (g)  
 Final Solid wt (g)  
 Solid weight loss/gain (g)

Notes:-

Sample	Date	Time	Elaps. Time		T °C	P (psig)	Volume			Flow Rate	pH	Comments
			Total	t			Flush	Samp	Left			
	27/09/05	16:42	0	00	12.05	200						ON 377m
	28/09/05	17:47			11.22	200						324.59 ml
	29/09/05	07:25	39 hours		11.01	200						308.44 ml - d
		17:00			3.06	200						298.15 ml
	30/09/05	14:06			2.97	200						284.53 ml
	4/10/05	16:47			3.02	200						208.66 ml
	6/10/05	18:01			3.08	200						171.46 ml
	7/10/05	10:04			3.02	200						158.27 m
	11	10:44			2.24	200						Additional run per 50 hrs (week) sh About 138 ml used
												repressurising refill pump
		10:48			2.90	200						temp when shut
		10:57			4.14	200						microbar
		11:40			5.46	200						rise values for
		13:07			4.59	200						Run 32
		14:36			4.25	200						Run 33 and 34 temp reduced O=F
	10/10/05	12:47			2.33	200						









# Laboratory Sheet 13a

## HYDRATE Laboratory Run Sheet

Run No. 36

Experiment Clay cap with CO<sub>2</sub> (l) bubble  
 in sand fully saturated with seawater. He to pressure  
 incubator Water to pressure

Vessel 868 C16

Thermocouple # Added

Run Temperature Variable

Rupture disc

Applicable Procedures:-

Notes:-

Initial Solid + capsule wt (g)  
 Initial capsule wt (g)  
 Initial Solid wt (g)  
 Initial Fluid volume (ml)  
 Fluid : Solid ratio  
 Solid Area  
 Weight after welding (g)  
 Final Solid + capsule wt (g)  
 Final Solid wt (g)  
 Solid weight loss/gain (g)

Sample	Date	Time	Elaps. Time		T °C	P. (psig)	Volume			Flow Rate	pH	Comments
			Total	t			Flush	Samp	Left			
	5/04/06	13:45			19.0	200						ON 16.2
	6/04/06	10:08			10.4	150						Perme dropped
	"	10:17			10.9	200						1.5 ml of H <sub>2</sub> O
	"	"			"	"						3.45 ml
	7/04/06	09:43			10.5	200						very low much the
	"	11:05			10.9	200						injection leak
	"	15:30			11.4	200						refilled pump
	"	16:36			11.15	200						36.0ml in pump
	12/04/06	10:00			11.1	0						37.6ml
	"	"			"	"						All pressure was
	"	"			"	"						pump & valve
	"	"			"	"						Have to load with
	12/04/06	11:31			11.5	200						Assessed with log
	"	"			"	"						water - 35% water
	12/04/06	16:30			11.4	200						measured about 90
	"	"			"	"						CO <sub>2</sub>
	"	16:59			12.01	200						Refilled pump
	"	"			"	"						lowered temp to
	"	17:10			12.10	200						New profile present
	20/04/06	11:21			6.28	200						1.5 ml left for
	21/04/06	11:39			4.55	200						7.5 ml left refill
	21/04/06	12:09			4.87	200						raised temp to
	24/04/06	12:00			9.79	200						inject CO <sub>2</sub>
	"	15:34			9.63	200						inject CO <sub>2</sub> - dead
	27/04/06	15:40			10.33	200						inject CO <sub>2</sub> & refill
	"	16:21			11.44	200						inject
	"	"			"	"						lower temp to
	28/04/06	17:21			6.33	200						lower temp to



# Laboratory Sheet 14

## HYDRATE Laboratory Run Sheet

Run No. 38

Experiment 300-600µm sand fully  
 submerged with artificial seawater  
 & stirrer bench  
 incubator

Cubicle

Vessel B45018

Thermocouple # Added

Run Temperature Variable

Rupture disc

Initial Solid + capsule wt (g)  
 Initial capsule wt (g)  
 Initial Solid wt (g)  
 Initial Fluid volume (ml)  
 Fluid : Solid ratio  
 Solid Area  
 Weight after welding (g)  
 Final Solid + capsule wt (g)  
 Final Solid wt (g)  
 Solid weight loss/gain (g)

Applicable Procedures:-

Reverse at (2)

Notes:-

Sample	Date	Time	Elaps. Time		T °C	P (psig)	Volume			Flow Rate	pH	Comments
			Total	t			Flush	Samp	Left			
	22/05/06	18:24			10.1	200						9N
	"	"			12.2	200						refill pump 45
	"	18:22			18.6	200						cool incubator to 3
	"	18:38			18.6	200						
	"	18:00			18.4	200						turn stirrer off
	25/05/06	10:48			17.6	200						thermocouple broken
	26/05/06	18:54			22	200						41.3ml
	1/06/06	18:07			22	200						39.375ml
	09/06/06	18:25										39.84ml
	26/06/06	18:04			19.6	200						33.263ml
	5/07/06	12:54			2°C	200						31.4ml of